



Development of a microfluidic device for gaseous formaldehyde sensing

Zur Erlangung des akademischen Grades eines
DOKTORS DER INGENIEURWISSENSCHAFTEN (Dr.-Ing.)

von der KIT-Fakultät für Maschinenbau des
Karlsruher Instituts für Technologie (KIT)

angenommene

DISSERTATION

von

M. Sc. Daniel Măriuța

aus Răucești, Rumänien

Tag der mündlichen Prüfung: 20.06.2022

Hauptreferenten: Jan G. KORVINK
Jürgen J. BRANDNER
Lucien BALDAS

Korreferenten: Thomas HANEMANN
Jens ANDERS
David NEWPORT
Christine BARROT-LATTES
Stéphane COLIN

Karlsruher Institut für Technologie
Institut für Mikrostrukturtechnik
Hermann.-v.-Helmholtz Platz 1
76344 Eggenstein-Leopoldshafen, Germany



This document is licensed under a Creative Commons Attribution-NonCommercial-ShareAlike 4.0 International License (CC BY-NC-SA 4.0):
<https://creativecommons.org/licenses/by-nc-sa/4.0/deed.en>



THÈSE

**En vue de l'obtention du
DOCTORAT DE L'UNIVERSITÉ DE TOULOUSE
Délivré par l'Institut National des Sciences Appliquées de
Toulouse**

Cotutelle internationale: KARLSRUHE INSTITUTE OF TECHNOLOGY (KIT)

**Présentée et soutenue par
Daniel MARIUTA**

Le 20 juin 2022

**Développement d'un dispositif microfluidique pour la détection
de formaldéhyde à l'état gazeux**

Ecole doctorale : **MEGEP - Mécanique, Energétique, Génie civil, Procédés**

Spécialité : **Dynamique des fluides**

Unité de recherche :
ICA - Institut Clément Ader

Thèse dirigée par
Lucien BALDAS et BRANDNER Juergen J.

Jury

M. Thomas HANEMANN, Rapporteur
M. David NEWPORT, Rapporteur
Mme Christine BARROT-LATTES, Examinatrice
M. Stéphane COLIN, Examineur
M. Jens ANDERS, Examineur
M. Jan G. KORVINK, Examineur
M. Lucien BALDAS, Directeur de thèse
M. Veit HAGENMEYER, Président

Université de Toulouse
Institut National des Sciences Appliquées Toulouse
135 Av. de Ranguel,
31400, Toulouse, France

*“Never discourage anyone who continually makes progress,
no matter how slow.”*

Plato

*Dedicated to my parents
and to my dear wife.*

Acknowledgment

I would like to express my gratitude to my supervisors who guided and encouraged me with patience throughout this experience. Without the continuous assistance of Prof. Lucien Baldas and Prof. Dr. Jürgen J. Brandner, it is difficult to imagine how this thesis would have been finished.

I am also thankful to Prof. Jan G. Korvink, Prof. Stéphane Colin, Dr. Christine Barrot-Lattes, Dr. Stéphane Le Calvé, and Prof. Aldo Frezzotti for providing unconditional support and valuable guidance. I would like to express my gratitude to Prof. Veit Hagenmeyer for presiding the examination committee and also to the reviewers of the manuscript, Dr. David Newport, Prof. Thomas Hanemann, and Prof. Lucien Baldas for their constructive feedback and comments.

I am very thankful to the staff personnel from the Institute of Microstructure Technology (IMT) at KIT, Karlsruhe, Institute Clement Ader Toulouse, and ICPEES Strasbourg for their support and help during the design, fabrication, and experimental works.

Moreover, I would like to express my gratitude to the Marie Skłodowska-Curie Actions for the training and career development opportunities which I was able to pursue as a MIGRATE network Marie-Curie Fellow.

The emotional support, care, and love received from my dear wife during this time was very precious. Thank you, Lidia! I feel so happy to have the chance to acknowledge my parents for their effort in educating and raising three children. Veronica, you are highly missed and I also dedicate this achievement to you.

In the end, I want to thank all the people I met and friends I made during my stays in Toulouse, Karlsruhe, Strasbourg, and Milan. Thank you for the wonderful time we spent and for the great memories we made together.

Abstract

Formaldehyde (HCHO), a chemical compound used in the fabrication process of a broad range of household products, is present indoors as an airborne pollutant due to its high volatility caused by a low boiling point ($T = -19\text{ }^{\circ}\text{C}$). Miniaturization of analytical systems towards palm-held devices has the potential to provide not only more efficient, but also more sensitive tools for real-time monitoring of this hazardous air pollutant.

This thesis presents the development of a microfluidic device for HCHO sensing based on the Hantzsch reaction method with an emphasis on the fluorescence detection component.

An extensive literature survey summarizing the state-of-the-art in the field of fluorescence sensing miniaturization has been performed. Based on this study, a modular fluorescence detection concept designed around a CMOS image sensor (CIS) has been proposed. Two three-layer fluidic cell configurations (configuration 1: quartz – SU-8 3050 – quartz, and configuration 2: silicon – SU-8 3050 – quartz) have been envisaged and tested in parallel in the same experimental conditions. The microfabrication procedures of the fluidic cells have been described in detail, here including the off-the-shelf components integration process and the experimental procedures.

The CIS-based fluorescence detector proved its capability to detect an initial $10\text{ }\mu\text{g/L}$ HCHO concentration fully-derivatized into 3,5-diacetyl-1,4-dihydrolutidine (DDL) for both the quartz and silicon fluidic cells, both possessing a $3.5\text{ }\mu\text{L}$ interrogation volume. An apparent higher signal-to-noise ratio (SNR) has been observed for the silicon fluidic cell ($SNR_{silicon} = 6.1$) when compared to the quartz fluidic cell ($SNR_{quartz} = 4.9$). The signal intensity enhancement in the silicon fluidic cell was attributed to silicon absorption coefficient at the excitation wavelength, $a(\lambda_{abs} = 420\text{ nm}) = 5 \cdot 10^4\text{ cm}^{-1}$ which is approximately five times higher than the absorption coefficient at the fluorescence emission wavelength, $a(\lambda_{em} = 515\text{ nm}) = 9.25 \cdot 10^3\text{ cm}^{-1}$.

HCHO is absorbed very fast into the liquid reagent due to its relatively high Henry's law constant. Thus, the selection of the molecular trapping method (slug flow, annular flow, or membrane-based flow interaction) depends on the fluorescence detector reading performances. A preliminary concept using a gas-liquid membrane-based interaction for continuous trapping of gaseous HCHO has been introduced by identifying the compatible materials and the fabrication methodologies. Moreover, CFD simulations have been run to estimate the microchannel length in various hydrodynamic conditions required for a full HCHO derivatization.

In the future, an improvement and simplification based on very sensitive fluorescence detectors with low limits-of-detection could thus be possible based on, e.g., slug flow or annular flow.

Kurzfassung

Formaldehyd (HCHO) ist eine chemische Verbindung, die bei der Herstellung einer großen Zahl von Haushaltsprodukten verwendet wird. Charakteristisch ist seine hohe Flüchtigkeit aufgrund einer niedrigen Siedetemperatur ($T = -19\text{ °C}$). Daher ist HCHO fast überall als Luftschadstoff in Innenräumen vorhanden. Die Miniaturisierung analytischer Systeme zu Handheld-Gerät hat das Potenzial, nicht nur effizientere, sondern auch empfindlichere Instrumente für die Echtzeitüberwachung dieses gefährlichen Luftschadstoffs zu ermöglichen.

Die vorliegende Doktorarbeit präsentiert die Entwicklung eines Mikrofluidik-Geräts für die Erfassung von HCHO basierend auf der Hantzsch-Reaktion. Hierbei wurde der Schwerpunkt auf die Komponente für Fluoreszenzdetektion gelegt.

Es wurde eine umfangreiche Literaturrecherche durchgeführt, die es erlaubt, den Stand der Technik auf dem Gebiet der Miniaturisierung des Fluoreszenzensors zusammenzufassen. Auf Grund dieser Studie wurde ein modulares Fluoreszenzdetektionskonzept vorgeschlagen, das um einen CMOS-Bildsensor (CIS) herum entwickelt wurde. Zwei dreischichtige Fluidikzellenkonfigurationen (Konfiguration 1: Quarz – SU-8 3050 – Quarz und Konfiguration 2: Silizium – SU-8 3050 – Quarz) wurden in Betracht gezogen und parallel unter den gleichen experimentellen Bedingungen getestet. Die Verfahren der Mikrofabrikation der fluidischen Zellen wurden detailliert beschrieben, einschließlich des Integrationsprozesses der Standardkomponenten und der experimentellen Verfahren.

Der CIS-basierte Fluoreszenzdetektor bewies seine Leistungsfähigkeit, eine anfängliche HCHO-Konzentration von $10\text{ }\mu\text{g/L}$ vollständig in 3,5-Diacetyl-1,4-dihydrolutidin (DDL-derivatisiert) sowohl für die Quarz- als auch für die Silizium-Fluidikzellen zu detektieren. Beide Systeme wiesenein Abfragevolumen von $3,5\text{ }\mu\text{L}$ auf. Ein offensichtlich höheres Signal-Rausch-Verhältnis (SNR) wurde für die Silizium-Fluidzelle ($SNR_{silicon} = 6.1$) im Vergleich zur Quarz-Fluidzelle ($SNR_{quartz} = 4.9$) beobachtet. Die Verstärkung der Signalintensität in der Silizium-Fluidzelle ist wahrscheinlich auf den Silizium-Absorptionskoeffizienten bei der Anregungswellenlänge zurückzuführen, $a(\lambda_{abs} = 420\text{ nm}) = 5 \cdot 10^4\text{ cm}^{-1}$. Dieser Koeffizient ist ungefähr fünfmal höher als der Absorptionskoeffizient bei der Fluoreszenzemissionswellenlänge $a(\lambda_{em} = 515\text{ nm}) = 9.25 \cdot 10^3\text{ cm}^{-1}$.

HCHO wird aufgrund seiner relativ hohen Konstanten für das Henry-Gesetz sehr schnell in ein flüssiges Reagenz aufgenommen. Somit hängt die Auswahl des molekularen Einfangverfahrens (Schwallströmung, Ringströmung oder membranbasierte Strömungswechselwirkung) von der Leistungsfähigkeit des Fluoreszenzdetektors ab. Ein vorläufiges Konzept, das auf der Verwendung einer Gas-Flüssigkeitsmembran-basierten Wechselwirkung zum ständigen Abfangen des gasförmigen HCHO basiert, wurde eingeführt. Hierzu wurden kompatible Materialien und Herstellungsmethoden identifiziert. Darüber hinaus wurden CFD-Simulationen durchgeführt, um die Mikrokanallänge unter verschiedenen

hydrodynamischen Bedingungen abzuschätzen, die für eine vollständige HCHO-Derivatisierung erforderlich sind.

Eine Verbesserung und Vereinfachung auf der Grundlage von sehr empfindlichen Fluoreszenzdetektoren mit niedrigen Detektionsgrenzen könnte zukünftig basierend z. B. auf Schwallströmung oder Ringströmung möglich sein.

Résumé du projet

Le formaldéhyde (HCHO), un composé chimique utilisé dans le processus de fabrication d'une large gamme de produits ménagers, est présent en environnement intérieur en tant que polluant atmosphérique en raison de sa volatilité élevée causée par un point d'ébullition bas ($T = -19\text{ °C}$). La miniaturisation des systèmes analytiques jusqu'à des appareils portables a le potentiel de fournir des outils non seulement plus efficaces, mais aussi plus sensibles pour la surveillance en temps réel de ce polluant atmosphérique dangereux.

Cette thèse présente le processus de développement d'un dispositif microfluidique de mesure du HCHO dans l'air, basé sur la méthode de détection du produit de la réaction de Hantzsch, en mettant l'accent sur la composante de détection de la fluorescence.

Une large étude bibliographique résumant l'état de l'art dans le domaine de la miniaturisation de la détection par fluorescence a été menée. Sur la base de cette étude, un concept de détection de fluorescence modulaire, conçu autour d'un capteur d'image CMOS (CIS), a été proposé. Deux configurations de cellules fluidiques à trois couches (configuration 1: quartz – SU-8 3050 – quartz, et configuration 2 : silicium – SU-8 3050 – quartz) ont été développées et testées en parallèle dans les mêmes conditions expérimentales. Les procédures de microfabrication des cellules fluidiques ont été décrites en détail, y compris l'intégration de composants standard et les procédures expérimentales.

Le détecteur de fluorescence basé sur le CIS a prouvé sa capacité à détecter une concentration initiale de $10\text{ }\mu\text{g/l}$ de HCHO entièrement dérivé en 3,5-diacétyl-1,4-dihydrolutidine (DDL) pour les cellules fluidiques de quartz et de silicium, toutes deux possédant un volume d'interrogation de $3,5\text{ }\mu\text{l}$. Un rapport signal sur bruit (SNR) apparent plus élevé a été observé pour la cellule fluidique en silicium ($SNR_{silicon} = 6.1$) par rapport à la cellule fluidique en quartz ($SNR_{quartz} = 4.9$). L'augmentation de l'intensité du signal dans la cellule fluidique en silicium était principalement attribuée au coefficient d'absorption du silicium à la longueur d'onde d'excitation, $a(\lambda_{abs} = 420\text{ nm}) = 5 \cdot 10^4\text{ cm}^{-1}$ qui est environ cinq fois plus élevé que le coefficient d'absorption à la longueur d'onde d'émission fluorescente, $a(\lambda_{em} = 515\text{ nm}) = 9.25 \cdot 10^3\text{ cm}^{-1}$.

Le HCHO est absorbé très rapidement dans le réactif liquide en raison de sa constante de Henry relativement élevée. Ainsi, le choix de la méthode de piégeage moléculaire (écoulement diphasique en régime de Taylor, écoulement diphasique en régime annulaire ou dispositif basé sur une membrane poreuse séparant les deux phases) dépend de la résolution du détecteur de fluorescence. Un concept préliminaire basé sur l'utilisation d'une membrane poreuse séparant les phases gazeuse et liquide a été introduit pour le piégeage continu du HCHO gazeux, en identifiant les matériaux compatibles, les méthodologies de fabrication et en analysant le mécanisme de diffusion à travers la membrane. De plus, des simulations CFD ont été exécutées pour estimer la longueur du microcanal dans diverses conditions hydrodynamiques requises pour une dérivation complète de HCHO.

Cependant, des détecteurs de fluorescence très sensibles avec de faibles limites de détection pourraient permettre la mise en œuvre de méthodes de piégeage plus simples, par exemple des écoulements diphasiques en régime de Taylor, qui pourraient simplifier et miniaturiser encore plus l'appareil.

Table of Contents

Acknowledgment.....	iv
Abstract	v
Kurzfassung	vi
Résumé du projet	viii
Table of Contents.....	x
List of Figures	xii
List of Tables	xvii
Nomenclature	xviii
Chapter 1. Introduction	1
1.1. Formaldehyde as an indoor air pollutant	1
1.2. Micro-Total-Analysis-Systems for environmental sensing.....	1
1.3. Motivation	3
1.4. Outline.....	3
1.5. Output of the thesis.....	4
Chapter 2. Fundamentals	5
2.1. Molecular fluorescence sensing in optofluidics	5
2.1.1. Fluorescence basics	5
2.1.2. Quantitative fluorometry and instrumentation	6
2.1.3. Optofluidic integrated devices	8
2.1.3.1. Materials and microfabrication technologies	8
2.1.3.2. Light-emitters	9
2.1.3.3. Waveguiding	11
2.1.3.4. Optical noise suppression	12
2.1.3.5. Photodetectors	12
2.1.4. Sensitivity and Limit-of-Detection	14
2.1.5. Particularities of fluorescence intensity sensing. Non-linearity effects.	15
2.2. Flow microreactors modelling	16
2.2.1. Introduction	16
2.2.2. Hydrodynamics of microfluidic flows.....	17
2.2.2.1. Single-phase flows	17
2.2.2.2. Two-phase flows.....	19
2.2.3. Gas trapping in microfluidic two-phase flows.....	21
2.2.3.1. Fick's laws. Convective-diffusive transport equation.....	21
2.2.3.2. Henry's law. Vapor-liquid phase equilibria	22
2.2.3.3. Two-film theory and Resistance-in-Series Model. Dimensionless numbers	22
2.2.4. Gas-liquid reactions. Pseudo-first order reaction.	24
2.2.5. Residence time distribution in reacting flows	25
Chapter 3. Current methods and devices used for real-time detection of indoor formaldehyde	27
3.1. Devices and sensing methodologies	27
3.2. Formaldehyde sensing based on Hantzsch reaction	32
3.2.1. Formaldehyde physicochemical properties	32
3.2.2. Description of the detection method and reaction kinetics	33
3.2.3. 3,5-diacetyl-1,4 dihydrolutidine (DDL) photochemical properties	35
Chapter 4. Concept of the microfluidic formaldehyde detector.....	37
4.1. State-of-the-art of the fluorescence sensing in optofluidic devices	37
4.1.1. Miniaturized off-chip fluorescence sensing architectures	37
4.1.2. Towards on-chip fluorescence sensing architectures	41
4.1.2.1. Optical-fiber-based designs.....	42
4.1.2.2. Optics layer-integrated designs	45
4.1.2.3. Organic electronic-based designs	55
4.1.2.4. CMOS-based fluorescence sensing	59
4.2. Gas-Liquid Microreactors for continuous trapping of gaseous molecules	63
4.2.1. Gas-liquid direct contactors.....	63
4.2.2. Gas-liquid membrane-based contactors.....	65
4.2.3. Development stages of a microreactor.....	67
4.3. Towards on-chip integration of the Hantzsch-reaction-based formaldehyde sensing. State-of-the art.	71
4.4. Optofluidic detection concept.....	72
Chapter 5. CMOS-based fluorescence sensing device.....	75
5.1. Fabrication concept of the experimental device	75

5.2. Materials and methods.....	77
5.2.1. Microfluidic circuit.....	77
5.2.1.1. Flow characterization in the interrogation chamber using a CFD tool.....	79
5.2.2. Optical circuit.....	88
5.2.2.1. Flow-through microfluidic cell integrating the SU-8 3050 optical waveguide.....	89
5.2.2.2. Excitation source.....	91
5.2.2.3. Photodetector.....	92
5.2.2.4. Band-pass filter.....	93
5.2.2.5. Optical circuit configuration.....	93
5.2.3. Materials, chemicals, and reagents.....	95
5.2.3.1. Silicon wafer.....	95
5.2.3.2. Quartz wafer.....	95
5.2.3.3. SU-8 3050 epoxy negative photoresist.....	95
5.2.3.4. Black PolyLactic Acid (PLA).....	96
5.2.3.5. Preparation of DDL solutions.....	96
5.3. Fabrication and packaging.....	96
5.3.1. Upper and lower holders.....	96
5.3.2. Disposable flow-through microfluidic cell.....	96
5.3.3. Packaging.....	100
5.4. Experimental set-up.....	102
5.5. Results.....	106
5.6. Non-linearity analysis.....	112
Chapter 6. Designing a gas-liquid microfluidic reactor for formaldehyde separation.....	116
6.1. Design of the reagent carrying microchannel.....	116
6.1.1. HCHO reaction with Fluoral-P reagent in a microfluidic channel.....	117
6.1.2. Diffusive transfer in stationary direct gas-liquid contact.....	122
6.2. Materials selection process.....	126
6.3. Front-end microchannel fabrication.....	129
6.4. Back-end microfluidics bonding.....	130
Chapter 7. Summary and outlook.....	132
7.1. Summary.....	132
7.1.1. CMOS-based fluorimeter.....	132
7.1.2. Gas-liquid micro-reactor.....	133
7.2. Outlook.....	133
7.2.1. CMOS-based fluorimeter.....	133
7.2.2. Gas-liquid micro-reactor.....	134
Bibliography.....	136
Appendices.....	151
A1. ULS24 ANITOA CMOS-image sensor Data Sheet.....	151
A2. Excitation Light Emitting Diode Data Sheet.....	156
A3. Technical drawing of the fluorescence detector lower holder.....	160
A4. Technical drawing of the fluorescence detector upper holder.....	162
A5. Hydrophobic membrane Data Sheet.....	163
A6. Convective-diffusive transfer mechanism in gas-liquid membrane-based interaction.....	164
A7. Technical drawing of the gas carrying layer.....	168
A8. Technical drawing of the liquid carrying layer.....	170
A9. Convection-diffusion mass-transfer in slug flows.....	172
A10. Convection-diffusion mass-transfer in annular flows.....	173
List of publications.....	175

List of Figures

Figure 2.1.1. (a) Simplified representation of the Jablonski diagram. When excited (blue arrow), molecules absorb the energy, E , and its electrons move from the ground state, S_0 , to superior electric levels (0, 1, 3, etc.). De-excitation towards S_0 comprise: (1) a vibrational relaxation and an internal conversion until the first excitation level S_1 , and (2) a light emission characterized by a particular Stokes shift (green arrow) named fluorescence from S_1 towards S_0 . (b) Absorption and emission spectrums centered at λ_{abs} , respectively, λ_{em}	5
Figure 2.1.2. General detection scheme of a fluorimeter (orthogonal configuration).	7
Figure 2.1.3. (a) Relative radiant flux intensity, Φ_e , of a LED with the emission wavelength centered at $\lambda_{em} = 420 \text{ nm}$. (b) Radiant flux intensity depending on the emission angle, φ . Reproduced from SMB1N-420H-02 LED Data Sheet, Roithner Laser Technik, Austria.	9
Figure 2.1.4. (a) Relative radiant flux of a bare LED (Lambertian emission pattern). (b) Relative radiant flux of LEDs with various reflective cup structures. The angles represent the emission angles, φ , while the horizontal scale denotes the relative radiant flux intensity. Reproduced from Chen <i>et al.</i> , [12]	10
Figure 2.1.5. (a) Total internal reflection (TIR) principle for electromagnetic wave transport through waveguides, where the θ angle represents the incidence angle of the radiant flux emitted by the light source. (b) Planar waveguide circuit. Reproduced from Okamoto <i>et al.</i> , [14].	11
Figure 2.2.1. Development stages of a flow microreactor (FMR). Reproduced from Nakahara <i>et al.</i> , [21]	16
Figure 2.2.2. (a) Gas-liquid flow patterns in microfluidic channels. Reproduced with permission from Serizawa <i>et al.</i> , [30]. (b) The flow pattern transition map as a function of superficial gas and liquid velocities. Reproduced with permission from Rebrov <i>et al.</i> , [31].	19
Figure 2.2.3. Two-film transport model for a gas-liquid mass transfer from the gas phase towards the liquid phase, where x is the length, c is the concentration, v_g is the gas velocity vector, v_L is the liquid velocity vector, j is the total mass flux, δ_g is the gas stagnant film thickness, δ_L is the liquid stagnant film thickness, c_g is the gas bulk concentration, c_L is the liquid bulk concentration.	23
Figure 2.2.4. The principle of residence time distribution estimation in a volume of control using the pulse method. (a) The tracer is injected at the inlet as a Dirac impulse for one time-step. (b) The tracer concentration monitored at the outlet as an area-weighted average variation function over time.	26
Figure 3.1.1. (a) A 2,4-DNPH cartridge and an air sampling pump. (b) A High Performance Liquid Chromatography (HPLC) detection device [3].	27
Figure 3.1.2. (a) Top side view of the AeroLaser AL4021 HCHO Analyzer, with the main components displayed: A – the gas pump, B – the peristaltic pump controller, C – the air filter, D – the mass-flow controller, E – the photon multiplier tube (PMT), F – the flow-through fluidic cuvette for optical detection of DDL, G – UV-LED for optical excitation, N – peristaltic pump with H – the peristaltic pump motor, I – the 200 μL capillary, M – stripper debubbler, L – reactor where derivatization occurs, J – stripper, K, O, P, Q – liquid traps, R – zero valve. (b) AeroLaser AL4021 HCHO Analyzer displaying the HCHO concentration in real-time; Data from Aero Laser AL4021 – Instruction Manual [52].	31
Figure 3.2.1. HCHO sensing scheme based on Hantzsch reaction methodology [45]	34
Figure 3.2.2. (a) 3,5-diacetyl-1,4 dihydrouridine (DDL) excitation and emission spectrum. (b) Absorbance spectrum of Fluoral-P compound. Reproduced from Mariano <i>et al.</i> , [51].....	36
Figure 4.1.1 (a) Integrated fluorescence microscope, 2.4 cm ³ volume, 1.9 g weight. (b) Compact handheld quasi-confocal laser induced fluorescence. (c) Integration of LEGO-like blocks hosting elements of the optical, electrical, and fluidic circuits in order to modulate the optofluidic systems. (a) Reprinted from Ghosh <i>et al.</i> (2011) [4], Copyright 2011, with permission from Nature Publishing Group. (b) Reprinted from Fang <i>et al.</i> (2016) [5], Copyright 2016, with permission from Elsevier. (c) Reprinted from Lee <i>et al.</i> (2018) [10], Copyright 2018, with permission from Willey.....	38
Figure 4.1.2. (a) Compact fluorescence sensing scheme based on Hollow Core Bragg Fibers, serving as interrogation cuvette, collector, delivery channel for the fluorescence, and the filter for the residual noise. (b) Cross-section scheme of the device with the photonic band gaps of different refraction indexes [23].	45
Figure 4.1.3. (a) Parallel layering distribution of the detection functions with the PCB sandwiched in between the microfluidic layer and the detection layer [46,47]. (b) Cross-section of the microfluidic-PCB fluorescence detector, built	

using two PCBs. The design strategy avoided the direct illumination of the interrogation volume, a Söller thin film collimator being coated on top of the CMOS to reduce the background noise [1]. (c) Fluorescence detection system with back-side illumination scheme. Reproduced from Shin *et al.* (2015, 2017) [46,47], Copyright 2015, with permission from Elsevier. 47

Figure 4.1.4. (a) Lateral excitation onto a PDMS microfluidic device coupled to a photodiode PCB. The 50 μm air-gap separates the microfluidic device from the photodiode, in order to assure the TIR effect at the glass/air interface for the excitation light. (b) Multi-functional sensing device based on 150 μm optofluidic jet, equipped with a recirculation system. The detection scheme is based on the principle of the TIR in the liquid jet. Two possible ways of liquid jet excitation: (1) orthogonal fluorescence excitation, and (2) optical fiber for Raman excitation. (a) Reproduced from Novo *et al.* (2014) [48], Copyright 2014, with permission from The Royal Society of Chemistry. (b) Reproduced from Persichetti *et al.* (2017) [52], Copyright 2017, with permission from The Royal Society of Chemistry. 49

Figure 4.1.5. (a) Photonic lab-on-a-chip with the solid-state light emitter, air mirrors, multiple internal reflection system, biconvex lens, and the channel for fiber optics integration. (b) (a) Illustration of the flexible sensor design and fabrication methodology. (b) Scanning electron microscopy view of the VCSEL and the 3 μm thick Si-Photodiode. (c) Image of an array of sensors wrapped around a cylindrical bar. (a) Reproduced from Llobera *et al.* (2015) [53], Copyright 2015, with permission from Springer Nature. (b) Reprinted with permission from Kang *et al.* (2016) [55], Copyright 2016, American Chemical Society. 51

Figure 4.1.6. (a) Hybrid chip-scale system combining the automated microfluidic processing (automaton) and on-chip optical detection based on the ARROW principle. The scale in the figure - 1 cm. (b) Optical device schematic with a PEGDA waveguide used for excitation light coming from a 532 nm laser and another PEGDA waveguide used to collect the fluorescence emission from the interrogation volume. (a) Reproduced from Parks *et al.* (2014) [56], Copyright 2014, with permission from AIP Publishing. (b) CC-BY 4.0. 52

Figure 4.1.7. (a) Generic illustration of the fluorescence optofluidic detection based on organic electronics. (b) Schematic representation of OLEC excitation and OPD detection system. (a) OPD. (b) Linear polarizer filter. (c) Glass microfluidic chip. (d) Blue OLEC. (e) fully-processed blue OLEC. (c) Fabricated optofluidic system. (a) Reproduced from Lefèvre *et al.* (2015) [67], Copyright 2015, with permission from Elsevier. (b) and (c) Reproduced from Shu *et al.* (2017) [68], Copyright 2017, with permission from The Royal Society of Chemistry. 56

Figure 4.1.8. Lab-on-a-chip sensing architecture based on OLED display and photodiode active matrix technology for point-of-use diagnosis of multiple diseases [72]. 57

Figure 4.1.9. (a) CMOS image sensors in-depth working principle. (b) (a) CMOS image sensor with thin layer filter coated on top, the microfluidic channel, and the Fresnel Zone Plate (FZP) array. (b) Top view schematic of the device with the FZP array configuration and its design parameters. (c) Scanning Electron Microscopy image of the fabricated Fresnel lens. (d) Images of the fabricated laboratory devices. Reproduced from [84], Copyright 2011, with permission from The Royal Society of Chemistry. 60

Figure 4.2.2. The two-step polymer membrane embedding process into a polymer chip. (a) Hot-embossing step for membrane bonding. (b) Closing-up the chip by thermal bonding of a polymer cover layer. (c) PMMA layer with a 120 μm deep microchannel. (d) Membrane and the PMMA layer presented at c) after hot-embossing procedure. Reproduced from Wang *et al.* (2013) [118], Copyright 2013, with permission from Elsevier. 66

Figure 4.2.3. (a) Designing steps of a microreactor by Zhao *et al.* [95] (b) Development stages of a polymer-made microreactors by Tsao, (2016) [127]. The red line corresponds to the thermoplastic fabrication procedure, while the blue line corresponds to the PDMS fabrication procedure. (a) Reproduced from Zhao *et al.* (2017) [149], Copyright 2017, with permission from Annual Reviews, Inc. (b) Data from Tsao, (2016) [127] under Creative Commons 4.0 International license. 68

Figure 4.4.2. (a) Exploded view of the concept, where (A) – is the meandering microchannel carrying the reagent solution; (B) – is the meandering microchannel carrying the gas stream; (C) – is the hydrophobic membrane used to separate the gas and liquid phases, while allowing the HCHO diffusion from the gas-side towards the liquid-side; (D) – is a continuation of the reagent carrying microchannel placed in between the trapping region and (E) – the flow-through microfluidic cell to assure an optimal residence time of the last trapped HCHO molecules for a full derivatization process. (b) Top view, from the solution meandering channel network side. 73

Figure 4.4.3. Concept of the trapping and derivatization assigned component (Gas-Liquid Microreactor).	74
Figure 4.4.4. Concept of the fluorescence sensing system with (A) the three-layer flow-through microfluidic cell-made in two configurations (1) and (2), (B) the filter, (C) the CMOS-image sensor.	74
Figure 5.1.1. The concept of the CMOS-based fluorescence detector (46 mm × 30 mm × 10 mm). (a) Exploded view of the detector. (b) Transversal cross-section of the assembled sensing device.	75
Figure 5.2.1. Longitudinal cross-section of the microfluidic circuit, in scale three-dimensional representation.	77
Figure 5.2.2. (a) Flow-through microfluidic cell concept. (b) Exploded view of the microfluidic cell with the microfluidic circuit grooved into the intermediate layer, while the inlet/outlet are etched perpendicular to the upper layer. (c) Generic representation of the intermediate layer concept with the length, $L = 20$ mm, and the interrogation chamber centered in between the inlet and the outlet. (d) $V_3 = 0.35 \mu\text{L}$ – one inlet configuration, with $D_3 = 1.5$ mm. (e) $V_3 = 0.35 \mu\text{L}$ – three inlets configuration, with $D_3 = 1.5$ mm. (f) $V_2 = 1.4 \mu\text{L}$ – one inlet configuration $D_2 = 3.0$ mm. (g) $V_2 = 1.4 \mu\text{L}$ – three inlets configuration $D_2 = 3.0$ mm. (h) $V_1 = 3.5 \mu\text{L}$ – one inlet configuration, $D_1 = 4.7$ mm. (i) $V_1 = 3.5 \mu\text{L}$ – three inlets configuration, $D_1 = 4.7$ mm.	79
Figure 5.2.3. One of the geometrical configurations of interest and the computational domain.	81
Figure 5.2.4. 2-D representation of the streamlines in the $V_1 = 3.5 \mu\text{L}$ volume interrogation chamber obtained for three volumetric flow rates at the inlet, V_i , for the one-inlet configuration (left side - a), c), and e)) and the three-inlets configuration (right-side - b), d). t - represents the mean residence time obtained for each case.....	83
Figure 5.2.5. 2-D representation of the streamlines in the $V_2 = 1.4 \mu\text{L}$ volume interrogation chamber obtained for three volumetric flow rates at the inlet, V_i , for the one-inlet configuration (left side - a), c), and e)) and the three-inlets configuration (right-side - b), d). t - represents the mean residence time obtained for each case.....	84
Figure 5.2.6. 2-D representation of the streamlines in the $V_3 = 0.35 \mu\text{L}$ volume interrogation chamber obtained for three volumetric flow rates at the inlet, V_i , for the one-inlet configuration (left side - a), c), and e)) and the three-inlets configuration (right-side - b), d). t - represents the mean residence time obtained for each case.....	85
Figure 5.2.7. Residence time distribution curves for $V_1 = 3.5 \mu\text{L}$	86
Figure 5.2.8. Residence time distribution curves for $V_2 = 1.4 \mu\text{L}$	87
Figure 5.2.9. Residence time distribution curves for $V_3 = 0.35 \mu\text{L}$	87
Figure 5.2.10. Two-dimensional representation of the configuration 1, where $\Phi_{\lambda_{em}(q)}$ and $\Phi_{\lambda_{ex}(q)}$ are the resultant intensity of the fluorescence emission, respectively of the excitation light perpendicular to the photodetector surface at the fluid-lower layer interface. Dimensions are not in scale.	90
Figure 5.2.11. Two-dimensional representation of the configuration 2, where $\Phi_{\lambda_{em}(si)}$ and $\Phi_{\lambda_{ex}(si)}$ are the resultant intensity of the fluorescence emission, respectively of the excitation light perpendicular to the photodetector surface at the fluid-lower layer interface. Dimensions are not in scale.	90
Figure 5.2.12. Sensitivity of ULS24 CMOS image sensor as the function of wavelength vs QExFF [5], where QE is quantum efficiency and FF is the fill factor.	92
Figure 5.2.13. The optical transmittance of the bandpass filter measured with UV/VIS spectrometer at the emission wavelength, $\lambda_{em} = 515 \text{ nm}$ and at the excitation wavelength, $\lambda_{abs} = 420 \text{ nm}$ are $T_{\lambda_{em}} = 90.5\%$, respectively, $T_{\lambda_{abs}} = 0.0105\%$	93
Figure 5.2.14. Representation of the two optical circuit configurations. L is the abbreviation for light-emitting diode. $\phi_{\lambda_{em}(q)}$ and $\phi_{\lambda_{ex}(q)}$ are the resultant intensities of the fluorescence emission, respectively of the excitation light scattered perpendicular to the photodetector surface at the fluid-lower layer (quartz) interface in configuration 1. Similarly, $\phi_{\lambda_{em}(s)}$ and $\phi_{\lambda_{ex}(s)}$ are the resultant intensities of the fluorescence emission, respectively of the excitation light scattered perpendicular to the photodetector surface at the fluid-lower layer (quartz) interface in configuration 2.	94
Figure 5.2.15. a) Prime CZ silicon wafer (Microchemicals GmbH, Ulm, Germany, P/N WSA40400250B8314SNN1). b) AF 32® eco alkali-free flat glass (Schott AG, Mainz, Germany).	95
Figure 5.3.1. 3D printed lower holder with the PVA support structure.	96
Figure 5.3.2. Manufacturing process of the configuration 1 flow-through microfluidic cell. a) SU-8 3050 layer deposition on the quartz layer. b) UV photo-illumination using a photolithography mask for making the fluidic channeling of the intermediate layer. c) SU-8 developer and rinsing to remove the exposed part. d) After coating the Photec 2040 dicing protective film, the inlet and outlets have been created through sand blasting. e) A few micrometers SU-8 3050 layer	

has been coated on the lower layer of the freshly pierced quartz wafer. f) Longitudinal section of the final structure obtained after bonding the structure obtained at step c) and the structure obtained at step e).	98
Figure 5.3.3. Manufacturing process of the configuration 2 flow-through microfluidic. a) SU-8 3050 layer deposition on the quartz layer. b) UV photo-illumination using a photolithography mask for making the fluidic channeling of the intermediate layer. c) SU-8 developer and rinsing to remove the exposed part. d) After coating the 100 nm Si_3N_4 protective film, the inlet and outlets have been created through KOH etching. e) A few micrometers SU-8 3050 layer has been coated on the lower layer of the freshly etched Si-wafer. f) Longitudinal section of the final structure obtained after bonding the structure obtained at step c) and the structure obtained at step e).	99
Figure 5.3.4. (a) Flow-through microfluidic cell of 1.41 μL silicon – three inlets. (b) Microfluidic cell of 1.41 μL quartz – three inlets. (c) Microscope view of silicon (405 μm)–SU-8 3050 (232 μm)–quartz (508 μm) fluidic cell cross-section. (d) Microscope view of quartz (507 μm)–SU-8 3050 (224 μm)–quartz (508 μm) fluidic cell cross-section.	100
Figure 5.3.5. a) 1 - quartz flow-through microfluidic cell, 2 - silicon flow-through microfluidic cell, 3 - light-emitting diodes, 4 - band-pass filter, 5 - CMOS-image sensor, 6 - upper holder with integrated fluidic connectors, 7 - lower holder. b) The CMOS-image sensor is screwed and fixed into the structure of the lower holder - bottom side view. c) The CMOS-image sensor fixed into the lower holder structure, the band-pass filter ready to be integrated, and the 1.4 mm width slit - top side view; d) The LEDs are tightly fixed into their lower holder pockets using two screws and a piece of copper. The band-pass filter is placed on top of the CMOS image sensor. e) The photonic mask is glued on the flow-through microfluidic cell with opening in the interrogation region area. f) The flow-through microfluidic cell is placed into the pocket specially created for it into the structure of the holder. g) the N-333 connectors are fixed into the upper holder and the black circular O-rings from the bottom serve as liquid sealing when the two holders are screwed together. h) the upper and lower holders screwed together through the four screws - bottom side view. i) Final assembly before testing - top view.....	101
Figure 5.4.1. The experimental set-up used to test the optofluidic sensing prototype. (1) - the optofluidic prototype, (2) the syringe pump used to stream the reagent solutions into the device, (3) 24 V DC source used to power the LEDs connected in series, (4) microcontroller board that accompanied the ULS 24 CMOS-image sensor running the dark noise management system. The USB is plugged to a PC where an interface is used to collect the data. (5) Syringes filled with DDL solutions with different concentrations ready to be streamed into the device.....	103
Figure 5.4.2. a) Optical illumination pattern of a 3.5 μL cell with only one LED activated - view from top of the lower holder. b) Optical illumination pattern of a 3.5 μL cell with both LEDs activated. c) View of the illuminated interrogation chamber with no mask and no filter - view from the CMOS image sensor direction. d) View of the illuminated interrogation chamber with mask on and no filter - view from the CMOS image sensor direction. e) View of the illuminated interrogation chamber with mask off on and filter on - view from the CMOS image sensor direction. f) View of the illuminated interrogation chamber with mask on and filter on - view from the CMOS image sensor direction.	104
Figure 5.4.3. The pixel output matrix obtained for a particular assay with the 812 counts average of all pixels of the matrix.	105
Figure 5.5.1. The linear response obtained for the three-excitation optical powers at $c_0 = 0.00$ mg/L (blank sample) in $V_1 = 3.5$ μL . The error bars indicate the standard deviations for two independently prepared samples ($N = 2$). ..	107
Figure 5.5.2. ULS 24 CMOS image sensor 12×12 -pixel output for: dark current, blank signal, and the four HCHO concentrations tested for a quartz cell at $P_3 = 315$ mW.	108
Figure 5.5.3. SNRs obtained for quartz and silicon fluidic cells at $c_1 = 0.01$ mg/L formaldehyde concentration in DDL solution and different optical powers.	109
Figure 5.5.4. Experimental evaluation of the CMOS-based fluorescence detector realized using the mean values (X) of seven assays ($n = 7$) made on two independently prepared samples ($N = 2$) at each of the $c_i, i = 0, \dots, 4$ concentrations tested for the $V_1 = 3.5$ μL flow-through microfluidic cell. (a) Logarithmic fitting of the experimental points for quartz fluidic cell; (b) Logarithmic fitting of the experimental points for silicon fluidic cell. The error bars indicate one standard deviation ($N = 2$).	111

Figure 5.6.1. Relationship between the relative fluorescence intensity and HCHO concentration in the work of Belman [254].	112
Figure 5.6.2. Fluorescence intensity – HCHO concentration dependency found in the 0.00 – 0.10 μg HCHO/mL concentration range for quartz cell.	114
Figure 5.6.3. Fluorescence intensity – HCHO concentration dependency found in the 0.01 – 10.00 μg HCHO/mL concentration range for quartz cell.	114
Figure 5.6.4. Fluorescence intensity – HCHO concentration dependency found in the 0.00 – 0.10 μg HCHO/mL concentration range for silicon cell.	115
Figure 5.6.5. Fluorescence intensity – HCHO concentration dependency found in the 0.01 – 10.00 μg HCHO/mL concentration range for silicon cell.	115
Figure 6.1.1. Representation of the 2D fluidic domain of the channel, where w is the width and L is the length (not in scale).	117
Figure 6.1.2. Rectangular pulse function, $rect(t[1/s])$, as a function of time and used to sample a $c_t^N = c \cdot rect(t[1/s])$ HCHO concentration in the transient domain.	118
Figure 6.1.3. Averaged-HCHO concentration monitored over time for the virtual line probes settled along the 100 μm \times 200 μm cross-section microchannel for (a) $Q_1 = 5 \mu\text{L} \cdot \text{min}^{-1}$ and (b) $Q_3 = 15 \mu\text{L} \cdot \text{min}^{-1}$.	120
Figure 6.1.4. Inlet concentration distribution at (a) $t = 0 \text{ s}$, (b) $t = 1 \text{ s}$, (c) $t = 3 \text{ s}$ for a 300 μm \times 200 μm cross-section microchannel.	121
Figure 6.1.5. Representation of the 2D 200 μm \times 200 μm fluidic domains of the gas-liquid static interaction simulation.	122
Figure 6.1.6. (a) HCHO surface-averaged concentration distribution in both phases at $T_1 = 296.15 \text{ K}$, respectively $T_2 = 338.15 \text{ K}$. (b) HCHO exponential derivativization at $T_2 = 338.15 \text{ K}$.	124
Figure 6.1.7. Time-dependent HCHO concentration distribution in liquid and gas phases at $T_1 = 296.15 \text{ K}$. The first scale in the legend characterizes the liquid phase and the second one the gas phase. HCHO initial concentration in the gas phase is $c_2 = 4.09 \cdot 10^{-8} \text{ mol} \cdot \text{m}^{-3}$, while in the liquid phase is zero.	124
Figure 6.1.8. Time-dependent HCHO concentration distribution in liquid and gas phases at $T_2 = 338.15 \text{ K}$. First scale in the legend characterizes the liquid phase and the second one the gas phase. HCHO initial concentration in the gas phase is $c_1 = 4.09 \cdot 10^{-8} \text{ mol} \cdot \text{m}^{-3}$, while in the liquid phase is 0.	125
Figure 6.2.1. Scanning Electron Microscopy (SEM) analysis of (a) the double-layer Aspire, QL 217 hydrophobic membrane with the cross-section of the active and backer layers, (b) pore distribution on the upper-side of the active layer, (c) pore distribution on the lower-side of the backer layer.	127
Figure 6.2.2. The expanded-polytetrafluoroethylene (ePTFE) porosity, ε_m , depending on the reference pore size. The vertical and horizontal lines show the estimated porosity ($\cong 70 - 75 \%$) for a reference pore diameter of 200 nm. Reproduced from [256].	128
Figure 6.3.1. (a) Gas-liquid PMMA chip contactor with the on-chip integrated membrane; (b) Meandering channels micro-milled on PMMA flat structure.	129
Figure 6.3.2. Liquid carrying micro-channel. (a) 223 μm width - top side; (b) 210 μm width - bottom side.	130
Figure 6.4.1. (a) Gas-liquid micro-reactor concept, exploded view: Gas-liquid PMMA chip contactor with the on-chip integrated membrane (A), copper layers thermally fueled by cartridge heaters (B), upper holder (C), lower holder (D), liquid connectors (E), gas connectors (F), micro-O-ring (G). (b) Fabricated components.	131

List of Tables

Table 2.1.1. Properties of the main polymers used in microfluidic applications. Data from Tsao [7], Guckenberger <i>et al.</i> , [8], and Yen <i>et al.</i> , [9].....	8
Table 2.1.2. Microfabrication techniques used in optofluidic system fabrication. Data from Tang <i>et al.</i> [6].....	9
Table 2.2.1. Flow regimes given by the Knudsen numbers using mean free path, λ , and characteristic length, L_c [25].	17
Table 2.2.2. Dimensionless numbers used in continuous flow microfluidics.	18
Table 2.2.3. Dimensionless numbers used in flow microreactors (FMRs).	24
Table 3.1.1. List of portable sensors for indoor HCHO concentration measurements [79].	30
Table 3.2.1. HCHO physicochemical properties.	33
Table 3.2.2. Experimental values of the physical reaction rates, k , depending on the temperature [45].	35
Table 4.1.1. Off-chip fluorescence detection platforms.	40
Table 4.1.2. Microfluidic systems using optical fiber-based designs towards-on-chip integration of fluorescence detection.	43
Table 4.1.3. Microfluidic systems using optics layer-integrated designs towards-on-chip approaches for fluorescence detection.	53
Table 4.1.4. Microfluidic systems using organic electronic based-designs towards-on-chip approaches for fluorescence detection.	58
Table 5.5.1. Error distribution as standard deviation (σ) and relative standard deviation (RSD) for the $V_1 = 3.5 \mu\text{L}$ quartz fluidic cell at $P = 315 \text{ mW}$, where #1 and #2 represented the two independently prepared samples for each of the tested HCHO concentrations c_i for $i = 0, \dots, 4$ of DDL solutions.....	110
Table 5.5.2. Error distribution as standard deviation (σ) and relative standard deviation (RSD) for the $V_1 = 3.5 \mu\text{L}$ silicon fluidic cell at $P = 315 \text{ mW}$, where #1 and #2 represented the two independently prepared samples for each of the tested concentrations c_i for $i = 0, \dots, 4$	110
Table 6.1.1. Pressure-drop, Δp , calculated using the Hagen-Poiseuille equation and Re numbers calculated for the hydrodynamic conditions of reference for water.	116
Table 6.1.2. Reaction probability, P_R (%), for $100 \mu\text{m} \times 200 \mu\text{m}$ cross section, where k'_1 and k'_2 are the pseudo-reaction constants at $T_1 = 333 \text{ K}$, respectively $T_2 = 338 \text{ K}$	119
Table 6.1.3. Reaction probability, P_R (%), for $200 \mu\text{m} \times 200 \mu\text{m}$ cross section, where k'_1 and k'_2 are the pseudo-reaction constants at $T_1 = 333 \text{ K}$, respectively $T_2 = 338 \text{ K}$	119
Table 6.1.4. Reaction probability, P_R , for $300 \mu\text{m} \times 200 \mu\text{m}$ cross section, where k'_1 and k'_2 are the pseudo-reaction constants at $T_1 = 333 \text{ K}$, respectively $T_2 = 338 \text{ K}$	119
Table 6.1.5. The boundary conditions for the diffusive transfer in stationary direct-gas-liquid contacting.	123
Table 6.2.1. Polymers and their potential as material for on-chip integration of HCHO sensing.	126
Table 6.2.2. Characteristics of the double-sided hydrophobic membrane.....	127

Nomenclature

List of abbreviations

Abbreviations	Meaning
2D & 3D	Two-dimensional & three-dimensional.
CAD	Computational aided design
DDL	3,5-diacetyl-1,4 dihydrolutidine
CMOS	Complementary metal-oxide semiconductor
CIS	CMOS-image sensor
ePTFE	Expanded polytetrafluoroethylene
PLA	Black Polylactic Acid
PMMA	Poly (methyl methacrylate)
PEEK	Polyetheretherketone
SNR	Signal-to-Noise Ratio
CFD	Computational Fluid Dynamics
LED	Light-Emitting Diode
VOC	Volatile Organic Compound
PCB	Printed Circuit Board
TIR	Total Internal Reflection
HCHO	Formaldehyde
Ppm & ppb & ppt	Particle-per-million / billion / trillion
μ TAS	Micro-Total Analysis System
QE	Quantum efficiency
PMT	Photomultiplier tube
PD	Photodetector
LIF	Laser induced fluorescence
RTD	Residence time distribution
RSD	Relative standard deviation
DC	Direct current
LOD & LOQ & LOB	Limit-of-detection/quantification/blank
SD	Standard deviation
Fluoral-P	4-Amino-3-penten-2-one
Acetyl acetone	pentane-2,4-dione
UV	Ultraviolet
CAS	Chemical Abstracts Service

List of symbols

Symbol	Description	Unit
u	Velocity	$m \cdot s^{-1}$
ρ	Fluid density	$kg \cdot m^{-3}$
P	Optical power	mW
t	Time	s
T	Temperature	K
p	Pressure	Pa
M	Molecular mass	$g \cdot mol^{-1}$
ε	Porosity	[-]
Δp	Pressure drop	Pa
μ	Dynamic viscosity	$Pa \cdot s$
C	Courant number	[-]
σ	Surface tension	$N \cdot m^{-1}$
D	Mass diffusion coefficient	$m^2 s^{-1}$
c	Molecular concentration	$mol \cdot m^{-3}$
λ	Wavelength	nm
ϕ	Fluorescence quantum yield	[-]
R	Reaction rate	$mol \cdot m^{-3} \cdot s^{-1}$
θ	Contact angle	$^\circ$
k'	Pseudo-first order reaction rate	s^{-1}
α	Accommodation coefficient	[-]
H^{cp}	Henry's constant	$M \cdot atm^{-1}$
J	Total flux	$m^2 \cdot s^{-1}$
d_H	Hydraulic diameter	m
w	Width of the channel	m
d	Height of the channel	m
r	Molecular radius	m
δ	Film thickness	m
Q	Flow rate	$\mu L \cdot min^{-1}$
σ^2	Variance	[-]
Ra	Roughness	μm
L	Length of the channel	m
a	Absorption coefficient	[-]

Constants

Constant	Description	Unit
R	Universal gas constant	$m^3 \cdot Pa \cdot K^{-1} mol^{-1}$
$k_B = 1.38 \cdot 10^{-23}$	Boltzmann constant	$m^2 \cdot kg \cdot s^{-2} \cdot K^{-1}$

Subscripts

Subscript	Meaning
i	Species of interest
L	Liquid phase
G	Gas phase
abs	Absorption
em	Emission
ex	Excitation
eq	Equilibrium
TP	Two-phase
m	Membrane
OG	Overall characteristic in the gas phase
OL	Overall characteristic in the liquid phase

Superscripts

Superscript	Meaning
cc	Dimensionless Henry's law constant
OUT	Outlet
IN	inlet

Chapter 1. Introduction

1.1. Formaldehyde as an indoor air pollutant

People spend generally around 90% of their time indoor in industrial countries. Approximately 3.8 million people die yearly in the world from diseases related to the exposure to indoor pollution [1]. Among all the indoor pollutants, volatile organic compounds (VOCs) are particularly looked at, due to their high level of toxicity [2]. One of the VOCs that raises increased concern is formaldehyde (HCHO), which is an allergenic, mutagenic, and level 1 carcinogenic compound [3,4]. HCHO is largely used in the fabrication process of building materials, household products, and resins for wood products.

Consequently, indoor HCHO concentrations are up to fifteen times higher than those measured outdoors [5] and may usually have values from 10 to 100 $\mu\text{g}/\text{m}^3$ (8 to 82 parts-per-billion (ppb)) at room temperature and atmospheric pressure [6]. World Health Organization (WHO) standard for a safe daily exposure is settled to 100 $\mu\text{g}/\text{m}^3$ (82 ppb) concentration for a maximum period of 30 min. In France, recommendations are limiting the exposure at 30 $\mu\text{g}/\text{m}^3$ (25 ppb), and from 2023 this will be reduced to 10 $\mu\text{g}/\text{m}^3$ (8 ppb) [7,8]. In gaseous form, it is colorless and possesses a pickle-like strong odor at high concentrations.

Although there are research projects looking for a less-harmful HCHO alternative in the form of bio-based platform chemical 5-HMF (5-Hydroxymethylfurfural) [9], HCHO industrial consumption increases constantly. To measure indoor concentrations of VOCs, several measurement system concepts are available, amongst them also miniaturized ones.

1.2. Micro-Total-Analysis-Systems for environmental sensing

Downscaling chemical and biological sensors towards ultra-portable or in-vivo embeddable devices is a topic of high scientific and engineering interest nowadays. The progress registered in the last decades in fields such as nano/microfabrication technologies, integrated circuitry, optofluidics, computational methods (e.g., computational fluid dynamics (CFD), etc.), and information technology has enabled a huge development potential regarding the future of miniaturized sensing technologies.

Among the fields foreseen to benefit from this process, healthcare monitoring can be named [10–14], as well as organs-on-a-chip [15–17], drug screening [16], food monitoring [18], and environment monitoring [19–22]. Thus, potential applications are countless with a huge impact on the quality of life [23]. They are also directly linked to the next generation of smart homes and smart cities [24], artificial intelligence (AI), and Internet-of-Things (IoT).

Depending on the application, sensors may use a “dry” or “wet” sensing methodology. Dry sensors are capable to collect the data in its original environment using electronics or solid-state effects. On the other side, wet sensors use chemical reagents to further manipulate a specific

compound in order to obtain the aimed data. Thus, wet sensors involve by far more complexity in terms of development and optimization than dry sensors do, due to the issues raised by the microfluidic effects that are many times more difficult to be controlled precisely. Therefore, a sensing device being capable to perform all the steps of a complete analysis in integrated and automated way is named a Micro-Total-Analysis System (μ TAS) or Lab-On-A-Chip (LOC) device. This may include sampling, sample pre-treatment, chemical reaction(s), analytical separation(s), analyte detection, product isolation, and data analysis [25].

Even though the achievements reported in the literature are numerous, apparently the transition of these devices from lab prototyping to market is still limited, if not negligible [26–28]. The remaining challenges are still considerable. The main challenge is to identify and optimize strategies for the integration of all analysis functions into a cost-efficient, robust microstructure to be handled by non-trained people, in order to develop autonomous microanalysis systems.

μ TASs can be employed to automatize the precision detection process of specific environmental pollutants, such as VOCs. Analytical procedures used in environmental sensing often use a gaseous phase (sampled air from environment) and a liquid phase (sampled chemical reagent). Thus, this involves two-phase flows streamed in microchannels that are part of a closed system. Typically, the pollutants are trapped from the gaseous phase in the liquid phase where they are derived in special thermal conditions and quantified through a detection component.

Two-phase flows provide enhanced heat and mass transfer rates due to the large surface-to-volume ratios, specific to micro-scale flows [8, 15]. Other advantages include a low working fluid volume that speeds up the chemical reactions, improve the product yield, and reduce the reagent consumption [15]. However, the two-phase flow hydrodynamics in micro-channels are far from being completely understood [14]. Currently, it is difficult to replicate the flow, mass-transfer mechanisms, and reaction kinetics conditions from a single microchannel to more microchannels [29]. Flow parameters vary along the flow path making the fluid flow at one location dependent on the properties of the entire system.

To completely benefit from the analytical procedure downscaling, the detection component has to be miniaturized as well. Miniaturization of the detection component in a μ TAS means building a system capable to quantify the analyte presence in low detection volumes (e.g., μ L or nL volumes). This contributes to the minimization of the reagent consumption, increasing the autonomy of the system. Gas-liquid interaction processes are also influenced since they are characterized by specific mass-transfer rates occurring in a limited time over a specific common interface. Sometimes, large interface areas are requested in between the two fluids in order to achieve detectable analyte concentrations in the liquid phase. This is why a successful miniaturization of the detection component is highly beneficial with an impact over the entire downscaling process.

1.3. Motivation

The current trend is to develop dry methodologies for micro-sensing applications to reduce especially the operational complexity. However, in some cases, wet sensing methods cannot be replaced, at least up to now. There are contexts when both dry and wet sensing methodologies both exist to detect the presence of a compound, but the last perform much better in terms of sensitivity and accuracy.

This is the case for HCHO detection. For its real-time detection both dry and wet sensing methodologies exist, but wet methodologies perform much better. Even if the Hantzsch reaction-based method relies on “wet chemistry”, involving a continuous reagent consumption, this method is currently one of the most reliable candidates for developing an interference-free and sensitive palm-held continuous detector.

A research team from ICPEES Strasbourg and InAirSolutions start-up developed a real-time HCHO analyzer using Hantzsch derivatization reaction. The working principle of this analyzer is based upon the HCHO trapping from air into an Fluoral-P solution (0.01 M). The two phases are contacted through an annular flow inside a hydrophilic fused-silica capillary with a 530 μm internal hydraulic diameter and a 150 cm length [30]. The temperature at which the process occurs is $T = 338\text{ K}$. With a gas flow rate of 5 mL/min and a liquid flow rate of 5 $\mu\text{L}/\text{min}$, the device achieved a 100% trapping efficiency for concentrations in the range of 0 to 154 $\mu\text{g}/\text{m}^3$ (0–5.1 $\cdot 10^{-6}$ M) [31–33]. Although the detection range of the device satisfies the detection requirements recommended by the WHO, the current detector is semi-portable with approximately dimensions of a suitcase. Moreover, this detector relies on a 25 μL commercial detection cuvette and a photomultiplier tube for fluorescence intensity-based HCHO concentration quantification.

Therefore, the main motivation of this work is triggered by the need to miniaturize the fluorescence optical detection component in order to further downscale the entire analytical device towards a hand-held device. The main challenge relies on proposing a design and building and testing a fluorescence-intensity based detection prototype for low HCHO concentrations in low volumes of fluid. Afterwards, a gas-liquid micro-reactor concept to trap and derivatize the HCHO molecules before reaching the detector is desired.

1.4. Outline

This thesis consists of seven chapters.

Chapter 1 provides a brief introduction.

Chapter 2 presents the theoretical concepts implemented in the development and modelling processes involved in this work. The fundamental aspects related to intensity-based fluorescence sensing in optofluidic devices is discussed. Some considerations related to the gas-liquid micro-reactor modelling are also presented.

Chapter 3 discusses the main methods used nowadays for HCHO sensing. It presents the physicochemical properties of the HCHO molecule and the photochemical properties of DDL.

Chapter 4 proposes a microfluidic device concept for continuous HCHO sensing starting from a literature survey on miniaturization of optofluidic devices for fluorescence sensing.

Chapter 5 introduces the fluorescence sensing device built around a CMOS-image sensor. A detection device has been introduced, fabricated, and integrated using mainly off-the-shelf components (excepting microfluidic cells which were fabricated using standard microfabrication technologies). The sensing device was experimentally tested and the results have been analyzed. The results are presented and discussed.

Chapter 6 provides preliminary work related to a gas-liquid membrane-based microfluidic reactor. Some computational fluid dynamic simulations have been performed to determine the molecular spatial distribution depending on the Hantzsch reaction kinetics. Compatible materials and fabrication of the components for a first experimental prototype are presented.

Chapter 7 summarizes the achievements and identifies perspectives of the current work.

1.5. Output of the thesis

The main achievements of this work are related to the fluorescence sensing device which used a CMOS-image sensor as photodetector, and a SU8-3050 photoresist as waveguide for the light coming from a light-emitting diode and guided towards an interrogation chamber.

The fluorescence sensing concept proved its capability to detect HCHO molecules derivatized into DDL fluorophores in a 3.5 μL interrogation volume. HCHO concentration range tested was 0.001 – 10 mg/L. The device could distinguish fluorescence coming from DDL fluorophores, possessing a very low quantum yield at room temperature, $\phi_{DDL} = 0.005$. However, the response was not linear due to a possible combination of measurement, optical, and components alignment errors. Moreover, the fluidic cells tested were built in two configurations: One in quartz – SU-8 3050 photoresist – quartz and the other in silicon – SU8-3050 photoresist – quartz. The experimental tests ran in parallel under similar conditions. In the experiments, the configuration built upon the silicon as upper-layer proved an apparently higher SNR compared to the configuration where the upper-layer was made in quartz.

This part of the work was published in the *Micromachines* Journal (MDPI, Switzerland, IF: 2.943). Up to the current date (24.01.2022), it has been accessed 2545 times and 2 times cited.

A comprehensive literature survey that stands as the basis for the proposed sensing concept has been published in the *Microfluidics and Nanofluidics* Journal (Springer Publisher, IF: 2.612). Up to the current date (24.01.2022), it has been accessed 7621 times and cited 17 times.

A gas-liquid membrane-based micro-reactor design for HCHO trapping and derivatization has been introduced. Compatible materials and microfabrication technologies have been identified. A couple of CFD simulations have been run in order to determine the preliminary features of flow path.

Chapter 2. Fundamentals

2.1. Molecular fluorescence sensing in optofluidics

Optofluidics refers to a light-fluid interaction process occurring on a chip integrating (micro)fluidics and optics. The fluorescence phenomenon is one of the tools used to optically quantify the molecular concentrations in solutions. Thus, on-chip integrated optical and microfluidic functions using fluorescence for molecular detection are known as molecular fluorescence sensing in optofluidics.

2.1.1. Fluorescence basics

Fluorescence refers to the property of particular molecules to absorb photons at a particular wavelength (λ_{abs}) and re-emit them at a longer wavelength (λ_{em}) after a specific period of time ranging between $10^{-9} - 10^{-7}s$. The emission wavelength shift between λ_{abs} and λ_{em} is known as the *Stokes shift*. Molecules with this property are named fluorophores.

Under normal conditions, molecules occupy the lowest vibrational level or the ground state, S_0 . When excited by photons, molecules absorb them and their electrons move towards higher vibrational states reaching excited states [34]. Usually, fluorescence is observed at the vibrational relaxation from the first excitation level, S_1 , to the ground state, S_0 . For higher vibrational states, the energy is dissipated through internal conversion and vibrational relaxation.

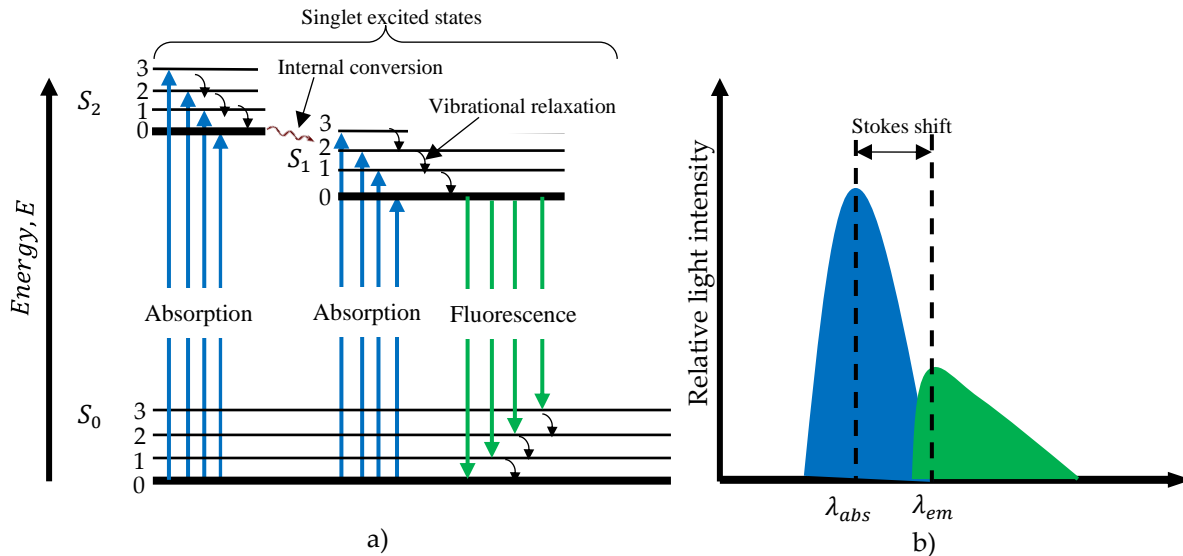


Figure 2.1.1. (a) Simplified representation of the Jablonski diagram. When excited (blue arrow), molecules absorb the energy, E , and its electrons move from the ground state, S_0 , to superior electric levels (0, 1, 3, etc.). De-excitation towards S_0 comprise: (1) a vibrational relaxation and an internal conversion until the first excitation level S_1 , and (2) a light emission characterized by a particular Stokes shift (green arrow) named fluorescence from S_1 towards S_0 . (b) Absorption and emission spectrums centered at λ_{abs} , respectively, λ_{em} .

The electronic state of the molecule is generally expressed using the Jablonski diagram (see Fig. 2.1.1.).

Quantification of the energy dissipation in the superior electronic levels is done through a parameter called quantum yield (Φ). Φ is defined as the ratio of the number of photons emitted to the number of the photons absorbed. The number of photons emitted as fluorescence are usually up to three orders of magnitude less than the photons being absorbed to excite the molecule [35].

$$\Phi(T) = \frac{\text{number of photons emitted}}{\text{number of photons absorbed}} = \frac{k_f}{k_f + k_{nr}} \quad (2.1.1.)$$

In Eq. 2.1.1., k_f and k_{nr} represents the first-order rate constant for fluorescence relaxation and the rate constant for non-radiative relaxation, respectively. Φ depends on the environment surrounding the fluorophore at the measurement time and its temperature. For example, a fluorophore excited in a specific solvent exerts a Φ that is different by that one obtained from other solvent. If temperature increases, Φ decreases and vice-versa. Both environment and temperature dependencies are explained by the Stern-Volmer relationship which is discussed in Demchenko [36].

When fluorophores are excited with a pulse excitation, the fluorescence emission intensity decays following first-order kinetics (see Eq. 2.1.2.).

$$F_t = F_0 e^{-k_f t} \quad (2.1.2.)$$

In this equation, F_0 is the fluorescence intensity at the initial emission time, $t = 0$, and F_t is the fluorescence intensity as a function of time. The fluorescence lifetime, τ_f , is defined as the time needed for fluorescence emission to decay to $1/e$ of its F_0 [35]. By introducing this condition in Eq. 2.1.2., τ_f is defined as the reciprocal rate constant, k_f (see Eq. 2.1.3.).

$$\tau_f = \frac{1}{k_f} \quad (2.1.3.)$$

2.1.2. Quantitative fluorometry and instrumentation

Fluorescence detection systems, also known as fluorimeters, are instruments used to quantify the fluorescence emission intensity, F . Traditional fluorimeters use a system of lenses and filters, high-performance light source, and very sensitive photon detectors (PDs) to capture the fluorescence emissions [37]. There are two types of filters usually integrated to filtrate the light. Emission filters (2) reject parasitic components of the excitation light beam (1), by narrowing the light broadband spectrum towards the excitation wavelength specific to the analyte of interest (3). Detection filters (4) stop the scattered light from reaching the PD surface and inducing optical noise (5) (see Fig. 2.1.2.).

Fluorescence intensity, F , is given by the number the photons emitted which is proportional to the light intensity absorbed (see Eq. 2.1.4.)

$$F = k_{inst} \Phi (I_0 - I) \quad (2.1.4.)$$

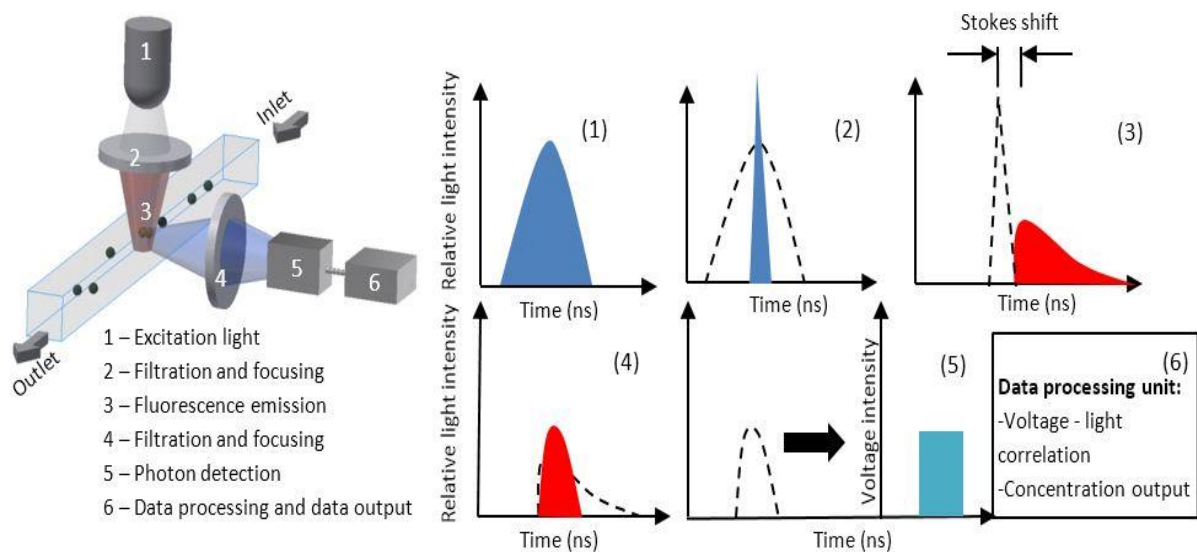


Figure 2.1.2. General detection scheme of a fluorimeter (orthogonal configuration). Reprinted from Mariuta *et al.* [38] under CC BY 4.0 License.

In this equation, I_0 is the intensity of the incident light and I is the light transmitted. I_0 and I are linked by the Beer-Lambert Law (see Eq. 2.1.5.) k_{inst} is a proportionality constant specific to the instrument.

$$\frac{I}{I_0} = 10^{-\epsilon lc} \quad (2.1.5)$$

Here, ϵ is the molar extinction coefficient, c is the molecular concentration, and l is the optical path length. By combining Eqs. 2.1.4 and 2.1.5., the following formulation of the fluorescence intensity, F , results in:

$$F = k_{inst} \Phi I_0 (1 - 10^{-\epsilon lc}) \quad (2.1.6)$$

For very low fluorescence intensities, F is given by the Eq. 2.1.7 [35].

$$F = 2.303 k_{inst} \Phi I_0 \epsilon lc \quad (2.1.7)$$

Thus, quantitative fluorimetry represents the measurement process of the fluorescence emission, F , from a sample, in order to find the molecular concentration, c . F is commonly measured in relative units (e.g., photon counts or analog signals averaged by the detection system) which are proportional to the number of the emitted photons. F depends on the intensity of the incident light, I , the geometry of the instrument, the detector sensitivity, and on the filter slit widths, etc. [36].

Quantitative analysis using intensity-based sensing requires a calibration process. Actually, this is the weak point of this sensing methodology since it makes the process more complicated and time-consuming. Measurements of undetermined concentrations have no meaning if they are not compared with standard measurements. Thus, it is mandatory to obtain a calibration curve by varying and measuring known molecular concentrations. The relative units

obtained from samples with undetermined concentrations are then related to this calibration curve.

2.1.3. Optofluidic integrated devices

2.1.3.1. Materials and microfabrication technologies

The ultimate aim in the development process of μ TAS is the integration of all the electrical, optical, chemical, and sensing functions on-chip [39]. As part of μ TAS, optofluidic integrated devices deal with fluid control, light manipulation, and signal transduction components.

Micro-valves, micro-pumps, and hydraulic components represent the fluid control component. Light emitters, waveguides, filtration and reflecting components, as well as functional photonic nanostructures are part of the light manipulation component, while photon-detectors deal with signal transduction [40].

The materials used in the fabrication process of the optofluidic components commonly include polymers, glass, and silicon. Polymers can be classified depending on the mechanical properties in rigid polymers (thermoplastics) and elastomer polymer (i.e., Polydimethylsiloxane – PDMS) (see Table 2.1.1.).

Table 2.1.1. Properties of the main polymers used in microfluidic applications. Data from Tsao [41], Guckenberger *et al.* [42], and Yen *et al.* [43].

	Polymer	Mechanical property	Thermal property	Solvent resistance	Acid / base resistance	Optical transmissivity		Contact angle with water
						Visible	UV	
	PDMS	Elastomer	~353 K	Poor	Poor	Excellent	Good	100°
Thermoplastics	PMMA	Rigid	373~398 K	Good	Good	Excellent	Good	64°
	PC	Rigid	413~418 K	Good	Good	Excellent	Poor	77°
	PS	Rigid	363~373 K	Poor	Good	Excellent	Poor	87°
	COC/COP/CBC	Rigid	343~428 K	Excellent	Good	Excellent	Excellent	95°~100°

PDMS is largely used in microfluidic applications due to its ease-of-fabrication and also in optofluidics due to its high light transmittance. However, it is many times incompatible with aggressive chemical reagents. Thermoplastics have been considered an alternative due to their improved mechanical properties, cost-efficiency, and improved chemical compatibility. The fabrication technologies that are compatible with common polymer functionalization are hot-embossing, mold injection, micro-milling, and femto-second laser welding (see Table 2.1.2. for microfabrication techniques).

Glass is characterized by high optical transmittance and it is chemically resistant to aggressive reagents. Glass exerts near-zero autofluorescence and it is often used as material for fluidic cell manufacturing (generally known as cuvettes in traditional fluorimeters).

Silicon is used due to the well-established micro- and nanofabrication technologies developed over the years for integrated circuits fabrication [44]. Generally, these are based on

film deposition, UV lithography, etching, and doping. Silicon is many times combined with the materials presented above to form integrated heterogeneous structures.

Table 2.1.2. Microfabrication techniques used in optofluidic system fabrication. Data from Tang *et al.*[40].

Technique	Application	Advantage	Disadvantage
UV lithography	Mold fabrication	High efficiency Large working area	2D planar structure limited
Two-photon stereolithography	Mold fabrication Integrated optical components	High resolution Complex structures	
3D printing	Mold fabrication Chip fabrication	Complex structures	Limited material choices
Milling	Mold fabrication Chip fabrication	Complex structures	Poor resolution
Direct laser writing	Integrated optical components Chip fabrication	High resolution Complex structures	Low efficiency
Hot embossing	Chip fabrication	High efficiency	Poor resolution
Injection molding	Chip fabrication	High efficiency	Poor resolution

2.1.3.2. Light-emitters

The light-emitter is the component of the optofluidic device that provides the excitation beam.

The selection process of the light-emitter starts with the identification of the fluorophore absorbance wavelength, λ_{abs} . Ideally, the light-emitter should possess an infinitely narrow emission bandwidth with the maximal peak at the absorption (or excitation) wavelength, $\lambda_{abs} = \lambda_{ex}$. In practice, this is impossible. The emission bandwidth introduces parasitic photons into the optical circuit that create an optical noise (see Fig. 2.1.3.). Thus, the emission bandwidth

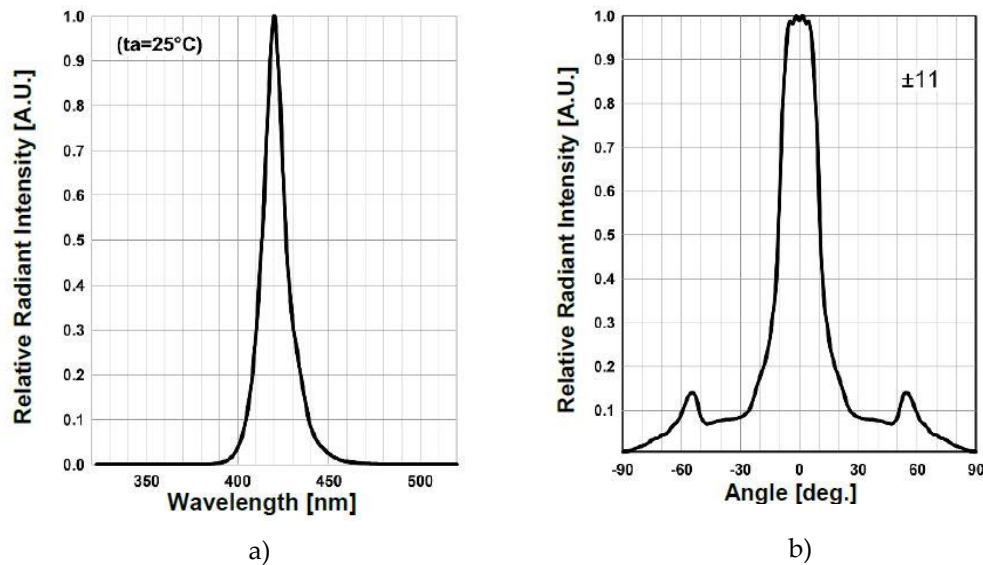


Figure 2.1.3. (a) Relative radiant flux intensity, Φ_e , of a LED with the emission wavelength centered at $\lambda_{em} = 420 \text{ nm}$. (b) Radiant flux intensity depending on the emission angle, φ . Reproduced from SMB1N-420H-02 LED Data Sheet, Roithner Laser Technik, Austria.

is related to the background noise the light-emitter might bring into the system. The narrower the emission bandwidth, the lower the noise is, and vice-versa.

Generally, light-emitters are characterized by the radiant flux, Φ_e , the beam coherence, γ , the emission angle, φ , and stability of the light emission bandwidth.

Laboratory fluorimeters use bulky argon, xenon, halogen, mercury, or incandescent lamps as light-emitters [45]. Optofluidic sensing devices focus on the integration of high-power micro-laser diodes, solid-state light emitters (such as light-emitting diodes (LED), organic light emitting diodes (OLED), and polymer light-emitting diodes (PLED)).

Solid-state light emitters (SSLE) with tunable properties have been frequently used in embedded configurations aiming to monolithically integrate fluorescence detection on-chip. However, the light emission process in SSLEs produces heat. Temperatures above specific values make the solid-state to shift the emission bandwidth. This is detrimental since the SSLE emission bandwidth will not be centered at λ_{abs} of the fluorophore anymore.

A LED is a p-n junction that emit photons under the influence of an electric field. The emissions of photons directly from the LED surface is done at large angles without reflective cups. A reflective cup is a lens system mounted on top of the LED surface to model the radiation flux emission pattern, Φ_e , using the total internal refection (TIR) principle (see Fig. 2.1.4.).

High-power micro-lasers and LEDs have been mainly used when modular and robust miniaturized fluorimeters were targeted. In terms of performance, micro-lasers perform the best. Commercially-available LEDs and micro diode lasers have been widely implemented in microfluidic detection devices since their early development stage. Nowadays, OLEDs and dye lasers are very promising alternatives due to their capability to be monolithically integrated onto optofluidic structures [46].

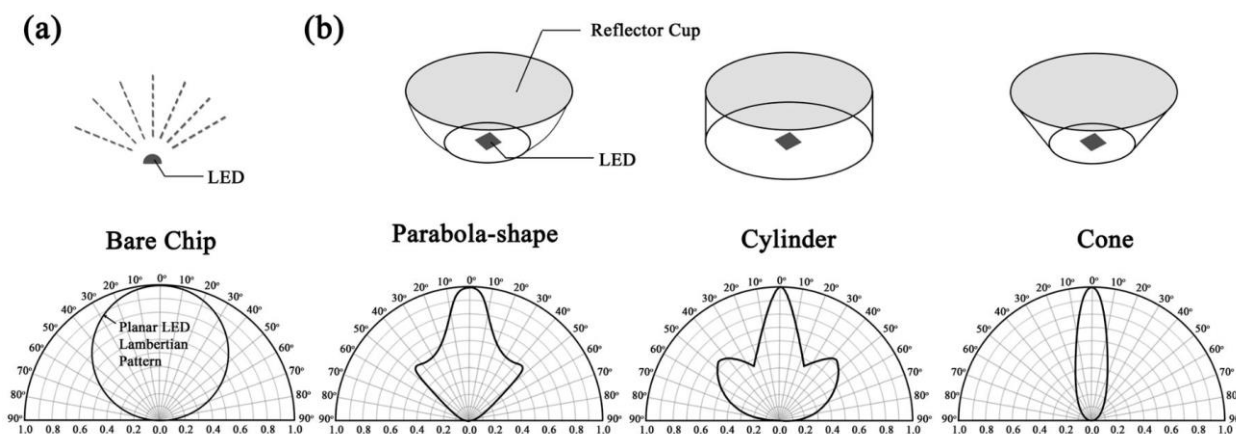


Figure 2.1.4. (a) Relative radiant flux of a bare LED (Lambertian emission pattern). (b) Relative radiant flux of LEDs with various reflective cup structures. The angles represent the emission angles, φ , while the horizontal scale denotes the relative radiant flux intensity. Reproduced from Chen *et al.* [47], Copyright 2015, with permission from Royal Society of Chemistry.

Commonly, the waveguide is located perpendicularly on the light-emitter surface. The zero degrees emission radiation angle, φ , of the light-emitter is concurrent to the optical axis of the waveguide. Thus, the light-emitter should have the maximum relative radiant flux intensity, Φ_e , located at zero degrees emission radiation angle, φ . Respecting this condition, the excitation light, I , reaching the sample in the interrogation chamber is maximized.

2.1.3.3. Waveguiding

The propagation of the excitation beam from the light source towards the interrogation chamber, is normally made through a waveguide (see Fig. 2.1.5.).

Waveguides have a core and a cladding, each characterized by a refractive index. The refractive indexes of the core, n_1 , is larger than the refractive index of the cladding, n_0 . The light beam has to respect the total internal reflection (TIR) condition in order to be efficiently confined in the core and transported towards the interrogation chamber (see Eq. 2.1.8.). Incident angle, θ , and the refractive angle, ϕ , (see Fig. 2.1.5.), are related to each other by Eq. 2.1.9. Then, the critical TIR condition is obtained in Eq. 2.1.10.

$$n_1 \sin\left(\frac{\pi}{2} - \phi\right) \geq n_0 \quad (2.1.8.)$$

$$\sin\theta = n_1 \sin\phi \leq \sqrt{n_1^2 - n_0^2} \quad (2.1.9.)$$

$$\theta \leq \sin^{-1}\sqrt{n_1^2 - n_0^2} \equiv \theta_{max} \quad (2.1.10.)$$

When travelling through the core, the light is attenuated mainly due to absorption and scattering (see Eqs. 2.1.11. - 2.1.12.). The attenuation is dependent on the material physical properties. Each material shows a specific attenuation coefficient, μ , given by the sum of the absorption coefficient, μ_a , and the scattering coefficient, μ_s .

$$\mu = \mu_a + \mu_s \quad (2.1.11.)$$

$$\mu = -\frac{1}{\Phi_e} \frac{d\Phi_e}{dz} \quad (2.1.12.)$$

Moreover, the optical characteristics of the optical materials are function of the light wavelength traveling through it. Thus, the attenuation coefficient of a specific optical material could be higher or lower depending on the wavelength of the light. Information on the optical characteristics of

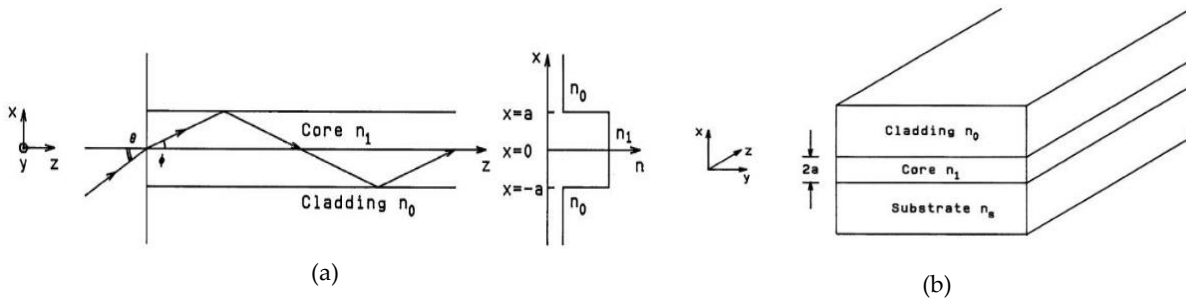


Figure 2.1.5. (a) Total internal reflection (TIR) principle for electromagnetic wave transport through waveguides, where the θ angle represents the incidence angle of the radiant flux emitted by the light source. (b) Planar waveguide circuit. Reproduced from Okamoto *et al.* [48].

each material at each of the wavelengths from the light spectrum, including the attenuation coefficients, can be obtained from literature for most of the optical materials.

Radiant energy transmission through a volume is described by transmittance, T . Thus, transmittance describes the ratio between the transmitted radiant flux, ϕ_e^t , and the received or incident radiant flux, ϕ_e^i . Energy loss due to internal absorption is called internal transmittance.

$$T = \frac{\Phi_e^t}{\Phi_e^i} \quad (2.1.13.)$$

The absorbance coefficient, a , is material and wavelength dependent and determines how far the light can propagate into that material at a specific wavelength. In Eq. 2.1.4., k_e is the extinction coefficient.

$$a = \frac{4\pi k_e}{\lambda} \quad (2.1.14.)$$

2.1.3.4. Optical noise suppression

After the light beam reaches the interrogation chamber and excites the fluorophores in the sample, a sum of events occurs. First, a fluorescence signal proportional to the fluorophore concentration in the sample is emitted. Second, the fraction of the excitation beam that has not been absorbed, it is scattered. A part of this scattered light travels towards the photon detector – if not suppressed by filter – where it is read out as optical noise.

Therefore, optical noise is an undesirable parameter quantifying the level of parasitic light reaching the detector. Noise sources in fluorimeters are both optical (unfiltered excitation light and shot noise) and non-optical (dark and technical noises, see [Section 2.1.3.5.](#)) [63]. Other optical noise sources may include compounds with different spectra present in the sample, i.e., other fluorophores.

To eliminate the optical noise, filters are usually used (band-pass and/or long-pass). However, the efficiency of most commercially available filters is limited. A small percentage of the parasitic light passes through towards the photon detector even for the best existing filters (filtration efficiency of 99.999%).

Undesirably, filters attenuate the radiant flux, Φ_e , as well. Thus, attenuation in [Eq. 2.1.11.](#) gains one more component given by the filter attenuation. This component is named reflectance, R . R is characterized as the ratio between the reflected radiant flux, Φ_e^r , and the incident radiant flux, Φ_e^i (see [Eq. 2.1.15.](#)).

$$R = \frac{\Phi_e^r}{\Phi_e^i} \quad (2.1.15.)$$

Nevertheless, there are currently filters based on artificial optical substances possessing zero reflectance for radiant fluxes characterized by specific wavelengths of the spectrum [49].

2.1.3.5. Photodetectors

Photodetectors (PD) count the absorbed incident photons on their surface and transform them into a voltage or current signal proportional to the intensity of the photons absorbed. PDs are

commonly characterized by a detection bandwidth, responsivity, dynamic range, noise level, active area, response time, and quantum efficiency (QE).

Detection bandwidth is the wavelength range for which PDs are sensitive to light and it can be expressed in nm or Hz . Moreover, wavelengths in the detection bandwidth are characterized by a specific responsivity. **Responsivity** is the ratio of the output current signal produced by the PD and the incident optical power on its surface. It is expressed in Ampere/Watt and it depends of the **quantum efficiency (QE)**. QE indicates the percentage of the incident photons contributing to the output current signal and it is wavelength specific. The best QE of the available PDs are situated around 0.9 and it is specific to photodiodes. **Dynamic range** is the domain between the lower and the larger signal that can be measured linearly. **Active area** is characterized by the width and length of the detection region.

The noise originates from shot, dark, read, and technical sources. **Shot noise** is induced due to the Poisson distribution of the photons at their arrival on PD surface. The shot noise in the photon counts induces a current shot noise in the PD. **Dark noise** is represented by the current intensity induced when PD surface is not illuminated. This current is named dark current. Dark current is induced due to the thermal excitation of the electrons. It accumulates over time and it is time-dependent. Dark current is also temperature-dependent. If PD temperature decreases, the dark noise decreases as well. **Read noise** is a thermally-induced variation in the load resistance of the transimpedance of the detection circuit. Exactly like the shot noise, it is unavoidable. It is temperature-dependent and has the property to decrease with lower temperatures. Technical noise comes from sources related to the flaws or imperfections in the PD design.

PDs currently used in the miniaturization attempts of the fluorescence-based sensing devices are photomultiplier tubes (PMT), avalanche photodiodes (APD), PIN photodiodes, image sensors (Complementary-Metal-Oxide-Semiconductor image sensors, known as CIS, and Charge-Coupled Devices, known as CCD), and more recently organic photodiodes (OPD).

PMTs are very sensitive photon detectors being capable to measure even single photons. They are equipped with photocathodes which convert the light into photoelectrons. Photoelectrons are emitted in vacuum. An electric field is created between the photocathode and anode in order to accelerate the photoelectrons to the first dynode. A dynode is an electrode that emits additional electrons. Thus, the emissive surface of the first dynode emits an amplified photoelectric signal. This process is repeated many times until the last dynode results in final gain larger than one million. The anode collects the multiplied electrons and an output signal is produced. Due to their sensitivity, most of the laboratory-scale commercial fluorimeters use PMTs as photon detectors. They exist in miniaturized (finger-tip) configurations.

APDs are semiconductor photodiodes that use the photoelectric effect to convert light into electrical signal. Its functionality is very similar to that of the PMTs, except that APDs uses semiconductors to detect and multiply the emission signal. APDs are named depending on the semiconductor used in their fabrication: silicon APDs, germanium APDs, and InGaAs APDs.

PIN photodiode is a photodiode with an undoped (intrinsic) region between p- and n-doped regions. The majority of the photons are absorbed in the intrinsic region where carriers are generated. They contribute to the photocurrent generation based on the incident light. Relative to the other PN detectors, they have an improved QE and a higher detection bandwidth.

CISs are a sub-category of the active-pixel sensors. They are integrated circuits with an array of pixel sensors. Each pixel sensor contains its own light sensor, an amplifier, and a pixel select switch. Thus, the main components are color filters, a pixel array, a digital controller, and an analog-to-digital converter. Currently there are various models applied to gather information from pixels, such as: RGB (Red, Green, Blue), HSV (Hue, Saturation, Value), HIS (Hue, Intensity, Saturation), CIELab or CIExyY [50]. There is an increased interest in employing the RGB model combined with an image sensor or a camera to determine the concentration of analytes [51]. Generally, for CIS, the performance of the filters is not sufficient and different filtration algorithms are implemented, in order to diminish the dark noise.

Although the **OPDs** have been around for some time, the progress registered recently brought their performances very close to their above presented inorganic counterparts. They are characterized by some unique features such as flexibility and customizable detection bandwidth. Thus, the organic material can be fabricated in such a way that it is sensible only for the light in a specific wavelength range, i.e., fluorescence emission of a specific fluorophore. This leads to filterless, simpler, and more compact configurations.

The selection process of a PD suitable for a particular application has to include the following criteria:

- maximized QE in the fluorescence emission wavelength
- minimized QE in the fluorophore absorption wavelength – zero would be ideal
- active area of the photon detector
- electronic level noise at the fluorescence emission wavelength
- dynamic range for the concentration range of interest to be quantified
- robustness and costs

2.1.4. Sensitivity and Limit-of-Detection

Limit-of-detection (LOD) represents the lowest fluorophore concentration, c_{LOD} , that can be accurately measured in a sample. c_{LOD} has to produce a signal that is distinguishable from the blank/background signal, X_{LOD} .

Sensitivity is the slope of the calibration curve (see [Section 2.1.2](#)) defined as the linear dependence of the analytical signal, X , on the fluorophore concentration, c [36]. The LOD value is calculated relative to the limit-of-blank (LOB) and to the standard deviation of the lower fluorophore concentration distinguishable, $SD_{low\ concentration\ sample}$.

$$LOD = LOB + 1.645(SD_{low\ concentration\ sample}) \quad (2.1.14.)$$

LOB is calculated using Eq. 2.1.15 by taking multiple counts of the blank sample (a solution with zero fluorophore concentration) which results in blank signals. In this equation, $mean_{blank}$ is the mean value of the blank signals and SD_{blank} is their standard deviation.

$$LOB = mean_{blank} + 1.645(SD_{blank}) \quad (2.1.15.)$$

Determination of these parameters has to be done for at least 20 independent samples to be statistically significant [52].

Signal-to-noise ratio (SNR) is used to characterize the performance of the detection instrument. It is the ratio between fluorescence signal intensity, P_{signal} , and background noise intensity, P_{noise} , quantified by the photodetector.

$$SNR = \frac{P_{signal}}{P_{noise}} \quad (2.1.16.)$$

There are mathematical and signal treatment methods that can be used to artificially decrease the level of the background noise, P_{noise} . Signal treatments use electronic filters implemented at the photodetector level. Although the P_{noise} is reduced, the signals coming from the small concentrations are also removed due to over-smoothing. Alternatively, mathematical models such as Gaussian convolution, Fourier transform, or wavelet transform can be used to avoid this issue.

Method sensitivity and its LOD are limited by the noise of the detection instrument which is given by the SNR. Thus, LOD is the fluorophore concentration for which the fluorescence intensity is three times higher than the background noise, P_{noise} , measured by the instrument. LOQ is the fluorophore concentration corresponding to the fluorescence intensity which is ten times higher than the background noise. LOQ can be similar or higher to the LOD, but never lower.

2.1.5. Particularities of fluorescence intensity sensing. Non-linearity effects.

Fluorescence intensity sensing is characterized by a series of particularities that might affect the expected linear response of an assay. These particularities are further characterized.

Quenching is a reversible process resulting in fluorescence intensity decreasing due to short-range interactions between the fluorophore and the other molecules located in the sample. When the interaction takes place with the other fluorophores, it is called self-quenching.

Photobleaching is a permanent process resulting in the decrease of fluorescence intensity due to the high-intensity of the excitation power.

Non-linearities can appear in the following contexts [36]:

- When the excitation light passes through a strongly absorbing sample and the light decreases in intensity. The primary inner filter effect is induced.
- For samples with high fluorophore concentration, the emitted light can be reabsorbed by the interrogation sample and emission does not reach the PD. The secondary inner filter effect is induced.

- Primary and secondary inner filter effects can be eliminated by reducing the optical path. When the absorbance is below 0.05 – 0.1, these effects should not be present.
- When fluorescence occurs at high intensities of the excitation light. In this context, a part of the fluorophores is in the excited state and, consequently, the ground state becomes depopulated. Fluorescence intensity being proportional to the ground-state concentration, the light quenching effect occurs.

2.2. Flow microreactors modelling

2.2.1. Introduction

Gas-liquid microreactors for continuous gaseous molecular trapping are a particular class of flow microreactors (FMR) involving a high degree of complexity and unsolved challenges. Conceptually, FMRs are not providing only devices having a lower size characterized by high volume-to-surface ratios, short diffusion and mixing paths, but also mass- and heat-transfer coefficients that are orders of magnitude higher comparative to the macroscale reactors [53].

The gas-liquid microreactors are currently under intense research interest due to the development potential enabled by the microfluidics and nanotechnology synergy. This is mainly triggered by research fields such as personalized medicine, organs-on-chip, and real-time environmental sensors. Their successful scaling-down process would create new routes towards applications, such as point-of-care medical devices, portable environmental sensors, etc. [55].

A Gas-Liquid FMR for continuous detection of gaseous molecules involves: (1) gas-liquid interactions, followed by (2) mass-transfer processes of the molecules from the gas phase towards the liquid phase, (3) chemical reactions of the trapped molecules into the liquid reagent.

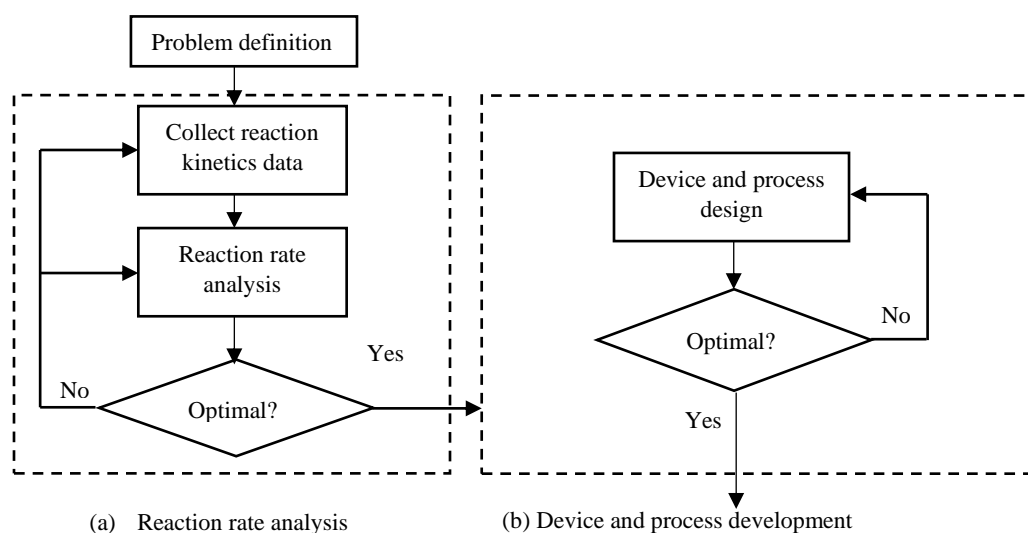


Figure 2.2.1. Development stages of a flow microreactor (FMR). Reprinted with permission from Nakahara *et al.* [54]. Copyright 2015, American Chemical Society.

One of the most important challenges in the gas-liquid FMR development is the precise and reproducible contacting of the two phases [56]. Gas-liquid FMRs may be designed with a direct gas-liquid contacting of the phases or with a hydrophobic porous membrane as a phase separator. Their performance is evaluated depending on the process operation variables (hydrodynamic properties, temperature, pressure, flow rates). Thus, in the development process of a gas-liquid micro-reactor (modelling, design, and optimization), the hydrodynamic conditions have to be precisely known and controlled.

2.2.2. Hydrodynamics of microfluidic flows

2.2.2.1. Single-phase flows

Microfluidics is the study of fluid dynamics events at a micro-scale. Microfluidics begins when the surface forces start dominating the volumetric forces.

Thus, at the transition from macro to micro-scales, dimensionality is changed. At macro scale, three dimensions are important, the flow being volume-defined. At micro-scale, the flow is surface-dominated and this means that two dimensions are most important. Going to nano-scale, the flow becomes “one dimensional”, only lines or even dots become important [29].

Generally, liquid and gas pressure-driven microfluidic flows can be usually treated using the continuum approach (see Eqs. 2.2.1. and 2.2.2.).

$$\frac{\partial \rho}{\partial t} + \nabla \cdot (\rho u) = 0 \quad (2.2.1.)$$

$$\rho \left(\frac{\partial u}{\partial t} + u \cdot \nabla u \right) = -\nabla p + \mu \nabla^2 u + f \quad (2.2.2.)$$

When $Re \ll 1$, the $u \cdot \nabla u$ term can be neglected and the Navier-Stokes equation becomes the Stokes equation. Due to low Re numbers, the flow regime in microfluidics is dominated by laminar flows, but turbulent flows may exist as well. It was demonstrated that the transition limit towards the turbulent flow decreases with higher roughness [57].

In pressure-driven gas flows, continuum approach applying the conservation of momentum and mass as described by the Navier-Stokes equations can be applied until a certain extent which is given by the Knudsen number, Kn . Knudsen number is used to define the boundaries between the flowing regimes (see Table 2.2.1.).

A couple of dimensionless numbers have been generally accepted for understanding the interplay between the volumetric and surface forces in microfluidics (see Table 2.2.2.).

Table 2.2.1. Flow regimes given by the Knudsen numbers using mean free path, λ , and characteristic length, L_c [58].

Formulae	Flow regimes			
$Kn = \frac{\lambda}{L_c}$	Continuum	Slip flow	Transition	Molecular
$\lambda = \frac{k_B T}{\sqrt{2} \pi d^2 p}$	$Kn < 0.001$	$0.001 < Kn < 0.1$	$0.1 < Kn < 10$	$Kn > 10$

* d is the diameter of the molecule, k_B is the Boltzmann’s constant and p is the local pressure.

Dimensionless numbers are used as well to define the transition from the macro to the micro domain. For example, Bretherton proposed the use of the Eötvös number, $Eo = 0.84$, as the criterion for the transition from macro to microfluidics [59]. When $Eo \ll 1$, the contribution of the gravitational forces can be ignored.

Table 2.2.2. Dimensionless numbers used in continuous flow microfluidics.

Dimensionless number	Formulae	Meaning
Reynolds number (Re)	$Re = \frac{\rho du}{\mu}$	Ratio of the inertial forces to viscous forces.
Eötvös number (Eo) / Bond number (Bo)	$Eo = Bo = \frac{\Delta \rho g d^2}{\sigma}$	Ratio of the gravitational to capillary forces.
Capillary number (Ca)	$Ca = \frac{\mu u}{\sigma}$	Rate of the viscous forces to surface tension forces across gas-liquid interface.
Ohnesorge number (Oh)	$Oh = \sqrt{\frac{We}{Re}} = \frac{\mu}{\sqrt{\rho d \sigma}}$	Rate of the viscous forces to inertial and surface tension forces.
Webber number (We)	$We = Re \cdot Ca = \frac{\rho u^2 d}{\sigma}$	Ratio between deforming inertial forces and stabilizing cohesive forces.

Pressure-driven flows in microchannels generate pressure drops, Δp , along the channel length, L . Pressure-drop is defined as the difference in total pressure between two points of a fluid system. More precisely, the larger L is, the higher the pressure needed to drive a flow through it at specific velocity. Therefore, pressure-driven flows generate a pressure increase from the outlet towards the inlet which is influenced by the flow rate, the shape, the cross-section area, the length of the channel, fluid properties, and roughness of the micro-channels. Its estimation is one of the crucial calculations to be performed in the initial development stages. Otherwise, the channel or the system may physically collapse due to the very high local forces generated by the pressure.

In fluid dynamics, Hagen-Poiseuille equation is used to calculate empirically the pressure drop in channels. In microfluidics various correlations exist for estimation of pressure drop in single, respectively multiphase flows which are more or less accurate depending on the assumption made and the context in which they are applied. In liquid single-phase flows, pressure drop in constant cross section microchannels can be estimated using the equation [60]:

$$\Delta p = f \frac{L}{d_h} \frac{\rho u^2}{2} \quad (2.2.3.)$$

Here, d_H , is the hydraulic diameter of rectangular channels, the most spread type of microchannel in microfluidic devices due to its ease-of-fabrication, is calculated depending on the channel's width, a , and channel height, b :

$$d_h = \frac{4ab}{2a+2b} \quad (2.2.4.)$$

The function $C_f \equiv f \times Re$ is often used to characterize the pressure drop variation as a function of Re number [60]:

$$C_f \equiv f \times Re = \frac{8\rho\Delta p a^3 b^3}{L\mu(a+b)^2 m} \quad (2.2.5.)$$

In gas single phase flows, pressure drop in constant cross section microchannels can be estimated based on the momentum theory using the equation [60]:

$$\frac{dp}{dx} = -\frac{f}{d_H} \rho \frac{u^2}{2} - \rho u \frac{du}{dx} \quad (2.2.6.)$$

Many correlations exist for calculation of the friction factor, f . Their validity range and accuracy is discussed broadly in Asadi *et al.*, [61] and Triplett *et al.*, [62] from which it results that the wall roughness plays a very important role, especially in turbulent microfluidics. Eq. 2.2.7. states the general correlations for finding the friction factor in circular microchannels.

$$f = \begin{cases} \frac{64}{Re} & (\text{for laminar flow}) \\ 0.316Re^{-0.25} & (\text{for turbulent flow}) \end{cases} \quad (2.2.7.)$$

2.2.2.2. Two-phase flows

Gas-liquid interactions are a particular category of multiphase flows occurring in microfluidic channels when a gaseous and a liquid phase are pressure-driven in the same confined space. As a consequence, various flow patterns may form depending on the gas and liquid flow rates, the resultant of the surface and volume forces interplay, and depending on the wettability properties of the microchannel's walls.

The main two-phase flow patterns that may occur in microfluidic gas-liquid interactions are bubbly flow, slug / Taylor / segmented flow, annular flow, and churn flow. However, transition flow patterns may occur, e.g., slug-annular flow (see Fig. 2.2.2., a). **Bubbly flow** is

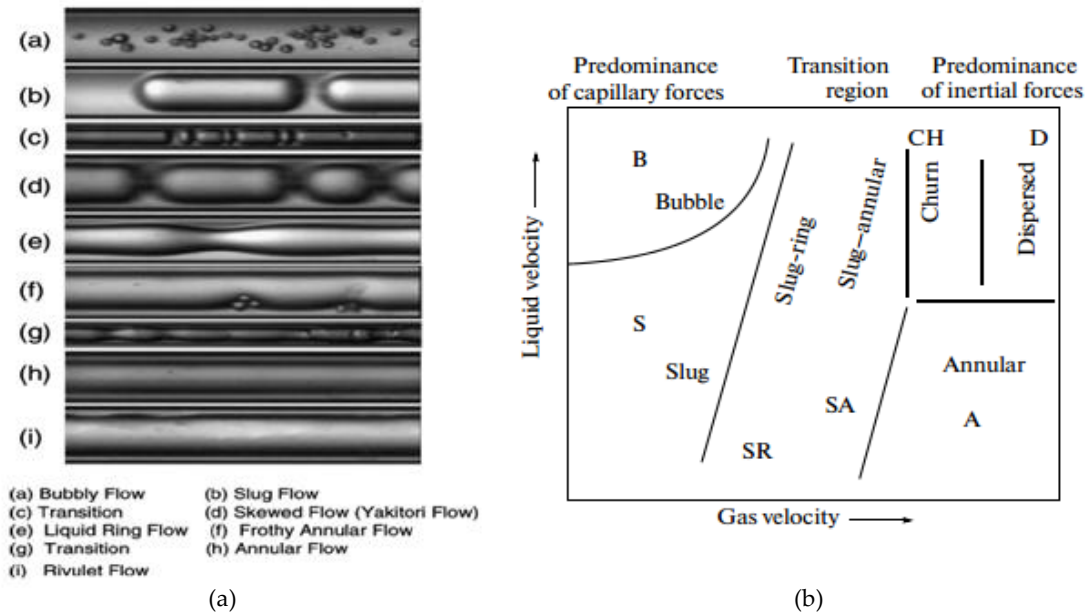


Figure 2.2.2. (a) Gas-liquid flow patterns in microfluidic channels. Reproduced from Serizawa *et al.* [63], Copyright 2002, with permission from Elsevier (License number 5235900263267). (b) The flow pattern transition map as a function of superficial gas and liquid velocities. Reproduced from Rebrov *et al.* [64], Copyright 2010, from Springer Nature (License number 5235891301174).

characterized by the presence of gas bubbles which are smaller than the channel diameter flowing with the liquid inside a microchannel.

Slug flow/Taylor flow/Segmented flow is a flow regime characterized by gas bubbles with the length usually several times wider than its width which are surrounded by liquid films in the wall adjacent region and liquid plugs in between them.

Annular flow is described as a liquid film flowing on the channel wall with gas flowing in the channel core at a velocity around three orders of magnitude higher than the liquid velocity. The inertia of the gas core has to overcome the interfacial tension forces to keep the interface stable. Annular flow possesses much higher surface-to-volume ratios, a , compared to the Taylor flow and all other flow patterns.

Churn flow is a transition flow pattern between the slug flow and annular flow pattern. This regime is reached when the elongated slug bubbles become unstable leading to their disruption and some small bubbles occur into the liquid slug [65].

Reproducibility is yet challenging in microfluidic gas-liquid two-phase flows. Pattern boundary positioning on the flow maps is influenced by gravity, inlet region geometry, diameter of the channel, cross-section, liquid viscosity, wettability, and surface tension. Also, the instruments used to drive the fluids into the channels can exert a considerable influence over the position of the boundaries [64].

In gas-liquid two-phase microfluidics, pressure drop estimations are based upon a classical homogenous flow model (HFM) and a separated flow model (SFM) [61,62]. The same Eq. 2.2.7. is used to estimate the pressure drop, but this time f_{TP} is the two-phase Fanning friction factor and ρ_{TP} is the two-phase homogeneous density. f_{TP} is calculated differently depending on the value of the two-phase Reynolds number, Re_{TP} .

$$\left(\frac{dp}{dx}\right)_{TP} = \frac{f_{TP}G^2}{2\rho_{TP}d_h} \quad (2.2.8.)$$

$$f_{TP} = \begin{cases} \frac{16}{Re_{TP}} \text{ for } Re_{TP} \leq 2000 \\ 0.079Re_{TP}^{-0.25} \text{ for } Re_{TP} > 2000 \end{cases} \quad (2.2.9.)$$

$$Re_{TP} = \frac{Gd_H}{\mu_{TP}} \quad (2.2.10.)$$

$$\mu_{TP} = \left(\frac{\chi}{\mu_G} + \frac{1-\chi}{\mu_L}\right)^{-1} \quad (2.2.11.)$$

$$\chi = \frac{m_{vapor}}{m_{liquid}+m_{total}} \quad (2.2.12.)$$

HFM assumes that flow velocities of the phases are equal. Therefore, this model is more suitable to estimate pressure drop in two-phase flows such as slug flow, but not in annular flows where the model tends to overpredict it [62]. On the other hand, SFM assumes that gas and liquid flow separately in the channel. Each phase occupies a specific sector of the cross section. Though, the model is more suitable for predicting the pressure drop in annular flow.

2.2.3. Gas trapping in microfluidic two-phase flows

2.2.3.1. Fick's laws. Convective-diffusive transport equation

Thermal motion of gas and liquid chemical species at temperatures above the absolute zero is called molecular diffusion. Assuming a specific chemical species, i , into a control volume with its concentration generically noted as c_i , a local higher species concentration causes a concentration gradient, ∇c_i , which leads to a diffusive flux, j_{diff} , towards the regions of lower concentration. After a particular period of time, equilibrium is reached, the concentration gradient being zero in each point of the control volume. However, at zero concentration gradient, the molecules continue to move and this is called self-diffusion.

Diffusion coefficient, D_i , denotes the proportionality constant between the diffusive flux and the concentration gradient of species i into a mixing of other species. D_i is constant only for dilute solutions, this case being known as Fickian diffusion. D_i can be determined by implementing the Stokes-Einstein equation from the kinetic theory (see Eq. 2.2.13.) which includes temperature, T , kinematic viscosity, μ , Boltzmann's constant, k_B , dynamic viscosity, η , and radius of the molecule.

$$D_i = \frac{k_B T}{6\pi\mu r} \quad (2.2.13.)$$

Though, the first Fick's law states that diffusive flux is proportional to the magnitude of the concentration gradient (see Eq. 2.2.14.). In this equation, D_i denotes the diffusion coefficient expressed as area per unit time.

$$j_{diff} = -D_i \nabla c_i \quad (2.2.14.)$$

Moreover, for describing the variation of the concentration gradient depending on the unit time, t , there is a second Fick's law (see Eq. 2.2.15.) which is derived from the equation of mass conservation (see Eq. 2.2.16.).

$$\frac{\partial c_i}{\partial t} = \nabla \cdot (D_i \nabla c_i) \quad (2.2.15.)$$

$$\frac{\partial c_i}{\partial t} + \nabla \cdot j_i = 0 \quad (2.2.16.)$$

When the fluid inside the control volume is not at rest i.e., its momentum is not zero, it is said that there is a bulk motion of the fluid. In this situation, an additional transport mechanism named convection (or advection) accounts for the movement of the mass due to its momentum (see Eq. 2.2.17.).

$$j_{conv} = -\nabla \cdot (uc_i) \quad (2.2.17.)$$

Again, the convection-diffusion equation can be derived from the continuity equation (see Eq. 2.2.18.) where the total flux, j , is:

$$j_i = j_{conv} + j_{diff} \quad (2.2.18.)$$

Coupling the convection transport and the diffusion transport results in the convective-diffusion equations which accounts for the transport of species in a moving fluid (see Eq. 2.2.19.).

$$\frac{\partial c_i}{\partial t} = \nabla \cdot (D_i \nabla c_i) - \nabla \cdot (uc_i) + R \quad (2.2.19.)$$

In this equation, R is the source, the sink term or the reaction rate, describing the creation or destruction of the species in situations involving chemical reactions. If the reaction produces more species, increasing their concentration, then $R > 0$ and it is called a source term. Otherwise, if $R < 0$, the reaction consumes the species, decreasing their concentration and it is called a sink term (see [Section 2.2.4.](#)).

2.2.3.2. Henry's law. Vapor-liquid phase equilibria

The complexity increases in the case of two-phase interactions. Species follow the same laws above stated, but in the process of moving towards the region having a lower concentration, the species have to pass through the interface separating the two phases. This event created the phenomenon called gas-liquid interface transport. The diffusion process across the interface may be found as a static or dynamic equilibrium.

In molecular kinetics, one parameter used to characterize the interface diffusion is the mass accommodation coefficient, α , (also known as sticking coefficient or condensation coefficient), $0 \leq \alpha \leq 1$. The accommodation coefficient describes the interface penetration probability of the gas or vapor molecules when they collide with the interface (see [Rel. 2.2.20.](#)).

$$\alpha = \frac{\text{no. of molecules entering the liquid phase}}{\text{no. of molecular collisions with the surface}} \quad (2.2.20.)$$

At the mass transport from a gaseous phase towards a liquid phase, it was demonstrated that there is a proportionality constant, H^{cp} , between the species allowed to accommodate in the liquid phase, c_L , and the partial pressure of the species in the gaseous phase, p_i (see [Eq. 2.2.21.](#)).

$$H^{cp} = \frac{c_L}{p_i} \quad (2.2.21.)$$

This constant is named Henry's law constant or the air-water partition coefficient and characterizes the species distribution when the system reached the equilibrium. Henry's law dictates the gas species amount that can be practically absorbed by the liquid phase from the gas phase. The law is valid until the liquid phase reaches the solubility limit.

The Henry's law constant can be expressed in dimension (see [Eq. 2.2.22.](#)) or dimensionless form (see [Eq. 2.2.24.](#)). The constants are specific to each gas species and it depends on temperature. They are determined experimentally.

$$H^{cc} = \frac{c_L}{c_G} \quad (2.2.22.)$$

$$H^{cc} = H^{cp} RT \quad (2.2.23.)$$

2.2.3.3. Two-film theory and Resistance-in-Series Model. Dimensionless numbers

The two-film model assumes the existence of two hypothetical stagnant films, one above and one below the interface (see [Fig. 2.2.3.](#)). The model assumes that equilibrium is reached instantly at the interface, so that the Henry's law can be applied at the interface:

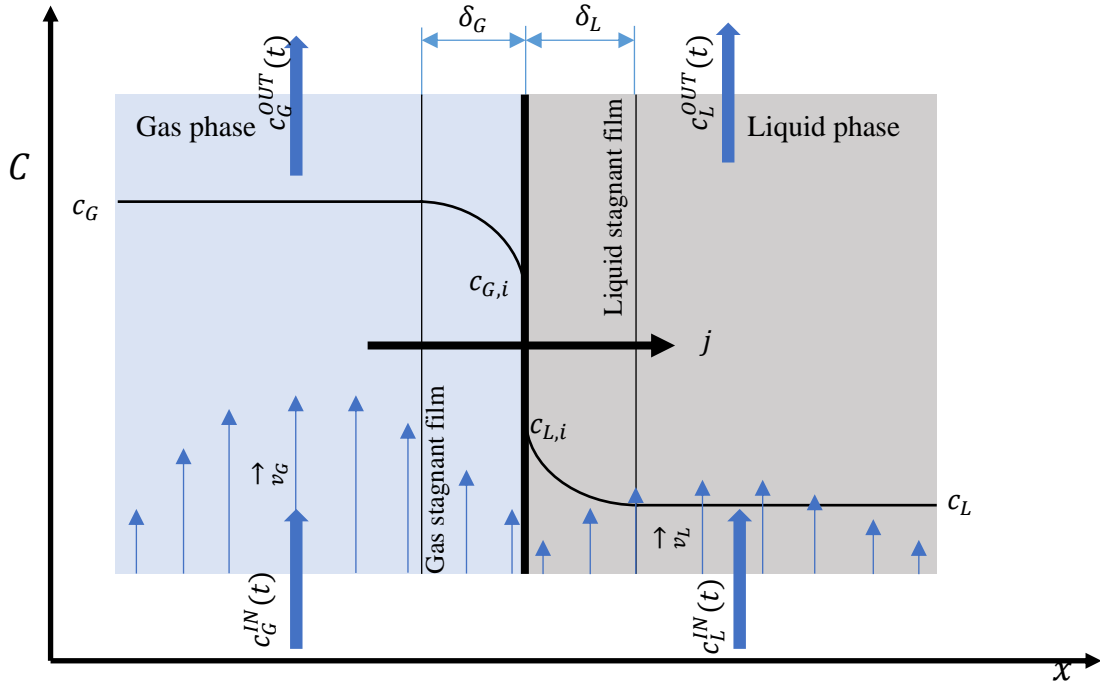


Figure 2.2.3. Two-film transport model for a gas-liquid mass transfer from the gas phase towards the liquid phase, where x is the length, c is the concentration, \vec{v}_G is the gas velocity vector, \vec{v}_L is the liquid velocity vector, j is the total mass flux, δ_G is the gas stagnant film thickness, δ_L is the liquid stagnant film thickness, c_G is the gas bulk concentration, c_L is the liquid bulk concentration.

$$c_{G,i} = \frac{c_{L,i}}{H_{cc}} \quad (2.2.24.)$$

Therefore, a steady-state flux governs the molecular diffusion across the stagnant films with $j = j_{diff, G} = j_{diff, L}$ (see Eqs. 2.2.25. and 2.2.26., assuming the flux from the gaseous phase towards the liquid phase).

$$j_{diff, G} = -D_{i,G} \frac{\partial c_i}{\partial x} = -D_{i,G} \frac{\partial c_G}{\partial \delta_G} = -D_{i,G} \frac{c_{G,i} - c_G}{\delta_G} = k_G (c_G - c_{G,i}) \quad (2.2.25.)$$

$$j_{diff, L} = -D_{i,L} \frac{\partial c_i}{\partial x} = -D_{i,L} \frac{\partial c_L}{\partial \delta_L} = -D_{i,L} \frac{c_{L,i} - c_L}{\delta_L} = k_L (c_L - c_{L,i}) \quad (2.2.26.)$$

Returning to the Eqs. 2.2.25. and 2.2.26., concentrations at the interface cannot be measured, the two-film model defines the so-called overall mass-transfer coefficients for liquid phase, K_L , respectively gas phase, K_G . These coefficients are defined considering fictive concentrations, c_G^* , respectively, c_L^* , for which the concentration in the bulk of one phase would be in equilibrium with the bulk concentration of the other phase (see Eqs. 2.2.27. and 2.2.28.).

$$j = K_G (c_G - c_G^*) \quad (2.2.27.)$$

$$j = K_L (c_L - c_L^*) \quad (2.2.28.)$$

Introducing Eqs. 2.2.29. and 2.2.30. in Eqs. 2.2.27. and 2.2.28., and assuming constant flux across the interface, the overall mass-transfer coefficients can be written as described in Eqs. 2.2.31. and 2.2.32. In these equations, $\frac{1}{K_L}$ and $\frac{1}{K_G}$ represent the transfer resistances generated by the liquid,

respectively the gas film. It has to be mentioned that the interface resistance is neglected since instant equilibrium is considered.

$$c_L^* = c_G H^{cc} \quad (2.2.29.)$$

$$c_G^* = \frac{c_L}{H^{cc}} \quad (2.2.30.)$$

$$\frac{1}{K_L} = \frac{1}{k_L} + \frac{H^{cc}}{k_G} \quad (2.2.31.)$$

$$\frac{1}{K_G} = \frac{1}{H^{cc}k_L} + \frac{1}{k_G} \quad (2.2.32.)$$

Depending on the k_G , k_L , and H^{cc} , one of the two resistances may dominate over the other. In other words, the solubility of the species, the renewal rate, and the film thicknesses dictates which of the two resistances are dominant. For example, the gases with high H^{cc} i.e., highly soluble, encounter the dominant resistance in the gas-phase, and vice-versa, and the gases with low H^{cc} encounter the dominant resistance in the liquid-phase.

The various effects in convective-diffusive species transport in FMRs are characterized in terms of dimensionless numbers presented in Table 2.2.3. Generally, correlations that describe a specific phenomenon are many times presented in terms of these dimensionless numbers.

Table 2.2.3. Dimensionless numbers used in flow microreactors (FMRs).

Dimensionless number	Formulae	Meaning
Péclet number (Pe)	$Pe = \frac{ud}{D}$	It relates the convective and transport phenomena.
Sherwood number (Sh) / Nusselt number (Nu)	$Sh = \frac{kd}{D}$	Ratio of the convective mass transfer to the rate of diffusive mass transport.
Bejan number (Be)	$Be = \frac{\Delta p L^2}{\mu D}$	In the context of mass transfer, it is the dimensionless pressure drop along a channel of length L .
Schmidt number (Sc)	$Sc = \frac{\mu}{\rho D}$	It represents the ratio between the viscous diffusion rate and the molecular diffusion rate.
Hatta number (Ha) (pseudo-first order reaction)	$Ha = \sqrt{\frac{k'D}{k_L}}$	It describes the ratio of reaction to diffusion rates in the thin film.
Dean number (De)	$De = Re \sqrt{\frac{d_H}{2R}}$	Study flows in curved sections of the microchannels.

2.2.4. Gas-liquid reactions. Pseudo-first order reaction.

The gas-liquid interface transport might be accompanied by a chemical reaction in the receiving phase. If the reaction is fast enough, then the concentration of species in the film near the interface is rapidly diminished. Consequently, this means a higher concentration gradient when compared to the same case, but no-reaction.

A higher concentration gradient results in a higher diffusive flux across the interface. This is named a chemically-enhanced mass transfer. The enhancement factor due to the chemical

reaction, E , is calculated as the ratio between the diffusive flux in the presence of the chemical reaction, j_{diff_R} , and the diffusive flux with no reaction, j_{diff} (see Eq. 2.2.33.).

$$E = \frac{j_{diff_R}}{j_{diff}} \quad (2.2.33.)$$

The relationship between the species concentration in a solution and the reaction rate, R , is known as the reaction order. R is practically the speed at which the reaction occurs and it is defined by the rate equation (see Eq. 2.2.34.). In this equation, k is the rate constant.

$$R = k[A]^x[B]^y \quad (2.2.34.)$$

The overall reaction order is given by the sum of the partial reaction orders, x and y . Thus, depending on that, there are zero-order, first order, second order, and n th order chemical reactions. A particular case is represented by the pseudo-first order reaction – examples are reactions in which one component is in large excess to the other. The excess reactant consumption during the reaction is insignificant and therefore its value is assumed to be constant.

Assuming $[B]$ (concentration of reactant B) being in excess relative to $[A]$ in Eq. 2.2.35., then $[B]$ can be included in the rate constant as stated in Eq. 2.2.36., where k' is the pseudo-reaction constant. Eq. 2.2.37. expresses the pseudo first-order reaction mechanism.

$$-\frac{d[A]}{dt} = k[A][B] \quad (2.2.35.)$$

$$k' = k[B] \quad (2.2.36.)$$

$$-\frac{d[A]}{dt} = k'[A] \quad (2.2.37.)$$

2.2.5. Residence time distribution in reacting flows

Generally, a residence time distribution (RTD) function can be estimated through experimental (e.g., stimulus-response tracer experiments) and computational (e.g., computational fluid dynamics (CFD)) methods by introducing a (virtual) tracer signal at the inlet and monitoring its concentration at the outlet. The tracer should have similar properties with the fluid used in the system and be completely soluble in mixture.

In an ideal FMR, the flow behaves as a plug flow. The plug flow means that the velocity is uniformly distributed in the cross section along the flow direction and the tracer introduced at the inlet reaches the outlet under the same concentration, but with a time delay. This time delay is named residence time.

In real flows, the tracer concentration reaching the outlet, $c^{OUT}(t)$, is time-dependent. It is monitored using RTD curves that give relevant information about the species flow behavior inside the volume of control. In real flows occurring in closed systems, the species actually never leave the volume of control completely. A small fraction of them adheres on the solid parts and others remains blocked in zones with zero flow velocity.

For a tracer introduced in form of a pulse function (Dirac delta function) the response is measured using the function $E(t)$ (see Fig. 2.2.4.). If the volumetric flow rate at the inlet is constant, the residence-time distribution function, $E(t)$ can be written as:

$$E(t) = \frac{c(t)}{\int_0^{\infty} c(t)dt} \quad (2.2.38.)$$

The function $E(t)dt$ represents the fraction of the tracer having a residence time between the time intervals $(t, t + dt)$. The fraction of the tracer that has resided in the system in between the interval $t = 0$ and $t = \infty$ is 1 if no-chemical reaction occurs:

$$\int_0^{\infty} E(t)dt = 1 \quad (2.2.39.)$$

For a tracer introduced as a step function the response is measured using a cumulative distribution function, F_t (see Eq. 2.2.40.).

$$F_t(t) = \frac{c^{OUT}(t)}{c^{IN}(t)} \quad (2.2.40.)$$

There are two very important moments used to describe the RTD curves. The first is the mean residence time, \bar{t} , describing the mean time spend by the species in the volume of control from their entrance up to their exit at the outlet (see Eq. 2.2.41.). The second is the variance, σ^2 , that is used to assess the degree of flow non-uniformity and how far the flow deviates from the ideal plug flow (see Eq. 2.2.42.). In other words, the variance is the indication of the distribution spreading. The higher the value of the variance, the larger the spread of the distribution is.

$$\bar{t} = \int_0^{\infty} tE(t)dt \quad (2.2.41.)$$

$$\sigma^2 = \int_0^{\infty} (t - t_m)^2 E(t)dt \quad (2.2.42.)$$

In chemical MFRs with a first-order reaction characterized by a reaction rate, k , the reaction probability of the molecules depends on their residence time in the system:

$$P_R = e^{-kt} \quad (2.2.43.)$$

The mean reaction probability is the ratio of $c^{OUT}(t)$ and $c^{IN}(t)$:

$$\bar{P}_R = \frac{c^{OUT}}{c^{IN}} = \int_0^{\infty} e^{-kt} E(t)dt \quad (2.2.44.)$$

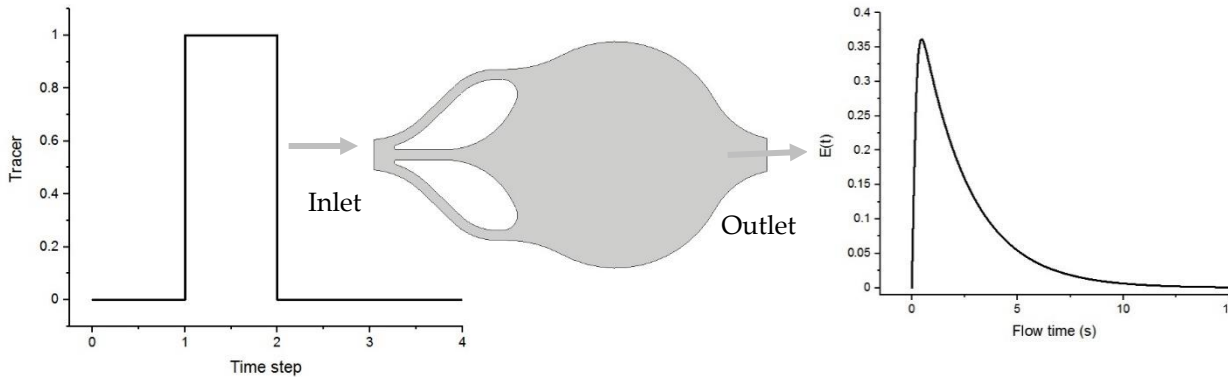


Figure 2.2.4. The principle of residence time distribution estimation in a volume of control using the pulse method. (a) The tracer is injected at the inlet as a Dirac impulse for one time-step. (b) The tracer concentration monitored at the outlet as an area-weighted average variation function over time.

Chapter 3. Current methods and devices used for real-time detection of indoor formaldehyde

3.1. Devices and sensing methodologies

Currently, there are already a multitude of methods developed for real-time detection of low concentrations of indoor HCHO, some of them possessing a high embedding potential into an ultra-portable device. However, the determination of HCHO concentrations in different environments relies most of the time on the off-line NIOSH-2016 method (2,4-dinitrophenylhydrazine (DNPH) cartridge + HPLC/UV detection) [66]. The real-time portable sensors developed until now are either not precise and not selective enough, or too expensive.

The NIOSH-2016 method is based on on-site DNPH cartridge tube sampling followed by an off-line laboratory HPLC analysis (see Fig. 3.1.1.). It exhibits the lowest LOD, $0.048 \mu\text{g}/\text{m}^3$ (0.04 ppb), among all the detection methods developed. However, it provides average concentrations over time intervals ranging from one hour to a week for both active and passive samplings, respectively [30,66]. Sampling of a known volume of air is done through a silica gel cartridge coated with DNPH using a gas pump at a specific sampling speed for a specific period of time. The HCHO molecules are trapped in the cartridge and react with the DNPH to form hydrazones. Once the sampling process is finished, the cartridges are stored in capped borosilicate tubes and kept at a low temperature until they are analyzed in the laboratory. In the laboratory, the hydrazone is eluted from the cartridge using acetonitrile and afterwards the resulted derivative is analyzed with an ultraviolet detector (360 nm) using HPLC, reference method ISO16000-3 [67].

The main alternative methods used for real-time HCHO quantification are high-performance liquid chromatography (HP-LC) [68,69], gas chromatography – mass spectrometry

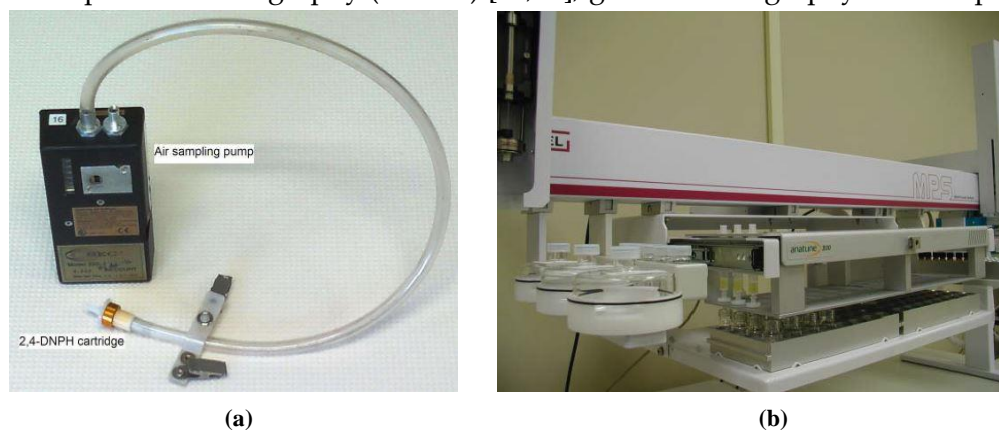


Figure 3.1.1. (a) A 2,4-DNPH cartridge and an air sampling pump. (b) A High Performance Liquid Chromatography (HPLC) detection device [67].

(GC-MS) [70], ion chromatography [71], infrared diode laser spectroscopy [72,73], proton-transfer-reaction – mass spectrometry (PTR-MS) [74,75], electro-chemistry, chemo-resistivity, colorimetry, and fluorometry.

Chromatographic and the spectroscopic methods mentioned above can measure ppb and sub-ppb HCHO concentrations. However, their integration onto ultra-portable devices have not yet been achieved due to their increased complexity and current existing devices are not portable, are very expensive, and have too long measurement times [76,77].

Electrochemical sensors (amperometric and conductometric/impedance-based) use nanomaterials (nanoparticles, nanowires, nanotubes, etc.) as electrodes for HCHO electrooxidation. These electrodes under a specific voltage produce an electrical signal proportional to the HCHO concentration in the air. The drawbacks of this type of sensor are related to their life-time which is dependent on the volume of gas getting in contact with the electrode and the LODs achieved which are not satisfactory. Up to the author's knowledge, the lowest LOD for this type of sensing method was reported in the work of Li *et al.*, [78].

Chemoresistive sensors (or semi-conductor sensors), similarly to the electrochemical sensors, work by measuring the property of a material being in direct contact with the gas. The space between two electrodes is filled with a material (metal-oxide semiconductors – *ZnO*, *CuO*, *SnO₂*, *In₂O₂*, *WO₃*, *Co₃O₄*, *NiO* –, conductive polymers, graphene, nanotubes, nanoparticles) that changes its electrical resistance proportionally to the analyte concentration in contact with the material. Typically, the LOD achieved by these sensors are in ppm-range. However, there are recent promising works reporting LODs down to 5 ppb [79].

The majority of the commercially-available low-cost HCHO sensors are electrochemical and chemoresistive sensors. The research in these two developments directions is on-going and significant progress has been achieved within the last few years in terms of lowering the LODs. However, the interference problem, especially with other VOCs and humidity, continue to be unsolved, as recently highlighted by Baldelli *et al.*, (2020) [80].

Spectrophotometric methods of colorimetry and fluorometry involve trapping of the HCHO molecules into a liquid reagent. Once HCHO molecules are separated from the air and trapped into the liquid reagent, a derivatization process occurs transforming the HCHO molecules into a compound that can be detected optically by colorimetry or fluorometry. The common reagents used with these methods are chromotropic acid, pararosaniline, -methyl-2-benzothiazolone hydrazine (MBTH), DNPH, β -diketone, 4-aminohydrazine-5-mercapto- 1,2,4-triazole (AHMT) dimedone, Fluoral-P, and Acetyl acetone. Among them, no interference has been identified for Acetyl acetone, β -diketone, and AHMT, while chromotropic acid, pararosaniline, dimedone, Fluoral-P might interfere with other aldehydes [33,81]. The sensors based on colorimetry and fluorometry are extremely sensitive reaching LODs down to parts-per-trillion (ppt).

Depending on the nature of the fluid used for concentration quantification, the sensors using the above presented methods might be classified as (1) *dry chemical sensors* or *gas chemical*

sensors (the electrochemical sensors, chemoresistive sensors) and (2) *wet chemical sensors* or *liquid chemical sensors* (the diffusion-based sensors coupled to optical detection) (see [Table 3.1.1.](#)).

Sensitivity and selectivity are the properties where the wet sensors are superior to the dry sensors. However, they are typically bulkier and more difficult to be miniaturized due to the intermediate approaches required to manipulate and, many times, derive the molecules from non-fluorescent into fluorescent compounds.

[Table 3.1.1.](#) introduces a comparative list of the sensing platforms embedding the methods described above. Their LODs, analysis time, and selectivity achieved are presented. The last two platforms use the Hantzsch reaction coupled to the fluorescence optical detection [30,66,82] for continuous HCHO sensing. These instruments contain pumps for sampling, filters, heaters for precise control of the chemical reactions, complicated molecular counting systems that finally show in (almost) real-time the concentrations on a display. In conclusion, they are very complex, leading to high acquisition and maintenance costs. Although they are portable, only trained personnel can manipulate them (see [Fig. 3.1.2.](#)).

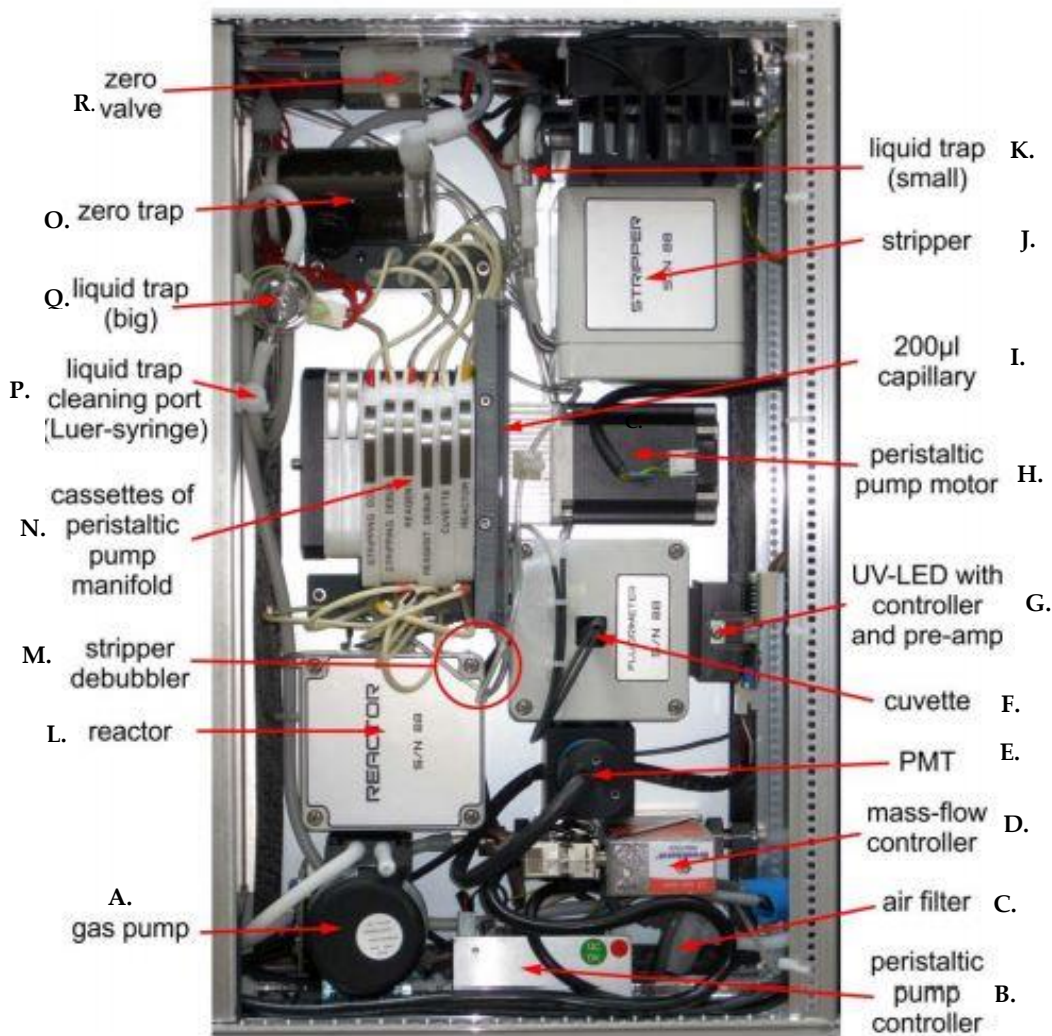
Generally, it might be affirmed that where dry sensors perform well, the wet sensors have a poor performance, and vice-versa. Although dry sensors are more suitable for miniaturization, being characterized by lower response times, much easier operation, and much lower prices, their sensitivity and selectivity is not yet compatible with the current and future indoor HCHO monitoring standards [79,83].

Summarizing, for the moment, none of the two categories managed to completely override the disadvantages of the other. Surveying the literature on miniaturized real-time HCHO sensors, it could be observed that actually there is an undecided tight-race for the pole-position among the two sensor categories. While the dry chemical sensors may benefit from higher simplicity of the methodology used, it still lacks from selectivity and accuracy [80]. Wet chemical sensors are more accurate, more sensitive, but much more complicated, requiring trained personnel for manipulation. However, microfluidics and nanofabrication technologies confer a new development direction that might overcome the actual disadvantages of the wet sensors.

Table 3.1.1. List of portable sensors for indoor HCHO concentration measurements [79].

Working principle	Reference	LOD (ppb)	Analysis time (min)	HCHO selectivity, $\frac{S_{HCHO}}{S_x} (-)$						
				$C_2H_2O_2$	H_2O_2	CO	Acetaldehyde	MeOH	EtOH	Acetone
Chemoresistive	Meng <i>et al.</i> , (2018) [253]	1000	<1 min	N/A	N/A	N/A	N/A	7	3	42
	Wang <i>et al.</i> , (2018) [254]	1000	1	N/A	N/A	>1000	N/A	16	4	3
	Alizadeh <i>et al.</i> , (2013) [255]	50	12	N/A	N/A	N/A	N/A	7	7	11
	Tao <i>et al.</i> , (2012) [256]	50	<1	N/A	>1000	>100	N/A	N/A	N/A	N/A
	Kemmler <i>et al.</i> , (2012) [257]	20	6	N/A	N/A	>1000	N/A	N/A	>100	N/A
	Tian <i>et al.</i> , (2016) [258]	10 000	<1	N/A	N/A	N/A	N/A	7	8	11
	Güntner <i>et al.</i> , (2018a) [80]	30	8	N/A	N/A	N/A	N/A	>1000	>1000	>100
	den Broek <i>et al.</i> , (2020) [79]	5	1,8	∞	∞	∞	∞	∞	∞	∞
	Menart <i>et al.</i> , (2017) [259]	4 000	120	N/A	N/A	N/A	N/A	N/A	N/A	N/A
	Ghaffari <i>et al.</i> , (2015) [260]	100	1	N/A	N/A	N/A	N/A	N/A	N/A	N/A
Electro-Chemical	Li <i>et al.</i> , (2019) [78]	34.5	1	N/A	N/A	>17.5	N/A	N/A	N/A	N/A
	Chang <i>et al.</i> , (2018) [261]	600	1.5	N/A	N/A	N/A	N/A	N/A	N/A	N/A
	Kudo <i>et al.</i> , 2010 [262]	2.5	1	N/A	N/A	N/A	N/A	77	∞	∞
Optical based	Zhao <i>et al.</i> , 2018 [263]	30	60	>100	N/A	N/A	N/A	N/A	N/A	N/A
	AeroLaser, AL4021 model	0.1	5	123	100	N/A	N/A	>10 000	50 000	∞
	InAirSolutions, μ F1	1	10	∞	∞	∞	∞	∞	∞	∞

* N/A – data not available; ** - dry sensors; *** - wet sensors.



(a)



(b)

Figure 3.1.2. (a) Top side view of the AeroLaser AL4021 HCHO Analyzer, with the main components displayed: A – the gas pump, B – the peristaltic pump controller, C – the air filter, D – the mass-flow controller, E – the photon multiplier tube (PMT), F – the flow-through fluidic cuvette for optical detection of DDL, G – UV-LED for optical excitation, N – peristaltic pump with H – the peristaltic pump motor, I – the 200 μ L capillary, M – stripper debubbler, L – reactor where derivatization occurs, J – stripper, K, O, P, Q – liquid traps, R – zero valve. **(b)** AeroLaser AL4021 HCHO Analyzer displaying the HCHO concentration in real-time; Data from Aero Laser AL4021 – Instruction Manual [264].

3.2. Formaldehyde sensing based on Hantzsch reaction

3.2.1. Formaldehyde physicochemical properties

Formaldehyde molecule (HCHO), $M_{HCHO} = 30.026 \text{ g} \cdot \text{mol}^{-1}$, is the simplest organic compound. It is characterized by a boiling point of $T = 254 \text{ K}$ which makes it volatile in normal indoor conditions. HCHO concentrations are usually expressed in either parts-per-notation form (e.g., parts-per-million (ppm) or particles-per-billion (ppb)) or in weight-per-volume (e.g., $\frac{\text{ng}}{\text{L}}$, $\frac{\mu\text{g}}{\text{m}^3}$, $\frac{\text{mol}}{\text{m}^3}$).

With a kinetic diameter of 3.73 \AA , almost similar to the one of the air molecules, the HCHO diffusion coefficient in air, $D_{air, T_1=296 \text{ K}} = 1.76 \cdot 10^{-5} \text{ m}^2 \text{ s}^{-1}$, is also very close to the air self-diffusion coefficient. In water, diffusion is approximately four orders of magnitude slower, $D_{H_2O, T_1=296 \text{ K}} = 2 \cdot 10^{-9} \text{ m}^2 \text{ s}^{-1}$ [84,85] (see Table 3.2.1).

Interfacial phenomena in air-water phase interaction are characterized by a relatively fast HCHO absorption due to its high solubility in water. In most dynamic pressure-driven gas-liquid interactions, a transfer equilibrium at the gas-liquid is quickly reached. This was demonstrated in the works of Seyfioglu and Odabasi, [86] and Becker *et al.*, [87]. The output concentration measured in the liquid phase by Becker *et al.* varied linearly when the input concentration was increased linearly in the gas phase.

Therefore, vapor-liquid equilibria can be assumed when simulating a dynamic micro-reactor for continuous HCHO sensing. However, the vapor-liquid interaction involving HCHO molecules was demonstrated as a complex phenomenon due to HCHO reactivity with water and others compounds. It was demonstrated that HCHO reacts reversibly with water to form methane diol (hydrated-HCHO) into a time period similar to that of the diffusion time across the boundary layer. This effect results in a mass flux enhancement across the interface which is considered by the effective (or apparent) Henry's law constants [86]. Due to this reason, effective Henry's law constant has to be used in the modeling process instead of intrinsic (or physical) Henry's law constants.

Thus, the effective Henry's law constants determined in a couple of studies demonstrate a very high solubility in water. Allou *et al.*, [88], proposed an Arrhenius expression for HCHO Henry's law constant determination as a function of temperature resulted from experiments.

$$\ln H (FA) = \frac{6423 \pm 542}{T} - (13.4 \pm 2.0) \quad (3.2.1.)$$

At $T_1 = 296 \text{ K}$, the effective Henry's law constant, H_1^{cp} , was determined as $H_1^{cp} = 5020 \pm 1170 \text{ M} \cdot \text{atm}^{-1}$, while at $T_2 = 338 \text{ K}$, $H_2^{cp} = 291.44 \pm 112 \text{ M} \cdot \text{atm}^{-1}$ [89]. Therefore, its solubility in water decreases while temperature increases. Solubility remains relatively high even at higher temperatures.

Gas-liquid molecular transfer is usually characterized in terms of mass transfer coefficients. The gas and liquid mass transfer coefficients, k_G , respectively k_L , are determined in some studies both experimentally and/or theoretically [86,90]. Obviously, hydrodynamic conditions influence the values of the mass transfer coefficients. Some authors determined

correlations that link the convective mass-transport coefficients with the Reynolds number, Re , in macro-scale contexts [91]. Moreover, an empirical correlation characterizing the convective mass-transfer coefficients in microfluidic environments does not exist up to the author's knowledge.

Liu *et al.*, [90] estimated the overall-gas and liquid phase mass-transfer coefficients for HCHO, K_{OG} , respectively K_{OL} , at its emission from a small water pool and obtained results comparable to those obtained by Seyfioglu and Odabasi, [86] who estimated the coefficients using a water surface sampler. The average K_{OG} obtained by Seyfioglu and Odabasi, [86] who took in consideration in their evaluations an effective Henry's law constant is $K_{OG} = 0.0058 \pm 0.17 \text{ m} \cdot \text{s}^{-1}$. Liu showed that the mass transfer is dominated by the resistance in the gas-phase layer, the liquid-phase resistance being very low.

In evaluations based on molecular kinetics, the mass accommodation coefficient found at HCHO molecule collisions with the gas-liquid interface is $\alpha = 0.02 - 0.05$. This coefficient characterizes the adsorption probability of molecules at the gas-liquid interface interaction [92–94].

Table 3.2.1. HCHO physicochemical properties.

Property	Value	Reference
Molecular weight	$30.026 \text{ g} \cdot \text{mol}^{-1}$	[95]
Boiling point	254.05 K	Merk index, 2013
Melting point	181.15 K	Merk index, 2013
Water solubility, $T = 293 \text{ K}$	400 g/L	Merk index, 2013
Viscosity, $T = 298 \text{ K}$	0.1421 cP	Merk index, 2013
Surface tension, $T = 298 \text{ K}$	27.3797 dyn/cm	Merk index, 2013
Diffusion in air, $T_1 = 296 \text{ K}$	$1.76 \cdot 10^{-5} \text{ m}^2 \text{ s}^{-1}$	[84,85]
Diffusion in water, $T_1 = 296 \text{ K}$	$2 \cdot 10^{-9} \text{ m}^2 \text{ s}^{-1}$	[84,85]
Effective Henry's constant, $T_1 = 296 \text{ K}$	$5020 \pm 1170 \text{ M} \cdot \text{atm}^{-1}$	[88]
Effective Henry's constant, $T_2 = 338 \text{ K}$	$291.44 \pm 112 \text{ M} \cdot \text{atm}^{-1}$	[88]
Accommodation coefficient, α	$0.02-0.05$	[92–94]
Average overall-air mass transfer coefficient, K_{OG}	$0.0058 \pm 0.17 \text{ m} \cdot \text{s}^{-1}$	[86,90]

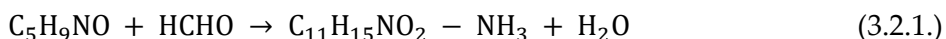
3.2.2. Description of the detection method and reaction kinetics

The methodology implemented to quantify the HCHO concentration is based on the Hantzsch reaction using the pentane-2,4-dione (acetylacetone) solution (0.01 M) as derivatization reagent (see Section 5.2.3.5) and it was developed and studied by Guglielmino *et al.*, [8,30,32,96]. This reagent is also known as 4-amino-3-penten-2-one (Fluoral-P) solution.

The main advantage of Fluoral-P solution is its relatively fast reaction kinetics and its selectivity. However, the reaction product which is 3,5-diacetyl-1,4 dihydrolutidine (DDL)

fluorophore has a relatively low fluorescence quantum yield (ϕ_{DDL}) when measured in this specific reagent (see Section 3.2.3.). New reagents have been developed aiming to preserve at least the reaction kinetics properties of the Fluoral-P solution and to enhance its quantum yield, ϕ_{DDL} [96]. Indeed, the reagents proposed provided much better ϕ_{DDL} , but the reaction times were much longer than in the case of Fluoral-P.

The detection methodology implemented [8,30,32,96] can be generally described as a four-stage process (see Fig. 3.2.1.). First, the air containing gaseous HCHO molecules (gaseous phase) and the Fluoral-P reagent (liquid phase) are continuously streamed and contacted into the system. Second, the trapping process of the HCHO molecules is governed by the Henry's law, the main diffusion driving force being the partial pressure of HCHO in the gaseous phase. Third, the trapped HCHO molecules are derivatized into DDL fluorophore ($C_{11}H_{15}NO_2$) under reaction kinetics influenced by the temperature of the thermodynamic system (see Eq. 3.2.1.).



Fourth, DDL fluorophore concentration can be optically quantified using intensity-based fluorescence measurements.

In continuous separators, phases are usually pressure-driven into channels and the contact occurs either by placing a porous membrane in between, allowing the interphase transfer through the pores, or by direct gas-liquid interaction, e.g., annular flow or slug flow.

Two-phase flow with continuous separation of the HCHO molecules from the air phase to the reagent phase is characterized by a convection-diffusion process [21]. The efficiency of this process is strictly related to a couple of parameters, such as contacting area between the two phases, contacting time, flow hydrodynamics, the diffusive flux across the gas-liquid interface inducing a mass-transfer rate, and HCHO physicochemical characteristics in the two phases involved in the process [97].

Within the third step, derivatization process is governed by a pseudo-first order chemical reaction with an effective reaction constant rate, k' , increasing with temperature. Chemical reaction kinetics is influenced by the residence time, t_d , of the HCHO molecules into reagent, at a specific derivatization temperature, T_d .

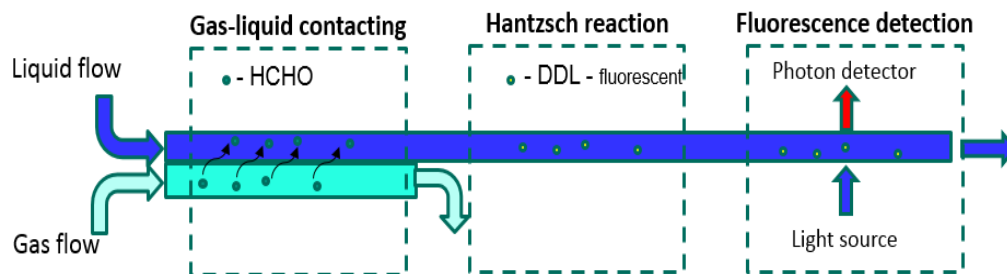


Figure 3.2.1. HCHO sensing scheme based on Hantzsch reaction methodology [96] .

The apparent and physical reaction rates constants, k' and k respectively, were obtained experimentally by Guglielmino *et al.*, [96] (see Table 3.2.2.), where the correlation between the two is given by the Eq. 3.2.3..

$$k = \frac{k'}{[\text{pentane-2,4-dione}]^2} \quad (3.2.3.)$$

In this study it was found out that reaction kinetics are so slow at room temperature, $T_1 = 296 \text{ K}$, that it takes the reaction a couple of hours to occur. As this is not compatible with a real-time detection methodology, the temperature has to be increased. Usually, the reaction temperatures at which the Hantzsch reaction occurs can go up to even $T = 363 \text{ K}$.

Being known that ϕ_{DDL} further decreases with increasing temperature (see Section 3.2.3.), a middle ground between the reaction kinetics and ϕ_{DDL} has to be found in order to make the detection methodology feasible for continuous detection.

Guglielmino *et al.*, [96] chose $T_2 = 338 \text{ K}$ empirically as a temperature that satisfies the following conditions: (1) induce a relatively short reaction time, (2) avoid destruction of the DDL compound, and (3) assures a reasonable fluorescence quantum yield, ϕ_{DDL} . It is known that for higher temperatures of the Hantzsch reaction, destruction of the DDL fluorophore occurs [30,33,89,96].

At $T_2 = 338 \text{ K}$, the apparent reaction rate constant obtained was $k' = 0.0376 \text{ s}^{-1}$ for a pentane-2,4-dione concentration of $[\text{pentane-2,4-dione}] = 20 \text{ mol} \cdot \text{m}^{-3}$ [96], acetylacetone being the compound in great excess. From Eq. 3.2.3., the physical reaction rate constant, k , was determined as $k = (94 \pm 5) \times 10^{-6} \text{ m}^6 \text{ mol}^{-2} \text{ s}^{-1}$.

Table 3.2.2. Experimental values of the physical reaction rates, k , depending on the temperature [96].

[Formaldehyde] ($\frac{\text{mol}}{\text{m}^3}$)	[pentane-2,4-dione] ($\frac{\text{mol}}{\text{m}^3}$)	k ($\frac{\text{m}^6}{\text{mol}^2 \cdot \text{s}}$)	T (K)
3.4×10^{-2}	20	$(12 \pm 1) \times 10^{-6}$	313.15
3.4×10^{-2}	20	$(18 \pm 1) \times 10^{-6}$	318.15
3.4×10^{-2}	20	$(27 \pm 1) \times 10^{-6}$	323.15
3.4×10^{-2}	20	$(54 \pm 3) \times 10^{-6}$	328.15
3.4×10^{-2}	20	$(72 \pm 4) \times 10^{-6}$	333.15
3.4×10^{-2}	20	$(94 \pm 5) \times 10^{-6}$	338.15

3.2.3. 3,5-diacetyl-1,4 dihydrolutidine (DDL) photochemical properties

The photochemical properties of 3,5-diacetyl-1,4 dihydrolutidine (DDL) in aqueous solutions, specific to the Hantzsch reaction, have been studied by Salthammer [98].

There are two light absorption regions for DDL molecules in aqueous solutions. The first one is in the ultra-violet region that has the peak located at $\lambda_{abs_UV} = 250 \text{ nm}$. The second one has the peak at $\lambda_{abs} = 412 \text{ nm}$. Fluorescence emission wavelength is $\lambda_{em} = 510 - 520 \text{ nm}$. Thus,

Stokes shift of the DDL fluorophore is around 100 nm which is relatively wide. This property makes it compatible with intensity-based fluorescence measurement process (see Fig. 3.2.2., a).

As it can be seen in Fig. 3.2.2., the absorption spectrum of Fluoral-P is centered at $\lambda_{abs_{FLUORAL-P}} = 300 \text{ nm}$. Beyond $\lambda_{abs} = 350 \text{ nm}$, Fluoral-P compound does not absorb light. Therefore, the absorption peak located at $\lambda_{abs} = 412 \text{ nm}$ is more suitable since Fluoral-P does not absorb parts of the excitation light sent to excite the DDL fluorophores.

$\phi_{DDL}(T = 293 \text{ K}) = 0.005$ and the molar absorption coefficient, ϵ , of the molecule is $\epsilon = 7500 \text{ M}^{-1}\text{cm}^{-1}$ [96,98]. It was demonstrated that the ϕ_{DDL} decreases by 11% when temperature is increased to $T = 303 \text{ K}$ and fluorescence intensity loss is about 40% at $T = 333 \text{ K}$ [98].

Therefore, thermal fluorescence quenching is an extremely important parameter to be considered when intensity-based measurements are made for HCHO measurements. Fluctuations of temperature induce measurement errors that might affect linearity. Temperature of the solution has to be maintained constant for meaningful measurements [98]. DDL fluorophores degrades in the presence of light and due to this reason DDL solutions used for HCHO concentration measurements should not be exposed to light [98].

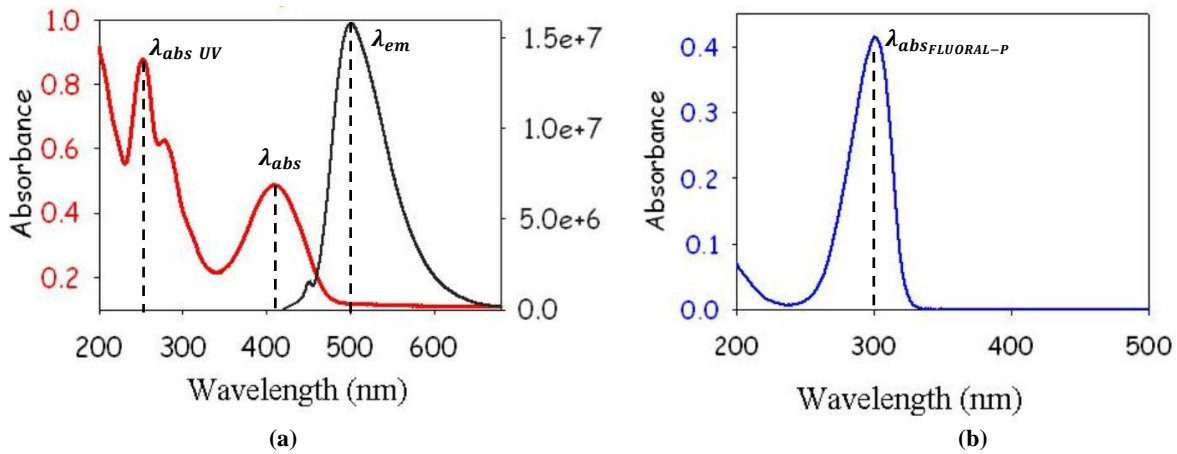


Figure 3.2.2. (a) 3,5-diacetyl-1,4 dihydrouridine (DDL) excitation and emission spectrum. **(b)** Absorbance spectrum of Fluoral-P compound. © IEEE. Reproduced, with permission, from Mariano *et al.* [99]

Chapter 4. Concept of the microfluidic formaldehyde detector

4.1. State-of-the-art of the fluorescence sensing in optofluidic devices

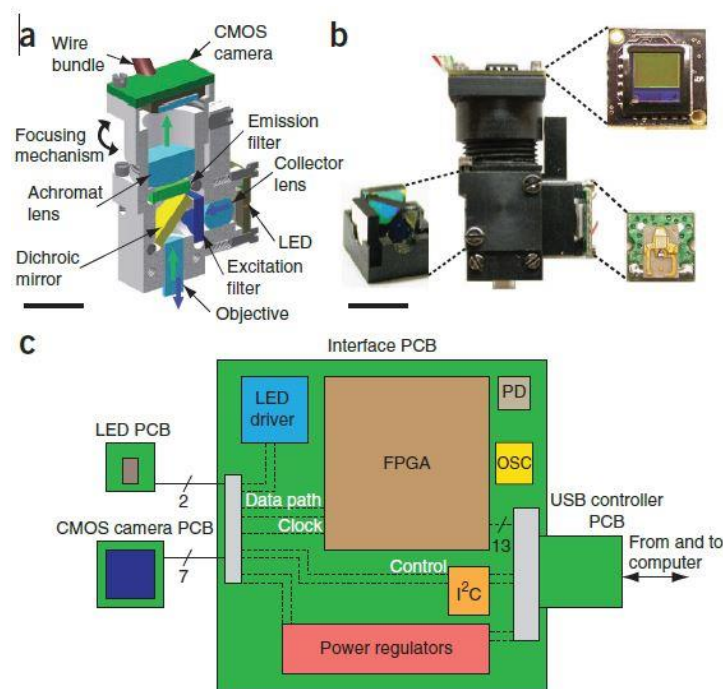
This sub-chapter was written based on the following review paper published by the author in the Microfluidics and Nanofluidics Journal:

Daniel Măriuța, Stéphane Colin, Christine Barrot-Lattes, Stéphane Le Calvé, Jan G. Korvink, Lucien Baldas & Jürgen J. Brandner, Miniaturization of fluorescence sensing in optofluidic devices. Microfluid Nanofluid 24, 65 (2020). <https://doi.org/10.1007/s10404-020-02371-1>.

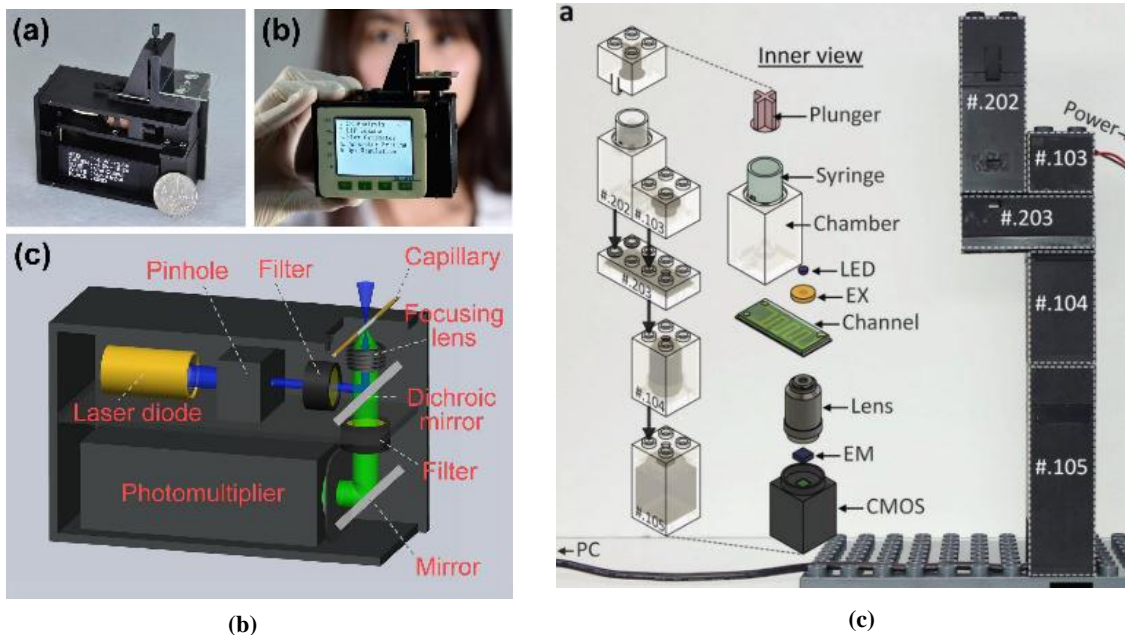
4.1.1. Miniaturized off-chip fluorescence sensing architectures

Off-chip approaches (or free-space designs) are usually miniaturized versions of conventional fluorescence detection systems [46,100]. They are generally linked with the use of pinholes at the focal points along the optical path, in order to couple macro-scale optical detection to micro-scale detection volumes. In this case, light propagates in free-space before and after interaction with the target molecule, and optical elements (filters, lenses, mirrors, light sources, detectors) are separated from the chip. Modular configuration confers them the advantage of convenient integration within a wide variety of already existing platforms, enabling them as plug-and-play microscopes [16]. Table 4.1.1. summarizes the achievements of some identified architectures.

The fluorescence microscope developed by Ghosh *et al.* (2011) [101] (see Fig 4.1.1. a) presented a high degree of miniaturization using state-of-the-art in the field of optoelectronics. It proposed an innovative design solution, embedding all optical elements within a 2.4 cm³ polyetheretherketone (PEEK) housing. A blue LED, integrated on a 6 × 6 mm² printed circuit board (PCB), was used as excitation source. A drum lens was used to collect the emitted light, which was then passed through a 4 × 4 mm² excitation filter. A dichroic mirror directed the light to the sample, via a focusing gradient refractive index (GRIN) objective lens. The fluorescent emission passed through the objective lens, dichroic mirror, an emission filter, and an achromatic doublet lens, which in turn focused the image onto a CMOS sensor. The 640 × 480 pixel CMOS sensor, mounted on a 8.4 × 8.4 mm² PCB, had a 60% quantum efficiency at 530 nm. The LED, image sensor, micro-lenses, and filters, were made using batch fabrication, decreasing the cost per unit. The device was built in an alignment-free configuration, but not stand-alone, requiring a computer for image processing. Data acquisition between microscope and computer was intermediated using an external PCB, allowing imaging at 35 Hz or 100 Hz over 300 × 300 pixels subregions.



(a)



(b)

(c)

Figure 4.1.1 (a) Integrated fluorescence microscope, 2.4 cm³ volume, 1.9 g weight. (b) Compact handheld quasi-confocal laser induced fluorescence. (c) Integration of LEGO-like blocks hosting elements of the optical, electrical, and fluidic circuits in order to modulate the optofluidic systems. (a) Reprinted from Ghosh *et al.* [101], Copyright 2011, with permission from Springer Nature (License number 5235910831361). (b) Reprinted from Fang *et al.* [102], Copyright 2016, with permission from Elsevier (License number 5235920365578). (c) Reprinted from Lee *et al.* [106], Copyright 2018, with permission from Wiley (License number 5235920630785).

More recently, other versions of miniaturized off-chip detectors were developed with fabrication costs per unit varying from \$2000 [102] to \$10 [16]. For example, a handheld fluorescence detector with a broad range of possible applications, compact size, and capability to work independently was proposed by Fang *et al.* (2016) [102] (see Fig. 4.1.1. b). This device embedded a light source (450 nm laser diode), an optical circuit module (a 450 nm band-pass filter, a dichroic mirror, a collimating lens, a 525 nm band-pass filter, a 1.0 mm aperture), an optical detector (miniaturized photomultiplier tube), and an electronic module (signal recording, processing and displaying units). The stability was tested for more than five hours for continuous detection of 100 nM sodium fluorescein, and the relative standard deviation was below 1%. Two configurations were tested, the quasi-confocal configuration was proven to be more advantageous compared to an orthogonal configuration, mainly from the perspective of possessing more top open space to be used for installing disposable interrogation cuvettes. The configuration used for positioning the optical elements is usually a compromise between the performance and the ease-of-use of the final device.

A hand-held orthogonal detector that was proposed by Pan *et al.* (2018) [103], where the fluorescence collection was performed at 45°, decreased the background scattering light intensity compared with a 90° configuration. Compared to a confocal configuration, in the orthogonal configuration the excitation and collection paths were separated, leading to a reduced background signal without using complicated optical components. This system was built for high-speed capillary electrophoresis (CE). It integrated in a modular way a picoliter scale sample injector, short capillary-based fast CE, high-voltage power supply, orthogonal laser induced fluorescence (LIF) detection, battery, system control, on-line data acquisition, processing, storage, and a display. The proposed architecture was embedded into a monolithic black ABS block of 44 mm × 42 mm × 40 mm dimension, the overall fabrication cost reaching \$150. The optical circuitry included a high intensity laser diode (18 mm length, 12 mm diameter, 80 mW) as light source, two small collimating lenses for laser beam focusing and fluorescence collection, and a photodiode (9 mm length × 6.2 mm diameter) as optical detector. The collimating lens consisted of three lenses and had a small size of 8.7 mm length × 9.6 mm diameter and 7 mm focal distance. A focusing spot of 10 μm for the laser beam could be obtained at the center of a capillary channel. The photodiodes achieved a larger degree of miniaturization compared to the photomultipliers, but the sensitivity was lower.

A design based on a reflective sphere, aiming at enhancing the excitation and collection efficiency, was proposed by Harmon *et al.* (2018) [104]. The interrogation volume was located in the center of a sphere, in order to produce effects that increased the collection efficiency. A hole was drilled in the sphere, perpendicular to the direction of a microchannel, serving as a light guide from the source located outside of the sphere. The incident light intersected the sample in the region of the interrogation volume, and the reflected light from the walls of the sphere

Table 4.1.1. Off-chip fluorescence detection platforms.

Reference	Description	Applications	LOD	Dimension	Cost
Zi <i>et al.</i> (2016) [14]	<ul style="list-style-type: none"> Time-resolved fluorescence fluorometer made out of off-the-shelf components. 	Detection of immunochromatographic strip to achieve quantitative inspection and analysis of analytes in human blood or body fluid.	1 $\mu\text{g/mL}$	26 \times 20 \times 13 cm^3	-
Zhang <i>et al.</i> (2015) [16]	<ul style="list-style-type: none"> Cost-effective detector built from off-the-shelf components and a webcam. 	Live cell imaging, long-term tracking of cellular processes, fluorescence analysis, and biosensing.	-	4.2 \times 5.5 cm^2 65 g	\$10
Ghosh <i>et al.</i> (2011) [101]	<ul style="list-style-type: none"> Miniaturized microscope permitting fluorescent cell counting. 	Detect tuberculosis bacteria in a fluorescence assay.	-	2.4 cm^3 1.9 g	-
Fang <i>et al.</i> (2016) [102]	<ul style="list-style-type: none"> First report on using a 450 nm laser diode in a miniaturized LIF detector. Higher miniaturization and integration level of the detector over most of the previously-reported miniaturized LIF detection systems. 	Capillary electrophoresis separation Online LIF detector for flow analysis systems (such as multiphase microfluidics and liquid chromatography). Could be combined with micro fluidic chips, microarray chips or biosensors. In-field analysis, point of care testing, environmental/industrial monitoring.	0.42 nM (S/N=3)	9.1 \times 6.2 \times 4.1 cm^3 , 350 g	\$2000
Pan <i>et al.</i> (2018) [103]	<ul style="list-style-type: none"> Hand-held detection device. Built by integrating miniaturized modules. 	High speed capillary electrophoresis Colorectal cancer diagnosis for detecting KRAS mutation status.	1.02 nM fluorescein.	90 \times 75 \times 77 mm^3	\$500
Harmon <i>et al.</i> (2018) [104]	<ul style="list-style-type: none"> Integrating a reflective sphere, enhancing excitation and emission intensity. 	Detecting the fluorescein solution and SYBR-Green stained dsDNA.	0.4 nM fluorescein.	-	-

refocused on the sample, rendering the excitation more efficient. A similar arrangement was available for the fluorescence that was collected through another drilled channel in the sphere.

A cost-efficient device built from off-the-shelf components, including a commercially-available CMOS-based USB camera was reported by Zhang *et al.* (2015) [16]. Four poly (methyl methacrylate) (PMMA) sheet frames with holes near the edges, for bolts/screws, were fabricated to serve as a layered modular support for the optical components. Screws were used to adjust the distance between the base and sample holders. The bottom PMMA layer contained the CMOS sensor. The lens was inverted to obtain magnification rather than the de-magnification mechanism of the camera. Resulted modularity allowed the integration with a large variety of preexisting platforms (e.g., cell culture plates, microfluidic devices, and organs-on-a-chip systems).

Time-resolved fluorescence is a methodology implemented for improving the sensitivity of the detection by sequentially powering the emitting source on and off in order to avoid autofluorescence or excitation light reaching the detector while fluorescence is quantified.

Biotechnology, electronics and chemical technology were combined in Zi *et al.* (2016) [14] to develop an integration scheme for a time-resolved fluorescence sensing system. Off-the-shelf miniaturized modules (UV-LED, silicon photodiode, signal processing units, displays, and optical paths) were integrated in a detection platform of 26 cm × 20 cm × 13 cm. This instrument was used for quantification of analytes in human blood and other body fluids.

Modular optofluidics is the solution proposed by Brammer and Mappes (2014) [105] and by Lee *et al.* (2018) [106], among others, aiming to make widespread implementation of the microfluidic systems more reliable (see Fig. 4.1.1, c). Lee *et al.* (2018) proposed a strategy based on modular blocks embedding the elements of the optical, electrical, and fluidic circuits into LEGO-like structures fabricated using rapid prototyping fabrication techniques.

4.1.2. Towards on-chip fluorescence sensing architectures

On-chip systems are defined as structures that have all the electrical, optical, chemical, and detection functions integrated within the microfluidic chip platform [39]. This integration strategy that combine optics and microfluidics, resulting in highly efficient liquid-solid interactions created the field of optofluidics [46]. The development process of integrated circuits established technological methodologies that have been successfully used to solve issues in fields outside of electronics, generally known as the Micro-Electro-Mechanical Systems or MEMS industry [44]. In this way, routes towards new technological fields appeared, such as micromechanics, microfluidics, and micro-optics (integrated optics) [107]. Soon after this, the limitations of integrated circuits on silicon chips (material mainly used for the development of integrated circuits) became apparent. The requirements of electronics frequently collided with those of optics and mechanics, so that integration on one and the same chip (monolithic integration) proved to be hard [108]. Thus, engineers had to consider new integration

methodologies and hybrid technologies have been envisaged, i.e., the final device was composed of complex subunits which were manufactured by different technological processes. Polymers are here considered due to their ease-of-fabrication and cost-efficiency. Within this section, a brief description of the latest achievements towards on-chip integration of fluorescence detection using hybrid technologies is provided.

4.1.2.1. Optical-fiber-based designs

Implementation of optical fibers-based designs in fluorescence sensing (see [Table 4.1.2.](#)) can be observed from two perspectives: (a) full-core optical fibers, and (b) microstructured hollow-core optical fibers. Integration of full-core optical fibers as waveguides intermediating the light transfer from external excitation sources towards the sample volume and/or the fluorescence transfer towards external photon detector has been one of the initial techniques used in fluorescence sensing miniaturization. Actualized theoretical aspects related to the implementation of optical fibers in fluorescence biosensing applications could be found in a comprehensive review of Benito-Peña *et al.* (2016) [109].

Optical fibers were adopted as waveguides in this field due to the fact that they are characterized as highly light transmission efficient, low-cost, free from electronic noise, providing protection for the electronic components when dangerous chemical environments are present [45,110]. However, their main drawback results from the fact that they are not user-friendly, requiring precise alignment, while coupling is sensitive to vibrations. Some recent works treated this topic [111,112], proposing some fabrication methodologies allowing free and relatively precise alignment of the fibers.

For example, Matteucci *et al.* (2015) [112] introduced a fabrication methodology that embedded standard commercially-available optical fibers with cyclic olefin copolymer (CoC) TOPAS 5013 hard-polymer chips, based on an injection molding technique (i.e. production-friendly). TOPAS 5013 polymer possesses characteristics that are compatible with the demands of the optofluidic chips. This polymer is highly transparent in the visible and UV spectrum, possessing a high glass transition temperature (413 K), very low water absorption, resistance to acids, alkaline agents and polar solvents, and avoids biofouling (minimal surface treatments are needed). The autofluorescence of TOPAS 5013 could be decreased to values that are 20% lower than the ones resulting in silica material by the addition of a master-batch of a blank dye to the polymer granulate used for injection molding of the devices [113].

Hatch *et al.* (2014) [114] used optical fibers with ball lenses at their tip, enhancing the light optical density, enabling the implementation of cost-effective and low-power LEDs as light sources. The device was portable, but still bulky relative to the current integration trends.

Table 4.1.2. Microfluidic systems using optical fiber-based designs towards-on-chip integration of fluorescence detection.

Reference	Achievements	Applications	LOD	Analyte	Further improvements [Author's suggestions]
Rodríguez-Ruiz <i>et al.</i> (2015) [111]	<ul style="list-style-type: none"> Hassle-free optical fiber connection fabrication method within a PDMS chip. Photonic / fluidic elements are fabricated in one single step, plasma activated, covalently bonded on a glass substrate. 	Monitoring enzymatic catalytic reactions.	1.14 μ M	-	-
Yang <i>et al.</i> (2015) [124]	<ul style="list-style-type: none"> In-fiber integrated fluorescence online optofluidic sensor based on specially designed hollow optical fiber with suspended core. Vertical micro holes drilled for inlet and outlet, while the molecules are excited through the evanescent field principle. The optical transmission and the microfluidic detection are entirely realized in the hollow fiber. 	Low-cost detection of nitrides.	0.1 mmol/L	Rh6G	The device architecture could be adapted for other fluids such as gas involving fluorescence quenching that can be further investigated.
Shang and Zheng (2017) [123]	<ul style="list-style-type: none"> Compact fluorescence sensing scheme based on hollow core Bragg fibers (HCBFs) serving as a sample cell, a collector, and a delivery channel for the desired fluorescence, as well as a filter for the residual excitation light mixed with fluorescence. Photonic bandgap effect (PBG) is studied in common HCBFs, the transverse resonant behavior in the defect HCBFs. They proved that can be successfully employed as integrated filtering solutions. 	Multi-mode silica fibers as fully-integrated fluorescence sensing optofluidic devices	-	Rh6G	-
Matteucci <i>et al.</i> (2015) [112]	<ul style="list-style-type: none"> Fabrication technique based on injection molding - integration of optical fibers with $2.7 \pm 1.8 \mu$m alignment accuracy. Broaden the number of possible lab-on-a-chip applications: optogenetic stimulation and detection, shape recognition, and flow cytometry. 	Self-alignment of optical fibers in optofluidic chips.	-	-	The use of mechanical supports when inserting fiber in order to further reduce the misalignment. Integration of fiber-based Bragg gratings.
Ngernsutivorakul <i>et al.</i> (2017) [117]	<ul style="list-style-type: none"> Implementation of TOPAS 5013 polymer optofluidic chips using injection molding fabrication technique. Free-standing probe with integrated optics that could focus and collect light from outside the probe, and can be easily coupled to fiber optics, as well as have separate input (e.g., excitation) and output (e.g., emission) paths; cost-efficient soft-lithography techniques used for fabrication. 	Remote detection.	6 nM	Resorufin	LOD could be improved by integrating optical filters directly onto the tips of the fibers.

Even if the current trend in the miniaturization of optical sensing is to bring the light source and the photon detector in the close vicinity of the interrogation sample, standard optical fibers are still used for those cases where robust modular systems are desired. Three-dimensional modular microfluidics have been recently introduced as an alternative method to overcome the issues appearing when monolithic design strategies fail [115].

Modularity is one of the solutions envisaged for bringing microfluidic devices closer to their large-scale commercial implementation. Thus, standard optical fibers are still used for the development of modular and reliable miniaturized fluorescence-based optical sensors.

Ackermann *et al.* (2016b) [116] introduced the Chip-to-World Interface (CWI) as a plug-and-measure sensing strategy based on a CO₂-laser machining fabrication technique, in order to create a low-cost and robust modular interface facilitating the connection to a large variety of external photon detectors and light sources. This concept refers to the implementation of an optical fiber with coaxial radio frequency SMA (SubMiniature version A) connectors, allowing manipulation of the detection system without special training of a potential user. Yue *et al.* (2015) [110] used also optical fibers with SMA connectors to develop a modular fluorometer for detection of fluorescein isothiocyanate. A concentration of 10 ng/mL could be measured, and the system presented a good linearity from 10 ng/mL to 10 µg/mL. The opto-electrical converter module and the signal acquisition device were modular and could be replaced for detection of other molecules. Moreover, an optical probe is a tool used to collect light from otherwise inaccessible volumes. Ngernsutivorakul *et al.* (2017) [117] proposed a 0.5 mm thick and 1 mm wide PDMS probe with two optical fibers integrated as inlet and outlet light waveguides. Also, the probe embedded pre-aligned mirrors, lenses, allowing separate input and output optical paths. The probe was disposable, reusable from one chip to another, but not alignment-free, requiring a specific instrument to couple it to a microfluidic chip.

Next implementation level of optical fibers in the miniaturization process of fluorescence sensing is represented by the Microstructured Optical Fiber (MOF) or Photonic Crystal Fibers (PCFs). The field of optofluidics in microstructured optical fibers was recently reviewed by Shao (2018) [118] and by Ertman *et al.* (2017) [119]. It gained high interest due to its capability of simplifying optical fiber sensors and improving the level of integration. Hollow Core Bragg Fibers (HCBF) working on the principle of evanescent waves are a promising solution that might converge towards a fully integrated detector [120]. Hollow core Bragg fibers are a particular class of photonic band gap (PBG) fibers [121] with a guiding mechanism that is capable of confining the light in the fiber core from all incidence angles and polarizations. Due to the PBG effect, the HCBFs have features of a wideband band-pass filter. The Bragg layers can be designed in such a way that they behave as a reflective surface for specific wavelengths and absorbing surface for others. By introducing a defect layer into the common cladding band, the excitation light is rejected, while fluorescence light is transmitted towards the photon sensing element. Also, the rejection filtering is narrowed due to the transverse resonant behavior [122].

Shang and Zheng (2017) [123] applied this principle, resulting in a very compact detection device where the detection cuvette, the collector, the delivery channel for the desired fluorescence, and the filter for residual excitation light mixed with fluorescence were all part of the fiber (see Fig. 4.1.2.). In Yang *et al.* (2015) [124], a hollow optical fiber with suspended core was proposed, fabricated, and characterized for detection of Rhodamine 6G. The outer diameter of the fiber was 350 μm , the inner diameter was 210 μm and the diameter of the core was 40 μm . The inlets and outlets were made on the surface of the hollow fiber by CO₂ laser etching, all the others optical elements being off-chip.

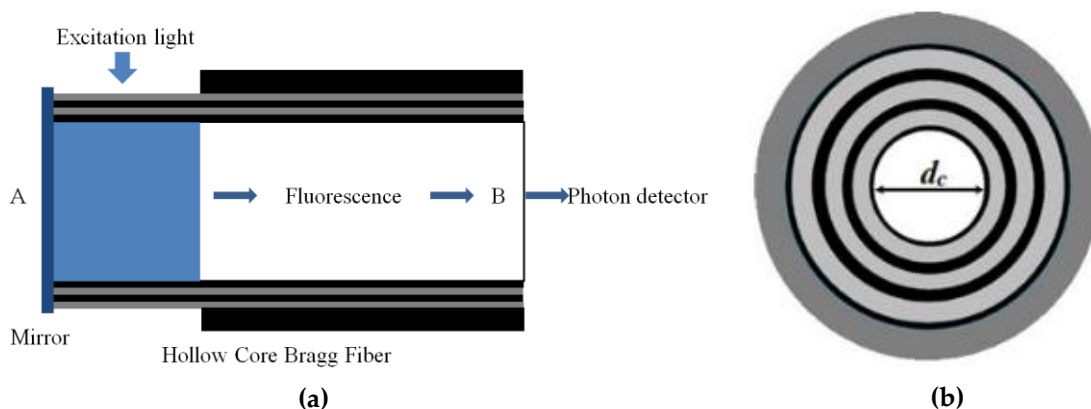


Figure 4.1.2. (a) Compact fluorescence sensing scheme based on Hollow Core Bragg Fibers, serving as interrogation cuvette, collector, delivery channel for the fluorescence, and the filter for the residual noise. (b) Cross-section scheme of the device with the photonic band gaps of different refraction indexes. © 2017. IEEE. Reproduced, with permission, from Shang *et al.* [123].

4.1.2.2. Optics layer-integrated designs

The basic principle of optics layer integrated designs is to integrate the active and passive optical components on a planar layer, mainly by using micro- and nano-fabrication technologies [125]. Transparent materials with high refractive indexes, such as polymers, are usually used as waveguides. The light remains confined by multiple total internal reflections [108]. Some of the main active current research directions are in-plane microfluidic lenses, printed-board microfluidics, anti-resonant reflecting optical waveguides (ARROWs), and on-chip integration of solid-state light emitters (SSLE). In-plane microfluidic lenses or on-chip lens systems mainly aim to robustly integrate light beam focusing customized solutions in the same functional layer as the fluidic layer [126]. Liquid-core cladding lenses, pressure-controlled liquid-air interface, and gradient refractive index lenses are some configurations recently reported in the literature tackling this subject (see Table 4.1.3.).

Femtosecond lasers revolutionized the three-dimensional micro-fabrication of the materials due to its very short pulse width and high peak intensity. Known as a complicated technique, recent advancements proved the femtosecond laser micromachining (FLM) as a cost-

effective and reliable fabrication technique for optofluidic systems [127–132]. An in-plane integrated microfluidic lens whose modulation could be on/off switched on demand was fabricated by Paiè *et al.* (2017) [133] using femtosecond laser micromachining fabrication technique.

Modulating light is a common technique used to enhance the measurement sensitivity by subtracting the noise. The focused light could be modulated by dynamically changing the liquid in the lens through a droplet generation module. Femtosecond laser micromachining and radio frequency (RF) sputtering were implemented for incorporation of a microfluidic network, excitation, filtering, and collection elements in one glass substrate, in a 90° configuration [134]. Here, the FLM was used to fabricate the microfluidic channel, the perpendicular fiber channels, perfectly aligned and embedded in a fused silica layer. A wavelength filter, behaving as a Bragg mirror, was fabricated by implementing an RF sputtering method. One-dimensional photonic crystals were used, since they are dielectric structures of different refractive indexes, permitting propagation of only specific wavelengths. They can be designed to have a photonic band gap in the wavelength region of excitation, similar with the concept explained in the previous subchapter. On the top of the filter, a binary Fresnel lens (BFL) was fabricated, leading the collected light out of the chip. Fresnel lenses are flat, low thickness structures with concentric rings designed to focus the light (40% efficiency) in optical microfluidic devices (see Fig. 4.1.9. b). Their fabrication within a microfluidic channel is based on the nanoimprint process [135]. Efficient beaming of the emitted radiation is very important since it can drastically affect the performance of the assay.

Ricciardi *et al.* (2015b) [136] proposed an optofluidic chip based on a multilayered photonic crystal structure embedded on a PDMS structure. The efficiency of fluorescence collection was experimentally demonstrated in an antibody–antigene immunoassay, resulting in a decrease of the LOD for labelled antigens by a factor of about 40. The measurements were demonstrated to occur in a robust and reproducible way, with reduced optical alignment issues. Here, the method proposed by Watts *et al.* (2012) [137] for an efficient beaming of the excitation light should be mentioned. This method eliminated the need for free-space optics and high-quality light sources, through on-chip 3D hydrodynamic focusing. The on-chip hydrodynamic focusing is achieved through introduction of micro-patterned optical components in SU-8 photoresist layer that hosts also the fluidic components.

The printed circuit board (PCB) is a mature technology used and improved for decades in electronics, to mechanically support and electrically connect components using conductive tracks etched in layers of copper onto and/or embedded between sheets of a non-conductive substrate. The materials usually used as substrates for the fabrication of PCBs are resistant at high temperatures (> 443 K). This characteristic makes them compatible with microfabrication techniques that involves elevated temperatures. The reliability and potential of PCBs for miniaturization of fluorescence sensing systems was demonstrated recently [100,138–141]. A PCB

offers an integration alternative to glass/polymeric microfluidic chips, which are not integration-friendly with standard, off-the-shelf optoelectronic elements [100].

Portable systems integrating light emitting diodes (LEDs) for multiple target analysis were proposed in Shin *et al.* (2015, 2017) [139,140]. Optical functions were modularly parallelized within three layers (see Fig. 4.1.3. a, c). The first layer (filtering and detection layer) hosted a photon detector, a dichroic lens, and a color filter. The intermediate layer was represented by a PCB with three LEDs of different wavelengths mechanically mounted around a circular orifice which illuminated the interrogation volume from the opposite direction of the photon detector.

Avoiding direct illumination of the detector was relevant for increasing the SNR. The circular cut assured that the emitted fluorescence was transferred from the third layer

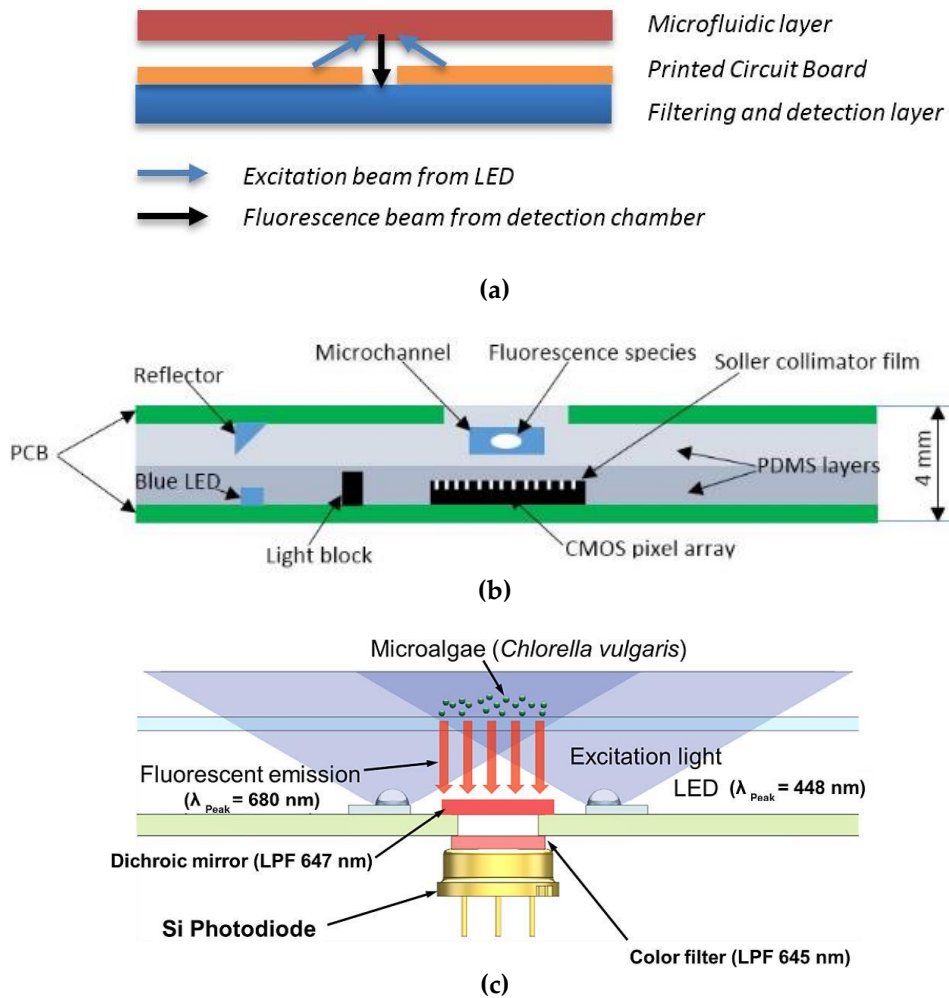


Figure 4.1.3. (a) Parallel layering distribution of the detection functions with the PCB sandwiched in between the microfluidic layer and the detection layer [139,140]. (b) Cross-section of the microfluidic-PCB fluorescence detector, built using two PCBs. The design strategy avoided the direct illumination of the interrogation volume, a Söller thin film collimator being coated on top of the CMOS to reduce the background noise. (c) Fluorescence detection system with back-side illumination scheme. (b) ©2017. IEEE. Reprinted, with permission, from Babikian *et al.* [100]. (c) Reproduced from Shin *et al.* [139,140], Copyright 2015, with permission from Elsevier (License number 5235930345211).

(interrogation volume) to the first layer (filtering and detection layer), while the PDMS microfluidic layer was disposable. All above mentioned components were embedded into a portable box equipped with a display, permitting the selection of the operation. A comprehensive review about LEDs implementation with fluorescence sensors is reported in [45].

As a predictable continuation of the above mentioned concepts, the microfluidic-PCB concept was introduced by Babikian *et al.*, (2017) [100]. This concept involved a three-layer device, integrating with the aid of two PCB parts, all the fluidic, electrical, mechanical and optical components within a compact system (see Fig. 4.1.3. b). One PCB was fixed and non-disposable, comprising all active components, and was denoted the reader chip. The second PCB, named the microfluidic chip, was disposable and encompassed the passive structures of the device such as microchannels, high voltage electrodes, micromachined light reflector. A standard surface-mounted blue LED ($\lambda_{em} = 470 \text{ nm}$) was used as light source. The detection was implemented using a standard surface-mount 2-megapixel CMOS imaging array with integrated RGB (Red-Green-Blue) filters. The CMOS sensors were inexpensive, compact, and compatible with the microfluidic-PCB approach. A surface-mount light reflector was used to reflect the excitation light path towards the detection channel. A rectangular slit was created in the upper PCB, above and along the microfluidic channel, in order to avoid light scattering and autofluorescence of the PCB substrate.

The background noise associated with the excitation light was further suppressed by a Söller collimator film, laminated on top of the CMOS pixel array. A Söller collimator collimates light by allowing the passage of rays that are almost parallel with its optical axis. It is used in lens-free fluorescence detection schemes, since uniform spatial distribution of light was crucial [142]. In this work, it also avoided the cross-talking between the light source and the CMOS image sensor. This heterogeneous method embeds individually manufactured components, such as electrodes, heaters, light sources, detectors, and microfluidic components between the electrical and microfluidic layers using standard fabrication processes. All the components (the light source, microchannel, optical guide, and detection sensor) were integrated within a structure having the approximate dimensions of a credit card, $7 \text{ cm} \times 5 \text{ cm} \times 4 \text{ mm}$.

Total internal reflection (TIR) takes place when a light beam meets a medium with a lower refraction index at an angle greater than the critical angle. This critical angle can be calculated knowing the refraction indexes of both media. The phenomenon can be used to mitigate direct illumination of the detector and, by consequence, to lower the noise level. For example, a design solution using a lateral excitation configuration, in order to (1) maximize the photon flux exciting the microfluidic channel while (2) preventing excitation light reaching the sensor, was proposed by Novo *et al.* (2014) [141]. This configuration (see Fig. 4.1.4. a) involved a prism-like PDMS microchannel sealed with a glass substrate. A PCB hosted a micro-fabricated a-Si-H photodiode and contained a two-level pocket which kept a $50 \mu\text{m}$ space between the microfluidic chip and photodiode needed for the total internal reflection condition. A 405 nm laser beam was directed

perpendicular to the lateral prism-like PDMS structure in which the sides made a 70° angle with the flat surface and was focused to illuminate the microchannel while experiencing TIR at the glass-air interface. This configuration improved the detectability range by two orders of magnitude as compared to a normally incident excitation configuration, SNR being ameliorated for detection of specific fluorophores.

Berner *et al.* (2017) [143] developed a method based on sandwiching a laser-cut double-sided adhesive tape coupled with the latest generation of thin film photodetectors, enabling miniaturization by custom fitting of amorphous silicon based photodiode arrays to the geometry of the flow channel.

One promising methodology using TIR phenomena was presented in Jang and Yoo *et al.* (2013) [144], where a fluorimeter integrating a total internal reflector was introduced, a condensing mirror and the detection chamber (width 1.5 mm \times depth 0.8 mm \times length 5 mm)

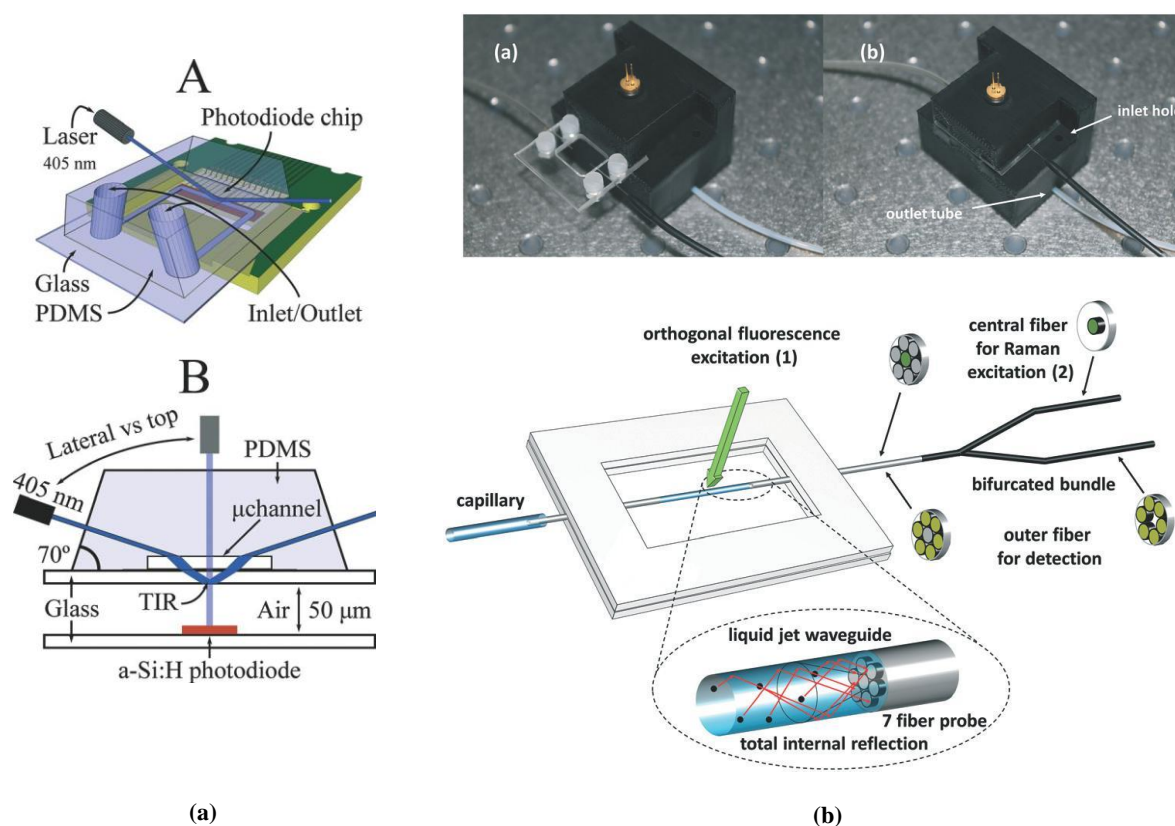


Figure 4.1.4. (a) Lateral excitation onto a PDMS microfluidic device coupled to a photodiode PCB. The 50 μm air-gap separates the microfluidic device from the photodiode, in order to assure the TIR effect at the glass/air interface for the excitation light. (b) Multi-functional sensing device based on 150 μm optofluidic jet, equipped with a recirculation system. The detection scheme is based on the principle of the TIR in the liquid jet. Two possible ways of liquid jet excitation: (1) orthogonal fluorescence excitation, and (2) optical fiber for Raman excitation. (a) Reproduced from Novo *et al.* [141], Copyright 2014, with permission from The Royal Society of Chemistry. (b) Reproduced from Persichetti *et al.* [145], Copyright 2017, with permission from The Royal Society of Chemistry.

within a single 1.2 mm thick polycarbonate substrate. The total internal reflector enabled orthogonal detection, and the condensing mirror increased the selectivity of the fluorescence emission. The LOD achieved was 5 nmol/L and the linearity was 0.994 for 6- fluorescein amidite (FAM) fluorescence dye. The condensing mirror was coated with a 200 nm thick aluminum layer, having the role of better fluorescence collection from the sample and more efficient distribution to the photon detector, located on the opposite side of the fluidic chamber, while the light source ($\lambda_{em} = 465 \text{ nm}$, LED) and the photon detector were externally located. A system based on an optofluidic jet waveguide (see Fig. 4.1.4. b) - a liquid micro-jet with 150 μm diameter - leading to highly efficient signal excitation and collection was introduced by Persichetti *et al.* (2017) [145].

Alignment of the light emitter and the optical circuit is a sensitive part of an optofluidic system. Small variations (less than 5%) may produce large performance variations that make the system unreliable [146]. Thus, monolithic integration of the solid-state light emitters (SSLE) is a field of high importance. Llobera *et al.* (2015) [146] proposed an innovative hybrid monolithic solution (see Fig. 4.1.5. a) for on-chip integration of a SSLE aligned with a multiple internal reflection (MIR) system. The SSLE was made of a fluorophore-doped hybrid xerogel material. The fabrication procedure involved a low-cost photolithographic fabrication step.

Air mirrors were made in order to assure light coupling from the light source to the MIR system. Robbins *et al.* (2018) [147] introduced a compact device embedding a $\text{SiO}_2/\text{Ta}_2\text{O}_5$ multilayer optical interference filter, a hydrogenated amorphous silicon (a-Si:H) pin photodiode, an asymmetric microlens, and a GaN micro LED. The system was capable to collect fluorescence light in a 100 μm microfluidic channel, the device reaching a 36 nM LOD for fluorescein solution. Integration of the micro-LED was concluded as being difficult due to its lack of directionality. However, the fabrication procedure paved the way towards planar heterogeneous integration of GaN micro-LED on an a-Si:H fluorescence sensor. Kang *et al.* (2016) [148] developed a fabrication methodology (see Fig. 4.1.5. b) for building mechanically flexible microfluidic fluorescence sensors. They managed to integrate microscale vertical cavity surface emitting lasers (micro VCSELs) and silicon photodiodes on a flexible substrate of polyethylene terephthalate (PET). This substrate integrated with elastomeric fluidic chips on plastics demonstrated potential for multiplexed, real-time operation.

Polymers or silicon-based materials with refractive indexes varying between 1.4 and 3.5 are usually used for the fabrication of optofluidic integrated systems. Since the refractive index of water is 1.33, the TIR condition required to confine the light when hollow-core optical waveguides are used simply cannot be satisfied for this particular case. Antiresonant Reflecting Optical Waveguides (ARROW), based on the thin-film interference principle and the conventional silicon microfabrication techniques, propose a solution for this inconvenient. A particular solution is represented by the aerogel waveguides. A series of alternating dielectric layers creates the conditions for interference-based guidance of leaky modes [149]. This technique proved to be very suitable for very sensitive fluorescence detection.

Parks *et al.* (2014) [149] used this technology for developing a programmable microfluidic chip with on-chip detection of fluorescence. The active control of the biological solutions was realized using programmable microvalve arrays (see Fig. 4.1.6. a). Measor *et al.* (2011) [150] introduced a methodology for the fabrication of on-chip interference filters with multiple high and low loss regions. Interference filters, compatible with silicon microfabrication techniques, possess less autofluorescence when compared with absorbance filters. In this work, they managed to decrease the number of dielectric layers requested for efficient working of the interference filter from more than 30 down to 3. Aerogels are materials with low-refractive indexes, making them suitable for solid-cladding in liquid-core optofluidic waveguides based on

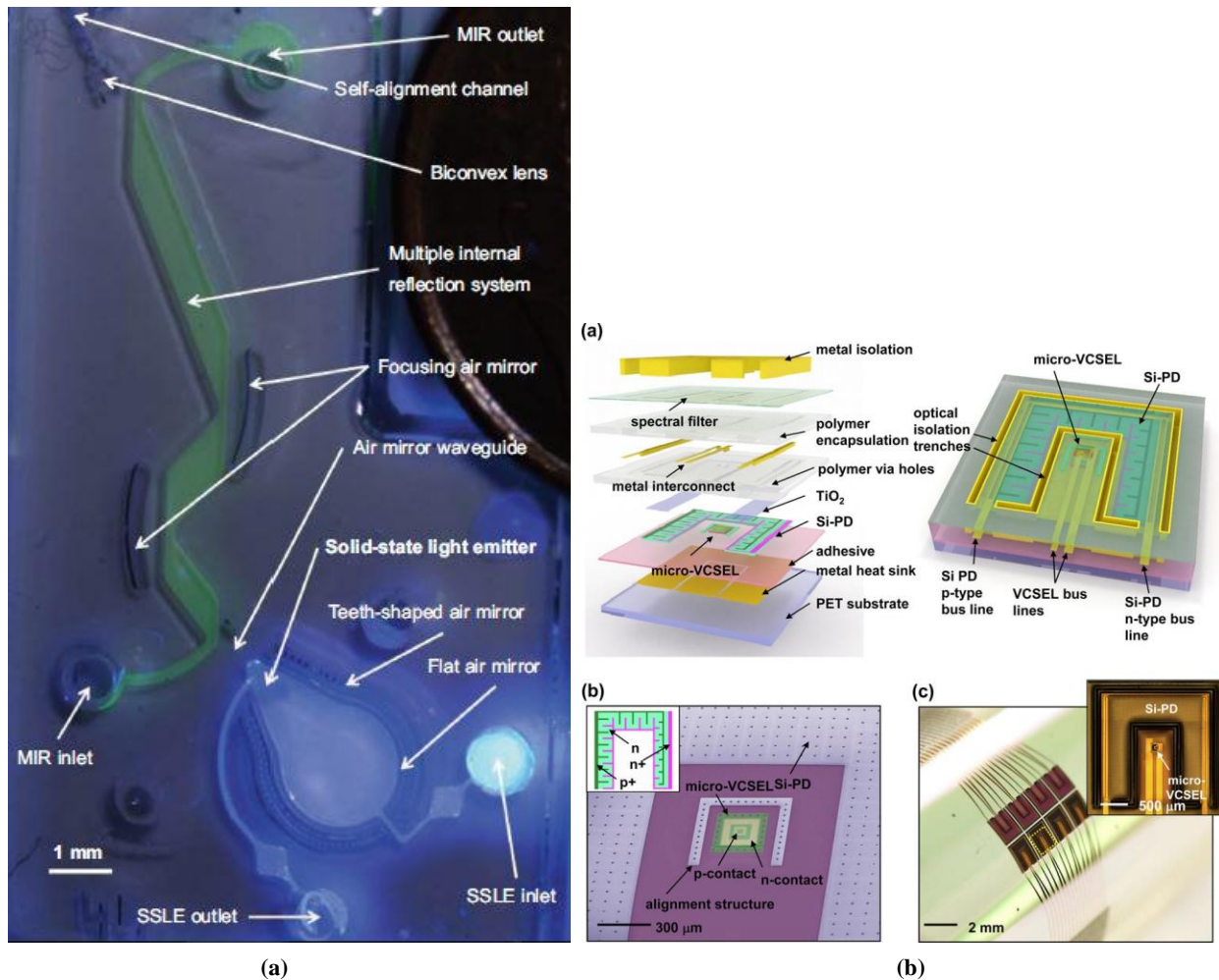
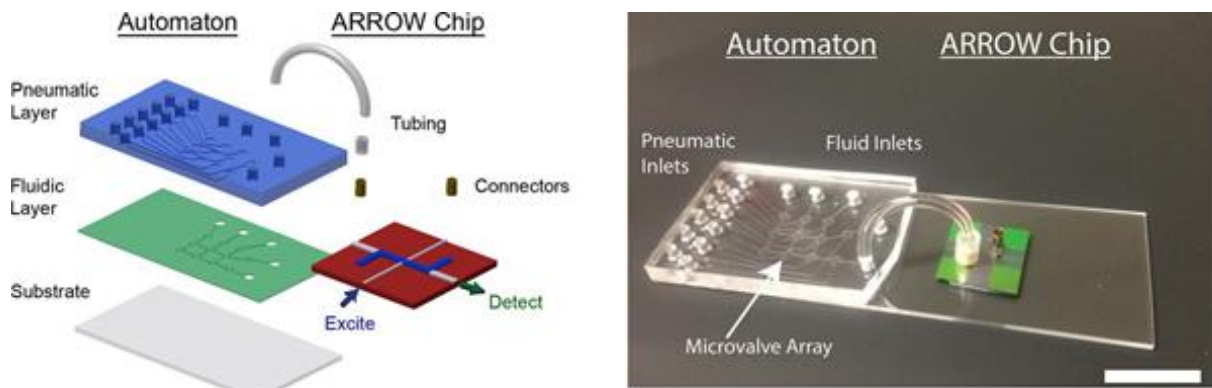


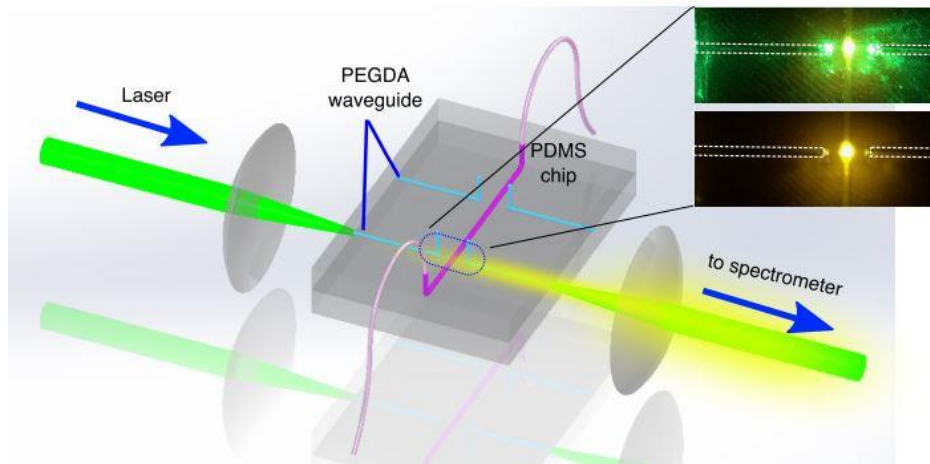
Figure 4.1.5. (a) Photonic lab-on-a-chip with the solid-state light emitter, air mirrors, multiple internal reflection system, biconvex lens, and the channel for fiber optics integration. (b) (a) Illustration of the flexible sensor design and fabrication methodology. (b) Scanning electron microscopy view of the VCSEL and the 3 μm thick Si-Photodiode. (c) Image of an array of sensors wrapped around a cylindrical bar. (a) Reproduced from Llobera *et al.* [146], Copyright 2015, with permission from Springer Nature. (b) Reprinted with permission from Kang *et al.* [148], Copyright 2016, American Chemical Society.

the TIR principle. A comprehensive review of aerogels used for optofluidic waveguides is presented in Özbakır *et al.* (2017) [151].

Following the trend of scaling down by 3D integration of various heterogeneous components, a SU-8 polymer-based methodology was developed by Nittala and Sen (2018) [152]. The cost-effective reported methodology allowed integration of commercially-available components in a relatively simple way. The key element of this approach was planarization of the layers with correctly chosen SU-8 parameters in such a way that the next layer could be stacked using epoxy-based bonding. This method allowed packaging a photon detector, the filters, the microfluidic chip, and a LED.



(a)



(b)

Figure 4.1.6. (a) Hybrid chip-scale system combining the automated microfluidic processing (automaton) and on-chip optical detection based on the ARROW principle. The scale in the figure - 1 cm. (b) Optical device schematic with a PEGDA waveguide used for excitation light coming from a 532 nm laser and another PEGDA waveguide used to collect the fluorescence emission from the interrogation volume. (a) Reproduced from Parks *et al.* [149], Copyright 2014, with permission from AIP Publishing. (b) CC-BY 4.0.

Table 4.1.3. Microfluidic systems using optics layer-integrated designs towards-on-chip approaches for fluorescence detection.

Reference	Achievements	Applications	LOD	Analyte	Further improvements [Author's suggestions]
Babikian <i>et al.</i> (2017)[100]	<ul style="list-style-type: none"> • Heterogeneous integration strategy integrating optical, electronic, electromechanical, and fluidic components on the same chip. • Demonstration of a digital signal processing (DSP) assisted lab-on-a-chip PCB that can extract the signal from an isotachopheresis assay. • PCB, ITP, microelectronics, and DSP integrated on-chip for fluorescence detection in a microfluidic-optoelectronic PCB device. 	Isotachopheresis assay	10 nM (SNR=9)	Fluorescein fluorophore.	More optimized designs and more sophisticated algorithms could further improve the detection sensitivity.
Païè <i>et al.</i> (2017) [133]	<ul style="list-style-type: none"> • In-plane integrated microfluidic lens, with tunable optical properties, combined with a droplet generation module. • The focusing of the lens could be changed by replacing the fluid streamed in the system. • Fabrication was done in fused silica: (1) femtosecond laser beaming; (2) ultrasonic bath etching. 	In-plane microfluidic lens.		Rhodamine	-
Guduru <i>et al.</i> (2016) [134]	<ul style="list-style-type: none"> • The microfluidic network, the excitation, the filtering, and the collection elements were embedded in the same glass substrate. • Fabrication methodology: (1) microfluidic channels created by femtosecond laser irradiation followed by chemical etching technique; (2) fabrication of the Bragg mirror and the buffer layer by RF sputtering, (3) surface ablation using FLM for the Fresnel lens. 	Fully-integrated fluorescence sensing in glass-made devices.	600 nM	Oxazine 720 perchlorate dye.	Bragg mirror reflectivity could be improved by adding thermal treatment after the deposition process.
Ricciardi <i>et al.</i> (2015b) [136]	<ul style="list-style-type: none"> • Optofluidic chip based on a multilayered photonic crystal structure was employed for an efficient beaming of the emitted radiation in a fluorescent microarray assay. 	Efficient focusing in point-of-care devices.	0.168 µg/ml	Actin-Alexa Fluor solutions.	-
Novo <i>et al.</i> (2014) [141]	<ul style="list-style-type: none"> • Prism-like PDMS microfluidic device coupled with amorphous silicon photodiodes and a lateral excitation scheme at a specific angle • Lateral excitation coupled to TIR to maximize the excitation light reaching the microchannel while preventing it reaching the detector. 	Improve the SNR using TIR principle.	5.6×10^{10} antibodies/cm ²	Antibodies labeled with an organic fluorophore.	By modifying the polymerization process, minimize the internal scattering of the PDMS.

Reference	Achievements	Applications	LOD	Analyte	Further improvements [Author's suggestions]
Berner <i>et al.</i> (2017) [143]	<ul style="list-style-type: none"> It successfully integrated line-focused laser excitation with sensitive amorphous silicon photodiodes and novel, disposable microfluidic chips to a device that has no need for space-consuming optics or bulky sensors. The innovative microfluidic chips formed by a transparent, laser-cut adhesive tape were not only essential for the presented concept, but also of general interest as an easy, versatile and scalable way to fabricate microfluidic channel chips. 	Point-of-care testing devices for continuous monitoring.	26 nmol/L	DY636 dye	Substitution of the silicon top plate of the microfluidic chip by a plate of another material to enable low fabrication cost of the disposable microfluidic chips.
Persichetti <i>et al.</i> (2017) [145]	<ul style="list-style-type: none"> Optofluidic detection scheme based on an optofluidic jet. Total internal reflection arises in a liquid jet of 150 μm diameter, leading to efficient signal excitation and collection. 	Pharmaceutical liquid sample analysis.	0.21 ng/mL	Riboflavin	-
Robbins <i>et al.</i> (2018) [147]	<ul style="list-style-type: none"> Monolithical integration of a $\text{SiO}_2/\text{Ta}_2\text{O}_5$ multilayer interference filter and hydrogenated amorphous silicon (a-Si:H) pin photodiode. Annular shape of the sensor combined with a transparent glass substrate allowed vertical illumination. 	Point-of-care microfluidic biochemical analysis.	36 nM (SNR=3)	Fluorescein solution	Heterogeneous integration of a GaN VCSEL on the a-Si:H fluorescence sensors; fabricate a planar LIF device resulting in better light directionality.
Nittala and Sen (2018) [152]	<ul style="list-style-type: none"> 3D heterogeneous integration methodology, allowing packaging of photodetector, filters, microfluidic chip, and LED in one system. Components were embedded through SU-8-based planarization and epoxy-based bonding. 	Point-of-care microfluidic systems.	1 μM	Rhodamine B and 6G.	-
Rodríguez-Ruiz <i>et al.</i> (2017) [153]	<ul style="list-style-type: none"> Master mold based on WBR2000 dry polymer films, fabricated in standard laboratory conditions, without requiring clean room facilities. Compared with SU-8 standard lithography technique, this method resulted in 10 folds reducing of the material costs. 	Fast, low-cost structures design and prototyping.	8.5 \pm 0.3 μM	Fluorescein	-

A low-cost master mold fabrication process based on a dry film photoresist for soft lithography, and operated in standard laboratory conditions was reported in Rodríguez-Ruiz *et al.* (2017) [153]. This protocol managed to reduce by ten times the material costs and reduced considerably the fabrication time compared with standardized SU-8 master mold techniques. The methodology initialized a simpler fabrication methodology of photonic devices. Integrated hydrogel waveguides potential for developing wearable and implantable lab-on-a-chip devices was evaluated by Torres-Mapa *et al.* (2019) [154]. They used self-aligned polyethylene glycol diacrylate (PEGDA) waveguides, which present tunable mechanical and optical properties, integrated via micro-molding technique into a PDMS structure in order to evaluate the fluorescence response from a rhodamine 6G solution. The PEGDA waveguides integrated in the PDMS showed high transmission, minimal absorption in the visible spectrum, and propagation losses lower than 1.1 dB/cm. Further investigations on mechanical and light guiding properties during stretching/bending are requested (see Fig. 4.1.6. b).

4.1.2.3. Organic electronic-based designs

Organic light emitting diodes (OLED) and organic photon detectors (OPD) are the subject of significant research efforts and continuous improvements (see Table 4.1.4.) due to their multiple applications and advantages compared to their inorganic counterparts [155]. Organic electronics introduced some unbeatable advantages, such as direct on-chip integration, easy emission and detection, and compatibility with flexible substrates. An OLED is a solid-state device composed of flexible thin films of organic molecules that emit light when subject to electricity, using less power than current available LEDs.

Currently, OLEDs are largely used in commercially available electronics (TVs, smartphones, etc.), being available in a large bandwidth emission spectrum. However, OLEDs possess lower efficiencies (around 80 lm/W) than inorganic LEDs (higher than 200 lm/W) [155]. For enhancing widespread OLED implementation, the PI-SCALE project (pi-scale.eu) aims to integrate existing European infrastructures into an “European flexible OLED pilot line”, operating in an open access mode and serving customers with individual product designs, validation of upscaling concepts, and system-level flexible OLED integration. Comprehensive reviews of the latest achievements in OLEDs used for fluorescence sensing may be found in [155–158]. In Jansen-van Vuuren *et al.*, [159], recent achievements in the field of OPDs were described, while the last comprehensive review about the integration of fluorescence sensors using organic optoelectronics with microfluidics (see Fig. 4.1.7. a) is presented by Lefèvre *et al.* (2015) [160].

A fluorescence light detector combining both an organic electrochemical cell (OLEC) and a photodiode-based OPD (PD-OPD) within one microchip (see Fig. 4.1.7. b, c) was introduced and tested by Shu *et al.* (2017) [161]. Moreover, linear polarizers were used as emission and excitation filters, enabling the possibility to detect fluorescent targets with emission and

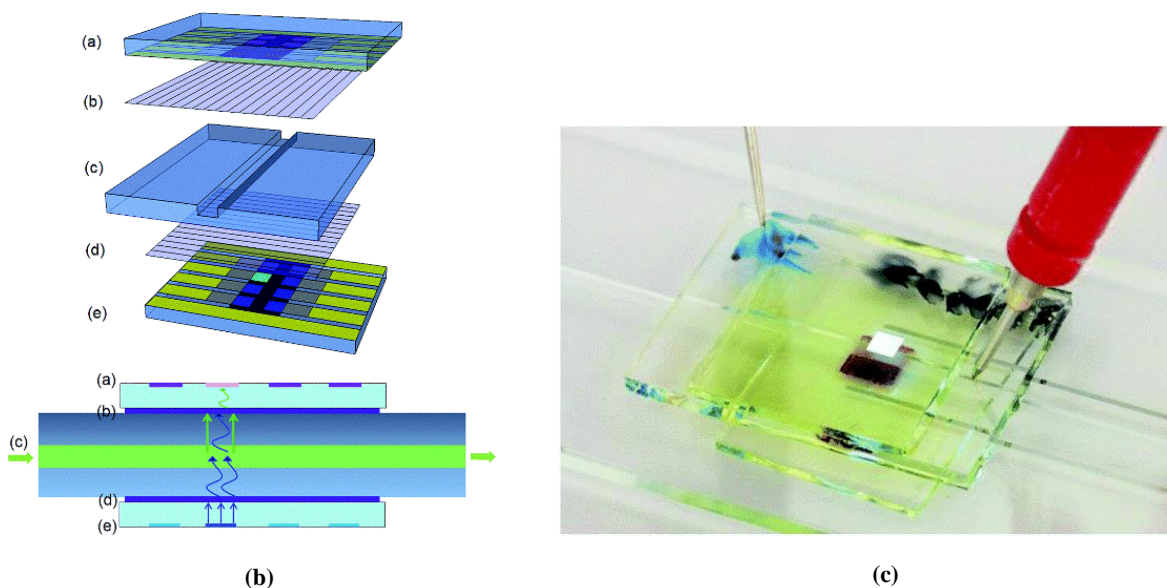
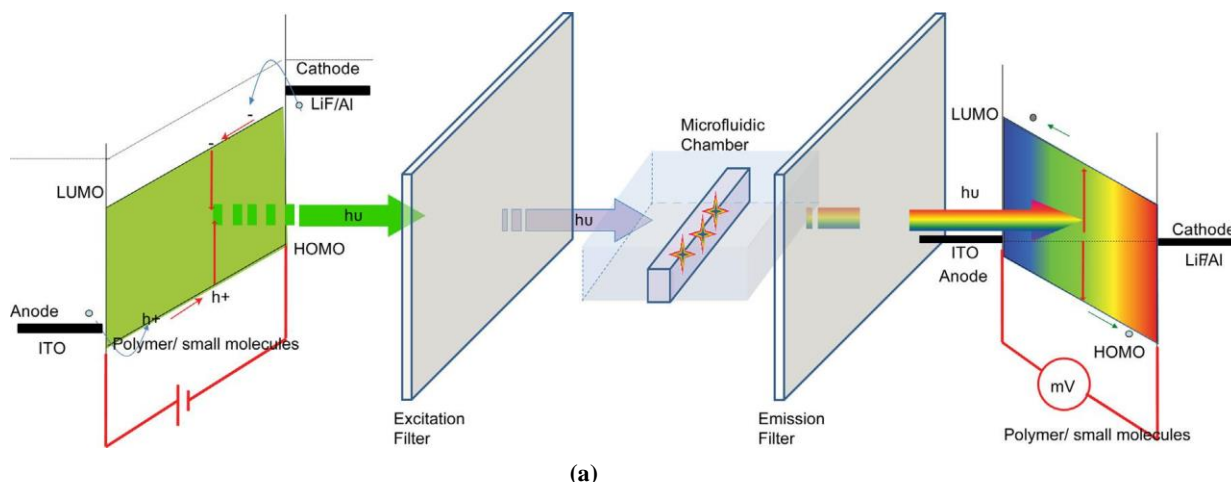


Figure 4.1.7. (a) Generic illustration of the fluorescence optofluidic detection based on organic electronics. (b) Schematic representation of OLEC excitation and OPD detection system. (a) OPD. (b) Linear polarizer filter. (c) Glass microfluidic chip. (d) Blue OLEC. (e) fully-processed blue OLEC. (c) Fabricated optofluidic system. (a) Reproduced from Lefèvre *et al.* [160], Copyright 2015, with permission from Elsevier. (b) and (c) Reproduced from Shu *et al.* [161], Copyright 2017, with permission from The Royal Society of Chemistry.

absorbing peaks very close to each other. The organic layers were manufactured using solution deposition processing, considerably decreasing the fabrications costs. The emission light peak of the OLEC was modified by choosing different light emitting polymers, enabling multiplexing. The OLEC was used in pulsed mode to detect fluorescein amidite, reaching a 1 μM LOD. The brightness of the OLEC was up to 2800 cd/m^2 at a driving voltage of 50 V. The brightness was not altered up to 10,000 pulses for a 30 ms pulse width, resulting in an autonomy of ten minutes. The proposed solution proved stability and high commercialization potential. Organic

optoelectronics for building compact lab-on-a-chip applications was used by Jahns *et al.* (2017) [162] who introduced two devices. For the first device, four 5 mm² OLEDs and four 5 mm² OPDs were manufactured separately on two 25 × 25 mm² glass substrates. A dichroic filter was used, in order to decrease the noise. The second device had a cylindrical form and used a reflection system, in order to facilitate the decrease of the noise and avoid additional filters.

A detailed description of the integration process of an organic optoelectronic system within a microfluidic platform has been presented in Poorahong *et al.* (2016) [163]. A system comprising a series of blue and green OLEDs, OPDs, and optical filters was designed, in order to develop a detection system for a PDMS multi-chambered structure with 9 μL detection volumes.

The 480 nm and 515 nm OLEDs, OPD, and optical filters were manufactured individually and then integrated within the microfluidic structure. The spectral width of the OLEDs was around 87-90 nm. Their durability was tested by applying pulses of different voltages (12 V for a blue OLED and 18 V for a green OLED). After some ten pulses, the emission intensity stayed constant.

An innovative OPD manufacturing solution, enabling a 14,000 hours lifetime under continuous operation was presented by Kielar *et al.* (2016) [164]. Thin film transistor array technology, inspired by the flat panel display and x-ray image industry, is a new approach used to enable low-cost multi-biomarker detection.

Smith *et al.* (2014) [165] introduced a miniaturized fluorescence-based lab-on-a-chip sensing architecture (see Fig. 4.1.8.) based on an OLED display and photodiode active matrix technology for point-of-use diagnosis of multiple diseases or pathogen markers in a cost-efficient disposable configuration. A straightforward concept, enabling a new approach using matrix active OLED and photodiode array technology for the multi-target analysis was implemented

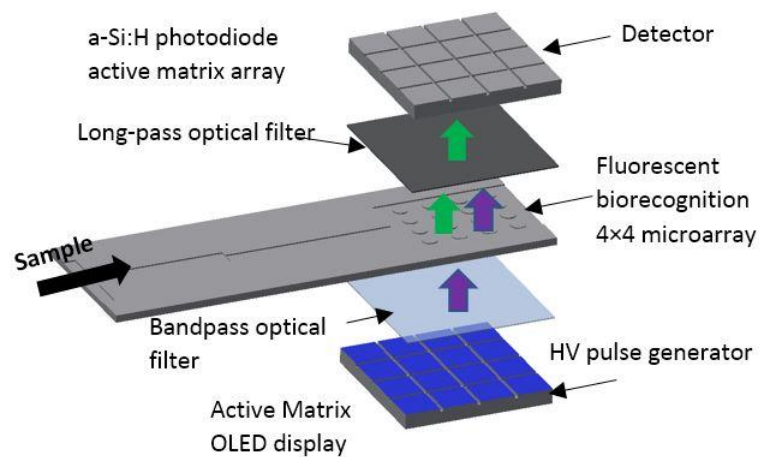


Figure 4.1.8. Lab-on-a-chip sensing architecture based on OLED display and photodiode active-matrix technology for point-of-use diagnosis of multiple diseases. ©2014. IEEE. Reproduced, with permission, from Smith *et al.* [165].

Table 4.1.4. Microfluidic systems using organic electronic based-designs towards-on-chip approaches for fluorescence detection.

Reference	Achievements	Applications	LOD	Analyte	Further improvements [Author's suggestions]
Shu <i>et al.</i> (2017) [161]	<ul style="list-style-type: none"> • Microfluidic fluorescent sensing system, with a fully solution processed light source and photodetector. • Blue OLEC was first introduced and demonstrated as a low-cost excitation light source. • The emission light peak could be relatively easily modified by selecting different light emitting polymers. • Two orthogonally oriented linear polarizers were included onto the micro fluidic glass chip. • Two organic lab-on-a-chip fluorescence detection designs and their fabrication methodologies described and demonstrated. • (1) OLED and OPD integrated on separate substrates. • (2) OLED and OPD integrated into a cylindrical geometry on a single substrate. It avoided usage of filters. 	Low cost, portable and disposable fluorescence sensors with a high sensitivity.	1 μ M FAM in water (S/N > 1.1)	Fluorescein amidite (FAM)	-
Jahns <i>et al.</i> (2017) [162]	<ul style="list-style-type: none"> • Two organic lab-on-a-chip fluorescence detection designs and their fabrication methodologies described and demonstrated. • (1) OLED and OPD integrated on separate substrates. • (2) OLED and OPD integrated into a cylindrical geometry on a single substrate. It avoided usage of filters. 	Water pollution detection.	520 nM (First system)	Acid Yellow 73	For the second system, performing further analysis to determine the behavior of the signal and the limit of detection.
Poorahong <i>et al.</i> (2016) [163]	<ul style="list-style-type: none"> • Fabrication methodology of OLEDs and OPDs for fluorescence detection, integrated with microfluidic chips using standard soft lithography techniques in PDMS. • Demonstrate organic photodetectors as possessing a competitive level of stability for successful commercialization, approaching the performance of Silicon-based photodiodes. • Three solution-processed layers and two low-temperature annealing steps used during the fabrication, resulted in a dark current density as low as 0.31 nA cm^{-2}, a responsivity of 0.32 A W^{-1}, and a detectivity of 3.21×10^{13} Jones at -2 V. • Photodiode with lifetime of over 14,000 hours under continuous operation. 	Cost-effective fully-integrated excitation light source.	0.5 nM	Diuron	-
Kielar <i>et al.</i> (2016) [164]	<ul style="list-style-type: none"> • Three solution-processed layers and two low-temperature annealing steps used during the fabrication, resulted in a dark current density as low as 0.31 nA cm^{-2}, a responsivity of 0.32 A W^{-1}, and a detectivity of 3.21×10^{13} Jones at -2 V. • Photodiode with lifetime of over 14,000 hours under continuous operation. 	Low-cost, disposable lab-on-a-chip point-of-care (POC) diagnosis system	3 nM (S/N=3)	Quantum dot	-
Venkatraman and Steckl (2015) [265]	<ul style="list-style-type: none"> • Thin film phosphorescent green OLEDs fabricated on plastic substrates integrated on-chip. • OLEDs were fabricated by sequential deposition of organic thin films (100 nm) onto ITO-coated PET substrates. 				

and tested. The 8×8 biorecognition array of 64 pixels based on this technology had an area less than $2 \times 2 \text{ mm}^2$, and was able to work with a $100 \text{ }\mu\text{L}$ volume of fluid. The array-based OLED was formed from multiple light emitting elements (pixels) which were individually activated, in order to emit light at specific wavelengths and to enable multiple target detection.

The same group proposed in Katchman *et al.* (2016) [166] a high density fluorescence, programmable, multiplexed recognition compact miniaturized device for point-of-care molecular diagnostics. The OLED technology was combined with protein microarray technology and 10 pg/mL LOD was achieved for human IgG.

4.1.2.4. CMOS-based fluorescence sensing

CMOS technology revolutionized the field of micro-electronics [167] and it holds the promise to do so for micro-optical sensing as well. On-chip CMOS-integration, coupled to microfluidics for detection at the micro-scale, was increasingly observed in the recent literature [37,168–170], especially for development of filterless prototypes (see [Table 4.1.5](#)).

The focusing and the filtration optics represent a barrier in the miniaturization process [10], alternative techniques replacing them being envisaged. The filterless discrimination between the excitation light and the generated fluorescence light emerged as a cost-effective, compact, and lightweight miniaturization method (see [Fig. 4.1.9. a](#)).

CMOS based contact sensing coupled with time-correlated photon counting (TCSPC) has proven to be a sound methodology [37]. Different strategies implementing CMOS image sensors have been recently proposed [171] with good results and enough space for further improvements. The challenges existing in combining the integrated circuits with biological or chemical components in lab-on-a-CMOS concept, such as thermal effects, floor-planning, signal coupling, electrochemical effects, surface treatments, sterilization, and microfluidic integration were detailed by Datta-Chaudhuri *et al.* (2016) [172].

One of the most critical challenges in lab-on-a-CMOS design and fabrication represents the interaction between the fluid samples and the chip surface, traditional wire-bonding packaging not being compatible with the planar microfluidic concept. Lindsay *et al.* (2018) [173] developed a heterogeneous integration solution of a CMOS sensor and a fluidic network using wafer-level molding process. A technology enabling monolithic integration of the read-out system within the sensor for general label-free miniaturized optical detection by integrating nanophotonic structures with CMOS photodiodes was reported in Shakoor *et al.* (2018) [167]. One-dimension grating structures with a CMOS integrated image sensor arrayed with photodiodes. The gratings were made of silicon nitride and refractive index changes were induced when different analytes were applied. Pang *et al.* (2011) [174] developed a CMOS based detection system by integrating Fresnel zone lenses (described above) (see [Fig. 4.1.9. b](#)).

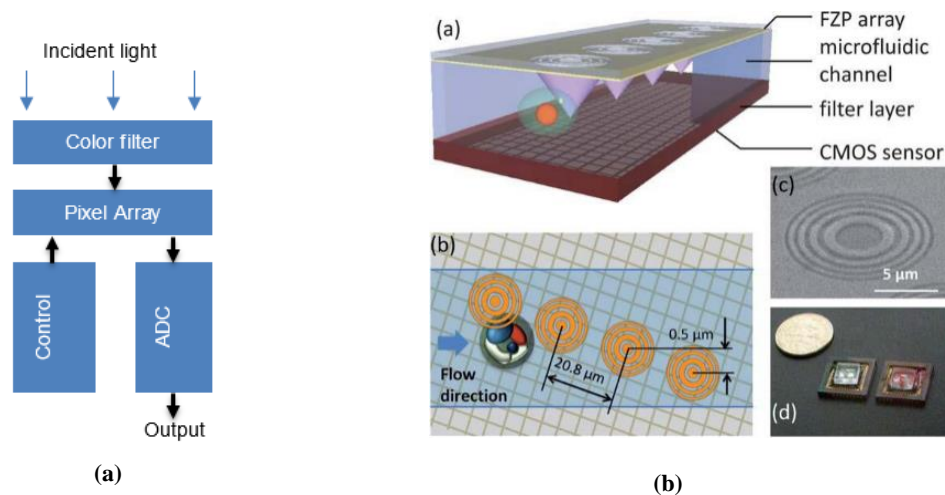


Figure 4.1.9. (a) CMOS image sensors in-depth working principle. (b) (a) CMOS image sensor with thin layer filter coated on top, the microfluidic channel, and the Fresnel Zone Plate (FZP) array. (b) Top view schematic of the device with the FZP array configuration and its design parameters. (c) Scanning Electron Microscopy image of the fabricated Fresnel lens. (d) Images of the fabricated laboratory devices. Reproduced from Pang *et al.* [174], Copyright 2011, with permission from The Royal Society of Chemistry.

Tanaka *et al.* (2017) [168] proposed a system based on charge accumulation techniques that simultaneously allowed filterless measurement of multiple low intensity fluorescence wavelengths (five in this work). The charge accumulation technique involves fluorescence detection by measuring the voltage change of a capacitor which is proportional to the accumulated signal charge quantity. This technique has the capability to increase the output signal level, reducing the noise induced by the incident light. From experiments, the dynamic range obtained was 100:1. The filter was fabricated by an older 2-poly, triple-well, $5 \mu\text{m}$ CMOS process. A lens-free system for breast cancer cell detection was developed by Papageorgiou *et al.* (2017) [10]. It integrated stacked CMOS metal layers above each photodiode to form angle-selective gratings, rejecting background light. Choi *et al.* (2016) [169] presented a filterless method for the suppression of forward scattering in silicon by surface planarization, resulting in a separation efficiency improvement from 550:1 to 1250:1. This was achieved mainly due to the low roughness of the polysilicon surface.

Plasmon enhanced fluorescence, or metal enhanced fluorescence, is a powerful amplification method used to increase the sensitivity and shorten detection times, and is based on the interaction between fluorophore labels that are coupled with the confined field of surface plasmons. A comprehensive review of this topic can be obtained from Bauch *et al.* (2014) [175] and a detailed overview is presented in Geddes (2017) [176]. The integration of nano-plasmonics with CMOS technology, without any other post-processing, enabled the possibility to integrate large multiplexed assays on the same chip. A detailed theoretical description of plasmon-enhanced fluorescence coupled with CMOS technology is found in Hong *et al.* (2017a) [177].

3D copper-based nanoplasmonics components were integrated within standard CMOS devices through sub-wavelength copper-based electrical interconnect lithography features by Hong *et al.* (2017a) [177], developing a bio-sensor with a nano-waveguide array-based filter. The sensor was developed by implementing a 65 nm process, managing to diminish the noise by 50 dB for a large variety of incident angles. It comprised an assay platform, a sensor, and read-out circuitry, making the integration of external optical components and any other post-fabrication techniques unnecessary, except for the light source that was a micro-laser diode or a LED. The optical fields could be manipulated in a controllable manner. Within the same team, the work of Lu *et al.* (2018) [178] analyzed the possibility of photonic crystal integration on a CMOS sensor, exploiting optical physical unclonable functions (PUF) for a better management of the background noise.

In Varsanik and Bernstein (2013) [179], a plasmonic resonator was designed, fabricated, and tested, proving both field enhancement and localization to nano dimensions. The proposed architecture enabled a solution for high-resolution and low-noise detection of fluorescence within an integrated microfluidic optical detection device. The microfluidic channel was built in a polymer on top of a glass substrate wafer. A diffused waveguide was embedded within the glass substrate, crossing the fluidic microchannel in the interrogation region. The width and the depth of the microchannel were 8 μm and 200 nm, respectively, enabling an extremely reduced interrogation volume and, by consequence, reduced noise. Finally, the system was capable to successfully detect 20 nm sized fluorescent particles.

The field of CMOS-based fluorescence sensing did not benefit from high-performance integrated optical filters until recently. This situation led to implementation of either time-resolved techniques with synchronized sources [180], or externally located optical filters and focusing optics [178]. The above mentioned methodologies, that were recently reported, enlarged the horizons toward more robust and compact fully-integrated solutions aiming to solve the chip-in-the-lab dilemma [167] with further improvements. The Internet-of-Things (IoT) field of applications requires low-power and low-cost sensors, and here CMOS based fluorescence detection is expected to play a major role [178]

Table 4.1.5. Microfluidic systems using CMOS-based designs towards-on-chip approaches for fluorescence detection.

Reference	Achievements	Applications	LOD	Analyte	Further improvements [Author's suggestions]
Hong <i>et al.</i> (2017a) [177]	<ul style="list-style-type: none"> Fully-integrated bio-molecular fluorescence sensor in 65-nm CMOS with integrated nanoplasmonic waveguide-based filters. 50 dB of rejection ratio across a wide range of incident angles. 	Enable parallelized sensing on a single chip.	48 zeptomoles	Quantum-dots	-
Tanaka <i>et al.</i> (2017) [168]	<ul style="list-style-type: none"> Developed a low-detection-limit filter-less fluorescence sensor by a charge accumulation technique. Sensor was fabricated with a photogate and a triple-well process. 	Implementation of filterless design strategies.	0.1 nW		Dynamic range 100:1, improvable optimizing the FD capacitance.
Choi <i>et al.</i> (2016) [169]	<ul style="list-style-type: none"> Suppressing forward scattering in silicon by surface planarization; improvement of a filter-less fluorescence sensor. Separation ability of the filter-less fluorescence sensor increased from 550:1 to 1250:1. 	Implementation of filterless design strategies.	-	-	-
Bueno Hernández <i>et al.</i> (2017) [51]	<ul style="list-style-type: none"> MATLAB interface developed for reading-out fluorescence signals with RGB model in CMOS sensor. First application of the use of RGB model with CMOS sensor to detect OTA in wine and beer samples. 	Portable detection of mycotoxins.	2 µg/L	Ochratoxin A (OTA)	-
Lindsay <i>et al.</i> (2018) [173]	<ul style="list-style-type: none"> Heterogeneous integration of microfluidics and silicon-integrated circuits using compression molding with a commercial fan-out wafer-level packaging approach. Electrical, fluidic routing in 0.18-µm CMOS optical sensor integrated circuit. Rapid prototyping fabrication methodologies for fluidic integration, resulting in millimeter-scale fluidic channels and sub-millimeter-scale fluidic channels (fabrication of monolithic SU-8 microchannels over the integrated circuit surface). 	Optofluidic lab-on-a-CMOS.	-2.5 nA	Quantum-dots	Long-term adhesion and material compatibility to be studied for liquid contact.
Hong <i>et al.</i> (2017b) [266]	<ul style="list-style-type: none"> Design methodology based on CMOS integrated nanoplasmonic filters, exploiting the sub-wavelength lithographic features of on-chip interconnects, eliminating the need for any post-fabrication, or external optical elements. First fully-integrated fluorescence-based CMOS bio-molecular sensor with integrated nano-plasmonic sensor. 	Low-cost, fully integrated, high performance, and fully-scalable biosensor for POC applications.	47 zeptomoles	Quantum-dots	-

4.2. Gas-Liquid Microreactors for continuous trapping of gaseous molecules

4.2.1. Gas-liquid direct contactors

The main advantage of the direct contacting is the lack of an additional mass transfer resistance at the gas-liquid interface, unlike for the membrane-based contacting. Slug and annular flows are the most frequently used flow patterns in the case of direct gas-liquid contacting due to their high surface-to-volume ratios. Since slug flow is a more stable and easier to reproduce pattern [181], gas-liquid contactors/microreactors based on slug flow are usually preferred.

Mass-transfer is better characterized in slug flow regime relative to the annular flow dominated by instabilities [182]. In the freshly published (2021) review of Yao *et al.*, [182], the authors suggest the mass transfer in annular flow regime as a direction that needs much more attention in the near future since the topic has not yet fully took shape.

Therefore, gas-liquid contactors/microreactors based on annular flow are scarcely studied despite their potential superiority for particular applications, apparently as a consequence of the short contact time between the phases [181]. In annular flow, the gas phase might be in contact with the liquid phase for a too short period of time since the gas velocity is up to three orders of magnitude larger than the liquid velocity. If the absorption of the molecules to be separated is not fast, the trapping efficiency might be actually low. There are few works in the literature related to the on-chip annular flow integration and even reviews on gas-liquid microreactors, such as Zhang *et al.*, [183] or Lam *et al.*, [184], only briefly mention it.

The difficulty in characterization and prediction of the annular flows originates from the Kelvin–Helmholtz instabilities at the gas-liquid interface. These interface instabilities are influenced by the wettability of the microchannel wall [185], roughness [186], curved sections of the microchannel [187,188], and pulsations of the micropumps used to supply the fluids.

Annular flow still lacks complete experimental observations [189]. However, some studies related to the hydrodynamics presented experimental observations. For a straight channel, Humphry *et al.*, [190] showed that by making the channel width comparable with the channel height, the interface instabilities can be suppressed. Sur *et al.*, [191] observed that usually the thickness of the liquid film decreases with the diameter of the microchannel. Takeda *et al.*, [188] presented the hydrodynamic effects of two-phase flows in meandering millichannels. An interesting observation from this study states that in a hydrophobic channel the pressure drop tends to reach its local maximum at the transition from slug flow towards slug-annular flow. In a hydrophilic channel, this effect is not observed since walls are always wetted. Up to the author's knowledge, there is no experimental method for visualization of the mass transfer from a phase to another, as it was recently developed and validated for the slug flows [192].

There are a couple of works developing numerical algorithms for studying annular flow hydrodynamics by Jesseela *et al.*, [193] and for the prediction of the Kelvin–Helmholtz instabilities from Guo *et al.*, [194,195]. Jesseela *et al.* developed a numerical algorithm using the continuum

approach in which they could determine the velocity distribution, the two-phase pressure drop, and the averaged-heat transfer coefficient. Guo *et al.* proposed a model in which the instabilities occurring at the gas-liquid interface are captured without spurious currents (unphysical velocities usually introduced by numerical models).

Advantages of pressure-driven two-phase flows in microfluidic meandering channels are obvious. Most probably, this is the choice that makes possible the compact on-chip integration of long microchannels. However, the slug and the annular pressure-driven flows in meandering channels are rarely studied. Roudet *et al.*, [196] studied the $k_L a$ in a $2 \times 2 \text{ mm}^2$ square meandering channel starting from a slug flow up to the slug-annular flow by maintaining the liquid superficial velocity constant, while gradually increasing the gas superficial velocity. In multiphase flows, the superficial velocity is defined as the velocity a fluid would have if it would flow alone in the channel. Whereas the mass transfer enhancement in the slug flow was insignificantly higher, not the same conclusion resulted for the slug-annular flow. $k_L a$ was considerably higher in the meandering slug-annular flow when compared to the straight channel. Yue *et al.*, [197] have demonstrated the same behavior for a $1 \times 0.5 \text{ mm}^2$ channel, obtaining $0.3 < k_L a < 21 \text{ s}^{-1}$. The lower values were obtained for slug flows, while the higher for the slug-annular flow.

The mass transfer in slug flows is enhanced by the intense recirculation taking place in the slug [198]. Fries *et al.*, [187,199] and Sotowa *et al.*, [198] showed that mass transfer is slightly enhanced [196] in slug flows by the curved sections of the meandering channels. For a similar channel width, the mass transfer is more effective over the channel center line if the bend radius is smaller. Larger Dean numbers are observed in meandering channels, leading to a more efficient mixing.

The CO₂ trapping from a CO₂/N₂ gas mixture to a NaOH water solution is one of the most widely used techniques for mass transfer coefficients quantifications. Sobieszuk *et al.*, [181] characterized an annular flow into a 292 μm hydraulic diameter square meandering microchannel made in (hydrophilic) glass. The CO₂ mass-transfer coefficients from a CO₂/N gas mixture to a NaOH (0.1 M, 0.2 M, 0.7 M, 1.0 M, and 1.5 M) water solution have been measured for different superficial velocities of the gas and liquid streams. Depending on the flow rates, the annular flow was fully-developed in either first part of the meandering channel network, or in the last 66% of the meandering channel length. Similarly to Yue *et al.*, [197], they found the same behavior of the $k_L a$ from its transition from slug flow towards the slug-annular flow [200]. In this work, it was also concluded that Higbie's model [201] overpredicts the mass transfer coefficients and cannot be used for annular flows, as it cannot be used for slug flows, as well.

Microreactors using annular flow as contacting method between the phases are currently more likely to be made using capillary tubes rather than microchannels, as it is the case of the research and development work that led to the HCHO detector [31,32] of *InAirSolutions* start-up from Strasbourg, France. This is due to the fact that a larger radius of the capillary bending and the hydrophilic surface allow a much more stable and reproducible flow.

An important parameter in microreactor functionality is its time resolution. For real-time measurement applications, the response time of the system is a priority. Moreover, some applications using real-time quantification of the molecular concentrations e.g., fluorescence sensing, are very sensitive to the liquid-side molecular concentration reaching the flow-through detection cell. This is why the volume of liquid relative to the volume of gas contacted with it and the $k_L a$ are equally important. In other words, it is more important to bring a concentrated solution in the flow-through cell which can be detected by the optical system, rather than having a very high $k_L a$, but a very diluted solution. A close look has to be dedicated to the possible saturation of the liquid-side stream. A criterion for controlling the liquid film saturation has been proposed by Pohorecki *et al.*, [202].

In conclusion, while slug flow is more stable, predictable, and currently more used, annular flow is less studied and apparently more difficult to be on-chip integrated, although there are a couple of studies claiming its relative superior liquid-side volumetric mass transfer coefficients. Annular flow has to be taken more in consideration for its low liquid volume relative to the volume of the gas streamed. For optofluidic applications this is translated as a lower reagent consumption and consequently a higher autonomy of the sensor.

4.2.2. Gas-liquid membrane-based contactors

Despite the mass-transfer resistance induced by the membrane and fouling issues that usually occur with time, membrane-based interaction has the advantage of keeping the two phases in separate channels while giving the designer the flexibility of varying the flow rates and keeping a specific and defined interface area [203]. Moreover, although keeping the interface area constant and reproducible was a challenge in direct contacting, for membrane-based contactors this is straightforward and easy to achieve. Membrane hydrophobicity on the liquid-side is mandatory and here is where the field recently advanced. There are already a couple of vendors commercializing super-hydrophobic polymer membranes, such as Clarcor Industrial Air® and Pall Corporation®. The higher the contact angle, the lower are chances for fouling the pores.

Indeed, the largest inconvenient of the membranes is related to the fouling issues caused by impurities and/or wetting. However, cost-effective disposable thermoplastic chips with on-chip integrated hydrophobic membranes might confer them an interesting potential. Unfortunately, membrane integration onto polymeric structures is still challenging and time-consuming.

Wang *et al.*, [204] developed a monolithic integration methodology of commercially-available porous membranes in PMMA-, PC-, and COC-made chips. The fabrication methods consist in, firstly, a pre-bonding process that integrates the membrane into the thermoplastic chip using hot-embossing and secondly, a bonding process of a cover plate to close the chip without altering the properties of the membrane (see Fig. 4.2.1).

Dyrda *et al.*, [205] integrated double-sided hydrophobic membranes into PMMA devices and successfully separated CO₂ from a water-methanol solution at the anode side of a μ Direct-Methanol-Fuel-Cell. The membrane was sealed using a rubber O-ring to avoid possible leakage.

Femmer *et al.*, [206] developed a gas-liquid contacting chip using a PDMS flat-sheet membrane with staggered herringbone engraved on it. These herringbone mixers proved to be very efficient in enhancing the mass transfer of oxygen from an air phase to a water phase. The pressure drop along the channels was reduced due to the herringbone's structures. Concentration polarization at the gas-liquid interface has been avoided. The membrane-based contacting chip consists of ten 21 mm long parallel microchannels with one inlet and one outlet. Each channel is 500 μm wide and 50 μm deep. The PDMS membrane separating the channels was 127 μm in thickness, plasma-bonded into the chip, and possessed a 105 mm² transport area.

Brinkmann *et al.*, [207] developed a CFD model used for the flow optimization in a flat-sheet membrane reactor. Malankowska *et al.*, [208] proposed a double-side meandering channel network with an embedded membrane for blood oxygenation. A mathematical model for the validation of the oxygen transfer has been developed and with an oxygen transfer rate of 92 mL/min · m² for a 1 mL/min blood flow rate and a 2.9 cm² gas-liquid interface area. Karatay *et al.*, [209] proposed a UV-based adhesive bonding methodology for a hydrophobic PVDF

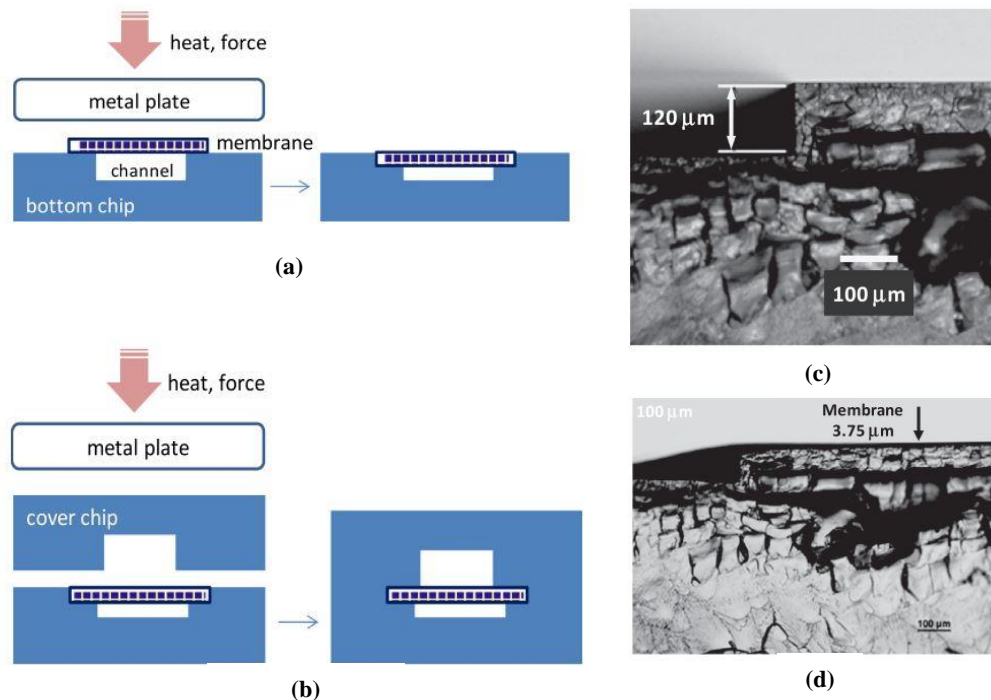


Figure 4.2.1. The two-step polymer membrane embedding process into a polymer chip. (a) Hot-embossing step for membrane bonding. (b) Closing-up the chip by thermal bonding of a polymer cover layer. (c) PMMA layer with a 120 μm deep microchannel. (d) Membrane and the PMMA layer presented at c) after hot-embossing procedure. Reproduced from Wang *et al.* [204], Copyright 2013, with permission from Elsevier.

membrane integration onto a standard glass-made chip. The methodology avoids membrane bending, leakages and short circuits, and it is time-effective. Preservation of the membrane's characteristics after on-chip embedding process is important. Any change in its morphology (e.g. pores distribution, tortuosity, etc) leads to different process performances.

In conclusion, a number of achievements in critical points of the gas-liquid microcontactor development process can be pointed out. Among them, the integration of herringbone structures with the purpose of lowering the pressure loss, as well as the concentration polarization. The on-chip integration of polymer membrane described by Wang *et al.* deserves attention since it can offer a solution to one of the challenges of the membrane-based microreactors, i.e., on-chip polymer membrane integration. More about the fabrication of the microfluidic membrane-based device may be found in the reviews of de Jong *et al.*, [56], Gerami *et al.*, [210] and more applications/design configurations are summarized in the review of Lam *et al.*, [184] and of Chen *et al.*, [211].

4.2.3. Development stages of a microreactor

Development stages of a microreactor are presented from two perspectives by Zhang *et al.*, [183] and Tsao [41] (see Fig. 4.2.2). The former proposed a methodology based on the evaluation of mixing, flow dynamics, and mass and heat transfer along with three strategies for scaling-up the microreactors. These strategies are parallel numbering-up, consecutive numbering-up, and scale-out (see Fig. 4.2.2, a). The latter proposed a three stages methodology to be considered for a proper development of a microreactor, with the focus on the microfabrication, bonding, and interfacing (see Fig. 4.2.2, b.). Considered together, these two strategies offer a complete development guideline.

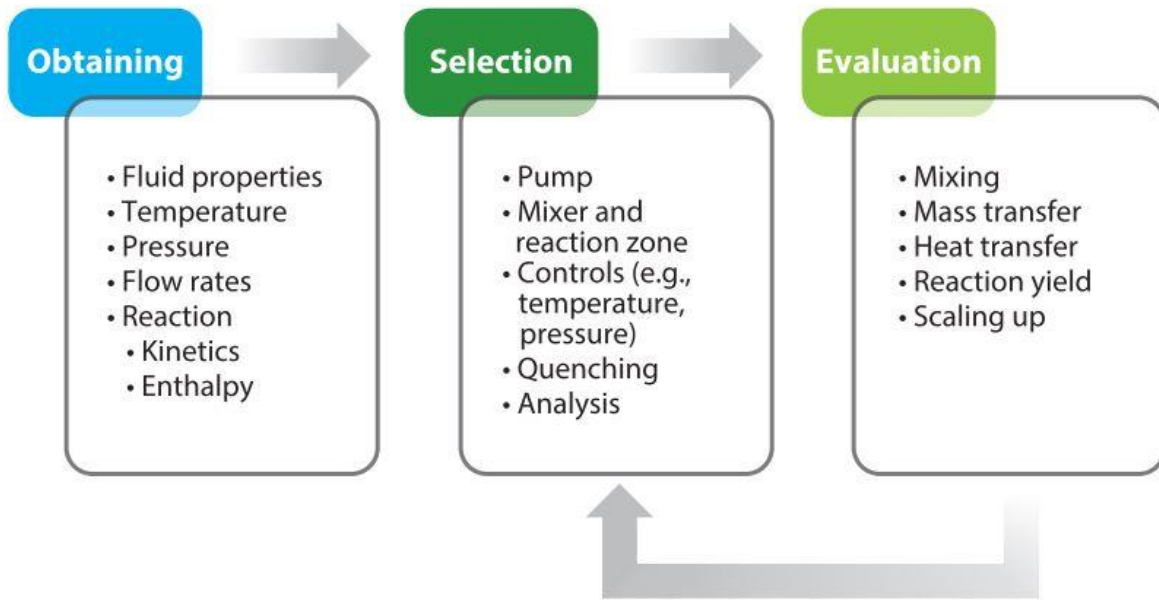
1st development stage: Microchannel design and material selection process

After acquiring in-depth knowledge of the analytical process to be integrated into the microreactor, the next steps are modeling and simulation of the convective-diffusion flow.

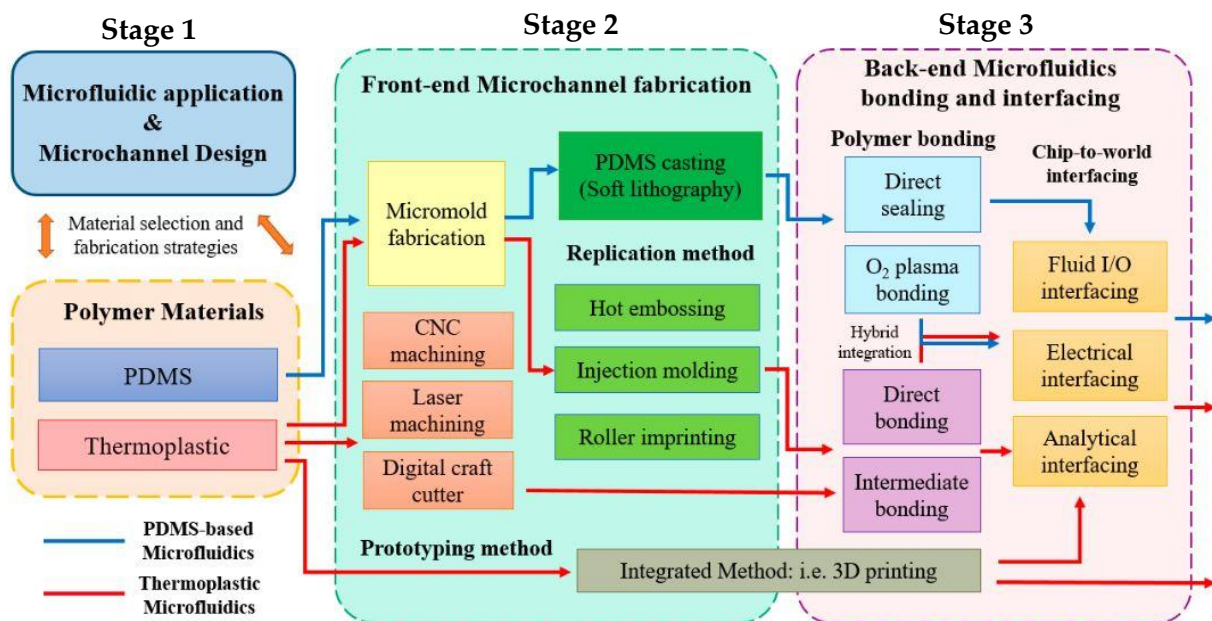
The modeling and simulation process aims to identify the suitable microfluidic channel design that will be further integrated into a physical device. The implementation process of the microfluidic channel network into a physical device cannot be done without considering the following criterion. The material in contact with the microfluidic streams has to be compatible with the microfluidic analytical process. In other words, mechanical properties, thermal property, solvent resistance, acid/base resistance, optical transmissivity, biocompatibility of the material have to be precisely known.

2nd development stage: Front-end microchannel fabrication

After selecting the suitable material, the fabrication strategy has to be selected. The microchannels can be fabricated either by rapid prototyping methods, or by replication methods.



(a)



(b)

Figure 4.2.2. (a) Designing steps of a microreactor by Zhao *et al.* [183] (b) Development stages of a polymer-made microreactors by Tsao [41]. The red line corresponds to the thermoplastic fabrication procedure, while the blue line corresponds to the PDMS fabrication procedure. (a) Reproduced from Zhao *et al.* [149], Copyright 2017, with permission from Annual Reviews, Inc. (b) Data from Tsao, (2016) [41] under Creative Commons 4.0 International license.

The rapid prototyping methods comprise computer numerical control (CNC) milling [42,212], laser ablation [213,214], and digital craft cutting [215,216]. These methods are mainly used by researchers for proving a concept. Mass production can be achieved through micro-mold- based fabrication methods such as hot embossing [217,218], and injection molding [219,220].

The following criteria when selecting the suitable microfabrication method for the material of choice should be kept in mind [42]:

- (1) Compatibility between the material and the fabrication method.
- (2) Capability to obtain the aimed features.
- (3) Quality of the obtained features.

State-of-the-art of the polymer microfluidic device fabrication is presented in some recent reviews from Scott *et al.*, [221], Reyes *et al.*, [222], Tsao *et al.*, [41].

CNC micro-milling is a relatively cost-effective technique used to rapidly prototype polymer-based microfluidic devices. The endmills available nowadays may go down to a 25 μm diameter or even smaller [42,221]. However, the lower the diameter, the slower the milling process and the lower milling depth are since, obviously, the endmills become very brittle at small diameters.

The surface roughness (Ra) resulting from milling process is in average 420 nm [42], with the lowest possible the author could find at 65 nm [221]. Roughness of the microchannels is a very important parameter since it can promote bubble formation or it can significantly influence the variation of the pressure drop. A procedure for Ra determination is detailed in Tsao *et al.*, [212] and Suriano *et al.*, [213]. Since the resulting Ra is not the optimum for microfluidic applications, a method based on solvent vapor has been developed to treat freshly milled surfaces in order to reduce the roughness resulting in surfaces with an improved optical quality.

According to Wenzel's condition for rough surfaces [42], roughness increases the hydrophobic behaviour ($\theta > 90^\circ$) if the polymer is naturally hydrophobic, or it increases the hydrophilicity if the surface is naturally hydrophilic ($\theta < 90^\circ$). Thus, for naturally hydrophilic polymers, the hydrophilicity is increased considering that the majority of the solvent solutions are aqueous.

The milling process does not affect the molecular orientation of the polymer chains, whereas this effect occurs during the hot embossing process. Changing the molecular orientation results in increased autofluorescence which is not suitable for optofluidic applications.

Laser ablation (LA) (or *excimer laser micromachining*) uses CO_2 lasers, femtosecond lasers [213], and recently more cost-effective diode lasers (the entire equipment price lower than 200 \$), which proved to be effective for PMMA microfluidic fabrication [223], in removing material from the polymer substrates in order to create features with dimensions smaller than 1 μm . In the case of polymers, the removal process is realized through photoablative decomposition [221]. The depth of the features depends on the laser pulse rate, the pulse power, and the polymer

characteristics [224]. Despite the intense research made on this topic, it is still difficult to determine the precise width and depth of a feature, because the influence played by the laser parameters and material properties are not clearly determined. This is stated in the latest review of the field by Ravi-Kumar *et al.*, [225]. However, this technique is advantageous when clean vertical cuts are primarily needed. LA is used in the fabrication process of high-performance photonic devices and in the fabrication process of micro-lenses. Among the common thermoplastics, PMMA is the most stable material for LA [213].

The PMMA degradation was found to be due to a thermal depolymerization process, while COP and PS suffer from oxidation and dehydrogenation. The average Ra of the laser ablated regions is 400 nm, with the lowest Ra at around 100 nm [221]. However, the Ra is considered high and not satisfactory by many researchers. Therefore, complementary techniques for improving the roughness have been developed [226]. The resolution in fast processing is also low. Depending on the laser used, the resolution varies between 20 μm and 100 μm [227].

Digital craft cutting for rapid prototyping has been demonstrated by Yuen and Goral, [215]. The minimum microchannel width achievable with this technique is 200 μm . Using this technique, functional microfluidic devices can possibly be fabricated using double-sided adhesive tape and laser printer transparency film. Although rapidity might be considered the main advantage of this technique, it still lacks accuracy and precision.

Hot embossing is a technique used especially for high-volume production, but it may be used as well for high-precision rapid prototyping. The minimum features achievable with this technique are 25 nm for the width and 100 nm for the depth [217]. The microchannels network to be imprinted on the polymer substrate is built as a negative on the mold. Molds are usually made by lithography from metals or silicon.

Generally, the entire process may be divided into three steps. (1) The polymer substrates are placed in between the molds, a vacuum environment is created, and afterwards the temperature is risen up or beyond the polymer glass temperature. (2) Once the desired temperature is obtained in the vacuum, a specific pressure is applied, whereas the negative features of the mold are transferred to the polymer substrates. (3) Before demolding the polymer substrates, the temperature of the environment is decreased below the glass transition temperature. For each microfluidics compatible polymer exists already well-established micro hot embossing technologies, as it can be checked in the works of Worgull [228], Hecke, and Schomburg [229].

Injection molding is already a mature technique, the method of choice when it comes to translation of proof-of-concepts into commercialized products [227]. The melted polymer is embossed under pressure inside a mold. There it is kept under pressure for a specific period of time. The temperature is decreased gradually below the glass transition temperature, while the material solidifies. In the end the molds are unclamped and the resulted structure is removed. A

fabrication cycle may last from a few seconds up to a few minutes [220]. Injection molding of PMMA-based microfluidics has been demonstrated by Ma *et al.*, [230].

In conclusion, micro-milling and hot-embossing are the micro-fabrication technologies reaching the lowest resolution. However, they are relative time-consuming, limiting mass-production. Although they are more rapid, the other methods existing suffer from poor resolution.

3rd development stage: Back-end microfluidics bonding and interfacing

After successful fabrication and validation of the microfluidic channel network, the following step is “closing and plugging up” the chip [231]. This step is maybe the most challenging. The limitations existing nowadays at this development stage inhibit the transition towards the widespread use of the microfluidic devices. Sealing methods used for polymer chip bonding include anodic bonding, fusion bonding, thermal bonding, solvent bonding, and surface chemical bonding.

4.3. Towards on-chip integration of the Hantzsch-reaction-based formaldehyde sensing. State-of-the art.

Up to the author’s knowledge, there is no attempt or work related to the on-chip integration of the continuous measurement of airborne HCHO based on the Hantzsch reaction and fluorescence sensing. However, some works related to on-chip optofluidic integration of HCHO detection in either food [232–234], Chinese herbs [235], or air [236] have been recently reported.

A microfluidic paper-based analytical device (μ PAD) was proposed by Guzman *et al.* [232] for detection of low HCHO concentrations in food. The detection was made using a CMOS camera. The concentration was found by interpreting the images based on RGB color analysis software on a smartphone. The detection mechanism worked offline and the HCHO detection range of the device was 0.2–2.5 mg/L. Improvements in terms of portability, response time, and detection range of 0–0.8 mg/L for this system was presented by Liu *et al.* [233].

Weng *et al.* [234] integrated four reaction reservoirs and one substrate reservoir on a PDMS microfluidic chip, enabling HCHO detection based on the absorption spectroscopy in 2 μ L food samples. A three-layer PMMA device with a detection range of 1–50 mg/L was presented by Liu *et al.* [235] for the detection of HCHO concentrations in Chinese herbs; it was based on laser-induced fluorescence.

A microfluidic lab-on-a-chip derivatization technique based on the GC-MS measurement technique for HCHO indoor air sensing was described by Pang *et al.* [236]. The method relied on a glass Pyrex microreactor with a 2.0 m long and 620 μ m internal diameter round microchannel as a reactor. The reaction of HCHO with two reagents (pentafluoro phenyl hydrazine and O-(2,3,4,5,6-pentafluorobenzyl) hydroxylamine) was studied in a microfluidic context, with the system achieving continuous sampling and analysis with a time resolution of 30 min and a LOD

down to $1.2 \mu\text{g}/\text{m}^3$ (1 ppb). The reagent flow rates were varied between 20 and 120 $\mu\text{L}/\text{min}$, while the maximum operating temperature and pressure were $T = 573 \text{ K}$ and $p = 3 \text{ MPa}$, respectively. Despite the evident advantages of low reactant flow rates, the operating parameters and the time resolution were too high to be compatible with the previously mentioned performances of a HCHO palm-held detector.

Becker *et al.* [6] developed a microfluidic analytical device ($20 \text{ cm} \times 25 \text{ cm} \times 15 \text{ cm}$) dedicated to air analysis based on the Hantzsch reaction, which reached a LOD of $0.13 \mu\text{g}/\text{m}^3$ (0.1 ppb) for a $17 \mu\text{L}/\text{min}$ reagent flow rate in a microporous tube (10.0 cm length, 0.9 mm internal diameter). The porous tube was placed in a gas microchamber where gaseous HCHO was streamed at a flow rate of 250 standard mL/min. The temporal resolution was two seconds and the response time was fifteen minutes, enabling near-real-time detection on a portable device. The system performance can possibly be enhanced by simplifying the fluorescence detection system based on a PMT detector and by reducing the interrogation volume.

4.4. Optofluidic detection concept

As it was described in Section 3.3., the HCHO detection method based on the Hantzsch reaction involves a continuous Fluoral-P reagent streaming that is put in contact with a continuous stream of air. Thus, it traps HCHO molecules and derivates them into DDL after a residence time of three minutes at $T = 338 \text{ K}$. Then, the presence of DDL molecules is quantified by fluorescence.

Considering the method presented above, a micro-total HCHO analysis system can be compartmented into the following interconnected units:

- (1) Auxiliary elements (i.e., fluidic reservoirs, micro-pumps, filters, humidity filters, heating elements, thermo-couplers, electrical and processing instruments).
- (2) HCHO separation unit.
- (3) HCHO derivatization unit.
- (4) Fluorescence detection unit.

Although the current project addressed the components in (2), (3), and (4) aiming to bring a contribution to the HCHO on-chip integration process, the target and the main focus were set on the fourth component, the fluorescence detection unit. The separation and derivatization components have been partially addressed solely due to the lack of time.

The work does not treat the other components usually involved in what is supposed to be a fully-operational μTAS , i.e., micro-pumps, filters, electrical, and processing elements, etc. The integration of these components within the optofluidic device towards a fully-operational $\mu\text{T-HCHO-AS}$ might be the topic of a separate research project due to the complexity of the issues involved and current technological limitations.

The initial aim of the project was to integrate an annular flow into a micro-chip, since the advantages of this type of gas-liquid interaction are obvious. However, it was decided to shift the research direction towards a gas-liquid interaction based on a hydrophobic porous membrane.

The literature review shed a light on the insufficient data and the complexity of the on-chip integration process of annular flow.

After browsing the last achievements in the fields of on-chip fluorescence sensing and membrane-based polymer microreactors, a concept design for a microstructure device has been proposed (see Fig. 4.4.1). Again, the trapping and derivatization units might be based on slug flows or annular flows in parallel studies. In this work, the trapping and derivatization units have been thought as a network of overlapping meandering channels with a hydrophobic membrane

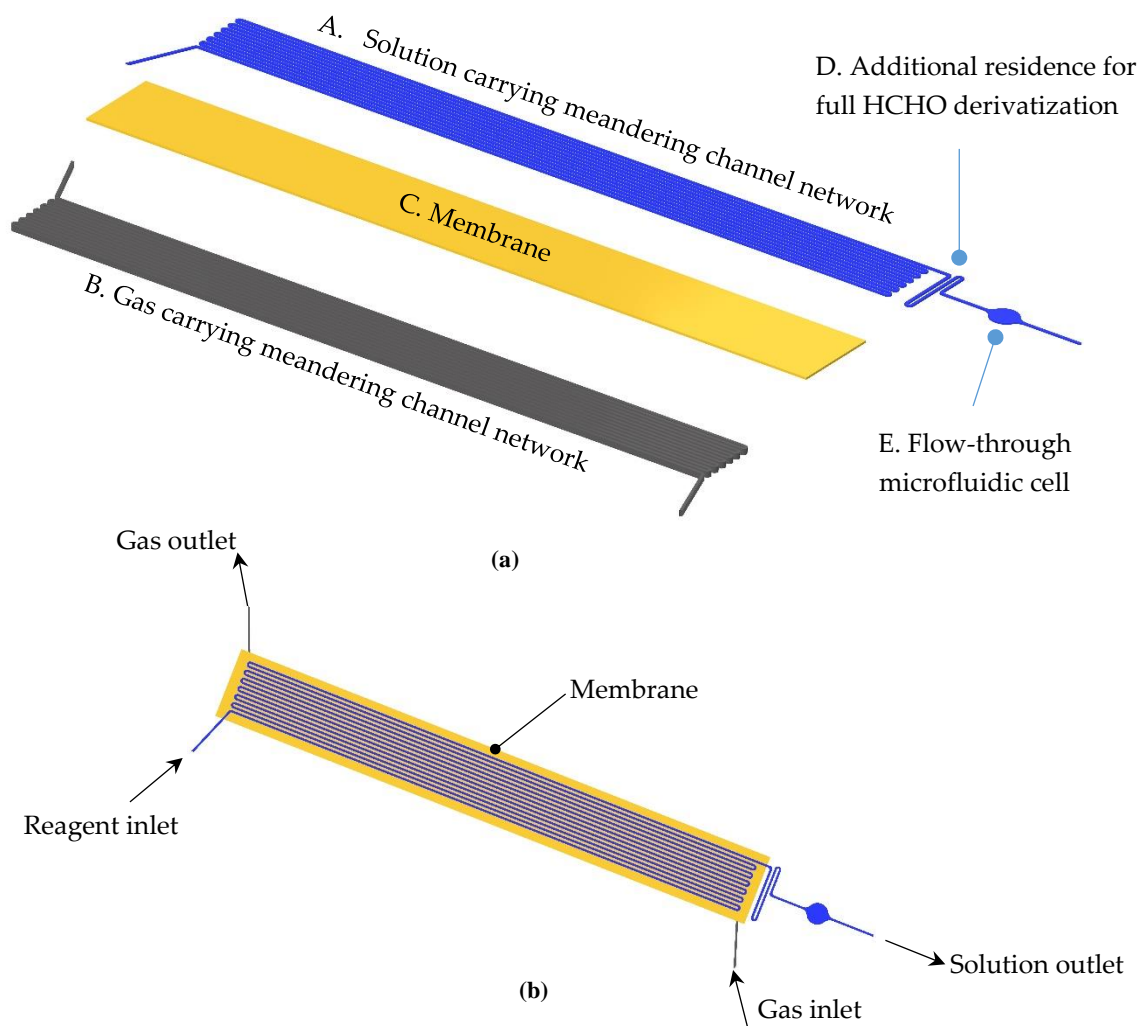


Figure 4.4.1. (a) Exploded view of the concept, where (A) – is the meandering microchannel carrying the reagent solution; (B) – is the meandering microchannel carrying the gas stream; (C) – is the hydrophobic membrane used to separate the gas and liquid phases, while allowing the HCHO diffusion from the gas-side towards the liquid-side; (D) – is a continuation of the reagent carrying microchannel placed in between the trapping region and (E) – the flow-through microfluidic cell to assure an optimal residence time of the last trapped HCHO molecules for a full derivatization process. (b) Top view, from the solution meandering channel network side.

placed in between and two heating foils supposed to heat up the fluids at the constant temperature, $T = 338\text{ K}$ (see Fig. 4.4.2). The suitable network configuration (length \times width \times height) has to be found after modelling the fluid hydrodynamics in both the gas (air) channel and the liquid (reagent) channel.

The fluorescence sensing device has been designed around a CMOS-image sensor. An orthogonal detection scheme with SU-8 photoresist as excitation light waveguide has been implemented. The flow-through microfluidic cell has been designed as a three-layer structure, but in two configurations (see Fig. 4.4.3).

For these laboratory investigations, trapping and derivatization has been assigned to a device, while the fluorescence sensing to another. Thus, the HCHO trapping and derivatization were assigned to a sub-system, named generically *Gas-Liquid Micro-Reactor*. The fluorescence detection system was assigned to a second sub-system, named *CMOS-based fluorescence detector*.

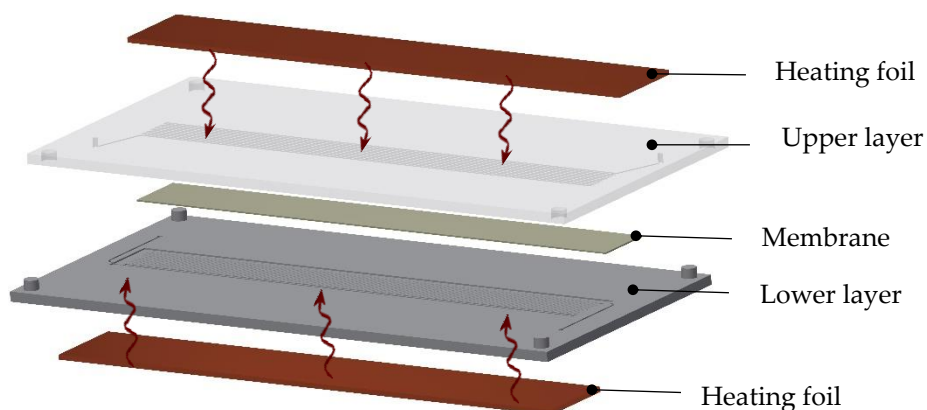


Figure 4.4.2. Concept of the trapping and derivatization assigned component (Gas-Liquid Microreactor).

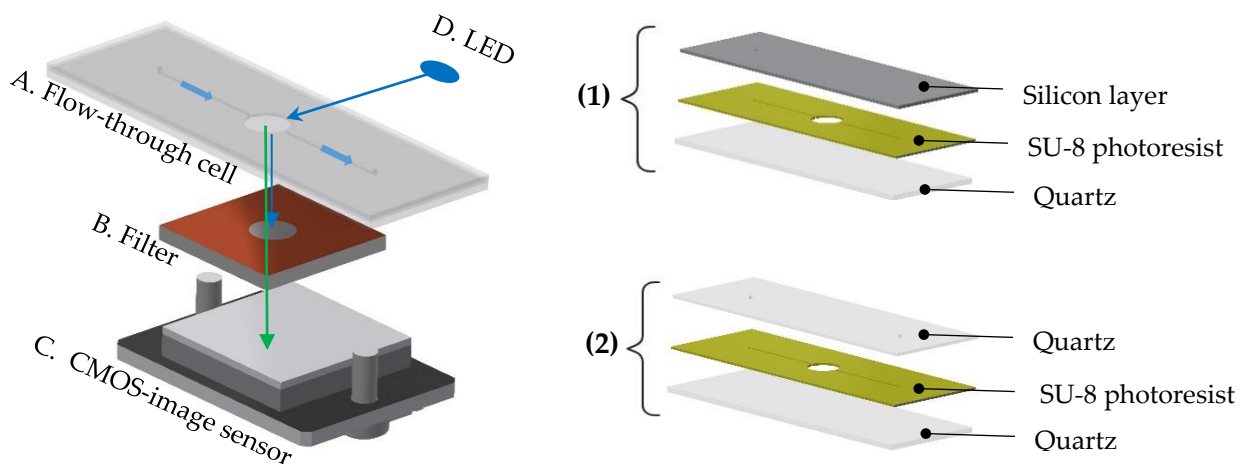


Figure 4.4.3. Concept of the fluorescence sensing system with (A) the three-layer flow-through microfluidic cell-made in two configurations (1) and (2), (B) the filter, (C) the CMOS-image sensor.

Chapter 5. CMOS-based fluorescence sensing device

This sub-chapter was written based on the following journal article published by the author in the *Micromachines Journal*:

Mariuta, D.; Govindaraji, A.; Colin, S.; Barrot, C.; Le Calvé, S.; Korvink, J.G.; Baldas, L.; Brandner, J.J. *Optofluidic Formaldehyde Sensing: Towards On-Chip Integration*. *Micromachines* 2020, 11, 673. <https://doi.org/10.3390/mi11070673>

5.1. Fabrication concept of the experimental device

The results of the literature survey presented in the previous section showed that fluorescence sensing miniaturization in optofluidic devices is a field currently experiencing intense research activity, aiming to identify fabrication and design methodologies for an ultraportable, monolithic, and multiplexing sensing architecture. Advances in micro- and nanofabrication technologies have been implemented to develop new design strategies in order to maximize the detection capability while shrinking dimensions.

Targeting similar objectives, this work introduces a new concept for sensing the presence of HCHO molecules in a microfluidic device, combining existing principles and components (see Fig. 5.1.1.). Although the functionality has been validated for a laboratory prototype made using mainly off-the-shelf components, it possesses the potential to be fully- integrated onto a

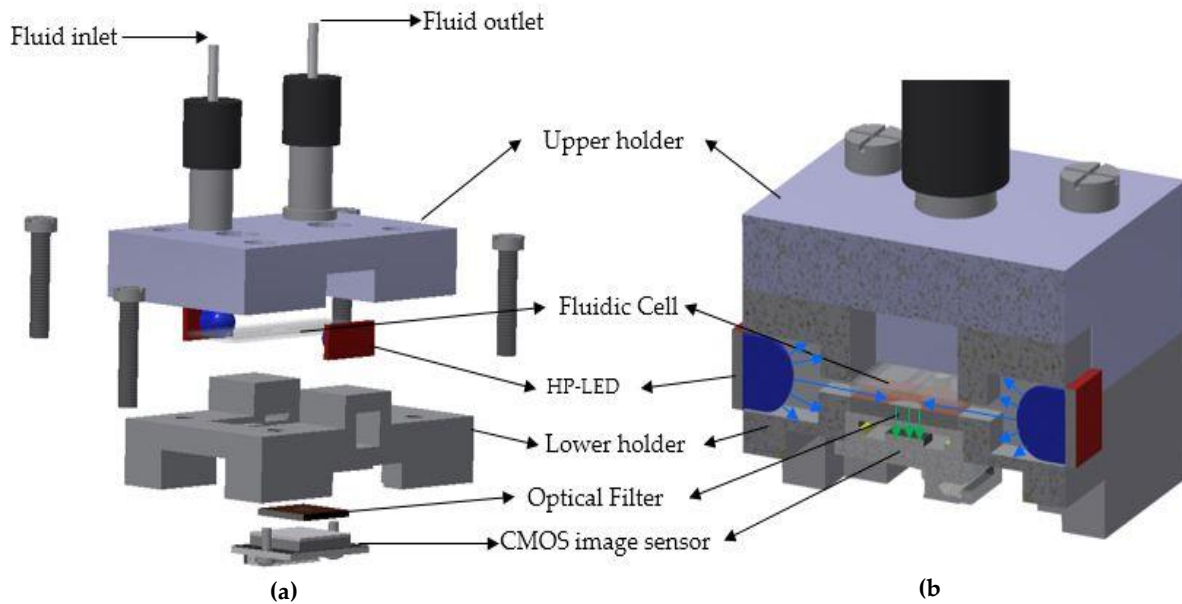


Figure 5.1.1. The concept of the CMOS-based fluorescence detector (46 mm × 30 mm × 10 mm). (a) Exploded view of the detector. (b) Transversal cross-section of the assembled sensing device.

monolithic structure, as it will be further explained. A couple of design particularities and material choices make this concept interesting and unique.

Firstly, the orthogonal illumination scheme has been implemented in combination with the contact sensing principle and a CMOS image sensor. The orthogonal scheme generally leads to a lower background noise without using complicated optical components. This is due to the fact that the excitation beam is not directly focused towards the photodetector, but oriented parallel to the photodetector. The excitation light reaching the detector is the consequence of the multiple reflections and scattering occurring in the interrogation chamber and surrounding claddings.

The orthogonal scheme has been implemented while respecting the contact sensing principle. Contact sensing means that the photodetector, the filtration component, and the flow-through microfluidic cell are all in contact [37]. This is advantageous since the optical path from the fluorescence source up to the photodetector is diminished, i.e., the optical loss is minimized.

Lab-on-a-CMOS is a research direction of the lab-on-a-chip field taking advantage of the superior capabilities achieved by the CMOS technology in terms of optical sensitivity and its capability to be integrated onto monolithically fabricated devices. In this work, the author does not claim to have developed such a system. However, he introduced a concept that has the potential to be further explored.

Secondly, the SU8-3050 epoxy negative photoresist, commonly used in the micro-fabrication and microelectronics fabrication processes, has been implemented as an inner core waveguide since it possesses very good optical transmittance at the excitation wavelength and a lower refraction index compared to the other materials selected (see Section 5.2.3.3.). The three-layer disposable microfluidic cell with a SU-8 3050 intermediate layer as waveguide, facilitates the implementation of the excitation source (LEDs) and the light detector (CMOS image sensor) into an orthogonal configuration.

Thirdly, the measurement of the fluorescence transmission efficiency has been realized in parallel for two flow-through microfluidic cells, one having the upper-layer made in a quartz / SU-8 3050 substrate and the other one in a Si / SiO₂ / SU-8 3050 substrate.

In order to achieve a miniaturized and efficient detection device, the author selected not only the ideal optical components, but also took in consideration the scientific perspective to study what is the difference in terms of optical signal gain produced by the two substrates.

To conclude, the implementation of the orthogonal scheme coupled to contact sensing has been made possible by developing a disposable three-layer microfluidic cell with an intermediate SU-8 3050 negative photoresist serving as waveguide for the excitation light transmission. Thus, while the lower layer (used for fluorescence transmission towards the photodetector) was made in quartz for both configurations, the upper-layer was made for the first configuration (1) in quartz / SU-8 3050 and for the second configuration (2) in Si / SiO₂ / SU-8 3050.

Configuration 1: quartz / SU-8 3050 layer – SU-8 3050 negative photoresist layer – quartz layer; referred also as the **quartz cell**.

- **Configuration 2:** Si / SiO₂ / SU-8 3050 – SU-8 3050 negative photoresist layer – quartz layer; referred also as the **silicon cell**.

5.2. Materials and methods

5.2.1. Microfluidic circuit

The microfluidic circuit assures the continuous flux of liquid reagent from the upstream reaction unit delivering time-dependent DDL molecular concentrations. At the inlet of the interrogation chamber, it is assumed that the chemical HCHO derivatization into DDL molecule has fully occurred.

The continuous analytical optical systems capture the signal from a volumetric space named interrogation chamber. The interrogation chamber may have different volumes and the intensity of the emission signal reaching the optical detector is proportional to this volume. Thus, the larger the interrogation volume is, the higher the emission signal. For portable continuous measuring systems, the interrogation volume should be the lowest possible since this feature enables high-portability and low-reagent consumption.

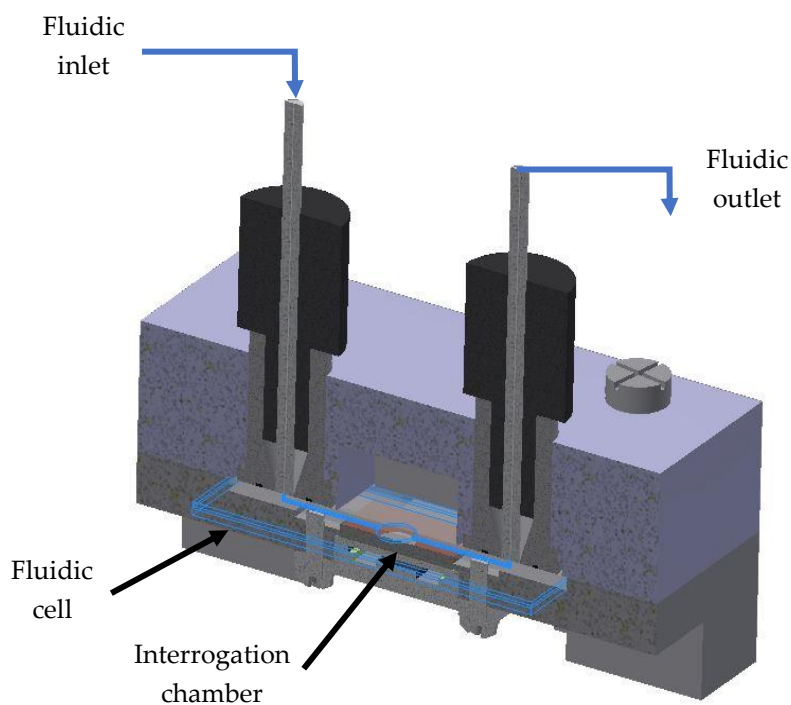


Figure 5.2.1. Longitudinal cross-section of the microfluidic circuit, in scale three-dimensional representation.

The lowest volume might be defined as the minimum interrogation volume from where the optical system could collect meaningful data. Thus, a compromise has to be found between the interrogation chamber volume and the LOD aimed.

A flow-through fluidic cell is designed properly when the fluid is evenly distributed and there are not stagnant or recirculation volumes at the flow rates of interest. Therefore, the replacement rate of the fluid located in the interrogation chamber is dependent on the volumetric flow rate at the inlet, Q_L , and the dimensional characteristics of the interrogation chamber.

The microfluidic circuit of the analytical system proposed in this work is simple (see Fig. 5.2.1.). The liquid reagent is supplied at a constant volumetric flow rate, Q_L , perpendicularly to the upper-layer surface of the flow-through cell. The upper-layer of the flow-through microfluidic cell has pyramidal shaped inlet and outlet, as described in Fig. 5.3.2. and 5.3.3. The inlet and outlet, placed at a $L = 20 \text{ mm}$ distance one by each other, are connected through a square longitudinal channel, $200 \mu\text{m} \times 200 \mu\text{m}$ cross section, located in the intermediate layer of the cell. The width component, D , of the interrogation chamber varies. Some different widths were considered resulting in different interrogation volumes (see Fig. 5.2.2.). To explain why, this has to be linked to the active area of the photodetector selected for this concept ($A = 4.8 \times 4.8 \text{ mm}^2$, see Section 5.2.2.3.) and the fact that the signal reading efficiency of the optical circuit is not known.

Experimental testing will start from larger interrogation volumes and go towards lower interrogation volumes since detection probability is higher at larger volumes. Therefore, for a more comprehensive study of the proposed sensing scheme capabilities, configurations with $D_1 = 4.7 \text{ mm}$, $D_2 = 3.0 \text{ mm}$, $D_3 = 1.5 \text{ mm}$ corresponding to $V_1 = 3.5 \mu\text{L}$, $V_2 = 1.4 \mu\text{L}$, and $V_3 = 0.35 \mu\text{L}$ have been proposed. A was arbitrarily chosen as the maximum possible area, that the interrogation chamber cross-section parallel to the surface of the photodetector might take. The depth/width ratios being quite large, it is quite probable to have recirculation zones and due to this reason a second configuration having three inlets has been created for each volume of reference V_1 , V_2 , V_3 . The cross-section of the inlets in the three-inlet configurations is $66 \mu\text{m} \times 200 \mu\text{m}$ (see Fig. 5.2.2. d, e, f, g, h, i).

Nevertheless, since this is a preliminary study trying to assess the capacity of the optical scheme to collect meaningful data from a volume of a fluid, the shape of the interrogation chamber might be further processed in the optimization step of the prototyping process. At this stage, it is important to have a uniformly-distributed flow in the interrogation chamber. Only respecting this condition, a valid evaluation of the device performance can be made. If the optical circuit proves to be efficient during the experimental campaign or after optimization, the interrogation chamber could be reduced to the $200 \mu\text{m} \times 200 \mu\text{m}$ straight channel itself or even lower.

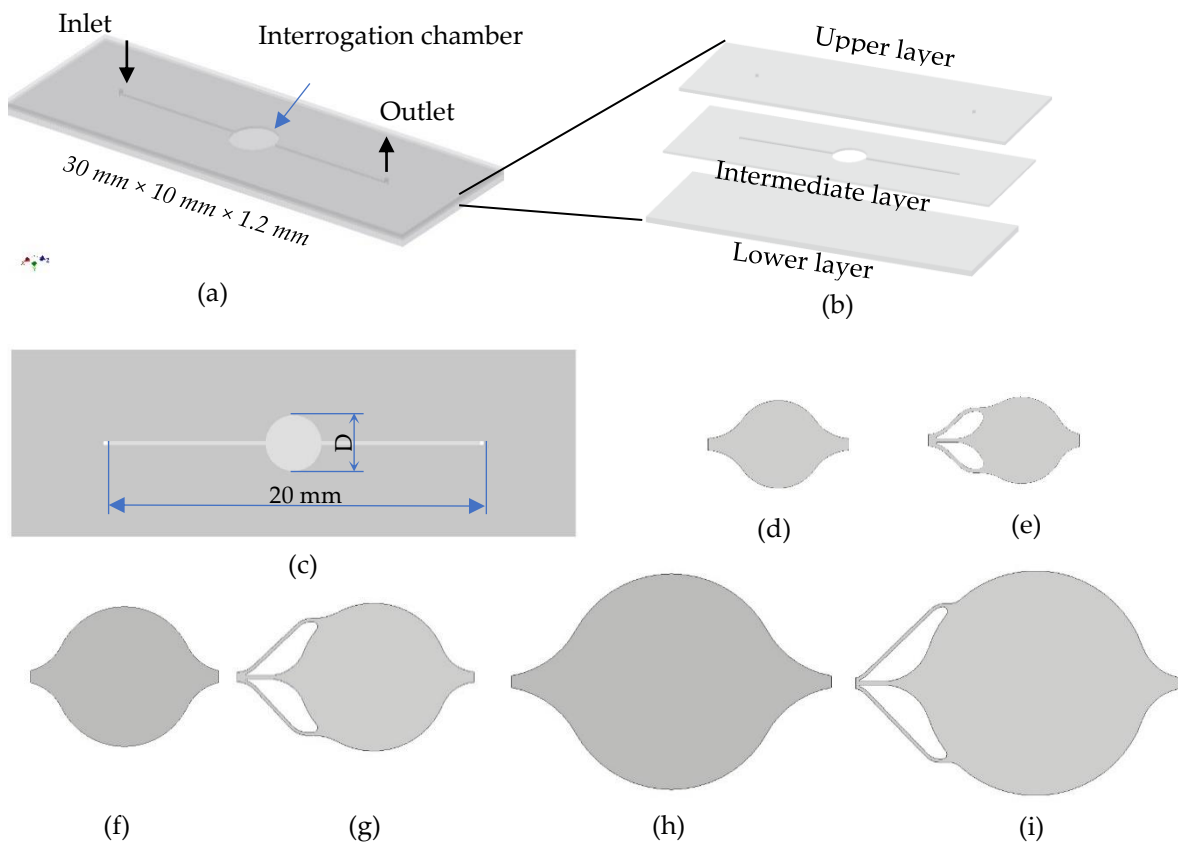


Figure 5.2.2. (a) Flow-through microfluidic cell concept. (b) Exploded view of the microfluidic cell with the microfluidic circuit grooved into the intermediate layer, while the inlet/outlet are etched perpendicular to the upper layer. (c) Generic representation of the intermediate layer concept with the length, $L = 20$ mm, and the interrogation chamber centered in between the inlet and the outlet. (d) $V_3 = 0.35 \mu\text{L}$ – one inlet configuration, with $D_3 = 1.5$ mm. (e) $V_3 = 0.35 \mu\text{L}$ – three inlets configuration, with $D_3 = 1.5$ mm. (f) $V_2 = 1.4 \mu\text{L}$ – one inlet configuration $D_2 = 3.0$ mm. (g) $V_2 = 1.4 \mu\text{L}$ – three inlets configuration $D_2 = 3.0$ mm. (h) $V_1 = 3.5 \mu\text{L}$ – one inlet configuration, $D_1 = 4.7$ mm. (i) $V_1 = 3.5 \mu\text{L}$ – three inlets configuration, $D_1 = 4.7$ mm.

5.2.1.1. Flow characterization in the interrogation chamber using a CFD tool

To verify whether recirculating volumes are formed inside the interrogation chamber, it is important to determine the residence time distribution (RTD) function, $E(t)$. Generally, the RTD function could be estimated through experimental methods (e.g., stimulus-response tracer experiments) and computational (e.g., computational fluid dynamics (CFD)) by introducing a tracer signal at the inlet and monitoring its concentration at the outlet. The tracer should have similar diffusive and transport properties as the fluid found in the system and be completely soluble in the mixture.

An ideal interrogation chamber is characterized by a plug flow, but the tracer concentration reaching the outlet is time-dependent in real flows and depends on the chamber shape. Inside an interrogation chamber affected by stagnant volumes, the photodetector captures the intensity of a signal that is a combination of a signal coming from the stagnant/recirculation volume and the fluid actually flowing through.

A CFD tool - Ansys Fluent® - has been used to estimate the flow distribution in the proposed interrogation chamber configurations. Two methods exist for solving the tracer species treated as a continuum by solving the transport equations: (1) species transport model and (2) user defined scalar (UDS) transport model.

Species transport model implies the tracer considered as species during the simulation process. The fluid flow (i.e., continuity and momentum equations) and the species transport equations are solved sequentially. The fluid flow equations are solved using a steady-state approach, while the species transport equation is solved based on a transient approach using the computed flow solution. There are two approaches used to estimate the RTD using the tracer analysis: (a) the pulse method and (b) the step method.

Therefore, to estimate the RTD characteristics for the configurations proposed in [Fig. 5.2.2.](#), the pulse method with the species transport model has been implemented. This method involves the injection of a rectangular impulse of a tracer at the inlet of the device at time $t = 0$. By injecting the tracer at time $t = 0$, its concentration, $c(t)$, is then monitored at the outlet as a function of time (see [Section 2.2.5.](#)).

CFD simulation and Boundary conditions

The simulations were performed in Fluent® 19.2 installed on x64 bit, Intel (R) Xeon (R) W-2123 CPU, 3.6 GHz, 32 GB RAM memory processor workstation. Quadrilateral elements were used in order to have as many as possible uniform elements on the mesh and finally leading to a more accurate solution. A mesh independence study has been carried out to determine the number of mesh elements necessary to obtain a mesh-independent solution until the difference between the mean residence times was lower than 1%.

Since it has been tested and observed that the difference between the three-dimensional (3-D) and the two-dimensional (2-D) simulation results are very low, the less time-demanding 2-D simulations have been performed to calculate mean residence time and residence time variance and to visualize the velocity streamlines in each configuration.

The Fluent® pressure-based solver was used for the simulations. The problem has been divided into six multiplied by three (eighteen) cases addressed in parallel. Thus, each out of the six configurations was tested at three flow rates in the range of interest: $Q_1 = 5 \mu\text{L} \cdot \text{min}^{-1}$, $Q_2 = 10 \mu\text{L} \cdot \text{min}^{-1}$, $Q_3 = 15 \mu\text{L} \cdot \text{min}^{-1}$ corresponding to $Re_1 = 0.46$, $Re_2 = 1.00$, and $Re_3 = 1.4$ respectively.

The uniform velocity profiles specified at the inlet as a velocity-inlet boundary conditions were calculated assuming the channel cross-section corresponding to a $200 \mu\text{m} \times 200 \mu\text{m}$ area for

the all the configurations simulated. The gauge static pressure at the outlet was set to zero, the operating pressure being set to $p_{atm} = 101\,325\text{ Pa}$, while the no-slip boundary condition was imposed at the walls.

In each of the eighteen cases, the convergence of the steady state fluid flows was firstly obtained. The model fluid is water since water is almost 99% of the reagent volumetric concentration. The density of water used was $\rho_{H_2O} = 998.2\text{ kg} \cdot \text{m}^{-3}$ and the viscosity was $\mu = 1.003 \times 10^{-3}\text{ Pa} \cdot \text{s}^{-1}$.

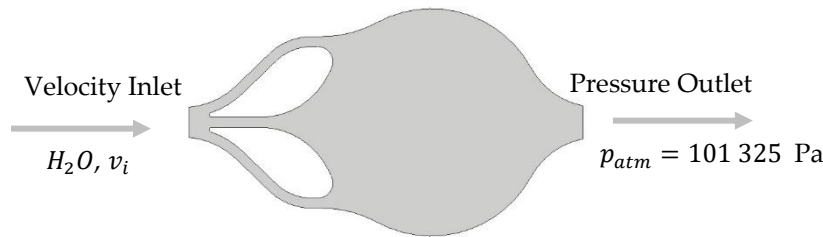


Figure 5.2.3. One of the geometrical configurations of interest and the computational domain.

Solution of species transport equations

After solving the flow equations and obtaining the converged solution, the flow equations were deactivated, while activating the tracer equation. The tracer mass fraction was settled to 1, the unsteady solution was calculated for one time step, then the mass fraction was settled back to 0 for the following time steps. The evolution of the area-weighted average concentration, $c(t)$, was monitored at the outlet as a function of time, t . The simulation ran for a not-defined number of time steps until the $c(t)$ was reaching the zero value.

The water-tracer diffusivity was settled at $D_{AB} = 1.5 \times 10^{-9}\text{ m}^2 \cdot \text{s}^{-1}$. To solve the equations describing the laminar mixing flow problem with minimized numerical diffusion, the least-square gradient scheme was implemented for spatial discretization with second order upwind schemes. The solution was considered convergent when: (1) the values of residuals were decreasing down to a constant level, in all the cases much below 10^{-10} ; (2) the function $E(t)$ obtained was respecting the Eq. 2.2.39. condition.

For the $V_1 = 3.5\ \mu\text{L}$ interrogation chamber - one inlet, it is obvious that the recirculation areas become larger and larger with the increase of the volumetric flow rate (see Fig. 5.2.4.). At each flow rate used, two symmetric vortices are formed. The center of the vortices is moving from the inlet towards the outlet when the volumetric flow rate is increased. Moreover, the recirculation areas almost occupied the entire surface at $Q_3 = 15\ \mu\text{L} \cdot \text{min}^{-1}$ ($Re_3 = 1.4$), excepting a center band with a width slightly larger than the inlet channel width ($200\ \mu\text{m}$) where the flow velocity is relatively very high. In the three-inlet configurations, the re-circulation areas decreased in size compared to their one-inlet counter-pair, but increased in number.

For the $V_2 = 1.4\ \mu\text{L}$ interrogation volume - one inlet, a similar behavior can be observed in terms of vortex formation as in $V_1 = 3.5\ \mu\text{L}$ - one inlet case. However, in this case, the vortices

areas are smaller relative to the surface of the chamber. Moreover, the center of the vortices moved towards the outlet with an increase in the volumetric flow rate, but with a shorter distance. This last behavior is further observed for the $V_1 = 0.35 \mu\text{L}$ interrogation chamber - one inlet. For this configuration it can be observed that the vortices formed for $Q_1 = 5 \mu\text{L} \cdot \text{min}^{-1}$ ($Re_1 = 0.46$) are small.

In [Table 5.2.1](#), it can be noticed that the mean residence times, \bar{t} , are larger for the three-inlet configurations compared to one-inlet configurations at similar flow rates in all the cases tested. Only two cases out of eighteen present streamlines with no re-circulation regions. It is the case of the $V_2 = 1.4 \mu\text{L}$ interrogation chamber, three-inlet configuration, at $Q_1 = 5 \mu\text{L} \cdot \text{min}^{-1}$ ($Re_1 = 0.46$) and the case of $V_3 = 0.35 \mu\text{L}$ interrogation chamber, three-inlet configuration, at $Q_1 = 5 \mu\text{L}/\text{min}$ ($Re_1 = 0.46$) (see [Fig. 5.2.6](#)).

Table 5.2.1. The mean residence times, \bar{t} , expressed in seconds, obtained by varying the number of inlets and the volumetric flow rates, Q , for each configuration.

Flow-through microfluidic cell configuration		Volumetric flow rate, Q ($\mu\text{L}/\text{min}$)		
		$Q_1 = 5$ ($Re_1 = 0.46$)	$Q_2 = 10$ ($Re_2 = 1.0$)	$Q_3 = 15$ ($Re_3 = 1.4$)
$V_1 = 3.5 \mu\text{L}$	One-inlet	36.3	18.9	12.7
	Three-inlets	41.5	21.38	14.2
$V_2 = 1.4 \mu\text{L}$	One-inlet	15.2	7.45	4.95
	Three-inlets	20.5	10.3	6.95
$V_3 = 0.35 \mu\text{L}$	One-inlet	5.08	2.66	1.82
	Three-inlets	5.65	2.77	1.88

Table 5.2.2. The variance, σ^2 , obtained by varying the number of inlets and the volumetric flow rates, Q , for each configuration.

Flow-through microfluidic cell configuration		Volumetric flow rate, Q ($\mu\text{L}/\text{min}$)		
		$Q_1 = 5$ ($Re_1 = 0.46$)	$Q_2 = 10$ ($Re_2 = 1.0$)	$Q_3 = 15$ ($Re_3 = 1.4$)
$V_1 = 3.5 \mu\text{L}$	One-inlet	1166.02	365.88	142.39
	Three-inlets	1579.29	464.62	156.62
$V_2 = 1.4 \mu\text{L}$	One-inlet	203.40	56.78	21.90
	Three-inlets	429.49	110.60	40.73
$V_3 = 0.35 \mu\text{L}$	One-inlet	22.19	6.48	2.71
	Three-inlets	30.17	7.10	2.88

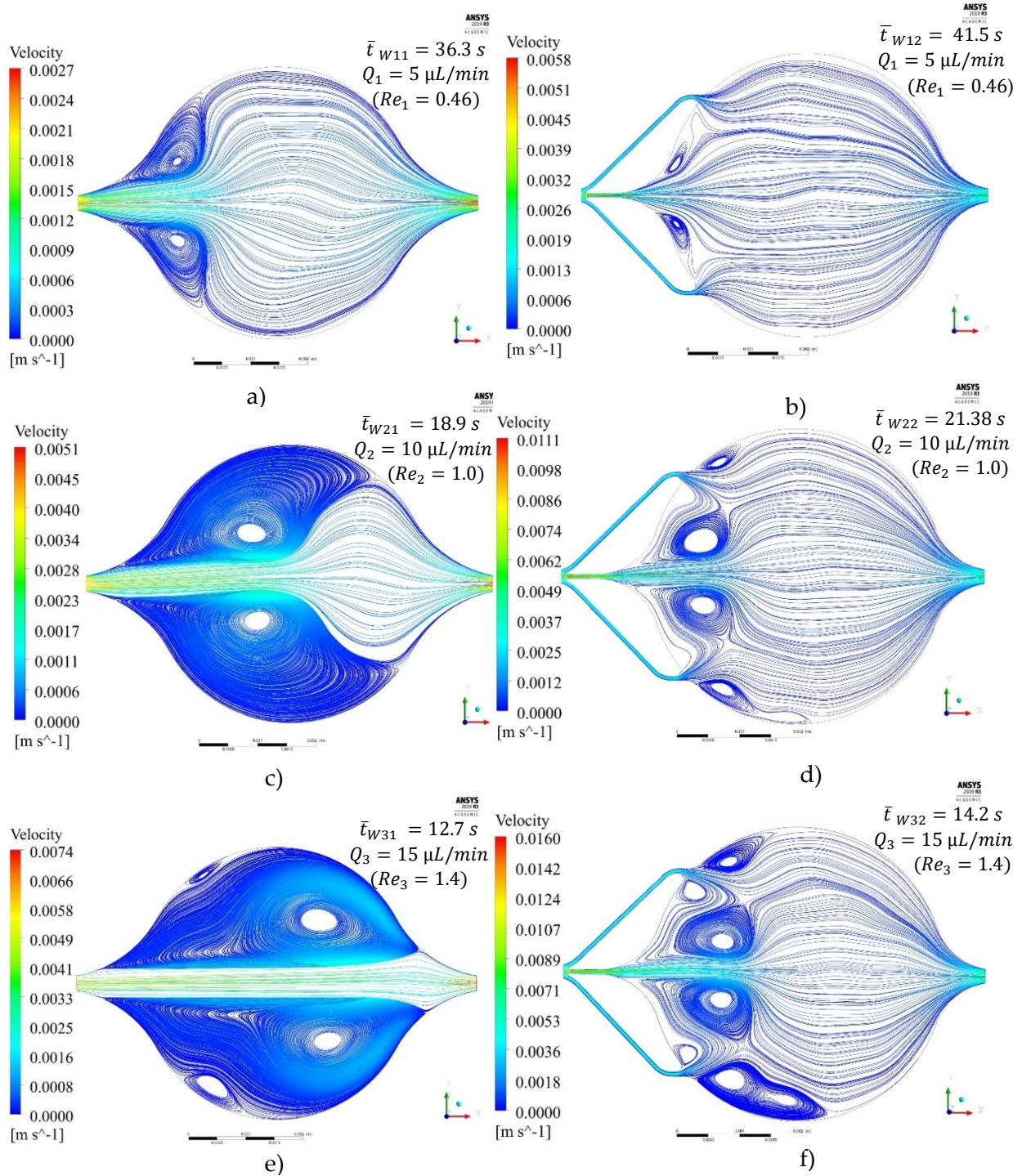


Figure 5.2.4. 2-D representation of the streamlines in the $V_1 = 3.5 \mu\text{L}$ volume interrogation chamber obtained for three volumetric flow rates at the inlet, V_i , for the one-inlet configuration (left side - a), c), and e)) and the three-inlets configuration (right-side - b), d). \bar{t} - represents the mean residence time obtained for each case.

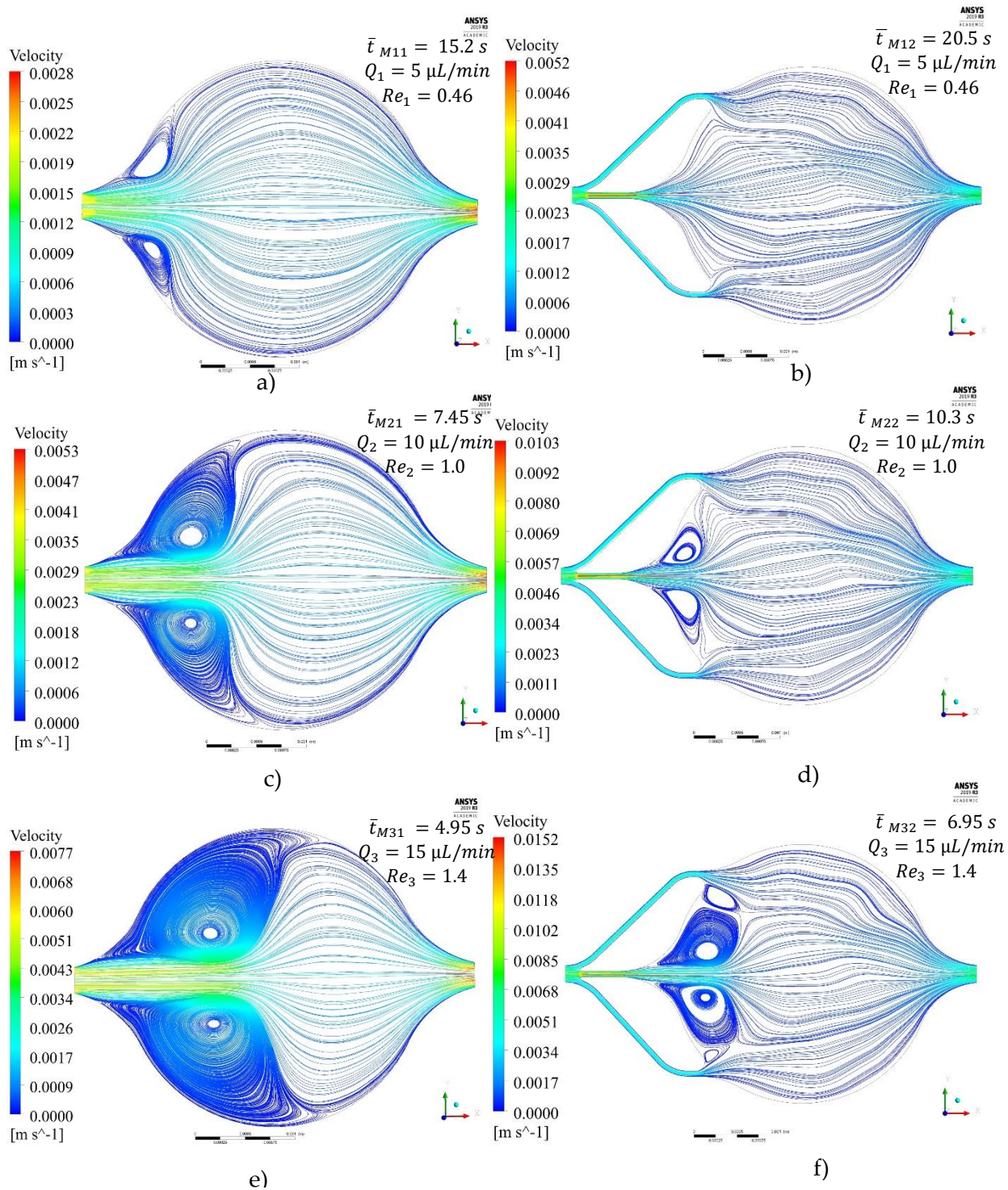


Figure 5.2.5. 2-D representation of the streamlines in the $V_2 = 1.4 \mu\text{L}$ volume interrogation chamber obtained for three volumetric flow rates at the inlet, V_i , for the one-inlet configuration (left side - a), c), and e) and the three-inlets configuration (right-side - b), d). \bar{t} - represents the mean residence time obtained for each case.

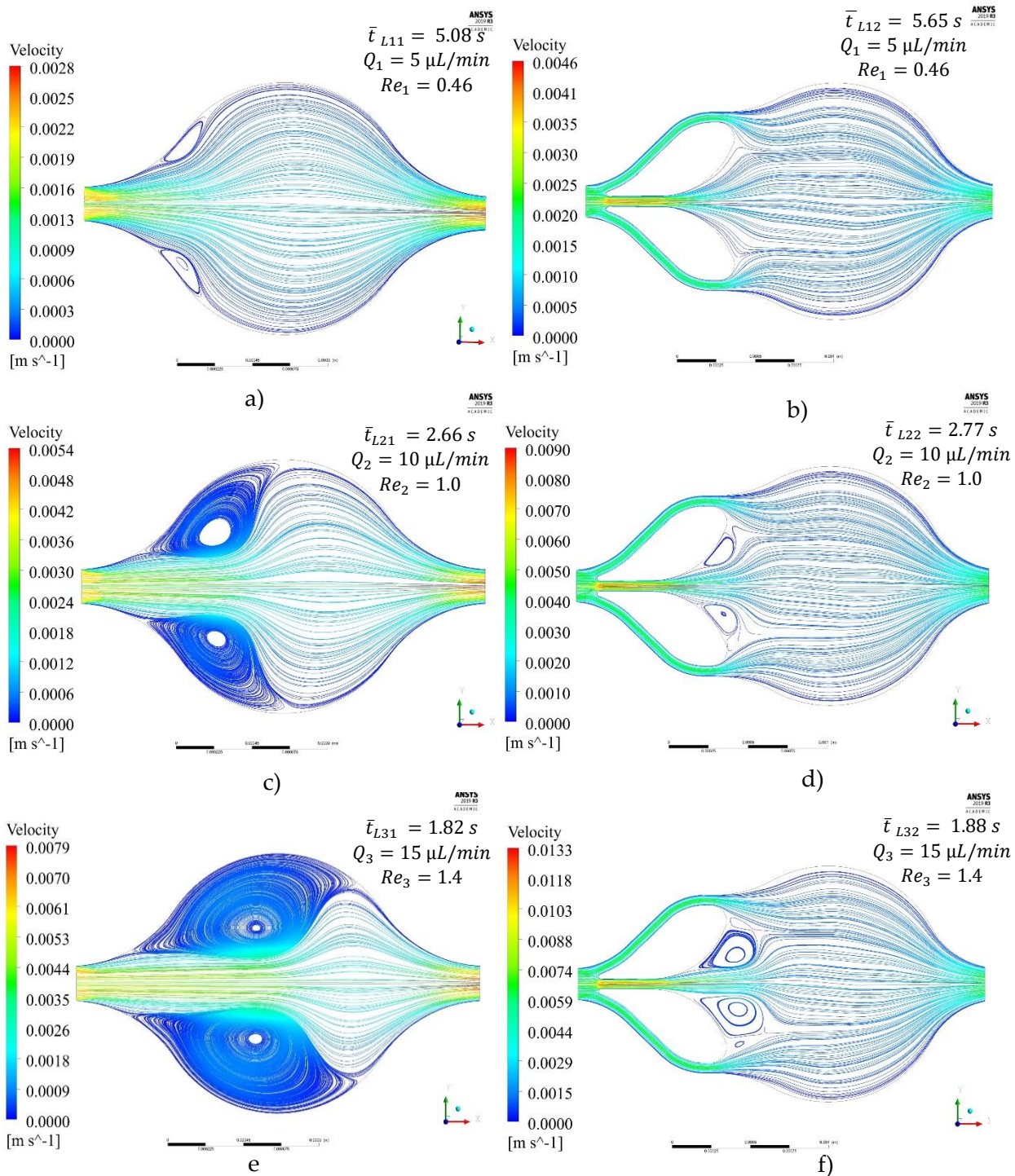


Figure 5.2.6. 2-D representation of the streamlines in the $V_3 = 0.35 \mu\text{L}$ volume interrogation chamber obtained for three volumetric flow rates at the inlet, V_i , for the one-inlet configuration (left side - a), c), and e)) and the three-inlets configuration (right-side - b), d). \bar{t} - represents the mean residence time obtained for each case.

Figs. 5.2.7. – 5.2.9. illustrate the RTD curves obtained from simulations. For all the cases studied, it can be observed in these figures that the amplitude of the concentration peaks at the outlet are higher for the one-inlet configurations when compared to the three-inlet configurations.

Therefore, by increasing the number of inlets, the $E(t)$ function amplitude was lower, while \bar{t} was higher (see Table 5.2.1.). This result was foreseeable since, by adding two inlets on either side of the central one, the volumetric flow rate in the central region from the inlet towards the outlet is reduced. At $Q_1 = 5 \mu L/min$, the right-side of the RTD curves needs more time to reach the zero value when compared to the $Q_2 = 10 \mu L/min$ and even more time when compared to the $Q_3 = 15 \mu L/min$. Instead, the peak amplitudes at this flow rate are always lower.

As it can be seen in the Fig. 5.2.7., which depicts the RTD curves for the $V_1 = 3.5 \mu L$ configuration, the tracer concentration reaches a maximum amplitude very quickly after the tracer injection, but it completely leaves the volume of fluid after different periods of time. For example, if for the one-inlet configuration, at $Q_3 = 15 \mu L/min$, it takes approximately $t = 85$ s for the last particle to leave the volume, for $Q_1 = 5 \mu L/min$ the time is approximately three times higher. Thus, it can be observed a proportionality relationship between the flow rate and the residence time.

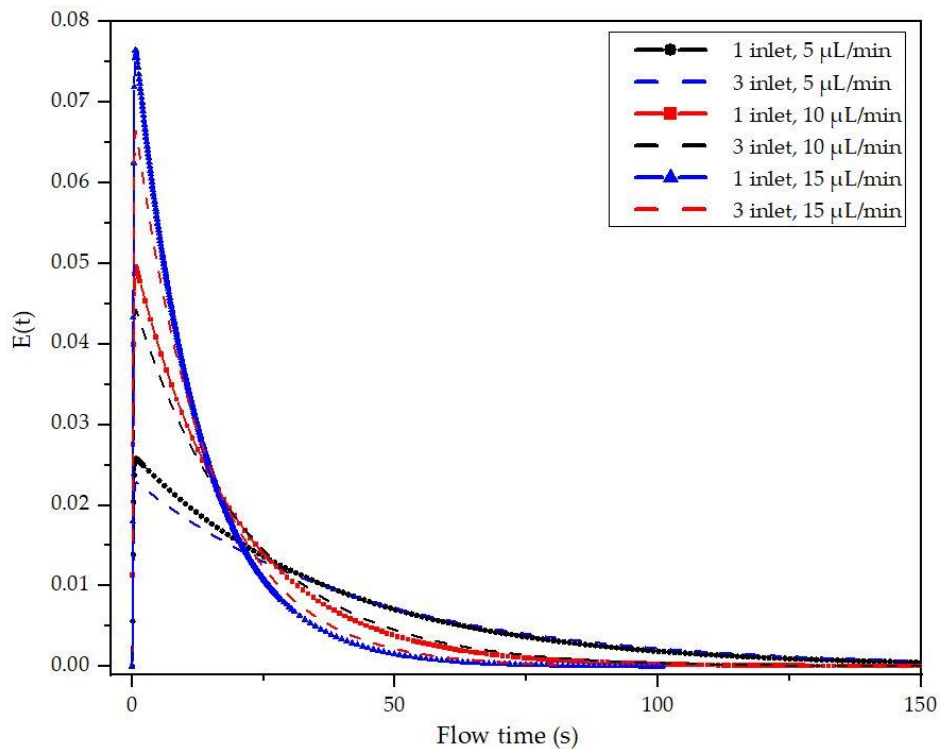


Figure 5.2.7. Residence time distribution curves for $V_1 = 3.5 \mu L$.

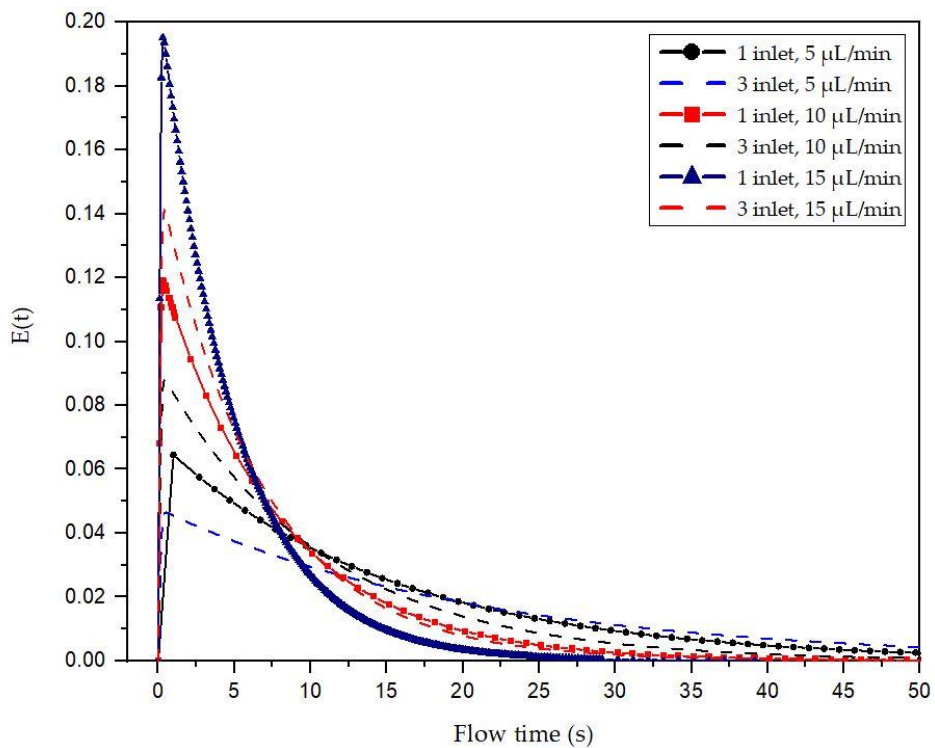


Figure 5.2.8. Residence time distribution curves for $V_2 = 1.4 \mu L$

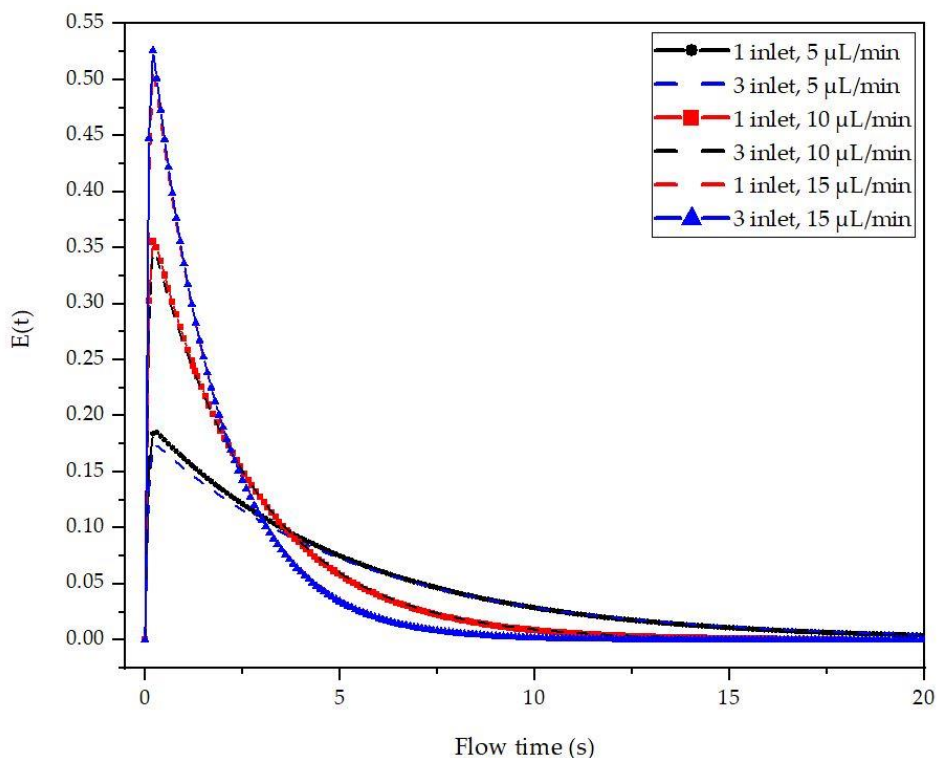


Figure 5.2.9. Residence time distribution curves for $V_3 = 0.35 \mu L$

The largest relative amplitude differences between the one-inlet - three-inlet configurations at similar volumetric flow rate can be observed for the $V_2 = 1.4 \mu\text{L}$ configuration (see Fig. 5.2.8.), while for the $V_3 = 0.35 \mu\text{L}$ case, the difference is the lowest (see Fig. 5.2.9.).

Moreover, in Table 5.2.2. can be noticed that for the $V_2 = 1.4 \mu\text{L}$ interrogation chamber, the variances doubles for the three-inlet configuration relative to the one-inlet configuration. In fact, it can be observed a correlation in terms of the amplitude magnitudes when single-inlet and multiple-inlet configurations are compared. At the same flow rate in a similar volume, the lower the amplitude magnitude difference is, the lower the variance difference (e.g., $V_3 = 0.35 \mu\text{L}$ case).

Overall, for each of the three configurations it can be observed that the mean residence time, \bar{t} , is larger when flow path is distributed along multiple inlets. Of course, this observation is made considering similar volumetric flow rate, Q .

The results of the CFD simulations show the importance of uniformly-mixed flow distribution in the interrogation chamber. Seen at a larger spectrum, these results have an impact on the sensitivity of the assay. If the time-dependent DDL concentration coming from upstream have relatively small variations lasting less than \bar{t} , it is very likely that these variations might not be precisely captured by the optical system.

In conclusion, the results obtained for the six configurations tested are far away from the ideal plug flow behavior. In order to assure the preliminary aim of the project - concept validation through experiments - the $V_1 = 3.5 \mu\text{L}$ interrogation chamber could be used only for static assays, e.g., the volume to be filled in only with one specific concentration. Only the three-inlets configuration of $V_2 = 1.4 \mu\text{L}$ interrogation chamber and both three-inlets - one-inlet configurations of the $V_3 = 0.35 \mu\text{L}$ interrogation chamber could be used for real-time continuous assays. This was concluded considering the mean residence times and variances obtained in simulations which influences the resolution of the continuous optical detector.

5.2.2. Optical circuit

The optical circuit of an optofluidic device is designed to control efficiently the light transfer. In fluorimeters, the light propagates through different media from the excitation source towards the fluorophores located in the interrogation chamber. After the fluorophore excitation, fluorescence emission propagates towards the photodetector, not before being (partially) filtered of the parasitic scattered light.

Among others, the performance of a fluorimeter is related to the light transmission efficiency of the optical circuit and to the photodetector characteristics. Light transmittance is a parameter that can be used to characterize optical losses of the two light beams of different wavelengths, i.e., the excitation beam and the emission beam.

Therefore, optical transmittance, T , of the excitation beam has to be maximized in its propagation towards the interrogation volume. On the other side, the optical loss due to absorbance and reflections of the excitation beam has to be minimized, if possible, to zero, in

order to reduce the optical noise reaching the photodetector surface. Moreover, if the fluorescence emission intensity can be amplified, ideally, this would result in an increased LOD of the sensor.

Consequently, the key in developing highly efficient devices is represented by the identification, selection, and interconnection of the suitable excitation light source, photodetector, filtration components, and materials used for fabrication.

The scheme selected to couple them is also particularly important to optimize the device performance. In this study, the optical circuit relies on two [excitation light sources](#), a [disposable flow-through microfluidic cell](#) (in two configurations, as described in Section 4.4.), a [bandpass filter](#), and a [monochromatic CMOS image sensor](#) as photodetector. Further, the selection and/or fabrication process of each component is individually addressed and the assembly design is detailed and justified.

5.2.2.1. Flow-through microfluidic cell integrating the SU-8 3050 optical waveguide

Two configurations of this element have been proposed, each of them presenting different advantages and drawbacks whose effects on the device have to be quantified.

In configuration 1 (see [Fig. 5.2.10.](#)), quartz (or fused silica, SiO_2) was selected due to its low autofluorescence emissions [31], this material being largely used for the fabrication of commercial flow-through fluidic cells. A 10 μm thick SU-8 3050 layer was used, as described in [Section 5.3.](#), due to microfabrication constraints. Since the refraction index of SU-8 3050 negative photoresist is higher than the surrounding cladding made in SiO_2 , the SU-8 3050 layer plays the role of a waveguide. SU-8 3050 negative photoresist has a transmittance of approximately $T_{SU-8\ 3050}(\lambda_{ex}) = 90\%$ at the excitation wavelength. Transmittance through SiO_2 is 100% at both excitation, λ_{ex} , and emission, λ_{em} , wavelengths.

In configuration 2 (see [Fig. 5.2.11.](#)), silicon has been used in the flow-through microfluidic cell fabrication process due to its optical characteristics. This material is widely used in the fabrication process of the chip technology; it possesses optical characteristics that makes it potentially appealing for the aim of the project.

The absorbance coefficients of silicon presented in the Handbook of Optical Materials [237] are $a(\lambda_{ex} = 420\ \text{nm}) = 5 \times 10^4\ \text{cm}^{-1}$ and $a(\lambda_{em} = 515\ \text{nm}) = 9.25 \times 10^3\ \text{cm}^{-1}$. In Aspnes and Studna [238], the absorption coefficients are $a(\lambda_{ex} = 420\ \text{nm}) = 7.1 \times 10^4\ \text{cm}^{-1}$, respectively $a(\lambda_{em} = 515\ \text{nm}) = 1.48 \times 10^4\ \text{cm}^{-1}$ for silicon with a $\langle 111 \rangle$ crystal orientation at room temperature. Thus, the absorption coefficient of silicon at the DDL molecule excitation wavelength, $\lambda_{ex} = 420\ \text{nm}$, is approximately five times higher than the absorption coefficient at the fluorescence emission wavelength, $\lambda_{em} = 515\ \text{nm}$. By consequence, the reflectivity of the excitation light, $\lambda_{ex} = 420\ \text{nm}$, seems to be higher than the reflectivity of the emission light, $\lambda_{em} = 515\ \text{nm}$.

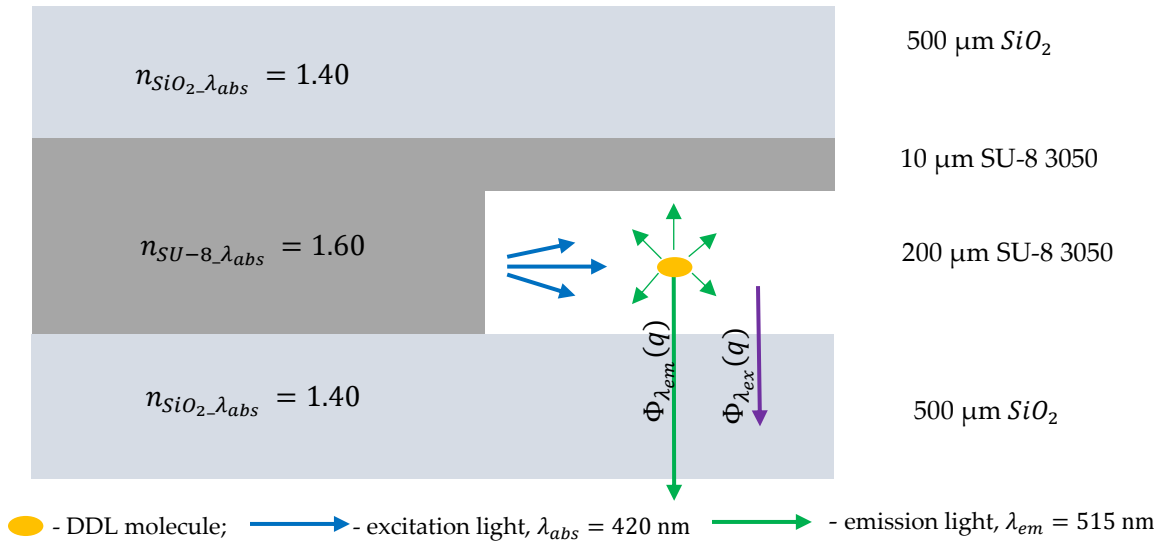


Figure 5.2.10. Two-dimensional representation of the configuration 1, where $\Phi_{\lambda_{em}}(q)$ and $\Phi_{\lambda_{ex}}(q)$ are the resultant intensity of the fluorescence emission, respectively of the excitation light perpendicular to the photodetector surface at the fluid-lower layer interface. Dimensions are not in scale.

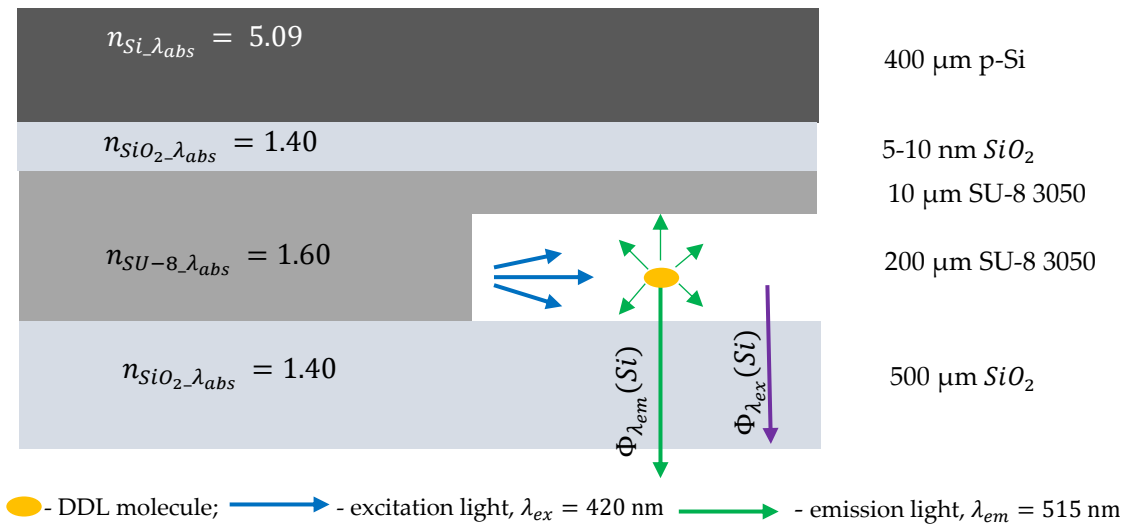


Figure 5.2. 11. Two-dimensional representation of the configuration 2, where $\Phi_{\lambda_{em}}(Si)$ and $\Phi_{\lambda_{ex}}(Si)$ are the resultant intensity of the fluorescence emission, respectively of the excitation light perpendicular to the photodetector surface at the fluid-lower layer interface. Dimensions are not in scale.

5.2.2.2. Excitation source

Solid-state light emitters with tunable properties and organic light emitting sources are embedded in devices aiming to monolithically integrate fluorescence detection on-chip [46], while high-power micro-lasers and LEDs are mainly used when modular and robust miniaturized fluorescence detectors are targeted.

The current LEDs available on the market are high-power and relatively cost-efficient. The main disadvantage of the LEDs when they are considered in optical sensing applications is related to the incoherence of the light beam, and here lasers perform better. LEDs are currently commercially-available in the 210–3800 nm spectral range, with their emission spectrum being compatible with the majority of the fluorophore's excitation bands.

For fluorescence-based detection, the excitation light source provides the energy at the specific frequency requested to excite the fluorophore of interest. Some parameters of the light source are of particular importance when fluorimeters are designed. Primarily, the excitation wavelength of the fluorophore should be taken into account. The light source has to possess a narrow bandwidth with the maximum peak very close (\pm few nanometers) to the excitation wavelength. The importance of the emission bandwidth is related to the background noise that the light source might introduce in the system. The narrowest bandwidth will result in the least noise.

Secondly, it should be assured that the selected light source can perform at the desired conditions for the constraints imposed by the application of the sensor. A couple of technical parameters such as the optical intensity, the beam coherence, emission angle, and the stability of the emission bandwidth are of great importance. As an example, a LED could produce large heat intensity values if used at high emission power which might cause a shift in the emission bandwidth and optical intensity. If not properly controlled during the prototyping stage, it might lead to flawed conclusions. The optical power range of the light source is selected by considering the fluorophore quantum yield and the detection sensitivity of the optical sensor.

DDL molecule has two absorption peaks: one in the ultra-violet (UV) range at $\lambda_{UV} = 255$ nm wavelength and the other in the visible spectrum range at $\lambda_{abs} = 412$ nm, while the fluorescence emission occurs at $\lambda_{em} = 515$ nm with a quantum yield $\phi = 0.005$ [22]. The $\lambda_{abs} = 412$ nm absorption peak was chosen for this prototype since the UV light sources are more health damaging and less efficient from the cost-perspective when compared to the violet light sources. Moreover, Fluoral-P reagent absorbs light in the UV spectrum and this would decrease the excitation light intensity reaching the fluorophores.

Therefore, a high-power light emitting diode (SMB1N-420H-02, Roithner Lasertechnik GmbH) with a maximum optical radiation power of $P_{LED} = 420$ mW at $\lambda_{ex} = 420$ nm emission wavelength, 22° viewing angle, and a maximum intensity concentrated at the center of its dispersion range was selected for this prototype. Two LEDs illuminate the detection chamber (see

Section 5.4.) to make sure that the excitation light penetrates entirely the bulk of the interrogation volume liquid.

5.2.2.3. Photodetector

Due to its large implementation in mobile industry, CMOS technology reached low fabrication prices, while its performance drastically increased within the last decade in terms of photon sensitivity, surpassing the benefits of the well-known photon detection technologies such as CCDs, PMTs, or more recently organic photodiodes. Moreover, the recent evolution of the CMOS technology introduced advantages, such as reduced dimensions, high sensitivity, coupled to filtration algorithms, low-power consumption, and integrated signal processing at low prices per unit, making it compatible with the goals aimed in the miniaturization of fluorescence detection.

On-chip integration of CMOS-based detectors for optofluidic applications is part of a relatively new field named lab-on-a-CMOS. Among the advantages introduced by this field, the following can be pointed out: the capability to develop monolithic optofluidic filterless devices using the well-established nanotechnology fabrication techniques or the capability to place the photodetector in contact with the detection volume by coating the surface of the CMOS photon sensors with thin filter layers. Therefore, it was decided to build the detection prototype based on a CMOS image sensor.

The CMOS image sensor (ULS24, Anitoa System LLC, USA) was selected as the photodetector for the current prototype, due to its ultra-low light sensitivity ($3 \cdot 10^{-6}$ lux), low-power consumption ($3.3 V / 1.8 V, 30 mW$), maximum sensitivity (60%) at $\lambda_{em} = 515 nm$ and minimum sensitivity (45%) at $\lambda_{ex} = 420 nm$ (see Fig. 5.2.12.). The CMOS image sensor (CIS) was fabricated on a $0.18 \mu m$ CIS technology with a die size of $4.8 \times 4.8 mm^2$. The CIS capabilities are enhanced by an algorithm implemented to diminish the dark current. This algorithm makes the

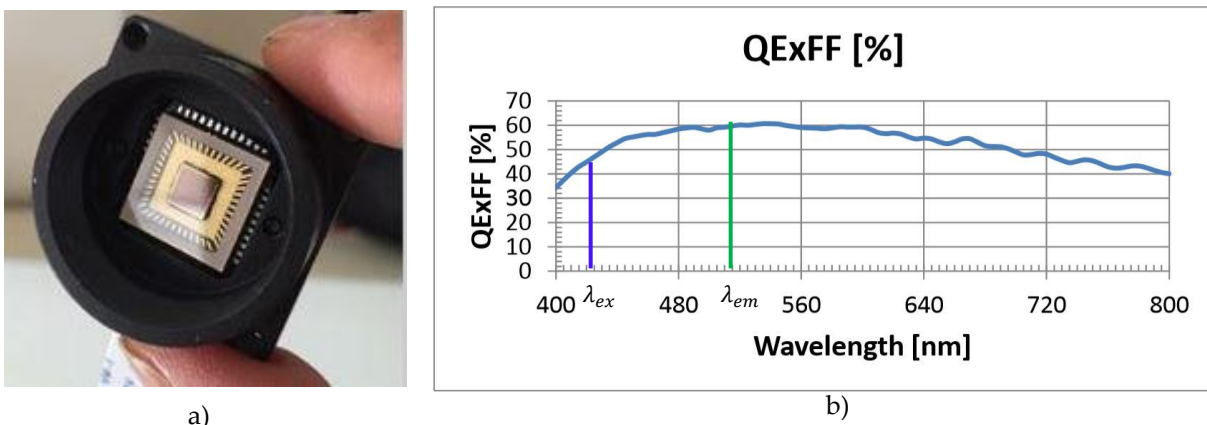


Figure 5.2.12. Sensitivity of ULS24 CMOS image sensor as the function of wavelength vs QExFF [239], where QE is quantum efficiency and FF is the fill factor.

image sensor capable to match the sensitivity of the cooled-CCD and PMT currently available on the market [240] (See Appendix A1. ULS24 ANITOA CMOS-image sensor Data Sheet).

5.2.2.4. Band-pass filter

The transmission efficiency of the 540 ± 60 nm bandpass filter (BP525-R10, 1 mm thickness, Midwest Optical Systems) was tested using a Perkin Lambda 950 UV/VIS spectrometer. It was found that the transmission efficiency was 0.0105% at the excitation wavelength and 90.5% at the emission wavelength (see Fig. 5.2.13.).

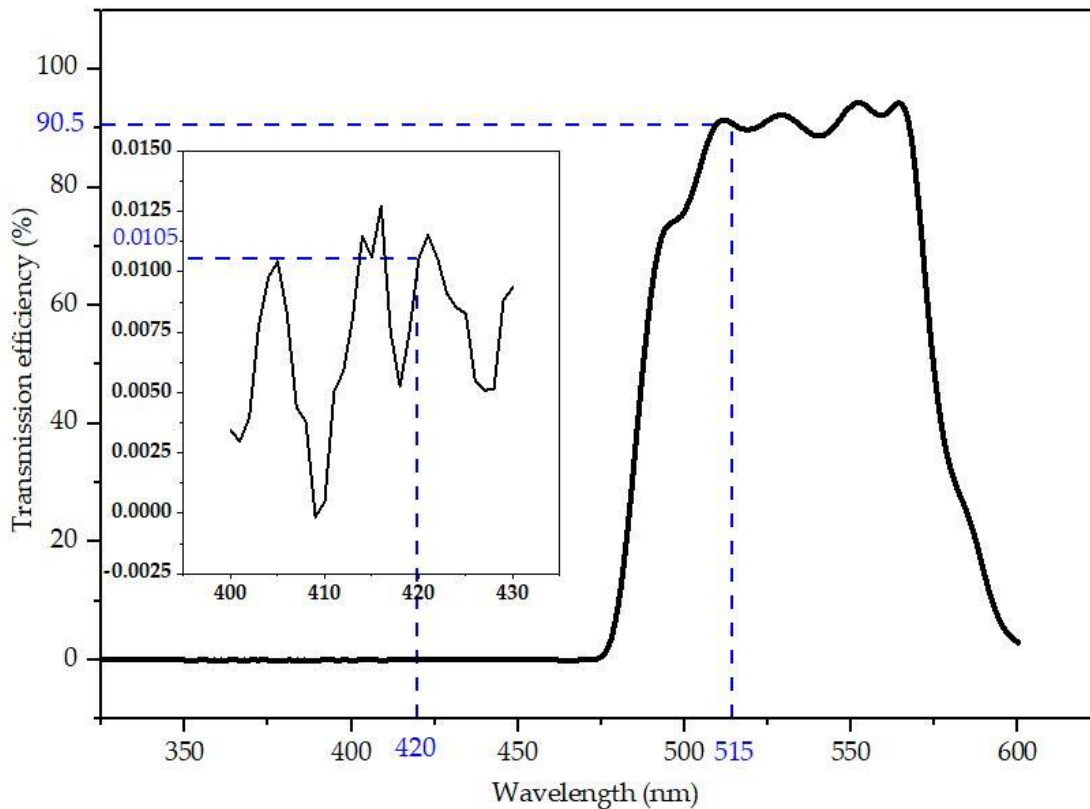


Figure 5.2.13. The optical transmittance of the bandpass filter measured with UV/VIS spectrometer at the emission wavelength, $\lambda_{em} = 515$ nm and at the excitation wavelength, $\lambda_{abs} = 420$ nm are $T_{\lambda_{em}} = 90.5\%$, respectively, $T_{\lambda_{abs}} = 0.0105\%$.

5.2.2.5. Optical circuit configuration

The two configurations of the optical circuit are presented in cross-section in Fig. 5.2.15. The figure presents a simplified description of the light optical transmission path through the SU-8 3050 optical waveguide towards the detection chamber and the optical detector. In its way towards the photodetector, both excitation and emission light suffer multiple optical phenomena that attenuate the light ray intensities.

$\mu_{\lambda_{em}}(q)$, $\mu_{\lambda_{ex}}(q)$, $\mu_{\lambda_{em}}(s)$, and $\mu_{\lambda_{ex}}(s)$ represent the attenuation coefficient of the fluorescence emission intensity for configuration 1, scattered excitation light for configuration 1, fluorescence emission intensity for configuration 2, respectively scattered excitation light for configuration 2 until each of them is digitally registered by the CMOS image sensor.

Each of the above-mentioned attenuation coefficient comprises the attenuation coefficient induced by the thin air layer between the flow-through microfluidic cell and the band-pass filter (caused by the mask - unknown), the attenuation coefficient induced by the band-pass filter, and the attenuation coefficients induced by the CMOS image sensor itself.

In conclusion, $\phi(q)$ and $\phi(s)$ represent the final optical gain obtained for the configuration 1 flow-through microfluidic cell, respectively configuration 2 flow-through microfluidic cell to be further characterized experimentally. As it can be observed in Fig. 5.2.14., $\phi(q)$ is the difference between the attenuated fluorescence intensity and the attenuated excitation light intensity reaching the surface of the CMOS image sensor for configuration 1 cell. $\phi(s)$ has a similar meaning, but for respectively configuration 2 cell.

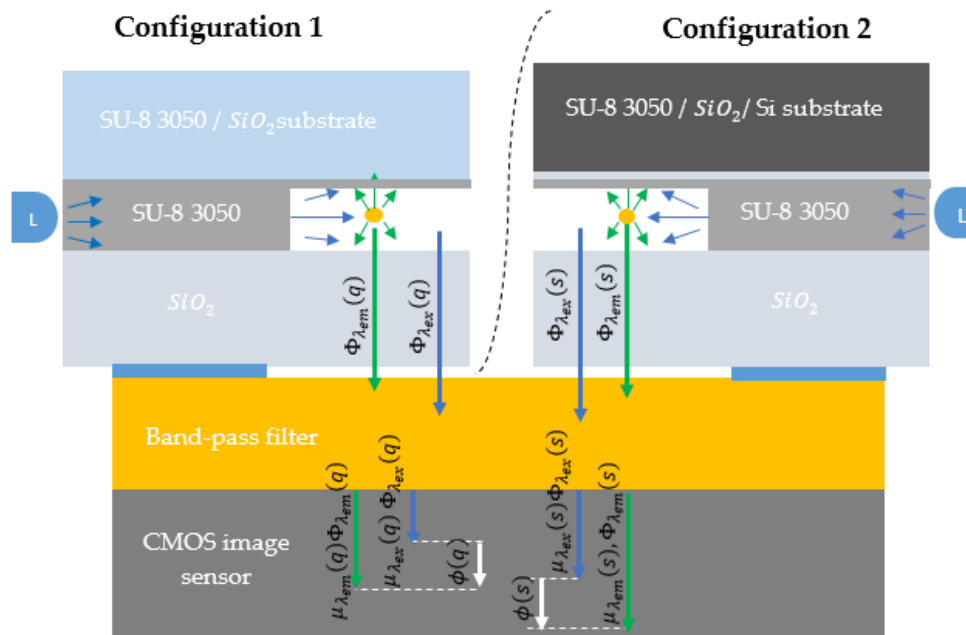


Figure 5.2.14. Representation of the two optical circuit configurations. L is the abbreviation for light-emitting diode. $\phi_{\lambda_{em}}(q)$ and $\phi_{\lambda_{ex}}(q)$ are the resultant intensities of the fluorescence emission, respectively of the excitation light scattered perpendicular to the photodetector surface at the fluid-lower layer (quartz) interface in configuration 1. Similarly, $\phi_{\lambda_{em}}(s)$ and $\phi_{\lambda_{ex}}(s)$ are the resultant intensities of the fluorescence emission, respectively of the excitation light scattered perpendicular to the photodetector surface at the fluid-lower layer (quartz) interface in configuration 2.

5.2.3. Materials, chemicals, and reagents

5.2.3.1. Silicon wafer

In the fabrication process of the configuration 2, named generically the silicon cell, it was used a 4-inch prime silicon CZ (Czochralski) wafer (Microchemicals GmbH, Ulm, Germany, P/N WSA40400250B8314SNN1) (see Fig. 5.2.15.). The silicon crystal orientation is $\langle 100 \rangle$. This wafer is boron doped (P-type), possessing a $\rho_{Si} = 8 - 12 \Omega \cdot cm$ resistivity. The total thickness variation (TTV) of the wafer is less than $10 \mu m$, while the maximum height difference between the center of the wafer and its edge (BOW) is less than $40 \mu m$. The side of the wafer in contact with the SU8-3050 waveguide is polished. The thickness of the silicon layer is $400 \mu m$.

The TTV and the tolerance of the wafer thickness are not negligible for an optical system. Nevertheless, the wafers characteristics are considered optimal to test the laboratory concept in this work. However, these relative tolerances may have an impact on the final read-out of the optical system and they might be more precisely controlled during the optimization stage, as discussed in Chapter 7.

5.2.3.2. Quartz wafer

The lower-layers of both cell configurations have been fabricated using AF 32[®] eco alkali-free flat glass manufactured by SCHOTT (see Fig. 5.2.15.). Eco-friendly means it was manufactured using refining agents instead of arsenic and antimony. The thickness of the quartz layer is around $500 \mu m$. The surface of the wafer is fire-polished generating low roughness. Furthermore, the thermal expansion coefficient of this quartz wafer is the same as that of silicon, making it compatible for optical packaging material in the semiconductor industry.



Figure 5.2.15. a) Prime CZ silicon wafer (Microchemicals GmbH, Ulm, Germany, P/N WSA40400250B8314SNN1). b) AF 32[®] eco alkali-free flat glass (Schott AG, Mainz, Germany).

5.2.3.3. SU-8 3050 epoxy negative photoresist

SU-8 3050 is an epoxy-based photoresist designed for micromachining and microelectronics applications. It is an improved version of the SU-8 and SU-8 2000 photoresists that have been widely used in the fabrication of MEMS devices, providing better adhesion and reduced coating stress. In addition, the viscosity allows for layer thicknesses between $4 \mu m$ and $120 \mu m$ in a single

coating process (Kayaku Advanced Materials, Westborough, MA, USA) (see Annexes for [Data Sheet and Optical Properties](#)).

5.2.3.4. Black PolyLactic Acid (PLA)

Black PolyLactic Acid (PLA) has been selected as the material used for 3D printing of the upper and lower holders. Black has been chosen due to the fact that it absorbs the excitation light, reducing the possible noise caused by not desired scattering / reflexions effects.

5.2.3.5. Preparation of DDL solutions

The Fluoral-P (0.01 M) was prepared by mixing 0.3 mL of acetic acid (100%, Merck, Molsheim, France), 0.2 mL of acetylacetone (99%, Merck), and 15.4 g of ammonium acetate (98%, Sigma-Aldrich, Lyon, France) in 200 mL Milli-Q water (18.2 M Ω · cm at 25°C, Millipore, Molsheim, France). The HCHO solutions ($C_1 = 20$ mg/L, $C_2 = 2$ mg/L, $C_3 = 0.2$ mg/L, $C_4 = 0.02$ mg/L) were prepared at ICPEES Strasbourg by mixing a commercial HCHO solution (37% in water, Sigma-Aldrich) with Mili-Q water (18.2 M Ω · cm at 25°C, Millipore). DDL solutions (0.01 mg/L, 0.1 mg/L, 1 mg/L, and 10 mg/L) were prepared by mixing Fluoral-P (0.02 M) and HCHO solutions (1:1 v/v), then placing it in the oven at $T = 338$ K for $t = 3$ min.

5.3. Fabrication and packaging

5.3.1. Upper and lower holders

After the computational aided design (CAD) models have been made in AutoCAD Inventor, the upper and the lower holders were 3D printed using a Ultimaker 3+ printing machine with 100 μ m precision (see [Fig. 5.3.1](#)). For the lower holder, a polyvinyl alcohol (PVA) has been used to sustain the multi-layer printing process. PVA was removed at the end of the printing process, being soluble in water (see Appendix A3. Technical drawing of the fluorescence detector lower holder and A4. Technical drawing of the fluorescence detector upper holder).

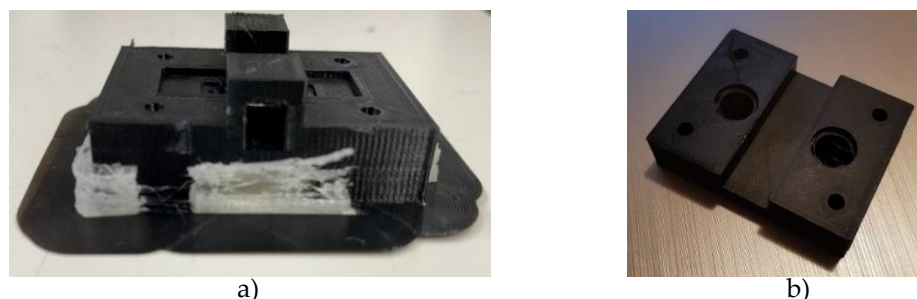


Figure 5.3.1. 3D printed lower holder with the PVA support structure.

5.3.2. Disposable flow-through microfluidic cell

The two configurations have been manufactured using similar procedures at the Laboratoire d'Analyse et d'Architecture des Systèmes (LAAS), Toulouse, France. The configuration 1, quartz fluidic cell, has been manufactured using 500 μ m thick AF32 quartz wafers (Schott AG, Mainz,

Germany). The wafers were initially cleaned with oxygen plasma ($P = 800 \text{ W}$, $t = 5 \text{ min}$). A $200 \mu\text{m}$ SU-8 3050 negative epoxy photoresist layer (Kayaku Advanced Materials, Westborough, MA, USA) was coated on one of the wafer side and baked using an EVG 120 machine (EVG, St. Florian am Inn, Austria). Afterwards, a mask was placed on top of the SU-8 3050 layer, allowing UV light exposure using a Suss MA6 gen4 instrument (SÜSS MICROTREC SE, Garching, Germany) ($\lambda = 365 \text{ nm}$, $t = 42 \text{ s}$, power density $P_d = 14 \text{ mW/cm}^2$) in order to create the desired channeling geometry of the intermediate layer, with a $200 \mu\text{m}$ width and $200 \mu\text{m}$ depth. The structure freshly manufactured was washed using an SU-8 developer to remove the exposed parts, then hard-baked ($T = 398 \text{ K}$, $t = 1 \text{ min}$). The fabrication masks necessary for SU-8 etching have been designed using QCAD software.

The fluidic inlet and outlet were created through a piercing process on the second $500 \mu\text{m}$ quartz wafer, after coating it with Photec 2040 dry film (Hitachi Chemical, Tokyo, Japan) to protect the structure during the piercing process. The piercing was done by sandblasting, followed by rinsing and cleaning with acetone and deionized water. An additional $10 \mu\text{m}$ SU-8 3050 negative photoresist layer was required on the lower side of the second wafer to facilitate the bonding with the SU-8 3050 layer from the first wafer. Once this layer was coated, the two freshly created structures were bonded using Nanonex NX Nanoimprint equipment (Nanonex, Monmouth Junction, NJ, USA) by applying uniform pressure on both sides. An AZ 4562 photoresist dicing protection layer (Microchemicals GmbH, Ulm, Germany) was coated in order to facilitate a smooth dicing process (see Fig. 5.3.2.).

In the making process of the lower-layer (quartz wafer / $200 \mu\text{m}$ SU-8 3050) of the silicon cell (configuration 2) the same fabrication procedure as in the quartz cell (configuration 1) is applied. The silicon wafer was coated instead with a 100 nm Si_3N_4 layer to facilitate the KOH etching process of the inlet and outlet. Due to the KOH etching features, the inlet and outlet had a pyramidal shape with the base upwards. The same thin SU-8 3050 layer was coated on the lower side of the Si-wafer to support the bonding process with the quartz wafer / $200 \mu\text{m}$ SU-8 3050 previously manufactured structure. For bonding the two separate manufactured structures, similar procedure as in the configuration 1 was implemented (see Fig. 5.3.3.).

Flow-through microfluidic cells have been obtained at the end of the process, but a part of them presented some cracks into the structure. Fig. 5.3.4. show images of a configuration 1 and 2 manufactured cells together with the microscope view of their cross-sections. The thickness of the layers has been measured and it was found that the SU-8 3050 layer was $20 \mu\text{m}$ thicker than expected due to some fabrication errors.

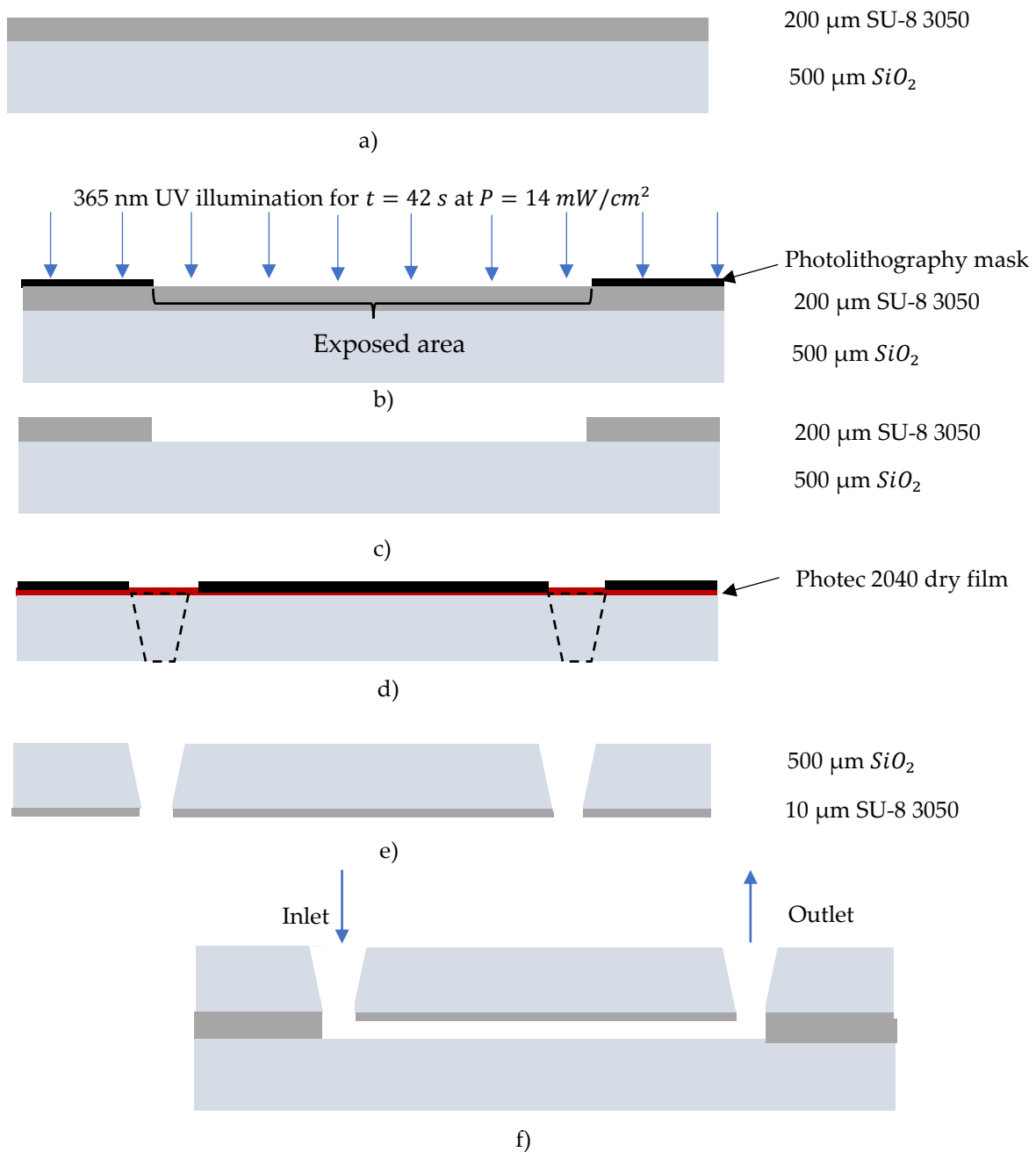


Figure 5.3.2. Manufacturing process of the configuration 1 flow-through microfluidic cell. a) SU-8 3050 layer deposition on the quartz layer. b) UV photo-illumination using a photolithography mask for making the fluidic channeling of the intermediate layer. c) SU-8 developer and rinsing to remove the exposed part. d) After coating the Photec 2040 dicing protective film, the inlet and outlets have been created through sand blasting. e) A few micrometers SU-8 3050 layer has been coated on the lower layer of the freshly pierced quartz wafer. f) Longitudinal section of the final structure obtained after bonding the structure obtained at step c) and the structure obtained at step e).

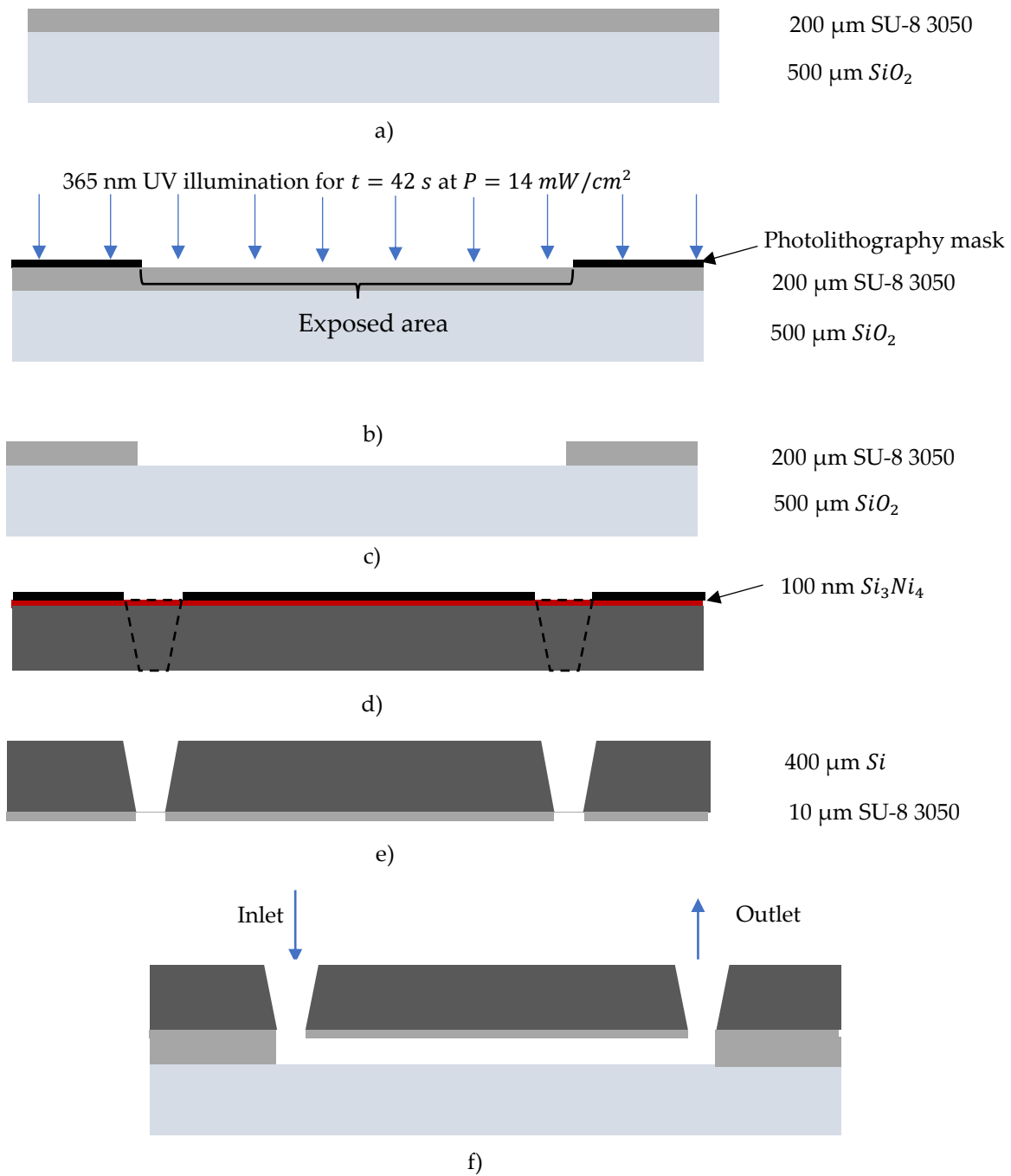


Figure 5.3. 3. Manufacturing process of the configuration 2 flow-through microfluidic. a) SU-8 3050 layer deposition on the quartz layer. b) UV photo-illumination using a photolithography mask for making the fluidic channeling of the intermediate layer. c) SU-8 developer and rinsing to remove the exposed part. d) After coating the 100 nm Si_3Ni_4 protective film, the inlet and outlets have been created through KOH etching. e) A few micrometers SU-8 3050 layer has been coated on the lower layer of the freshly etched Si-wafer. f) Longitudinal section of the final structure obtained after bonding the structure obtained at step c) and the structure obtained at step e).

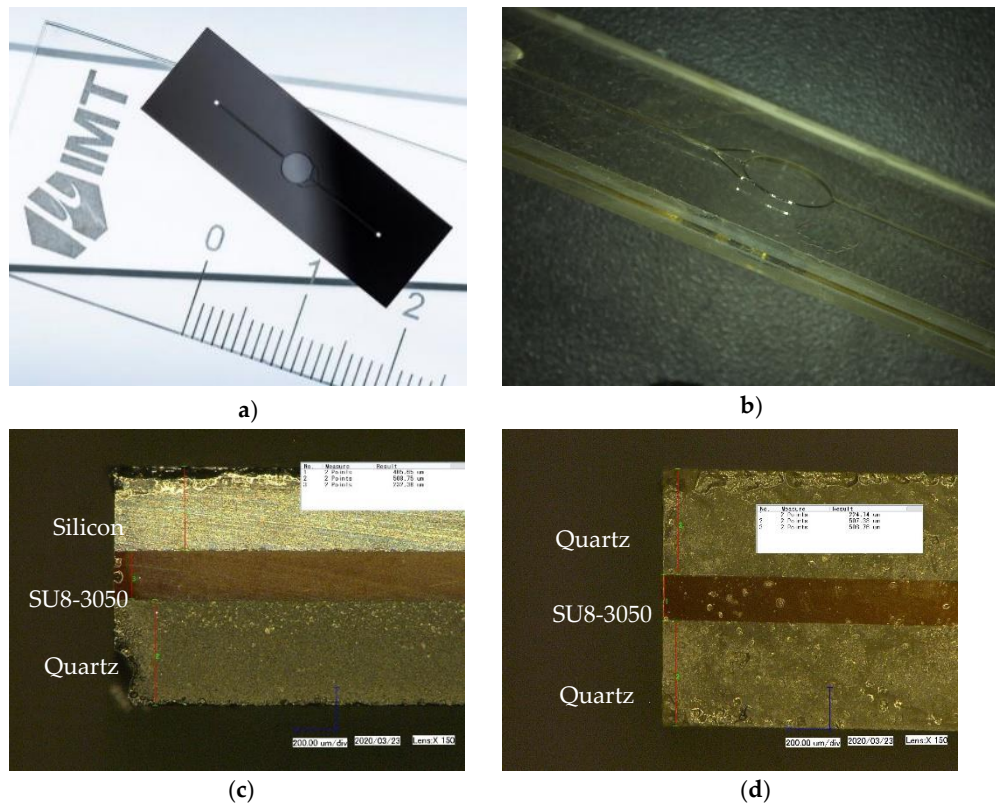


Figure 5.3. 4. (a) Flow-through microfluidic cell of 1.41 μL silicon – three inlets. (b) Microfluidic cell of 1.41 μL quartz – three inlets. (c) Microscope view of silicon (405 μm)–SU-8 3050 (232 μm)–quartz (508 μm) fluidic cell cross-section. (d) Microscope view of quartz (507 μm)–SU-8 3050 (224 μm)–quartz (508 μm) fluidic cell cross-section.

5.3.3. Packaging

Packaging refers to the procedures applied to integrate all the fabricated or selected components during the prototyping process (see all the steps described in Fig. 5.3.5.). The components that are packed into the device ready to be experimentally tested are: the upper and the lower holders, four screws, two LEDs, one CMOS image sensor, a band-pass filter, a photonic mask, the flow-through microfluidic cell, the fluidic connectors, and the fluidic capillaries.

The LEDs were soldered on a thin copper plate playing the role of a heat sink for the short period of time when the LED will be activated. Therefore, they have been introduced in the pockets specially created into the upper holders' structure. The pocket of the LED has slightly larger dimensions at the entrance. At the opposite side, the pocket ends with a circular slit that

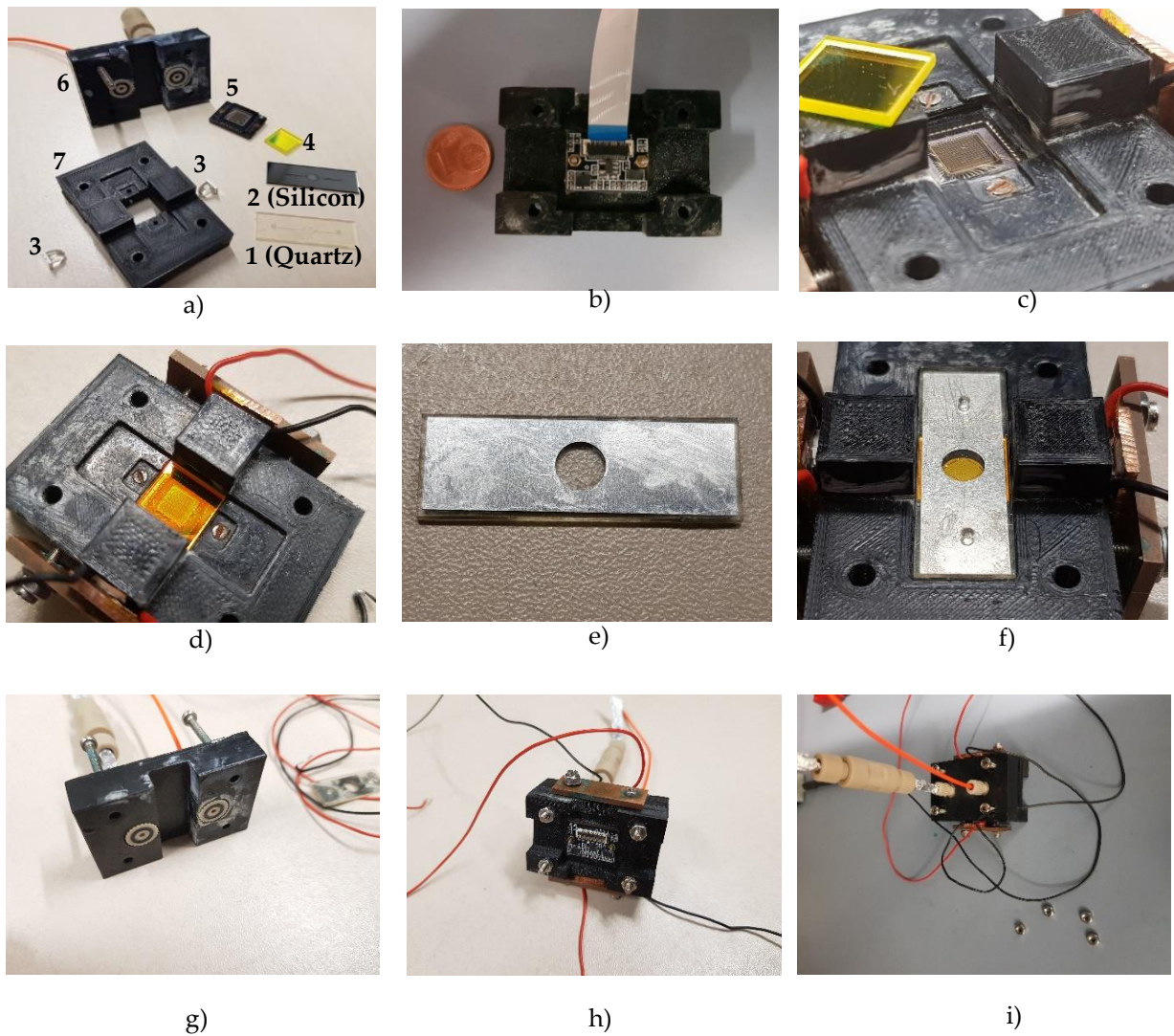


Figure 5.3.5. a) 1 - quartz flow-through microfluidic cell, 2 - silicon flow-through microfluidic cell, 3 - light-emitting diodes, 4 - band-pass filter, 5 - CMOS-image sensor, 6 - upper holder with integrated fluidic connectors, 7 - lower holder. b) The CMOS-image sensor is screwed and fixed into the structure of the lower holder - bottom side view. c) The CMOS-image sensor fixed into the lower holder structure, the band-pass filter ready to be integrated, and the 1.4 mm width slit - top side view; d) The LEDs are tightly fixed into their lower holder pockets using two screws and a piece of copper. The band-pass filter is placed on top of the CMOS image sensor. e) The photonic mask is glued on the flow-through microfluidic cell with opening in the interrogation region area. f) The flow-through microfluidic cell is placed into the pocket specially created for it into the structure of the holder. g) the N-333 connectors are fixed into the upper holder and the black circular O-rings from the bottom serve as liquid sealing when the two holders are screwed together. h) the upper and lower holders screwed together through the four screws - bottom side view. i) Final assembly before testing - top view.

has 1.4 mm width, slightly larger than the flow-through microfluidic cell width (see Fig. 5.3.5. c)). It was opted for this choice to avoid not useful penetration of the excitation light towards the cell location and consequently to reduce the probability of increased noise detected by the photodetector. A few microns thick stainless-steel layer was used to create a photonic mask that covers the quartz lower-layer surface excepting the interrogation chamber area. It has to be mentioned that this is a temporary solution to further avoid the excitation by scattered light that might reach the photodetector (see Fig. 5.3.5. e)).

Of significant importance in optofluidic sensors is the closing of the fluidic circuit. The N-333 type connectors (IDEX Health and Science LLC, Rohnert Park, CA, USA) were integrated into the upper holder structure (see Fig. 5.3.5. g)). The O-ring found at the bottom of the connector plays the role of a sealing when the two holders are held tightly together through four screws.

5.4. Experimental set-up

The experimental set-up used to test the optofluidic sensing prototype was composed of a syringe pump used to stream the reagent into the device, a 24 V DC source used to power the LEDs, a microcontroller board, and the ULS 24 CMOS-image sensor (see Fig. 5.4.1.).

The two LEDs connected in series are powered by an DC electrical power source. Heat might cause indeed a shift in the LEDs emission band, reducing the CMOS detection accuracy. Thus, in order to avoid the overheating, the illumination of the detection chamber was made by triggering on the LEDs for short periods of time ($t \cong 1$ s). Moreover, flat copper heat sinks were soldered on the surface of the LEDs to dissipate the heat produced during working periods.

Fig. 5.4.2. offers a perspective of the experimental device in various testing conditions. As it was presented in Fig. 5.1.1., between the LED and the flow-through cell, a 1 mm rectangular slit made in the PLA support material allows the excitation light to pass towards the SU-8 3050 waveguide. Nevertheless, the width of the slit could be even lower indeed to fit the width of the SU-8 3050 waveguide. The 1 mm width was taken here to avoid possible LED - waveguide misalignments due to the 3D printing tolerances. Fig. 5.4.2. a) and b) show how the fluidic chamber is illuminated through this rectangular slit when one LED, respectively two LEDs are triggered on. Fig. 5.4.2. c) and f) shows how the presence of the mask and the filter influence the light intensities and the spectrum reaching the photodetector. Without doubts, when the device was equipped with the filter and the mask during experiments, the background noises induced were the lowest. These observations were important in iteratively improving the prototype concept during the development stage.

The ULS 24 CMOS image sensor was connected to the microcontroller board (Anitoa Systems LLC, Menlo Park, CA, USA), which was linked to a PC via a USB cable. The excellent sensitivity and linearity of the CMOS image sensor response has been validated through a couple of laboratory experiments. The already-built CMOS image sensor interface allowed settling the

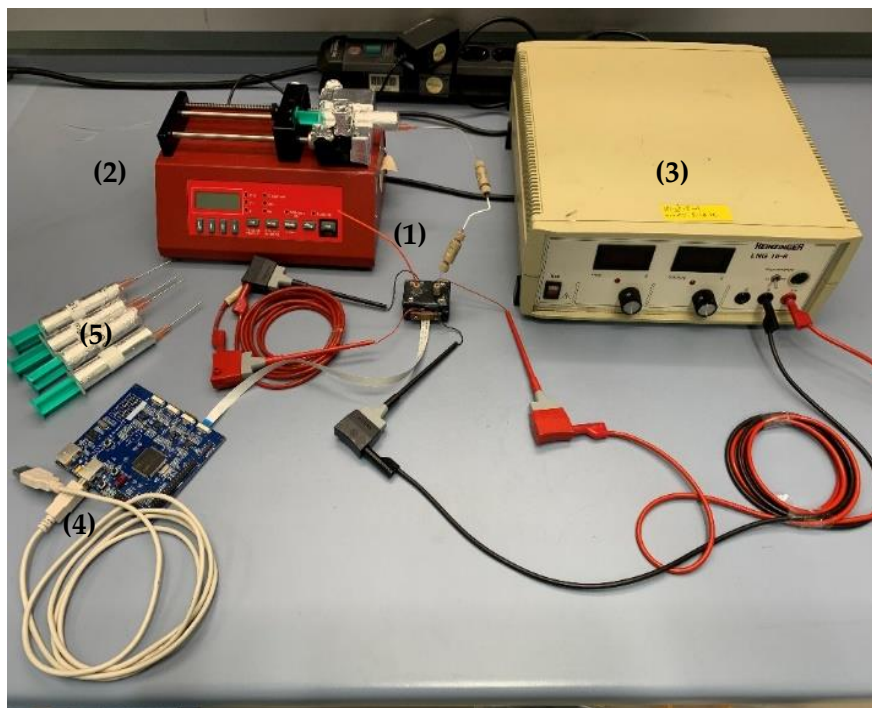


Figure 5.4.1. The experimental set-up used to test the optofluidic sensing prototype. (1) - the optofluidic prototype, (2) the syringe pump used to stream the reagent solutions into the device, (3) 24 V DC source used to power the LEDs connected in series, (4) microcontroller board that accompanied the ULS 24 CMOS-image sensor running the dark noise management system. The USB is plugged to a PC where an interface is used to collect the data. (5) Syringes filled with DDL solutions with different concentrations ready to be streamed into the device.

gain mode (low or high), the pixel configuration (12×12 -pixel configuration or 24×24 -pixel configuration), and the integration time (starting from 1 ms onwards).

It was concluded that the low-gain mode is the most suitable for the current prototyping stage. When the high-gain mode was used, the values of the read-out noise pushed the signal into saturation. However, it must be noted that superior sensitivity might be possible with an improved filtration component and implementation of the high-gain option.

Moreover, it was considered that 12×12 -pixel configuration is satisfactory for the aim of the project. For the majority of the assay performed, a $t = 1$ ms integration time was used since a higher integration time would have produced saturation in some or all pixels.

As a result of the settings before mentioned, the interface provided a 12×12 matrix representing the photon counts measured by each pixel, the temperature of the CMOS sensor at the assay time, and a mean value \bar{X} representing the average of all the 12×12 photon counts, X_i (see Fig. 5.4.3.).

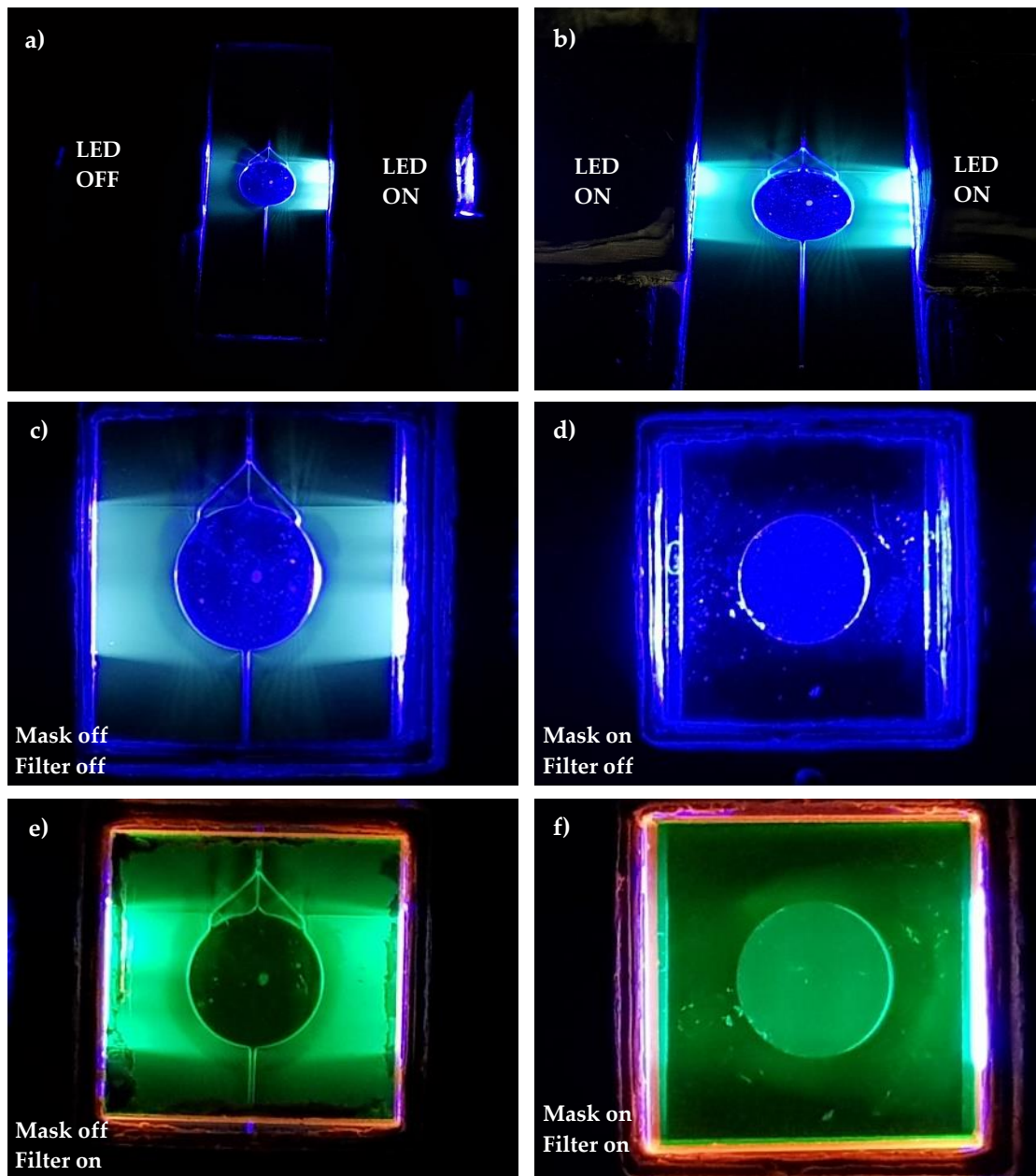


Figure 5.4.2. a) Optical illumination pattern of a 3.5 μL cell with only one LED activated - view from top of the lower holder. b) Optical illumination pattern of a 3.5 μL cell with both LEDs activated. c) View of the illuminated interrogation chamber with no mask and no filter - view from the CMOS image sensor direction. d) View of the illuminated interrogation chamber with mask on and no filter - view from the CMOS image sensor direction. e) View of the illuminated interrogation chamber with mask off on and filter on - view from the CMOS image sensor direction. f) View of the illuminated interrogation chamber with mask on and filter on - view from the CMOS image sensor direction.

The response of the system was iteratively tested for different DDL solutions at various HCHO concentrations already named before (see Section 5.2.3.5.) and a blank concentration of no HCHO in the solution at all. All the solutions were tested at three different optical powers P_1 , P_2 , and P_3 , representing 25%, 50%, and 75% out of the LED maximum power, $P_{LED} = 420 \text{ mW}$ (see Appendix A2. Excitation Light Emitting Diode Data Sheet).

At the beginning of the experiments, the DDL solutions were continuously sampled into the flow-through microfluidic cell. However, observing memory effects during experiments, it was concluded that the continuous streaming had no relevance anymore since the change in concentration could not be done without washing the microfluidic cell before.

In conclusion, the pixels matrix was registered manually using the image sensor interface within the time frame of the short excitation light pulses triggered also manually using the DC power source. The mean values of the pixels were used in building up the response of the optofluidic sensor at four different DDL concentrations.

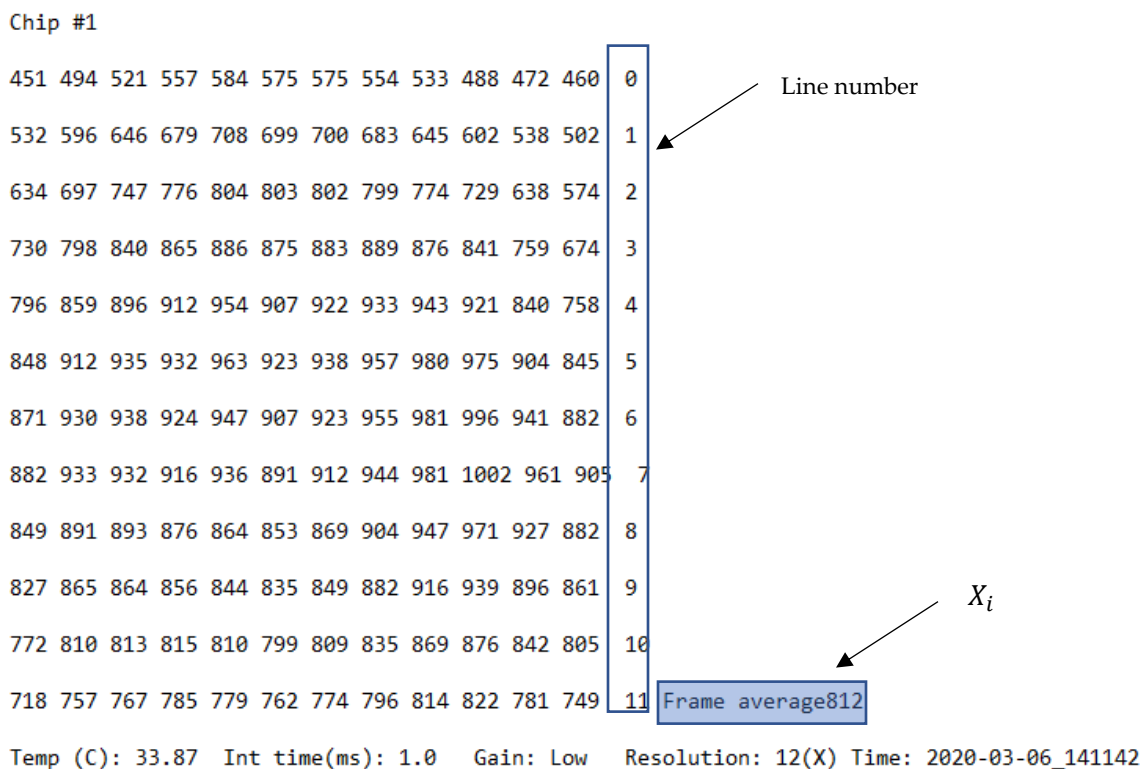


Figure 5.4.3. The pixel output matrix obtained for a particular assay with the 812 counts average of all pixels of the matrix.

5.5. Results

The response of the device has been tested for all the configurations of the interrogation chambers described in [Section 5.2.1](#).

Unfortunately, memory effects (see [Fig. 5.5.1](#).) were observed during the initial stages of the experimental campaign. Thus, the experiments with varying concentration have not been conducted in this study. The influence of the memory effects has not yet been studied. The fluidic cells used during the experimental campaigns were rinsed with acetone and dried in the oven after each sampling to minimize the memory effects.

Thus, the experiments have been performed continuously streaming the solutions, but with constant concentrations. Since the concentration remained constant, the influence of the residence time distribution of the DDL molecules inside the interrogation chambers could not be experimentally studied, but the influence of the volume of the interrogation chamber and its design on the experimental response has been investigated.

The fluorescence intensity could be measured with acceptable meaningfulness in the $V_1 = 3.5 \mu\text{L}$ flow-through microfluidic cell, some picks have been quantified in the $V_2 = 1.4 \mu\text{L}$ cell at high concentrations and higher integration time of the CMOS image sensor, and no meaningful result could be identified from the $V_3 = 0.35 \mu\text{L}$ cell.

The experimental response of the system has been evaluated for the $V_1 = 3.5 \mu\text{L}$ flow-through microfluidic cell by applying a regression analysis technique to the experimental data obtained from two independently prepared DDL samples ($N = 2$, sample #1 and sample #2) for each of the tested concentrations, $c_{i,i=0,\dots,4}$.

Each of the samples processed into the system have been analyzed by continuously taking seven measurements ($n = 7$) of the photon intensities, represented by X_i , $i=1,\dots,7$ in [Eq. 5.5.1](#).. X_i was in fact the mean value of all photon intensities given by the 12×12 pixels matrix obtained at the particular measurement time. $\bar{X}_{\#1}$ represented the mean value of the X_i , $i=1,\dots,7$ measurement taken for the first sample, while $\bar{X}_{\#2}$ represented the mean value for the second sample investigated at a specific HCHO concentration of the solution (see [Tables 5.5.1](#) and [5.5.2](#)).

The precision of the evaluation was quantified by calculating the absolute (σ) ([Eq. 5.5.1](#)) and relative standard deviations (RSD) ([Eq. 5.5.2](#).) and the performance of the device was estimated using the SNR ([Eq. 5.5.3](#).).. SNR has been used here to describe the signal increase relative to the blank sample response ($c_0 = 0.0 \text{ mg/L}$), but its relevance is limited due to the low number of independent samples tested.

While $\sigma_{\#1}$ and $\sigma_{\#2}$ represented the SD obtained for measurements taken for identical samples ($\bar{X}_{\#1}$ and $\bar{X}_{\#2}$), σ represented the standard deviation of $\bar{X}_{N=2} = (\bar{X}_{\#1} + \bar{X}_{\#2})/2$ values.

$$\sigma = \sqrt{\frac{\sum_{i=1}^n (X_i - \bar{X})^2}{N}}, \text{ with } \bar{X} = \frac{1}{n} \sum_{i=1}^n X_i \quad (5.5.1)$$

$$RSD = \frac{\sigma}{\bar{X}_{N=2}} \quad (5.5.2)$$

$$SNR(c_i) = \frac{\bar{X}_{N=2}(c_i) - \bar{X}(c_0)}{\sigma(c_i)} \quad (5.5.3)$$

For $V_1 = 3.5 \mu\text{L}$, the response of the CMOS-based fluorescence detector for a blank sample ($c_0 = 0.00 \text{ mg/L}$) was plotted in Fig. 5.5.1. at different values of the optical power. A linear response ($R^2 = 0.999$) has been obtained for both quartz ($y = 351.5x + 141$) and silicon ($y = 226.5x + 120.3$) cells. Moreover, lower values of the photon counts have been measured for the silicon cell. The lower intensity measured for the silicon cell can be explained by two main factors.

First, lower excitation radiant flux reaches the detection chamber, and by consequence the photodetector, due to the $400 \mu\text{m}$ thickness of the opaque silicon upper layer compared to the transparent $500 \mu\text{m}$ thickness of the quartz cell upper-layer (see Section 5.2.2.).

Second, silicon absorbs a part of the excitation radiant flux at $\lambda_{abs} = 420 \text{ nm}$. It is not clear how significant this behavior of silicon is for the proposed optical circuit, but it certainly exists.

It can be seen in Fig. 5.5.1. that the difference, $\Delta X(P_1)$, between the optical output of the two configurations, $X_{quartz}(P_2)$, $X_{silicon}(P_2)$ registered at $P_2 = 2P_1$ is not $2\times$ higher than the difference, $\Delta X(P_1)$, measured at the optical power, P_1 . Exemplifying, these differences, it has been found that: $\Delta X(P_1) = X_{quartz}(P_1) - X_{silicon}(P_1) = 486 - 344 = 142$, $\Delta X(P_2) = X_{quartz}(P_2) - X_{silicon}(P_2) = 857 - 579 = 278$, and $\Delta X(P_3) = X_{quartz}(P_3) - X_{silicon}(P_3) = 1189 - 797 = 392$.

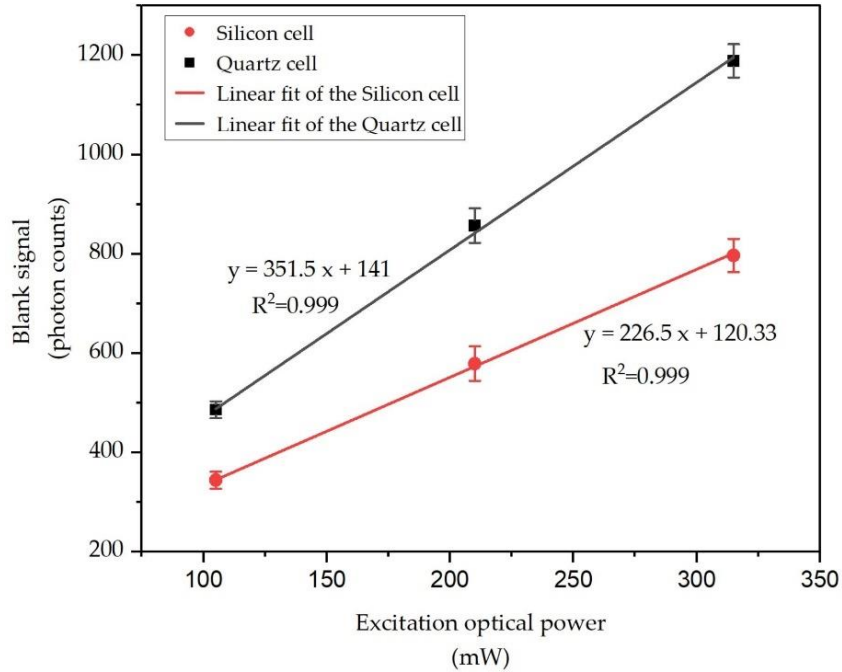


Figure 5.5.1. The linear response obtained for the three-excitation optical powers at $c_0 = 0.00 \text{ mg/L}$ (blank sample) in $V_1 = 3.5 \mu\text{L}$. The error bars indicate the standard deviations for two independently prepared samples ($N = 2$).

Thus, it results that $(\Delta X(P_2) = 278) < (2 \Delta X(P_1)) = 284$, while $(\Delta X(P_3) = 392) < (3\Delta X(P_1) = 436)$. In other words, when the optical power doubled at P_2 , the difference between the mean pixel values between the quartz cell and the silicon cell was less than double. It is difficult to predict at this research stage from where exactly this behavior has originated. It might come from a particular effect in the quartz cell, or, most probably, it is due to the reflectivity of the silicon substrate that slightly enhanced the intensity of excitation light on the CMOS image detector.

Related to the same Fig. 5.5.1., relatively high values of the photon counts were observed for the blank sample. This was mainly due to the fact that the transmission efficiency of the band-pass filter at the excitation wavelength was not exactly zero. This fact caused that 0.0105% of the optical excitation signal to reach the very sensitive ULS 24 CMOS image sensor.

The CMOS image sensor response as a light intensity 12×12 matrix is illustrated in Fig. 5.5.2. The image corresponding to the CMOS dark noise depicts its response in a complete dark environment (no excitation light). The second picture from the left to the right illustrates the CMOS image sensor response for a 0.0 mg/L concentration solution (blank sample), a value of 1225 counts being registered. As expected, higher values have been obtained once the DDL concentration streamed into the system has been increased. Due to the fact that the difference between the pixel outputs were relatively low compared to the dynamic range of the image sensor, the gray color gradient found was also low. However, there was a visible slight enhancement in the gray color intensity from the left to the right coming from the circular detection volume.

Experimental response of the CMOS-based fluorescence detector for $V_1 = 3.5 \mu\text{L}$ was presented in Fig. 5.5.4. for both flow-through cells and showed a logarithmic correlation between the fluorescence intensity and HCHO concentration which is unusual since a linear correlation was expected (see Section 5.6. Non-linearity analysis for possible reasons causing this effect). However, interestingly, an apparent higher SNR has been obtained for the silicon fluidic cell ($SNR = 6.1$, $RSD = 5.3\%$, $N = 2$) relative to the quartz fluidic cell ($SNR = 4.9$, $RSD = 9.1\%$, $N = 2$) at $P_3 = 310 \text{ mW}$ optical power. Similar behavior could be

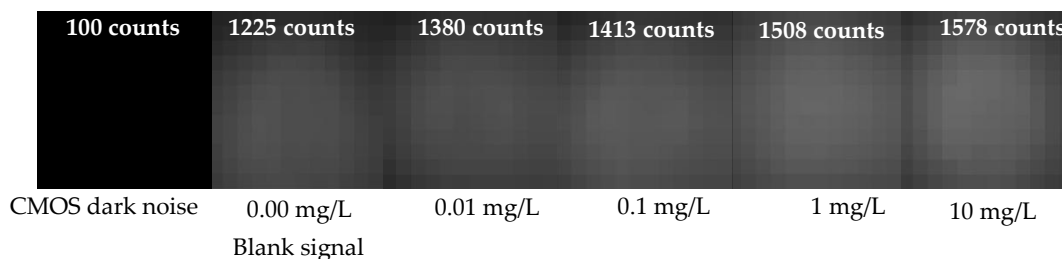


Figure 5.5.2. ULS 24 CMOS image sensor 12×12 -pixel output for: dark current, blank signal, and the four HCHO concentrations tested for a quartz cell at $P_3 = 315 \text{ mW}$.

observed at the other two optical powers used (see Fig. 5.5.3.). However, this result has to be checked for a higher number of reciprocates to confirm its statistical meaningfulness.

It can be observed that the correlation coefficients (R^2) increased proportionally with the excitation optical power for both cells. RSD showed values ranging from 0.06% up to 0.71% for the quartz cell (see Table 5.5.1.) and values ranging 0.09% to 1.59% for the silicon cell (see Table 5.5.2.). When RSDs was calculated for the duplicate samples, values ranging from 1.29% to 9.11% for the quartz cell and from 3.82% to 7.54% for the silicon cell were found.

Moreover, bubbles were observed sometimes inside the fluidic cell detection chamber at the end of the assay. The observed fluorescence intensity mean values were higher when bubbles were present inside the chamber compared to the situation when bubbles were absent. Thus, assays made in the presence of air bubbles in the detection chamber were not taken into consideration when the response of the sensor was determined.

A couple of assays were realized for the $V_2 = 1.4 \mu\text{L}$ and $V_3 = 0.35 \mu\text{L}$. The $V_3 = 0.35 \mu\text{L}$ flow-through microfluidic cells were insensitive to all the four concentrations streamed. For the silicon cell, the values obtained were slightly varying around the values obtained for the blank sample which is 460 counts at P_3 , 347 counts at P_2 , and 235 counts at P_1 . The $V_2 = 1.4 \mu\text{L}$ both cells were sensitive at $c_4 = 10 \text{ mg/L}$ concentration. For sure, the fluidic cells were not sensitive to the $c_1 = 0.01 \text{ mg/L}$ and $c_2 = 0.1 \text{ mg/L}$. Not meaningful results were obtained for the $c_3 = 1 \text{ mg/L}$ for both cells. The photon counts outputs were in the error range of the blank sample output.

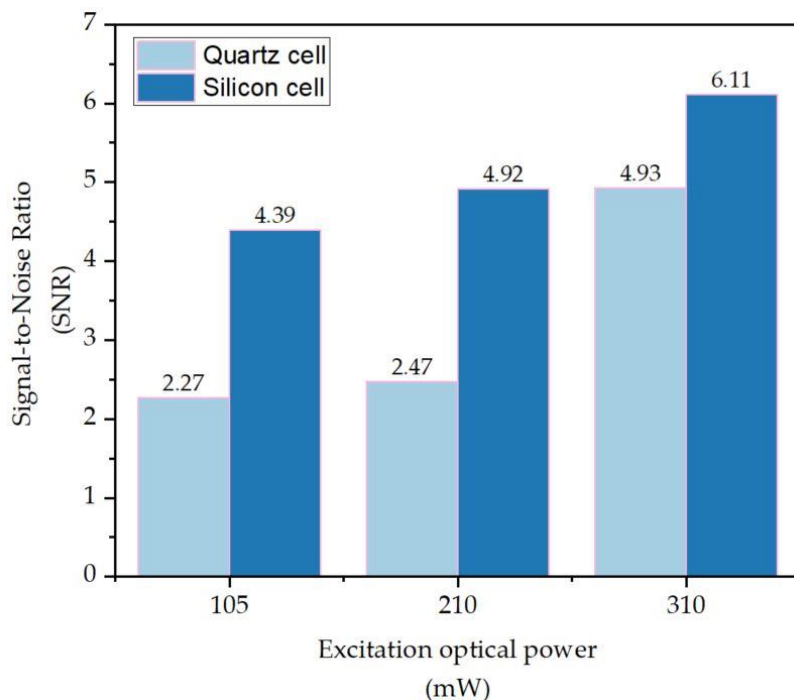


Figure 5.5.3. SNRs obtained for quartz and silicon fluidic cells at $c_1 = 0.01 \text{ mg/L}$ HCHO concentration in DDL solution and different optical powers.

Table 5.5.1. Error distribution as standard deviation (σ) and relative standard deviation (RSD) for the $V_1 = 3.5 \mu\text{L}$ quartz fluidic cell at $P = 315 \text{ mW}$, where #1 and #2 represented the two independently prepared samples for each of the tested HCHO concentrations c_i for $i = 0, \dots, 4$ of DDL solutions.

HCHO concentration (mg/L)	0.00	0.01	0.10	1.0	10.0
$\bar{X}_{\#1}$ (counts)	1,122	1,477	1,505	1,528	1,611
$\sigma_{\#1}$ (counts)	3	2	3	4	5
$RSD_{\#1}$ (%)	0.21	0.16	0.21	0.29	0.29
$\bar{X}_{\#2}$ (counts)	1,155	1,230	1,323	1,489	1,546
$\sigma_{\#2}$ (counts)	3	9	2	1	3
$RSD_{\#2}$ (%)	0.24	0.71	0.16	0.06	0.20
$\bar{X}_{N=2}$ (counts)	1,189	1,354	1,414	1,509	1,578
$\bar{X}_{N=2}$	34	123	91	20	33
RSD (%)	2.82	9.11	6.43	1.29	2.06
SNR	-	4.9	6.7	9.6	11.6

Table 5.5.2. Error distribution as standard deviation (σ) and relative standard deviation (RSD) for the $V_1 = 3.5 \mu\text{L}$ silicon fluidic cell at $P = 315 \text{ mW}$, where #1 and #2 represented the two independently prepared samples for each of the tested concentrations c_i for $i = 0, \dots, 4$.

HCHO concentration (mg/L)	0.00	0.01	0.1	1.0	10
\bar{X}_1 (counts)	771	902	988	966	1,018
$\sigma_{\#1}$	3	1	2	15	2
$RSD_{\#1}$ (%)	0.36	0.15	0.24	1.59	0.22
\bar{X}_2 (counts)	822	1,005	1,066	1,053	1,184
$\sigma_{\#2}$	4	8	2	2	1
$RSD_{\#2}$ (%)	0.44	0.75	0.21	0.16	0.09
$\bar{X}_{N=2}$ (counts)	797	954	1,027	1,010	1,101
$\bar{X}_{N=2}$	26	51	39	43	83
RSD (%)	3.21	5.39	3.82	4.27	7.54
SNR	-	6.1	9.0	8.3	11.9

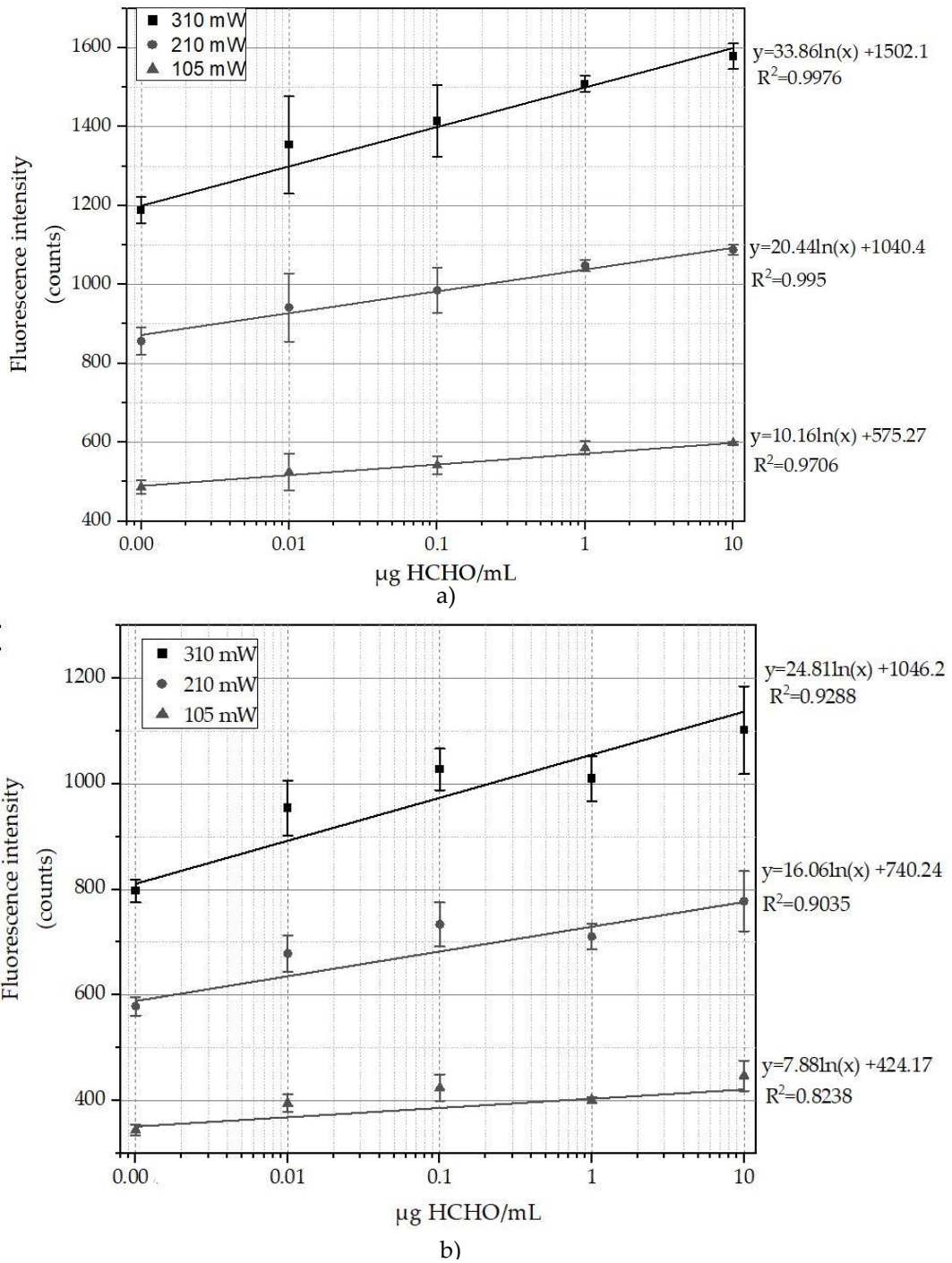


Figure 5.5.4. Experimental evaluation of the CMOS-based fluorescence detector realized using the mean values (\bar{X}) of seven assays ($n = 7$) made on two independently prepared samples ($N = 2$) at each of the $c_i, i = 0, \dots, 4$ concentrations tested for the $V_1 = 3.5 \mu\text{L}$ flow-through microfluidic cell. (a) Logarithmic fitting of the experimental points for quartz fluidic cell; (b) Logarithmic fitting of the experimental points for silicon fluidic cell. The error bars indicate one standard deviation ($N = 2$).

5.6. Non-linearity analysis

The experimental results showed a pronounced non-linear behavior of the fluorescence intensity. DDL fluorophore – photon counts correlation followed a logarithmic behavior in the 0.00 – 10 $\mu\text{g}/\text{mL}$ HCHO concentration range.

This is unusual, although there is a report of DDL fluorescence non-linearity measured in a similar reagent [241]. In that report it was found that DDL fluorescence intensity was linear from 0.005 $\mu\text{g}/\text{mL}$ to about 0.4 $\mu\text{g}/\text{mL}$ HCHO, but the line starts to slightly deviate from linearity from 0.4 $\mu\text{g}/\text{mL}$ to 1.0 $\mu\text{g}/\text{mL}$ (see Fig. 5.6.1.). Tests above this limit have not been made.

However, the non-linearity reported there is not as pronounced as the one found in the current work. Therefore, the non-linearity behavior registered here could be from a couple of sources, including:

- not-precise control of the sample's temperature during assays
- low number of independent replicates
- chemical mixing ratios related errors during sample preparation
- misalignment of the off-the-shell optical circuit components
- photobleaching
- optical reflections/refractions due to the curved shape of the interrogation chamber.

Temperature was not precisely controlled during assays. Fluoral-P solutions were prepared as

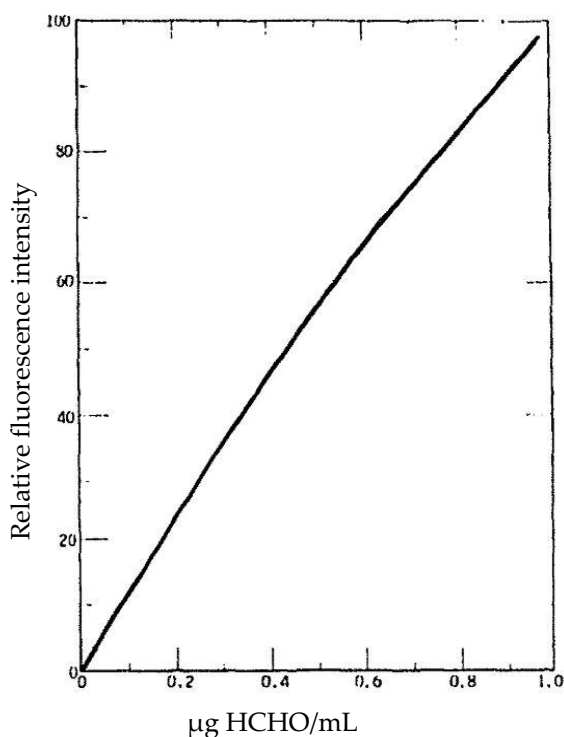


Figure 5.6.1. Relationship between the relative fluorescence intensity and HCHO concentration in the work of Belman [241].

stated in [Section 5.2.3.5.](#), by being introduced in the oven for 5 minutes at $T = 338\text{ K}$. Afterwards, the samples were cooled until they reached room temperature (varying between $T = 293\text{ K} - 298\text{ K}$) and pressure-driven in the flow-through-fluidic cell using a syringe pump. The syringe and the channels carrying the DDL solution were covered with reflective materials to avoid illumination and eventual photobleaching effects due to the environmental light.

A degree of error was introduced in the measurement process due to not-maintaining a constant temperature over the entire range of the samples tested. As stated in [Section 3.2.3.](#), $\phi_{DDL}(T = 293\text{ K}) = 0.005$ [96,98]. It was demonstrated that the ϕ_{DDL} decreases by 11% when temperature is increased to $T = 303\text{ K}$ and fluorescence intensity loss is about 40% at $T = 333\text{ K}$ [98]. Thus, a part of the large SD values discussed in [Section 5.5.](#) could come from the variation of the DDL fluorophore quantum yield due to the uncontrolled temperature of the assays.

Low-number of independent replicates ($N = 2$) contributes to the large SD values and most probably to the non-linear behavior as well. The number of the independent replicates means the number of replicated samples for each of the four concentrations in the concentration range. For each of these two independent replicates, 7 consecutive counts of the signal were registered. Thus, the plots are built upon 14 counts, 7 from one independent replicate and 7 from the other one. It has to be mentioned that the low-number of independent replicates tested was caused by the lack of time. Moreover, a couple of operational steps make the process time-consuming. Among them, the preparation process of the solutions for each of the concentrations tested, assembling /disassembling the device (precise integration of the flow-through detection cell in between the upper- and lower-holder) at each concentration tested, washing the flow-through fluidic cells after each of the concentration tested.

Misalignment of the off-the-shell optical circuit components is probably one of the error sources with the most consistent contribution due to the broad range of parameters being influenced by it. Position of the flow-through microfluidic cell and automatically of the SU-8 3050 waveguide, relative to the emission centerline of the LED was most probably not the same for each of the assay. This is, again, due to assembling /disassembling the device for each of the assay. This issue has been considered in the design phase of the device. However, there is a significant probability that small misalignments in μm -range existed. This affected the transmittance of the radiant flux across the optical circuits from the flow-through detection cell towards the CMOS-based image sensor.

Photobleaching could be the main cause for the prominent non-linearity measured. It is possible that the radiant flux of the fluorescence emission light destroyed parts of the DDL fluorophore in the sequential illumination of the sample. As it was already explained in [Section 5.4.](#), the sample found in the interrogation chamber of the flow-through cell was illuminated by the LEDs in short 1 s length pulses. This was done 7 times for each sample, with short 1-2 seconds breaks between the illumination pulses. Thus, this consecutive illumination of the sample probably induced a photobleaching effect. [Figs. 5.6.2. – 5.6.5.](#) offer a more detailed view of the

non-linearities.

Certainly, the fluorescence emission registered as counts decreases as the excitation optical power increases. This can be observed in all the four figures presented below. Moreover, SD increases by increasing the optical power at each of the four concentrations studied. Fig. 5.6.5. illustrates clearly the flawed results obtained at 1 $\mu\text{g}/\text{mL}$ concentration most probably due to chemical mixing ratios related errors during sample preparation.

Overall, non-linearity effects are clearly influenced by the parameters presented above. For the moment, the contribution for each of the error sources cannot be determined.

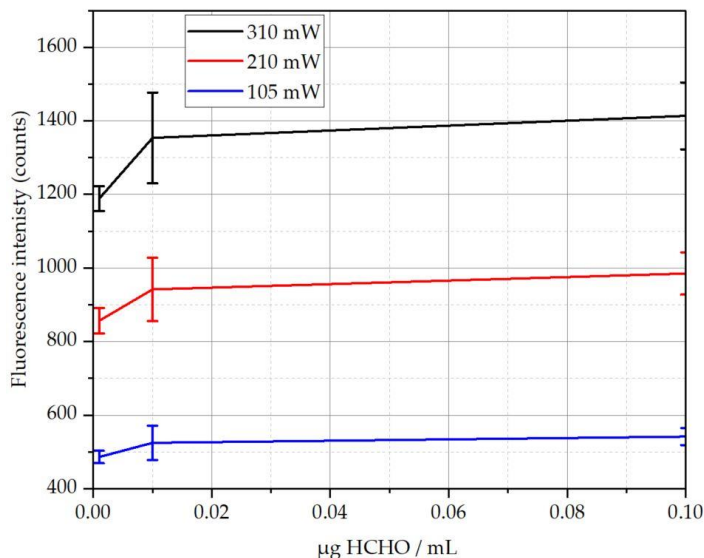


Figure 5.6.2. Fluorescence intensity – HCHO concentration dependency found in the 0.00 – 0.10 $\mu\text{g HCHO}/\text{mL}$ concentration range for quartz cell.

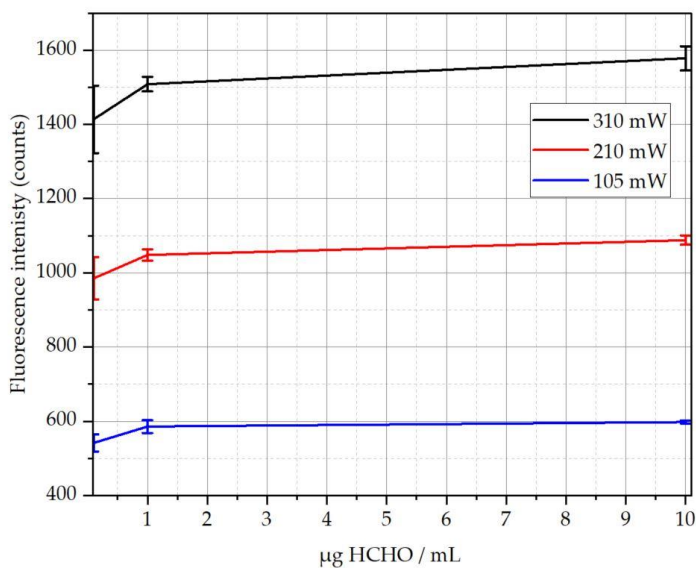


Figure 5.6.3. Fluorescence intensity – HCHO concentration dependency found in the 0.01 – 10.00 $\mu\text{g HCHO}/\text{mL}$ concentration range for quartz cell.

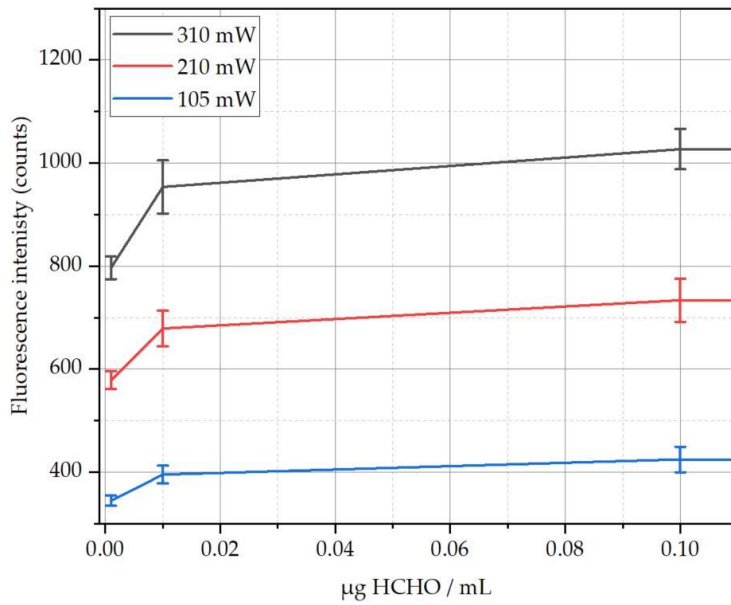


Figure 5.6.4. Fluorescence intensity – HCHO concentration dependency found in the 0.00 – 0.10 µg HCHO/mL concentration range for silicon cell.

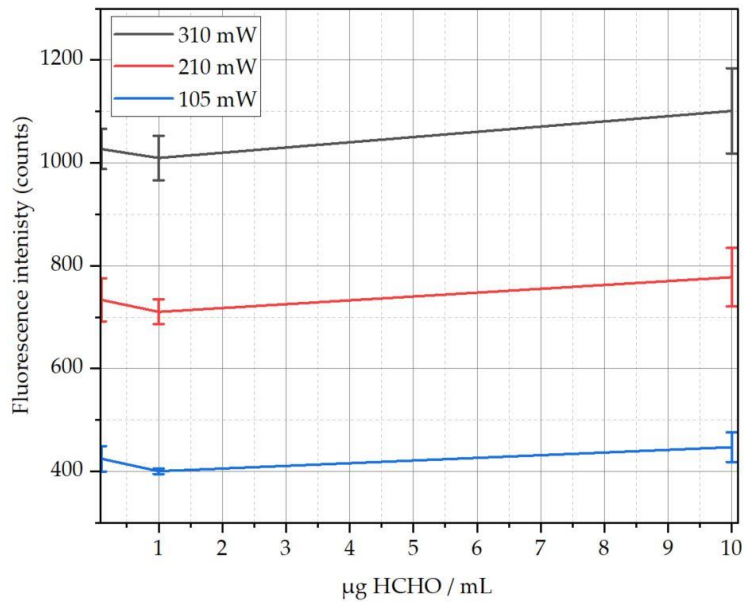


Figure 5.6.5. Fluorescence intensity – HCHO concentration dependency found in the 0.01 – 10.00 µg HCHO/mL concentration range for silicon cell.

Chapter 6. Designing a gas-liquid microfluidic reactor for formaldehyde separation

This part of the work presents the incipient steps made in the development process of a gas-liquid micro-reactor for HCHO separation and derivatization. Compatible materials for an experimental prototype based on the concept presented in [Chapter 4, Section 4.4](#), are identified. A series of simulations are run to understand the kinetics of the HCHO molecules in some arbitrary chosen microchannel configurations. A prototype concept that has to be further tested experimentally is introduced.

6.1. Design of the reagent carrying microchannel

Designing the microchannel means to establish its characteristic dimensions (length, width, and depth) that would allow a process to occur smoothly in specific hydrodynamic conditions. In the current context, this step involves the characterization of the flow in a rectangular microchannel coupled to the chemical kinetics of the Hantzsch reaction using Fluoral-P (0.01 M) reagent.

The cross-sections of the rectangular microchannels under study are presented in [Table 6.1.1](#). together with the theoretical estimations of the pressure drops, Δp , (see [Eqs. 2.2.3. – 2.2.7.](#)) and Reynolds numbers, Re , (see [Table 2.2.2.](#)) corresponding to each case. Flow rates settled as reference in the design process of the flow-through microfluidic cells in [Chapter 5](#) are further used here. Moreover, the width of the microchannel is maintained constant, $d = 200 \mu\text{m}$, while depth is varied.

It was demonstrated in several works [242] that theoretical assumptions for calculating the pressure drop at macro-scale are still valid in microchannels. However, the roughness of the material increases the pressure drop consistently in microfluidic turbulent flow [61]. In laminar flows, Δp was shown to be insensible to the roughness. However, it was demonstrated that by introducing herringbone structures on the channel's walls, Δp can be reduced [206].

Table 6.1.1. Pressure-drop, Δp , calculated using the Hagen-Poiseuille equation and Re numbers calculated for the hydrodynamic conditions of reference for water.

Cross-section [$\mu\text{m} \times \mu\text{m}$]	Temperature [K]	Flow rate [$\mu\text{L}/\text{min}$]					
		$Q_1 = 5$		$Q_2 = 10$		$Q_3 = 15$	
		Δp [Pa]	Re	Δp [Pa]	Re	Δp [Pa]	Re
100 × 200	296	6983	0.6	13965	1.19	20948	1.79
	338	3240	1.26	6480	2.52	9720	3.78
200 × 200	296	1552	0.45	3103	0.89	4655	1.34
	338	720	0.95	1440	1.89	2160	2.84
300 × 200	296	718	0.36	1437	0.72	2155	1.07
	338	333	0.76	667	1.51	1000	2.27

6.1.1. HCHO reaction with Fluoral-P reagent in a microfluidic channel

This step determines the reaction probability, \overline{P}_R , of the HCHO molecules with Fluoral-P solutions (see Sections 2.2.5. and 3.2.) in microchannels characterized by the hydrodynamic conditions specified in Table 6.1.1. Numerical simulations are used to monitor \overline{P}_R as a function of the channel length and the reaction-rate constant, k' . In the end, this step is important because it helps finding the position where the HCHO derivatization rate is maximized and, by consequence, where the flow-through microfluidic cell has to be placed in order to maximize the autonomy of the future device.

COMSOL Multiphysics® 5.6. (Stockholm, Sweden) is used for solving numerically, based on the finite element method (FEM), a model coupling the Navier-Stokes equations (see Eqs. 2.2.1.-2.2.2.) with the convection-diffusion equation (see Eqs. 2.2.14. and 2.2.19.). Therefore, Laminar Flow module, Transport of Diluted Species module, and Chemical Reaction of Species are coupled in the model. Laminar Flow module describes the fluid movement and it is coupled to the Transport of Diluted Species model which describes the species migration.

Algebraic Multigrid (AMG) solver based on GMRES (generalized minimum residual) method is used to couple the two modules. The convergence criterion on residuals is settled to 10^{-5} . Diffusion coefficients of species (HCHO molecules) are estimated using Eq. 2.2.13. The computational domain (see Fig. 6.1.1.) is discretized in 300 000 tetrahedral elements ($30 \times 10\ 000$).

Simulations are based on a couple of assumptions:

- System operates under normal pressure conditions.
- System is considered isothermal.
- Fluidic domain has a constant length of $L = 500\text{ mm}$.

Concentration considered for study is $c = 4.07 \cdot 10^{-6}\text{ mol} \cdot \text{m}^{-3}$ (100 ppb). HCHO species are introduced at the inlet using a rectangular function expressed in Fig. 6.1.2. HCHO concentration distribution as a function of space and time is monitored by implementing virtual probes along the channel (see Fig. 6.1.1.). No slip ($u = 0\text{ m/s}$) condition is settled for the lateral walls and the pressure at the outlet is the atmospheric pressure.

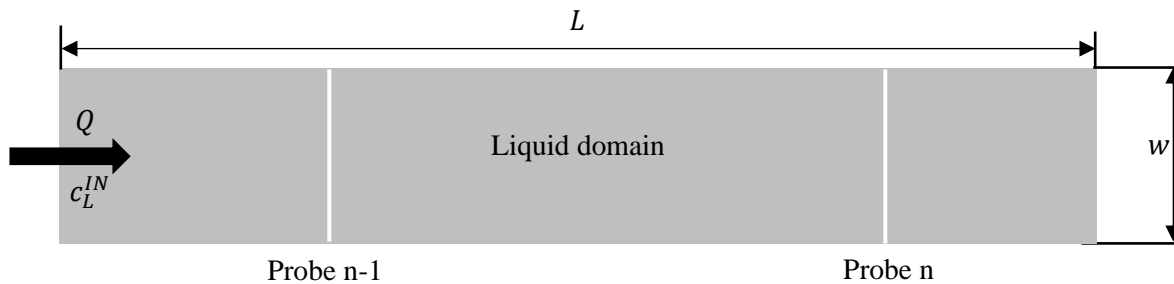


Figure 6.1.1. Representation of the 2D fluidic domain of the channel, where w is the width and L is the length (not in scale).

A stationary solver was used to compute the flow fields based on Navier-Stokes equations, while a time-dependent solver was used to solve the diffusion-convection equations. The coupling between the two was made through the AMG coupled to GMRES models. The time step for the time-dependent solver was taken as $\Delta t = 0.1$ s and the transient flow was simulated for 180 s. However, the solver could adjust the computational time-step if the convergence criterion was not fulfilled. Simulation times varied from 3 to 5 hours depending on the simulated cases (see Table 6.1.2).

The mesh and the time step were selected in such a way that the Courant number, C (see Eq. 6.1.1.), was kept below 1. In Eq. 6.1.1., Δx is the distance between two adjacent tetrahedral elements, Δt is the time step, and u is the velocity.

$$C = u \frac{\Delta t}{\Delta x} \quad (6.1.1.)$$

The probes are located at $x_0 = 0$ mm, $x_1 = 100$ mm, $x_2 = 200$ mm, $x_3 = 300$ mm, $x_4 = 400$ mm, $x_5 = 475$ mm. Distance is measured from the inlet towards the outlet. HCHO concentration is monitored as a function of time and space. Concentration given by a probe at a specific time, t , is a line-averaged concentration of the HCHO concentrations measured over the line at that time, t .

Simulations are run in parallel for two pseudo-first order reaction rates, $k'_1(T_1) = 0.0216$ s⁻¹ respectively $k'_2(T_2) = 0.0372$ s⁻¹, where $T_1 = 333$ K and $T_2 = 338$ K (see Section 3.2.2.). k'_1 and k'_2 have been calculated from the Eq. 3.2.3. stating the derivatization rule of HCHO into DDL in the experimental conditions of Guglielmino *et al.*, [96].

Reaction probability, \overline{P}_R , as stated in Eq. 2.2.44., is calculated at the position of each probe. Data obtained in simulations are summarized in Tables 6.1.2. – 6.1.3. In all these tables, cells colored in dark grey represent the reaction probabilities for which more than 99% of the HCHO

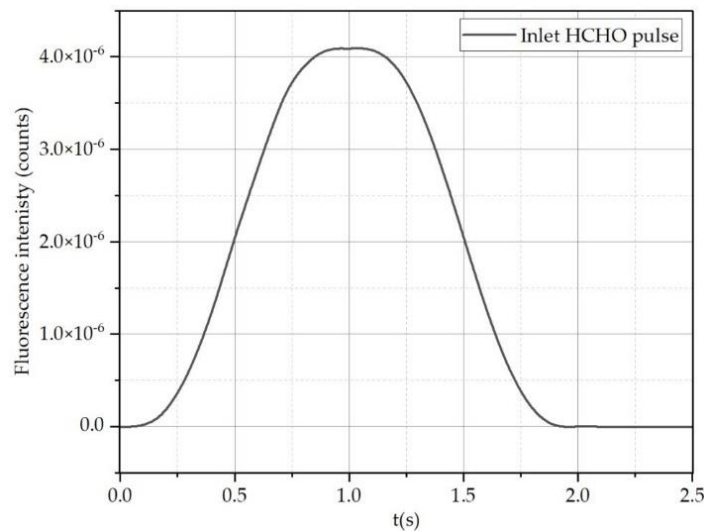


Figure 6.1.2. Rectangular pulse function, $rect(t[1/s])$, as a function of time and used to sample a $c_L^{IN} = c \cdot rect(t[1/s])$ HCHO concentration in the transient domain.

Table 6.1.2. Reaction probability, \overline{P}_R (%), for $100 \mu\text{m} \times 200 \mu\text{m}$ cross section, where k'_1 and k'_2 are the pseudo-reaction constants at $T_1 = 333 \text{ K}$, respectively $T_2 = 338 \text{ K}$.

Probe name	Flow rate [$\mu\text{L}/\text{min}$]					
	5		10		15	
	k'_1	k'_2	k'_1	k'_2	k'_1	k'_2
x_1	22.87	14	40.32	35.26	51.29	47.53
x_2	9.90	4.08	23.21	16.87	33.01	27.19
x_3	4.85	1.35	14.88	8.94	23.31	19.95
x_4	2.50	0.47	10.02	4.97	17.20	11.02
x_5	1.31	0.22	7.60	3.26	16.03	8.12

Table 6.1.3. Reaction probability, \overline{P}_R (%), for $200 \mu\text{m} \times 200 \mu\text{m}$ cross section, where k'_1 and k'_2 are the pseudo-reaction constants at $T_1 = 333 \text{ K}$, respectively $T_2 = 338 \text{ K}$.

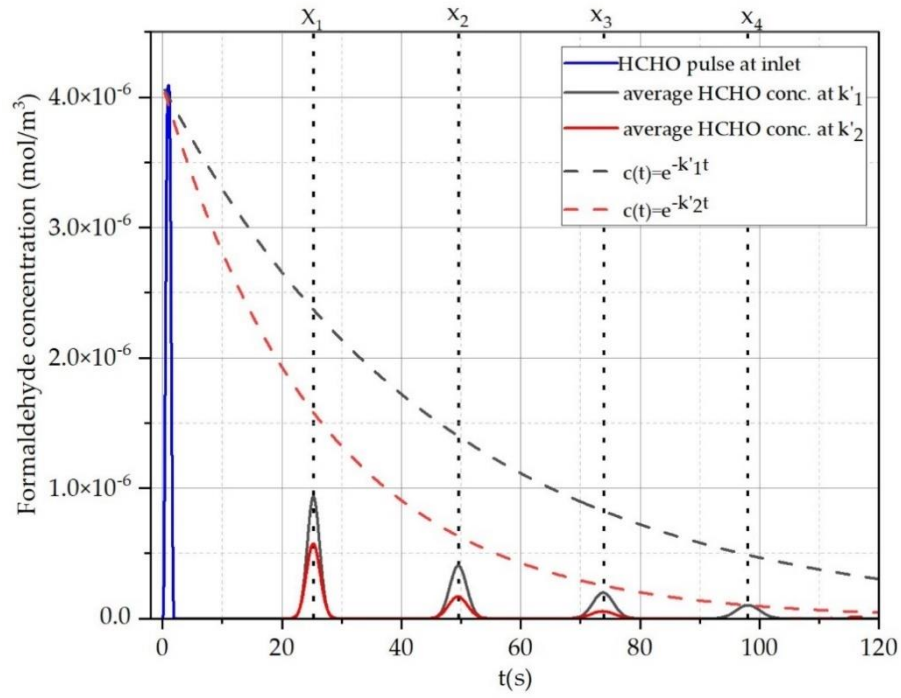
Probe name	Flow rate [$\mu\text{L}/\text{min}$]					
	5		10		15	
	k'_1	k'_2	k'_1	k'_2	k'_1	k'_2
x_1	5.31	4.92	12.60	9.21	18.25	15.02
x_2	1.22	1.40	5.31	2.64	9.00	5.85
x_3	0.38	0.46	2.57	0.87	5.31	2.58
x_4	-	0.16	1.32	0.30	3.25	1.24
x_5	-	0.076	0.82	-	2.30	0.72

Table 6.1.4. Reaction probability, \overline{P}_R , for $300 \mu\text{m} \times 200 \mu\text{m}$ cross section, where k'_1 and k'_2 are the pseudo-reaction constants at $T_1 = 333 \text{ K}$, respectively $T_2 = 338 \text{ K}$.

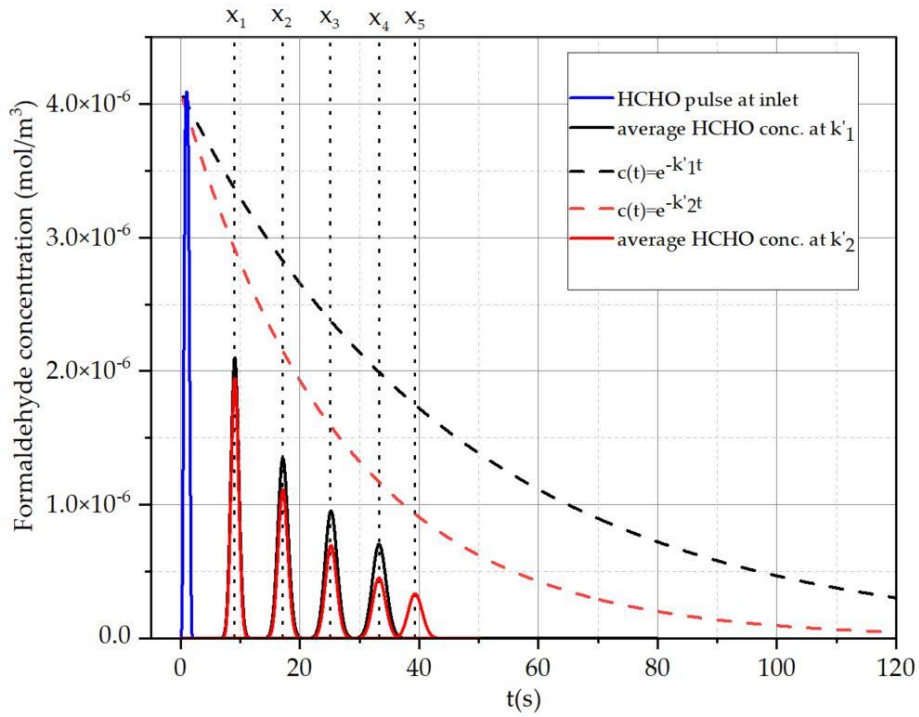
Probe name	Flow rate [$\mu\text{L}/\text{min}$]					
	5		10		15	
	k'_1	k'_2	k'_1	k'_2	k'_1	k'_2
x_1	1.77	0.41	4.69	2.8	8.09	5.94
x_2	0.26	0.02	1.48	0.48	3.40	1.70
x_3	-	-	0.54	0.09	1.65	0.56
x_4	-	-	0.20	0.02	0.84	0.19
x_5	-	-	0.16	0.006	0.12	0.09

have been derivatized into DDL. In the $100 \mu\text{m} \times 200 \mu\text{m}$ cross section microchannel, this happens only at k'_2 for a position located in the $[x_4, x_5]$ space range.

In the $200 \mu\text{m} \times 200 \mu\text{m}$ cross-section microchannel, the 99% conversion is expected to occur in $[x_1, x_2]$ range for $Q_1 = 5 \mu\text{L} \cdot \text{min}^{-1}$ at each of the constant rates. At $Q_2 = 10 \mu\text{L} \cdot \text{min}^{-1}$, it occurs in $[x_4, x_5]$ range for k'_1 , while for k'_2 , it occurs much faster in the $[x_2, x_3]$ range. At $Q_3 = 15 \mu\text{L} \cdot \text{min}^{-1}$, it does not occur at k'_1 over the studied domain. Instead, the conversion occurs in the $[x_4, x_5]$ range at k'_2 .



(a)



(b)

Figure 6.1.3. Averaged-HCHO concentration monitored over time for the virtual line probes settled along the $100\ \mu\text{m}\times 200\ \mu\text{m}$ cross-section microchannel for (a) $Q_1 = 5\ \mu\text{L}\cdot\text{min}^{-1}$ and (b) $Q_3 = 15\ \mu\text{L}\cdot\text{min}^{-1}$.

In the $300\ \mu\text{m} \times 200\ \mu\text{m}$ cross-section microchannel, the 99% conversion is expected to occur in $[x_1, x_2]$ range for $Q_1 = 5\ \mu\text{L} \cdot \text{min}^{-1}$ at k'_1 . At $Q_2 = 10\ \mu\text{L} \cdot \text{min}^{-1}$, it occurs in the $[x_2, x_3]$ range for k'_1 , while for k'_2 , it occurs faster in the $[x_1, x_2]$ range. At $Q_3 = 15\ \mu\text{L} \cdot \text{min}^{-1}$, the conversion occurs in the $[x_3, x_4]$ for k'_1 , while at k'_2 in $[x_4, x_5]$.

Fig. 6.1.3. exemplifies the simulation results for a $100\ \mu\text{m} \times 200\ \mu\text{m}$ cross-section microchannel at the $Q_1 = 5\ \mu\text{L} \cdot \text{min}^{-1}$, respectively $Q_3 = 15\ \mu\text{L} \cdot \text{min}^{-1}$ flow rate. It can be observed that the concentration peaks follow the exponential decay curve specific to HCHO derivatization of each reaction-rate constant. The exponential decay curves were calculated by averaging the concentration over the entire surface of the simulated domain. Fig. 6.1.4. shows the concentration distribution in a short channel section near the inlet of the channel at various times after the introduction of a concentration pulse of a specific concentration as illustrated in Fig. 6.1.2.

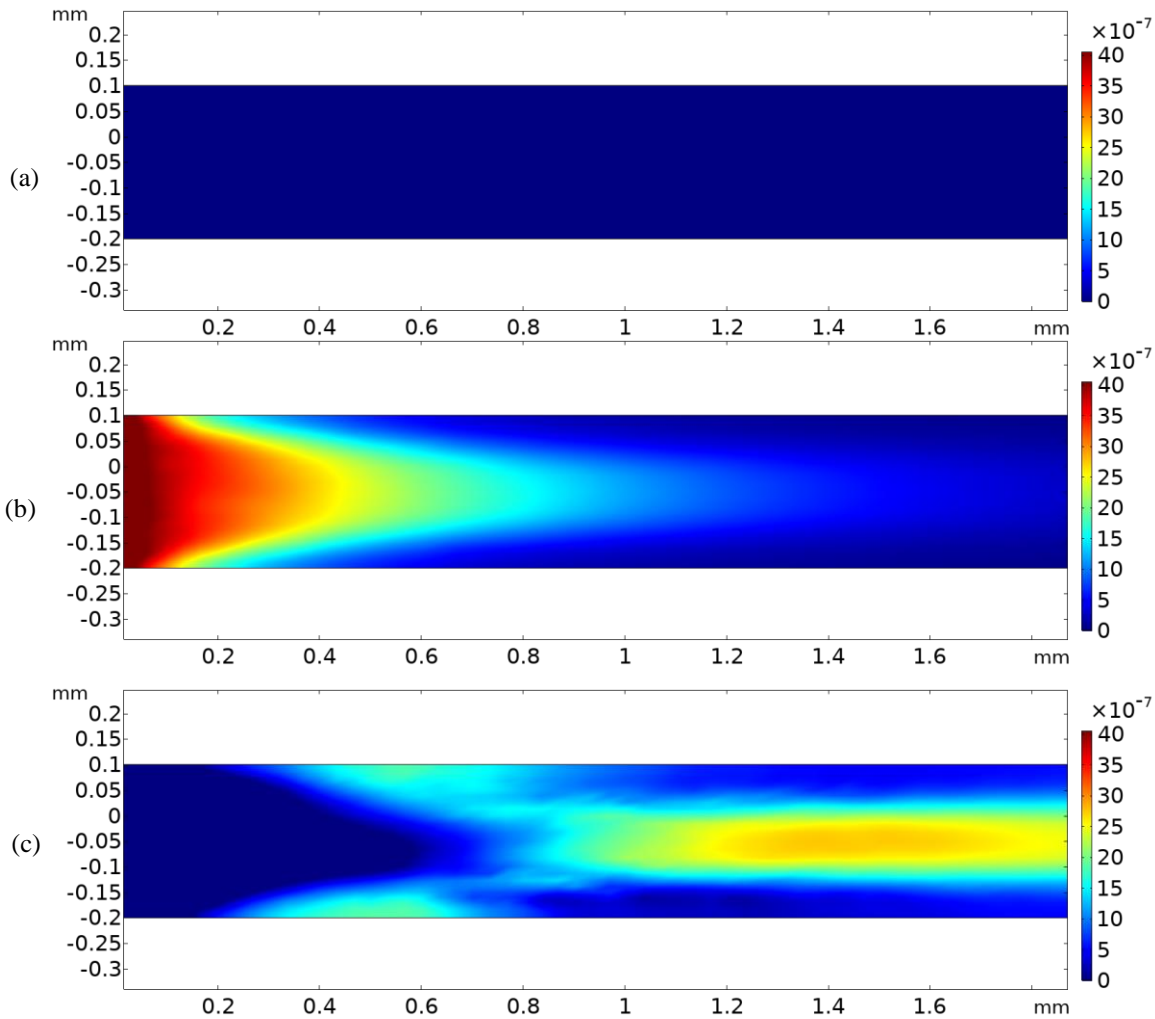


Figure 6.1.4. Concentration distribution in a near-inlet channel section at (a) $t = 0\ \text{s}$, (b) $t = 1\ \text{s}$, (c) $t = 3\ \text{s}$ for a $300\ \mu\text{m} \times 200\ \mu\text{m}$ cross-section microchannel.

In conclusion, mean residence time of HCHO molecules in the domain coupled to the mass flow rate dictates the position where 99% conversion is made and, by consequence, where the flow-through-microfluidic cell for DDL detection could be placed. However, the selection of the microchannel hydrodynamics and its dimensional characteristics does not depend only on the conversion rate and pressure drop. These are important parameters, but more information is required before deciding on their suitability. The mass-transfer flux magnitude and contact area of the gas and liquid phases are also very important. Thus, the next step should be devoted to the determination of the flux magnitude in the hydrodynamic conditions of the study.

6.1.2. Diffusive transfer in stationary direct gas-liquid contact

After the determination of pressure drops and channel length required for a HCHO conversion into DDL, the next step is represented by studying the air-Fluoral-P solution interaction for the simplest case, diffusive transfer in stationary direct gas-liquid contact (see Fig. 6.1.5.). This is here numerically calculated for an overall air-mass transfer coefficient, $K_{OG} = 0.0058 \pm 0.17 \text{ m} \cdot \text{s}^{-1}$ (see Section 3.2.), assumed to be constant. It was demonstrated that mass-transfer of gaseous HCHO molecules from air to water is dominated by the gas-phase since absorption in water is very fast.

COMSOL was used to simulate the absorption time until equilibrium is reached for $K_{OG} = 0.0058 \pm 0.17 \text{ m} \cdot \text{s}^{-1}$ experimentally found elsewhere [86]. Thus, a uniformly distributed concentration is considered in the gas domain at $t = 0 \text{ s}$, when the system is in thermodynamic equilibrium with zero HCHO concentration in the liquid domain. The two-phase domains (see Fig. 6.1.5.) were discretized into 10,000 quad elements. The density of the mesh was increased in the region of the interface, the time step used for simulation was 0.001 s. The system operates under normal pressure conditions and it is considered isothermal.

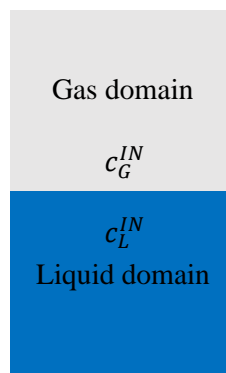


Figure 6.1.5. Representation of the 2D $200 \mu\text{m} \times 200 \mu\text{m}$ fluidic domains of the gas-liquid static interaction simulation.

A concentration saturation limit, c_L^{SAT} , has been imposed in the liquid domain although it is almost impossible to be reached in the concentration range of study. Solubility is very high ($400 \text{ g} \cdot \text{L}^{-1}$) which is equivalent to $c_L^{SAT} = 13319.5 \text{ mol} \cdot \text{m}^{-3}$. Thus, one of the conditions imposed in all states that the diffusive flux from the two-film theory is active as far as the HCHO concentration in the liquid phase, c_L , respects the condition:

$$c_L < c_L^{SAT} \quad (6.2.1.)$$

As presented in Chapter 2, the HCHO transfer from the gas-phase in the liquid-phase is governed by the Henry's law. According to this law, the higher the partial pressure, the higher the concentration that can be accommodated by the liquid phase is. Moreover, the Henry's law constant dictates the concentration distribution in the phases when the equilibrium is reached.

Gas-water dimensionless Henry's law constant, $H^{cc}(T)$, was obtained from $H(T)$ (see Table 3.2.1.) using the ideal gas law:

$$H^{cc}(T) = \frac{1}{H(T) \left[\frac{\text{M}}{\text{atm}} \right] \cdot 0.08206 \left[\frac{1 \text{ atm}}{\text{mol} \cdot \text{K}} \right] \cdot T[\text{K}]} \quad (6.2.2.)$$

The temperatures of interest are $T_1 = 296.15 \text{ K}$ and $T_2 = 338.15 \text{ K}$. Henry's law constants in dimensionless form calculated with the Eq. 6.2.2. are $H^{cc}(T_1 = 296.15 \text{ K}) = 7.9132 \cdot 10^{-6}$ and $H^{cc}(T_2 = 338.15 \text{ K}) = 1.24 \cdot 10^{-4}$, respectively. Considering the BCs from the Table 6.1.5. and the diffusion equation (see Eq. 2.2.19.), the concentration distribution is estimated until equilibrium is achieved in both domains. The same K_{OG} is taken for both temperatures, although in real scenarios the mass-transfer coefficient might have slightly different values at different temperatures.

Table 6.1.5. The boundary conditions for the diffusive transfer in stationary direct-gas-liquid contacting.

Boundary name	Boundary Condition
Lateral walls	$-n \cdot J_i = 0$
Gas-liquid interface	$J = K_{OG}(c_G - H^{cc}(T)c_L)$
Gas-phase	$c_G^{IN} = c_i$
Liquid-phase	$c_L^{IN} = 0$

Running the simulations, it was observed that the diffusion time until the two-phase domains reached the equilibrium was approximately $t_{eq} = 0.2 \text{ s}$ regardless of the concentration tested. The domain-averaged concentrations as a function of time are presented in Fig. 6.1.6 a). In this simulation, the HCHO initial concentration in the gas phase is $c_1 = 4.09 \cdot 10^{-8} \text{ mol} \cdot \text{m}^{-3}$ (1 ppb), while in the liquid phase the initial concentration is $c_0 = 0 \text{ mol} \cdot \text{m}^{-3}$. Fig. 6.1.6. b) shows the HCHO derivatization graphic as a function of time at $T_2 = 338.15 \text{ K}$. In the same figure it can be observed the fast absorption occurring very close to time $t = 0 \text{ s}$. Afterwards, the derivatization process starts slowly, the full-reaction occurring after 180 seconds. Though, a large part of the species is derivatized into DDL even at 120 seconds.

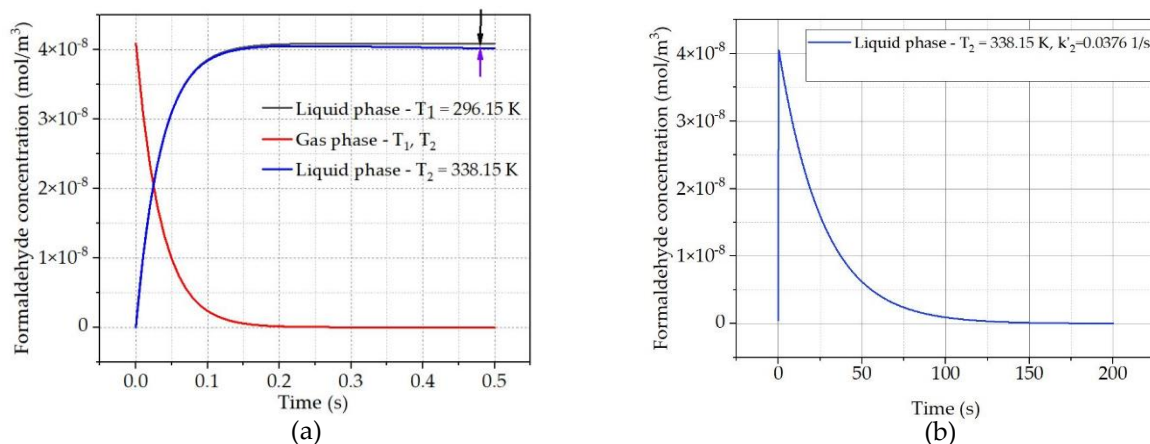


Figure 6.1.6. (a) HCHO surface-averaged concentration distribution in both phases at $T_1 = 296.15\text{ K}$, respectively $T_2 = 338.15\text{ K}$. (b) HCHO exponential derivatization at $T_2 = 338.15\text{ K}$.

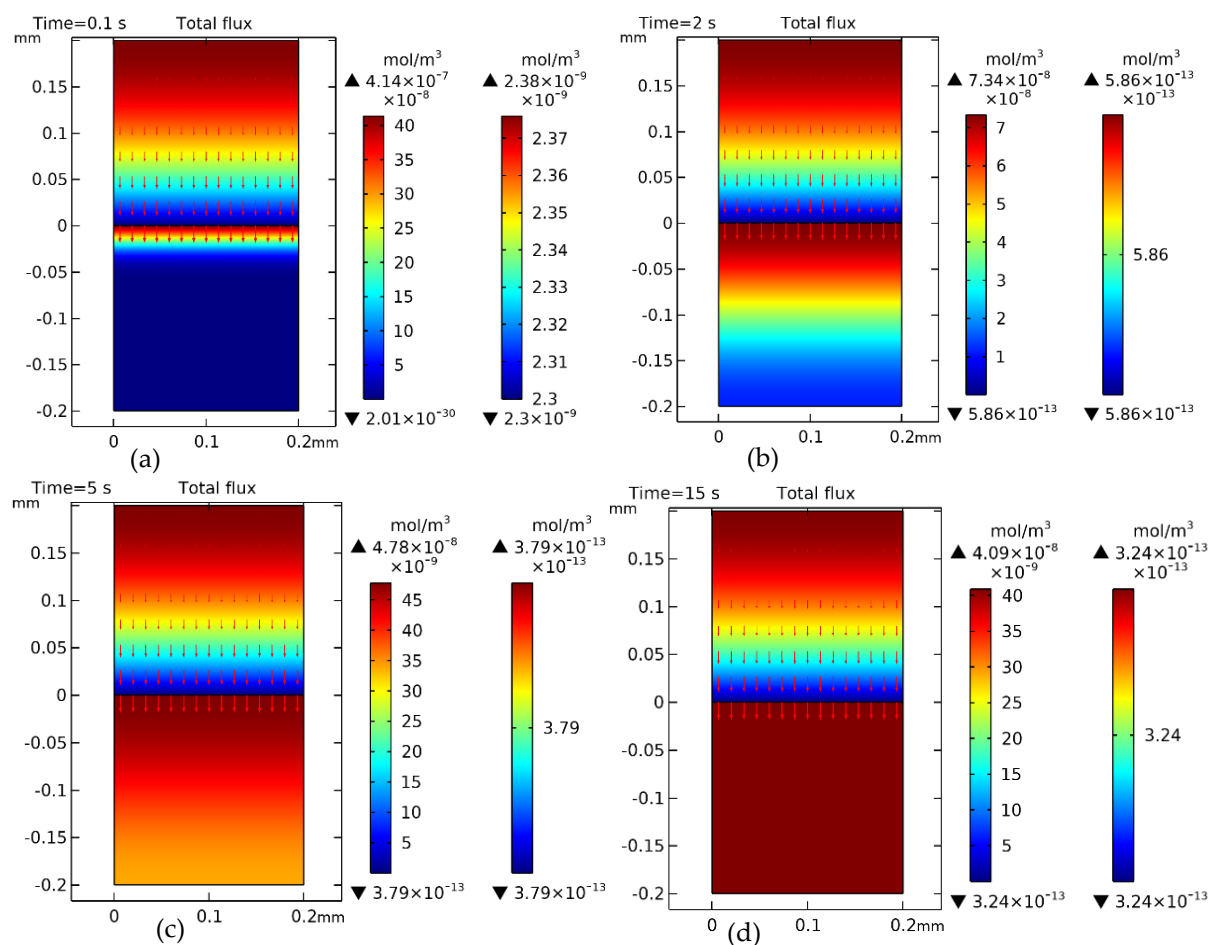


Figure 6.1.7. Time-dependent HCHO concentration distribution in liquid and gas phases at $T_1 = 296.15\text{ K}$. The first scale in the legend characterizes the liquid phase and the second one the gas phase. HCHO initial concentration in the gas phase is $c_1 = 4.09 \cdot 10^{-8}\text{ mol} \cdot \text{m}^{-3}$, while in the liquid phase is zero.

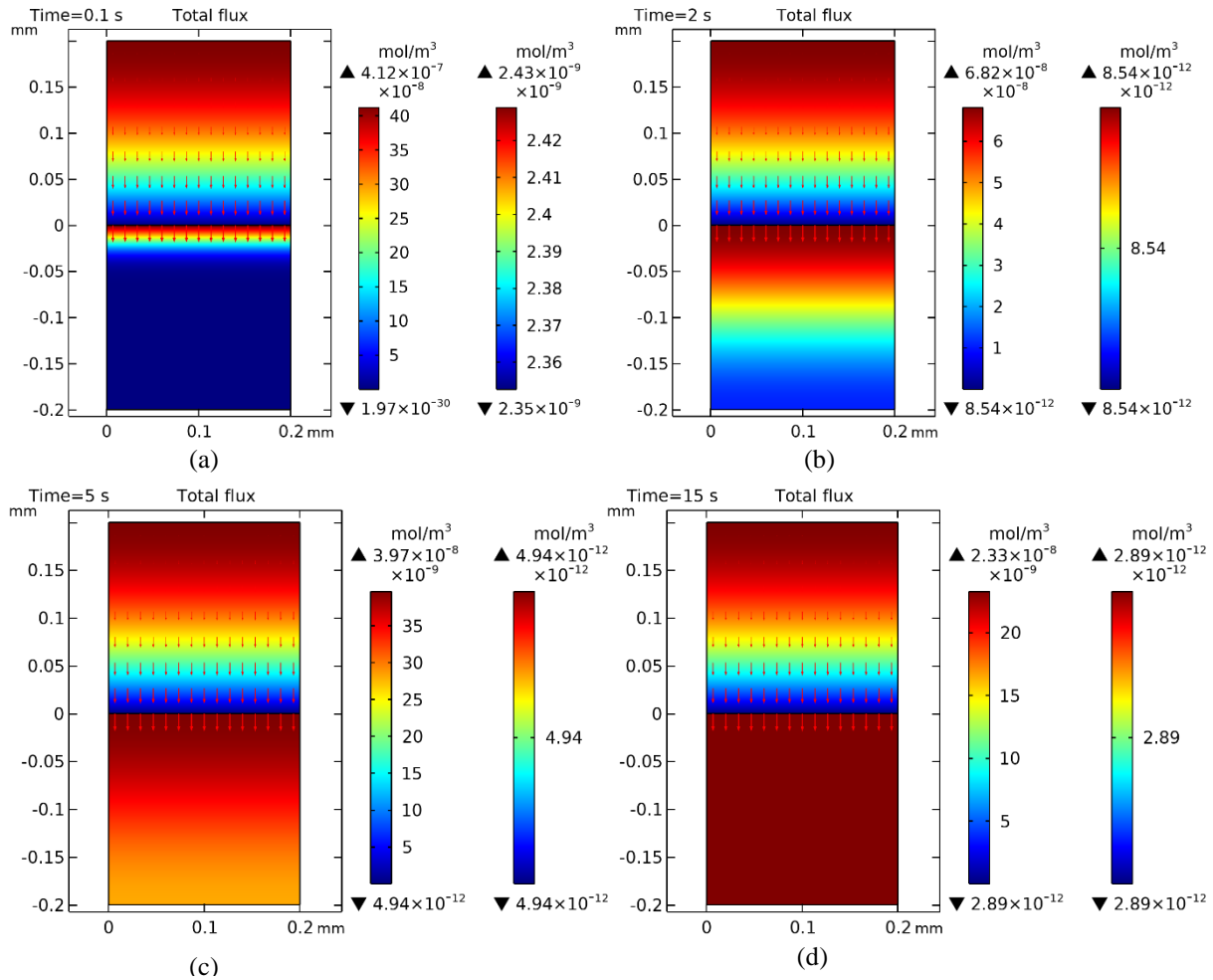


Figure 6.1.8. Time-dependent HCHO concentration distribution in liquid and gas phases at $T_2 = 338.15 \text{ K}$. First scale in the legend characterizes the liquid phase and the second one the gas phase. HCHO initial concentration in the gas phase is $c_1 = 4.09 \cdot 10^{-8} \text{ mol} \cdot \text{m}^{-3}$, while in the liquid phase is zero.

Figs. 6.1.7. - 6.1.8. illustrate the concentration distribution in the two domains at particular times from the simulation time range. From these simulations it results that a significant flux enhancement due to the chemical reaction would occur only if the absorption process would be significantly slower than the current one, $t_{eq} = 0.2 \text{ s}$. Moreover, if the equilibrium between the two phases is reached below one second, the chemically-induced mass-transfer enhancement might be negligible (see Fig. 6.1.6. a).

However, mass-transfer coefficient from the gas-phase might be lower in different scenarios. One example is when the two-phases are separated by a porous membrane. Thus, a longer time would be necessary to reach the equilibrium and reaction might have indeed an

impact over the transfer rate. This could be found out after the prototype proposed in the following sections are fully-fabricated and evaluated experimentally. Finding the precise permeability of the membrane in various hydrodynamic conditions can be done only by running experiments. Additionally, the model presented in the [Appendix A6](#). can be used to extend the current CFD study to the membrane-based interaction scenario.

6.2. Materials selection process

This step focuses on the identification of polymer materials that would be suitable for hosting the microfluidic channels and on the identification of a rigid hydrophobic membrane allowing diffusion of HCHO molecules through its pores (see [Fig. 4.4.2](#). to visualize the proposed structure).

Support structures of the gas and liquid channels

Polymers are targeted as first choice material in LOC applications since they are usually cost-effective and lightweight. Polymeric materials can be found nowadays in customizable forms satisfying many times the demands of the LOC applications where any slight variation of a specific characteristic may have huge overall influence.

Table 6.2.1. Polymers and their potential as material for on-chip integration of HCHO sensing.

Material	Transparency	Not releasing HCHO	Chemically inert	UV resistant
PEEK	No	Yes	Yes	Yes
PTFE	No	Yes	Yes	Yes
Polycarbonate	Yes	Yes	No	No
PVC	No	Yes (up to 200°C)	No	Yes
PMMA	Yes	Yes (up to 80°C)	Yes	Yes
POM	No	No	Yes	No

One of the main constraints is related to the compatibility with Fluoral-P reagent at temperatures around $T_2 = 338.15 K$. Whether the material releases or not HCHO from its bulk is also important. Some polymers contain in their structure HCHO molecules which are released in the fluid. Obviously, this has to be avoided in order to avoid the sample contamination. If the optical detection component is considered here, transparency is another key factor. Among typical polymers used for the fabrication of microfluidic chips, Poly (methyl methacrylate) (PMMA) has been selected for the current application as mechanical support structure for the meandering channels since, at least theoretically, it seems to obey the main constraints (see [Table 6.2.1](#)).

PMMA does not naturally release HCHO from its bulk structure up to $T = 353 K$ and it is not known as a HCHO absorbent. Moreover, PMMA does not react with Fluoral-P reagent. Its glass transition temperature may be compatible with the thermal mechanism of on-chip

membrane integration as presented in Wang *et al.*, [204]. PMMA is partially hydrophilic with a contact angle of approximately $\theta = 70^\circ$ [196].

Membrane

A double-layer hydrophobic membrane already used successfully into a related-approach has been selected. The membrane was used for carbon dioxide separation from a water-methanol solution resulting in a separation efficiency of 100 standard mL/min for a $A = 114.5 \text{ mm}^2$ contacting area [205] (see [Table 6.2.2.](#) and [Appendix A5. Hydrophobic membrane Data Sheet](#)).

The two layers which possess different thicknesses have different and complementary roles (see [Fig. 6.2.1.](#)). The upper-layer (or the active layer) is made of hydrophobic material with a contact angle around $\theta = 120^\circ$. The active layer of the selected membrane is $H_a = 10 \text{ }\mu\text{m}$ thick and it is made of expanded polytetrafluoroethylene (ePTFE). Practically, its main role is to avoid

Table 6.2.2. Characteristics of the double-sided hydrophobic membrane.

Membrane	Pore diameter	Contact angle	Support layer	Backer layer
Aspire, QL 217	200 nm	120°	ePTFE (30 μm)	Polyester (170 μm)

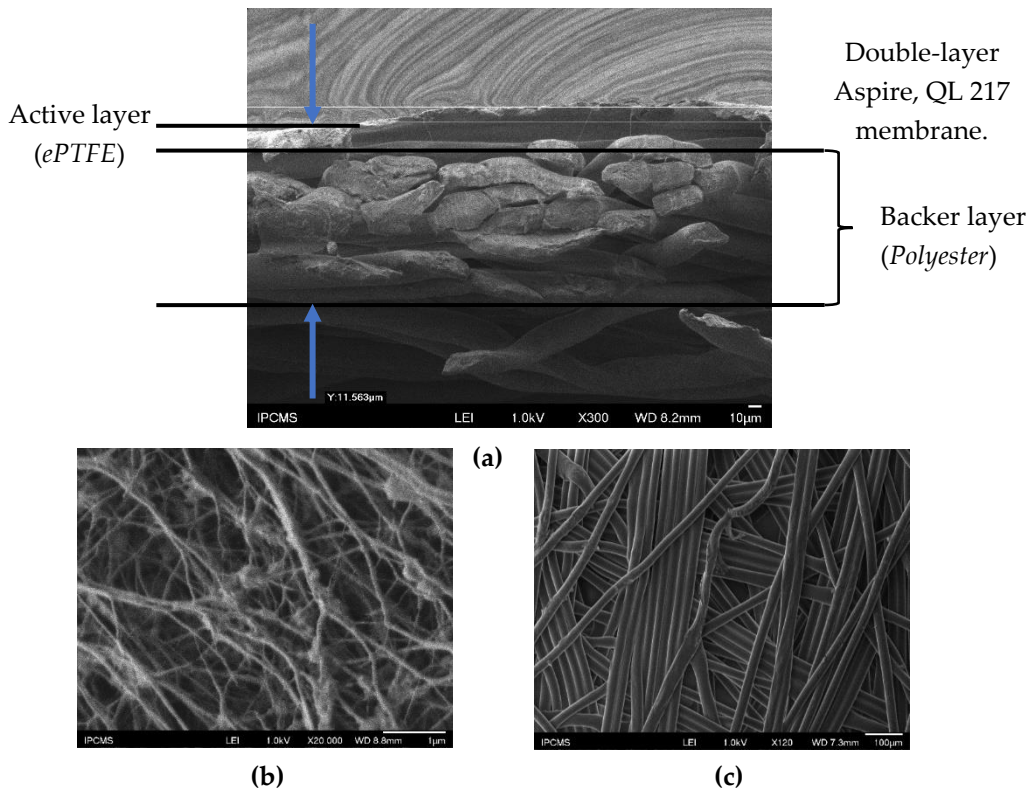


Figure 6.2.1. Scanning Electron Microscopy (SEM) analysis of (a) the double-layer Aspire, QL 217 hydrophobic membrane with the cross-section of the active and backer layers, (b) pore distribution on the upper-side of the active layer, (c) pore distribution on the lower-side of the backer layer.

reagent-fouling of the pores which would drastically decrease the diffusive flux across the membrane. Majority of the ePTFE materials are characterized by high porosities, $\varepsilon_m = 70 - 75\%$ for $d_p = 200 \text{ nm}$ (see Fig. 6.2.2.), which is advantageous in terms of flux diffusion rates.

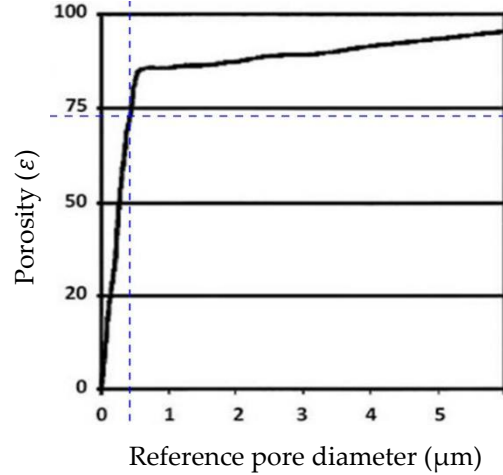


Figure 6.2.2. The expanded-polytetrafluoroethylene (ePTFE) porosity, ε_m , depending on the reference pore size. The vertical and horizontal lines show the estimated porosity ($\cong 70 - 75\%$) for a reference pore diameter of 200 nm. Reproduced from [243].

The backer layer which is thicker ($H_b = 190 \mu\text{m}$ thickness) is made of polyester. It mechanically supports the active layer. Its pore reference diameters are usually much larger compared to those of the active layer and diffusion is usually much faster here. In the active layer, the pore diameters are usually comparable with the molecular mean free path, λ . This aspect activates the Knudsen diffusion. This adds an additional mass-transfer resistance component to the diffusive flux and it is the compromise made to avoid the fouling of the membrane.

The mean free path of the HCHO molecules in a porous media with a reference pore diameter of $d_p = 200 \text{ nm}$ and the Knudsen number are calculated using the equations stated in Table 2.2.1. It is found that mean free path is $\lambda_1 = 6.63 \cdot 10^{-8}$ for $T_1 = 296.15 \text{ K}$ and $\lambda_2 = 7.58 \cdot 10^{-8}$ for $T_2 = 338.15 \text{ K}$. Kn is found as $Kn_1 = 0.33$ at $T_1 = 296.15 \text{ K}$ and as $Kn_2 = 0.37$ at $T_2 = 338.15 \text{ K}$. Mean free path is influenced by pressure. The above values are calculated at the atmospheric pressure.

Thus, HCHO diffusion in the pores is characterized by a transition regime with a combined viscous and Knudsen diffusion (see Eq. A.6.3. in Appendix A6.), the overall-effective diffusion coefficient, D_{eff} , being calculated using Eq. A.6.4. from the same Appendix. Bruggeman correlation [244] was used to link the membrane porosity to the tortuosity:

$$\tau_m = \varepsilon_m^{-1/2}$$

$$D_{eff1} = \frac{\varepsilon_m}{\tau_m} \left(\frac{1}{D_{Kn_1}} + \frac{1}{D_G} \right)^{-1} = 7.98 \cdot 10^{-6} \frac{\text{m}^2}{\text{s}} \quad (6.2.1.)$$

$$D_{eff2} = \frac{\varepsilon_m}{\tau_m} \left(\frac{1}{D_{Kn_2}} + \frac{1}{D_G} \right)^{-1} = 8.17 \cdot 10^{-6} \frac{m^2}{s} \quad (6.2.2.)$$

6.3. Front-end microchannel fabrication

Next step involves the fabrication of the microchannels supposed to carry the air and liquid streams. A two-layer structure with the hydrophobic membrane in-between was proposed using PMMA, the polymer identified as potentially-compatible with the Fluoral-P reagent interaction (see Fig. 6.3.1.).

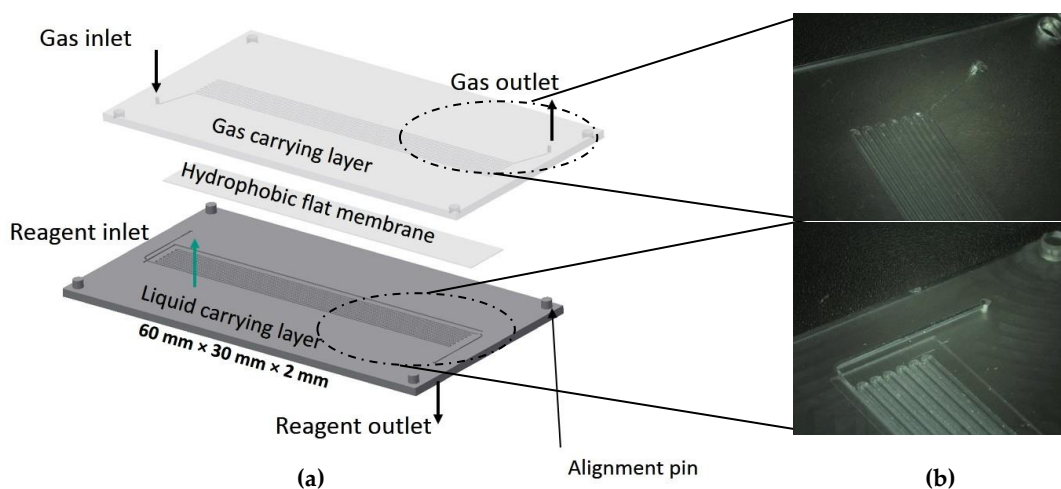


Figure 6.3.1. (a) Gas-liquid PMMA chip contactor with the on-chip integrated membrane; (b) Meandering channels micro-milled on PMMA flat structure.

Each PMMA layer hosted a meandering micro-channel of rectangular cross-section (see Fig. 6.3.1. b). The meandering channels started and ended with vertical holes serving as fluidic inlets and outlets. One layer was assigned to the reagent streaming (liquid carrying layer) and one to the gas streaming (gas carrying layer).

The meandering channels were micro-milled (LT Ultra Milling, MMC600 Z2) with $\pm 20 \mu\text{m}$ precision (see Fig. 6.3.2.). During the micro-milling process, a vacuum chuck was used to maintain the horizontality of the PMMA sheets in order to assure a constant depth of the channel.

The micro-channels were finally rinsed and washed with deionized water to remove the impurities resulting from the milling process. This process was not fully efficient, some micro-particles being observed in the channel at the end of the rinsing process, potentially clogging the channel.

The liquid carrying layer has been equipped with a rectangular pocket (150 μm depth) for hosting the polymeric membrane (see Fig. 6.3.1. b and Appendix A7. Technical drawing of the gas carrying layer).

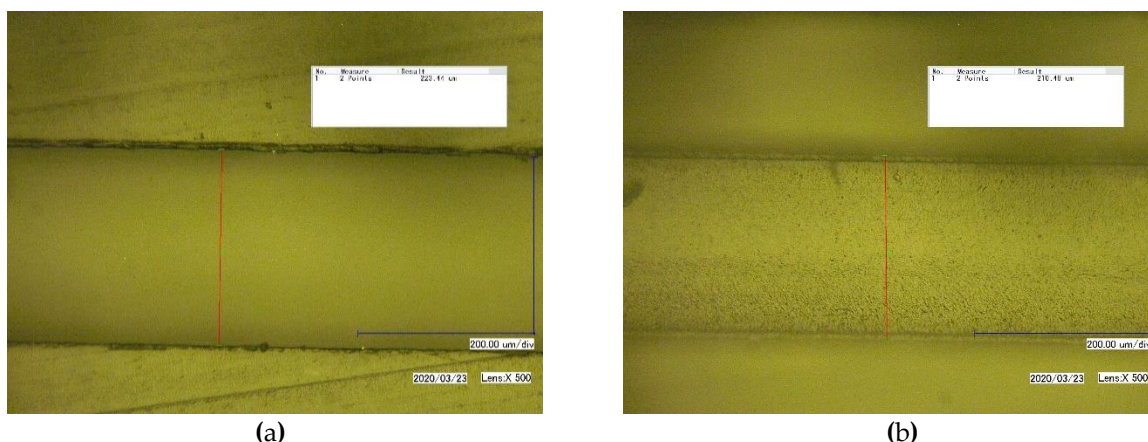


Figure 6.3.2. Liquid carrying micro-channel. (a) 223 μm width - top side; (b) 210 μm width – bottom side.

6.4. Back-end microfluidics bonding

After the fabrication of the PMMA carrying layers and their rinsing, the next step involves membrane cutting and chip sealing. The hydrophobic membrane was cut using a CO_2 laser to fit the 150 μm deep pocket created on the gas PMMA layer (see [Appendix A7. Technical drawing of the gas carrying layer](#)). When the two structures were assembled, the two meandering channels were overlapped. The overlapping was assured through a system of four pins and holes (see [Fig. 6.3.1.](#) and [Appendixes A7 and A8. Technical drawing of the liquid carrying layer](#)).

The 50 μm length difference between the membrane thickness and the pocket depth was considered a possible solution to avoid fluidic short circuits between the meandering channels. More exactly, when the two PMMA layer structures were clamped and bonded together, the polymeric membrane was supposed to be $d = 50 \mu\text{m}$ compressed. The feasibility of this solution to avoid the fluidic short-circuits is supposed to be further tested experimentally.

First, a hot embossing procedure was tested, but it failed. The very thin ePTFE active layer melted in the process or the milled channels collapsed under the pressure cycles involved in this method. Second, a solvent-enhanced femtosecond laser welding was implemented showing promising perspectives. Sealing procedures based on this last method were not completed in the time frame of the current project.

The gas-liquid chip contactor was integrated in between two holders (see [Fig. 6.4.1.](#)). Each holder was equipped with an integrated heating and fluidic streaming system. On the gas carrying layer side of the PMMA chip contactor, the holder was equipped with leakage-free gas connectors (Swagelok, SS-100-1-1, 1/16" diameter tubing) and, on the liquid carrying layer side, with liquid connectors (IDEX HS, N-333, 10-32 coned, 1/16" diameter tubing).

At the current stage, the heat power is provided through cartridge heaters (Watlow, C1A-9602, 30 W power, 24V voltage) connected to copper foils (see [Fig. 6.4.1.](#)). The

holders were micro-machined in polyether ether ketone (PEEK) which was selected due to its low thermal conductivity, $q = 0.25 \text{ W}/(\text{m}^2\text{K})$ that would allow a better thermal control of the interior temperature.

Leakage is supposed to be avoided by implementing micro-O-rings (Parker, 6-1735 E540-80, $0.7 \text{ mm} \times 0.5 \text{ mm}$) for each fluidic inlet and outlet hosted by holders. When the PMMA chip contactor is clamped in-between the holder using screws, half of the O-ring is placed inside, the other half outside (see Fig. 6.4.1. b) - G) for each of the four inlets/outlets.

At this point, mechanical force supposed to act uniformly from the outside towards the interior PMMA chip contactor when the two holders are screwed together has to be considered. The pressure applied towards the inward part of the PMMA chip contactor should prevent inflation of the PMMA layers due to the flow-induced force (pressure drop), which has the resultant oriented outwards.

Overall, the influence of the force resultants impact can only be partially estimated analytically or computationally. A most reliable evaluation could be made through experimental validations. This can also determine whether the microfluidic path is short-circuited or not. Short-circuiting might indeed occur since the configuration of the micro-contactor does not consider bonding/welding of the regions between the channels (see Fig. 6.3.1. b)).

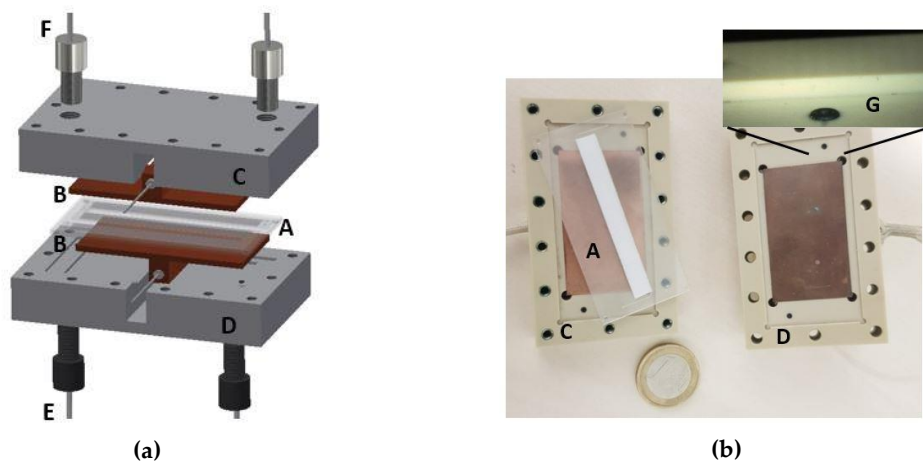


Figure 6.4.1. (a) Gas-liquid micro-reactor concept, exploded view: Gas-liquid PMMA chip contactor with the on-chip integrated membrane (A), copper layers thermally fueled by cartridge heaters (B), upper holder (C), lower holder (D), liquid connectors (E), gas connectors (F), micro-O-ring (G). (b) Fabricated components.

Chapter 7. Summary and outlook

7.1. Summary

7.1.1. CMOS-based fluorimeter

In conclusion, it has to be pointed out that the main achievements registered in this work are related to the intensity-based fluorescence detector built using mainly off-the-shelf components. Some guidelines to a possible gas-liquid flow micro-reactor for gaseous formaldehyde trapping and derivatization have been also discussed.

The response of the fluorescence detector integrating a CMOS-image sensor was tested for reagents containing HCHO concentrations ranging from 0.01 $\mu\text{g/mL}$ to 10 $\mu\text{g/mL}$. The signal obtained was not linear as expected in fluorescence-intensity based-assays. Although there is a report in the literature showing a non-linearity effect in the same concentration range, the non-linear effect observed in this work is very prominent. This result is not only unusual, but also unexpected.

However, the fluorescence detector proved its capability to clearly differentiate between the fluorescence signal and the background noise signal obtained for a 10 $\mu\text{g/L}$ HCHO derivatized into DDL ($\phi(20\text{ }^\circ\text{C}) = 0.005$) in 3.5 μL interrogation volume. This was the lowest concentration that could be distinctly distinguished out of the background noise.

The assays were conducted in parallel for two flow-through-microfluidic cell configurations. Both configurations were made of three overlapped thin layers. The lower- and middle-layers were similar, while the upper-layer was configuration specific. The quartz lower-layer is transparent in the fluorescence emission wavelength spectrum. The middle-layer was made of SU-8 3050 negative photoresist. This layer plays a double role. First, it hosts the fluidic circuit and the interrogation chamber. Second, it is the waveguide for the excitation light beam emitted by the LEDs. The upper-layer is made of quartz for the first configuration and of silicon for the second. The selection of silicon for the second configuration is justified by its absorption coefficient at the LED emission wavelength, $a(\lambda_{abs} = 420\text{ nm}) = 5 \cdot 10^4\text{ cm}^{-1}$, which is approximately five times higher than the absorption coefficient at the emission wavelength, $a(\lambda_{em} = 515\text{ nm}) = 9.25 \cdot 10^3\text{ cm}^{-1}$.

The two configurations have been tested in similar conditions and the signals registered for the two flow-through microfluidic cells were compared. An apparent higher SNR has been obtained for the silicon fluidic cell ($SNR = 6.1$, $RSD = 5.3\%$, $N = 2$) relative to the quartz fluidic cell ($SNR = 4.9$, $RSD = 9.1\%$, $N = 2$). However, this result has to be checked for a higher number of reciprocates to confirm its meaningfulness.

The non-linearity of the fluorescence signal intensity is attributed to the errors introduced by the experimental procedure, modular distribution of the off-the-shelf components, possible

photobleaching effects due to repeated excitation of the same sample, or to optical events due to the shape of the SU-8 3050 optical waveguide caused by the shape of the interrogation chamber.

7.1.2. Gas-liquid micro-reactor

A gas-liquid micro-reactor concept for formaldehyde trapping and derivatization was introduced. Preliminary steps regarding the hydrodynamic conditions, compatible materials, and sub-components fabrication have been done.

After fabrication of the sub-systems of the gas-liquid micro-reactor, further results are expected in order to experimentally prove the concept. The interest here is to enable enhanced and efficient HCHO trapping using cost-efficient on-chip membrane-based polymer chips.

A mathematical model for the estimation of HCHO trapping into the reagent stream using a hydrophobic membrane was developed and presented in Mariuta *et al.* [21] (see [Appendix A6](#)).

7.2. Outlook

The above section summarized the achievements with respect to the two components developed. Now, a couple of possible directions to improve them are presented.

7.2.1. CMOS-based fluorimeter

Although the repeatability of the results has to be tested for more independently prepared samples in order to fully-validate the system, this work presented a solution with a quantifiable potential for the on-chip integration of the detection component.

Reasons that generate the non-linearity have to be identified and quantified. The author proposes the following list of possible tests and improvements based on the flaws and mistakes identified in the design and experimental procedure implemented:

1. Quantification of the memory effects

Sticking molecules were observed inside the flow-through cells after measurements. It was not clear if their presence was due to accumulation in the continuous streaming process or if they were present after the rapid evaporation of the solution. If the memory effects are confirmed, then continuous sampling is not feasible in flow-through cell. However, there are coating materials that could be used in order to avoid them, although this will introduce more optical complexity.

2. Precise control of the LED excitation light intensity

The high-power LED used for current experiments was shot-on at relatively low-powers for short periods of time (approximately 1s) and shot-off for approximately similar periods of time. This was done mainly to avoid excitation wavelength shift due to thermal effects. However, the radiant flux intensity was not measured at the current research level.

3. Quantification of possible photobleaching effects

Moreover, the impact of the radiant intensity over the fluorophores in terms of irreversible destruction may be studied. From the author's point of view, this could be the main cause of the non-linear behavior observed. In the design process, it was estimated that two LEDs are needed

to properly illuminate the interrogation chamber which has a relatively high width-to-depth ratio. However, doubling the excitation light might have contributed to the photobleaching effects as well.

4. Control the temperature in the interrogation chamber

In order to avoid large variations of the fluorophore quantum yield, ideally, the sample temperature should be maintained constant and monitored.

5. Coat a thin-filtration layer on top of the CMOS-image sensor surface

The 1 mm thickness band-pass filter could be replaced by a filtration layer, coated directly on top of the CMOS image sensor, as described by Guduru *et al.* [134] or Sunaga *et al.* [245]. This would further diminish the optical path length and lead towards a fully-integrated monolithic device. Moreover, a filterless configuration based on time-resolved detection methodology could be employed as described by Măriuța *et al.* [21]. This methodology avoids practically the optical background noise, but its implementation is strictly related to the working frequency of the processor involved, since the DDL molecule fluorescence decay time is only limited to 2 ns.

6. Replace quartz with a compatible polymer

PMMA polymer, providing very good optical properties, might be considered as a potential material for the fabrication and testing of a new configuration of the fluidic cell in order to reduce the fabrication cost and its complexity. Its implementation as waveguide for biomedical applications and its potential for wearable and in vivo applications, is currently studied [154], making it a promising material for such an application. Here attention has to be paid on the surface roughness that results from the fabrication process, possible swelling by liquids and its autofluorescence.

7. Study the effect of the concave ending of the waveguide

The light beam travels from the LED towards the detection chamber through the SU-8 3050 waveguide, crossing the flat beginning and getting inside the interrogation chamber through the concave ending as it can be observed in [Fig. 5.4.2. a](#). In the same figure, the diverging behavior of the light passing through the end of the wavelength can be seen. In perspective, it might be quantified whether the beam diverging effect at the end of the waveguide affect the illumination homogeneity in the liquid bulk.

8. Lab-on-a-CMOS concept

A possible direction could concern the development of a fully-made silicon structure considering the CMOS image sensor validation for this application and the SNR enhancement observed for silicon. The potential of this device could go beyond this specific application, contributing to the rapid developing field of on-chip fluorescence sensing for various applications of rapid and low-cost monitoring in chemistry, biology or in the environment monitoring.

7.2.2. Gas-liquid micro-reactor

The author proposes here a list of steps for further development of the prototype:

1. On-chip membrane integration using solvent-enhanced femtosecond laser welding.
2. Heat transfer study in order to assure a uniform and constant temperature in the micro-reactor.
3. Experimental evaluation of the gas-liquid micro-reactor concept in terms of leakage-free operation, memory effects freedom, mass-transfer coefficients, trapping efficiency.
4. System integration study has to be performed in order to identify solutions for low-noise, cost-effective fluid pumping.
5. Coupling the miniaturized optical fluorimeter with the gas-liquid micro-reactor (cooling down of the solution and enough residence time have to be assured).

Finally, the author dares to anticipate that for an instrument LOD lower than 1 $\mu\text{g/L}$ in detection volumes lower than 1 μL , the slug two-phase flow pattern might be successful in trapping HCHO molecules into an ultra-miniaturized μTAS system.

Bibliography

1. Balmes, J.R. Household air pollution from domestic combustion of solid fuels and health. *J. Allergy Clin. Immunol.* **2019**, *143*, 1979–1987, doi:10.1016/j.jaci.2019.04.016.
2. Squire, R.A.; Cameron, L.L. An analysis of potential carcinogenic risk from formaldehyde. *Regul. Toxicol. Pharmacol.* **1984**, *4*, 107–129, doi:10.1016/0273-2300(84)90034-5.
3. Casset, A.; Marchand, C.; Purohit, A.; Le Calve, S.; Uring-Lambert, B.; Donnay, C.; Meyer, P.; de Blay, F. Original article Inhaled formaldehyde exposure : effect on bronchial response to mite allergen in sensitized asthma patients. *Allergy* **2006**, *61*, 1344–1350, doi:10.1111/j.1398-9995.2006.01174.x.
4. Nielsen, G.D.; Larsen, S.T.; Wolkoff, P. Re-evaluation of the WHO (2010) formaldehyde indoor air quality guideline for cancer risk assessment. *Arch. Toxicol.* **2017**, *91*, 35–61, doi:10.1007/s00204-016-1733-8.
5. Salthammer, T.; Mentese, S.; Marutzky, R. Formaldehyde in the indoor environment. *Chem. Rev.* **2010**, *110*, 2536–2572, doi:10.1021/cr800399g.
6. Becker, A.; Andrikopoulou, C.; Bernhardt, P.; Ocampo-Torres, R.; Trocquet, C.; Le Calvé, S. Development and Optimization of an Airborne Formaldehyde Microfluidic Analytical Device Based on Passive Uptake through a Microporous Tube. *Micromachines* **2019**, *10*, 807, doi:https://doi.org/10.3390/mi10120807.
7. ANSES—Agence nationale de sécurité sanitaire de l’alimentation, de l’environnement et du travail. Valeurs Guides de Qualité d’Air Intérieur (VGAI). Le Formaldéhyde. Available online: <https://www.anses.fr/fr/system/files/AIR2017SA0041Ra.pdf> (accessed on Mar 17, 2022).
8. Guglielmino, M.; Allouch, A.; Serra, C.A.; Le Calvé, S. Development of microfluidic analytical method for on-line gaseous Formaldehyde detection. *Sensors Actuators, B Chem.* **2017**, *243*, 963–970, doi:10.1016/j.snb.2016.11.093.
9. 5-HMF: The key to green chemistry. Available online: <https://5-hmf.com/> (accessed on Mar 17, 2022).
10. Papageorgiou, E.P.; Boser, B.E.; Anwar, M. Chip-scale fluorescence imager for in vivo microscopic cancer detection. In Proceedings of the IEEE Symposium on VLSI Circuits, Digest of Technical Papers; Kyoto, Japan, 2017; pp. C106–C107.
11. Wessels, L.; Raad, H. Recent advances in point of care diagnostic tools: A review. *Am. J. Eng. Appl. Sci.* **2016**, *9*, 1088–1095, doi:10.3844/ajeassp.2016.1088.1095.
12. Boppart, S.A.; Richards-Kortum, R. Point-of-care and point-of-procedure optical imaging technologies for primary care and global health. *Sci. Transl. Med.* **2014**, *6*, doi:10.1126/scitranslmed.3009725.
13. Sharma, M.K.; Göstl, R.; Frijns, A.J.H.; Wieringa, F.P.; Kooman, J.P.; Sijbesma, R.P.; Smeulders, D.M.J. A Fluorescent Micro-Optofluidic Sensor for In-Line Ion Selective Electrolyte Monitoring. *IEEE Sens. J.* **2018**, *18*, 3946–3951, doi:10.1109/JSEN.2018.2816986.
14. Zi, C.; Shi, J.; Tai, Y.; Yang, H.; Li, X. Design of Portable Time-Resolved Fluorometer. *Adv. Biosci. Bioeng.* **2016**, *4*, 79, doi:10.11648/j.abb.20160406.13.
15. Kilic, T.; Navaee, F.; Stradolini, F.; Renaud, P.; Carrara, S. Organs-on-chip monitoring: sensors and other strategies. *Microphysiological Syst.* **2018**, *2*, doi:10.21037/mps.2018.01.01.
16. Zhang, Y.S.; Ribas, J.; Nadhman, A.; Aleman, J.; Selimović, Š.; Leshner-Perez, S.C.; Wang, T.; Manoharan, V.; Shin, S.R.; Damilano, A.; et al. A cost-effective fluorescence mini-microscope for biomedical applications. *Lab Chip* **2015**, *15*, 3661–3669, doi:10.1039/c5lc00666j.
17. Si Hadj Mohand, H.; Frezzotti, A.; Brandner, J.J.; Barrot, C.; Colin, S. Molecular tagging velocimetry by direct phosphorescence in gas microflows : correction of Taylor dispersion. *Exp. Therm. Fluid Sci.*

- 2017, 83, 177–190, doi:10.1016/j.expthermflusci.2017.01.002.
18. Bhattacharya, B.; Singha, S.; Basu, S. *Fluorescent nanosensors: rapid tool for detection of food contaminants*; Elsevier Inc., 2017; ISBN 9780128043011.
 19. Calvé, S. Le; Trocquet, C.; Bernhardt, P. A Novel Microfluidic Formaldehyde Microanalyser for Continuous Real-Time Monitoring in Indoor Air: Analytical Development and Validation. In *Proceedings of the Multidisciplinary Digital Publishing Institute Proceedings*; Barcelona, Spain, 2017; Vol. 1, p. 740.
 20. Ricciardi, A.; Crescitelli, A.; Vaiano, P.; Quero, G.; Consales, M.; Pisco, M.; Esposito, E.; Cusano, A. Lab-on-fiber technology: A new vision for chemical and biological sensing. *Analyst* **2015**, *140*, 8068–8079, doi:https://doi.org/10.1039/C5AN01241D.
 21. Măriuța, D.; Baldas, L.; Colin, S.; Calvé, S. Le; Korvink, J.G.; Brandner, J.J. Prototyping a Microfluidic Sensor for Real - Time Detection of Airborne Formaldehyde. *Int. J. Chem. Eng. Appl.* **2020**, *11*, 23–28, doi:10.18178/ijcea.2020.11.1.774.
 22. Rezende, G.C.; Le Calvé, S.; Brandner, J.J.; Newport, D. Chemical Micro photoionization detectors. *Sensors Actuators B. Chem.* **2019**, *287*, 86–94, doi:10.1016/j.snb.2019.01.072.
 23. Chen, Y.-F.; Jiang, L.; Mancuso, M.; Jain, A.; Oncescu, V.; Erickson, D. Nanoscale Optofluidic opportunities in global health , food , water and energy. *Nanoscale* **2012**, 4839–4857, doi:10.1039/c2nr30859b.
 24. Zhao, Z.; Luan, W.; Yin, S.; Brandner, J.J. Metal crack propagation monitoring by photoluminescence enhancement of quantum dots. *Appl. Opt.* **2015**, *54*, 6498–6501, doi:10.1364/ao.54.006498.
 25. Ríos, Á.; Zougagh, M.; Avila, M. Miniaturization through lab-on-a-chip: Utopia or reality for routine laboratories? A review. *Anal. Chim. Acta* **2012**, *740*, 1–11, doi:10.1016/j.aca.2012.06.024.
 26. Ackermann, T.N.; Dietvorst, J.; Sanchis, A.; Salvador, J.P.; Munoz-Berbel, X.; Alvarez-Conde, E.; Kopp, D.; Zappe, H.; Marco, M.-P.; Llobera, A. Modular Optofluidic Systems (MOPS). In *Proceedings of the SPIE BioPhotonics Australasia*; Adelaide, Australia, 2016; Vol. 10013, p. 100131C.
 27. Mohammed, M.I.; Haswell, S.; Gibson, I. Lab-on-a-chip or Chip-in-a-lab: Challenges of Commercialization Lost in Translation. *Procedia Technol.* **2015**, *20*, 54–59, doi:10.1016/j.protcy.2015.07.010.
 28. Volpatti, L.R.; Yetisen, A.K. Commercialization of microfluidic devices. *Trends Biotechnol.* **2014**, *32*, 347–350, doi:10.1016/j.tibtech.2014.04.010.
 29. Gunther, A.; Kreutzer, M.T. *Part I: Fluid dynamics in microchannels*. In *Micro Process Engineering, Vol.1: Fundamentals, Operations and Catalysts*; WILEY-VCH Verlag GmbH & Co. KGaA, Weinheim 2009; ISBN 9783527315505.
 30. Guglielmino, M.; Allouch, A.; Serra, C.A.; Calvé, S. Le Development of microfluidic analytical method for on-line gaseous formaldehyde detection. *Sensors Actuators, B Chem.* **2017**, *243*, 963–970, doi:10.1016/j.snb.2016.11.093.
 31. In'Air μ F-1: Analyseur microfluidique transportable pour la détection du formaldéhyde en air intérieur. Available online: http://www.verification-etv.fr/upload/Le_programme_ETV/Decla_ETV_InAirSolutions.pdf (accessed on Mar 17, 2022).
 32. Guglielmino, M.; Bernhardt, P.; Trocquet, C.; Serra, C.A.; Le Calvé, S. On-line gaseous formaldehyde detection by a microfluidic analytical method based on simultaneous uptake and derivatization in a temperature controlled annular flow. *Talanta* **2017**, *172*, 102–108, doi:10.1016/j.talanta.2017.05.038.
 33. Trocquet, C.; Bernhardt, P.; Guglielmino, M.; Malandain, I.; Liaud, C.; Englaro, S.; Le Calvé, S. Near real-time monitoring of formaldehyde in a low-energy school building. *Atmosphere (Basel)*. **2019**, *10*, 1–19, doi:10.3390/atmos10120763.
 34. Geddes, C.D.; Lakowicz, J.R. *Reviews in Fluorescence 2016*; Springer, 1st Ed. 2017; ISBN 9783319482590.
 35. Christopoulos, T.K.; Diamandis, E. Fluorescence Immunoassays. In *Immunoassay*; Academic Press,

- Inc., 1996; pp. 309–335 ISBN 978-0-12-214730-2.
36. Demchenko, A.P. *Introduction to fluorescence sensing*; Springer Science + Business Media B.V, 2009; ISBN 9781402090035.
 37. Wei, L.; Yan, W.; Ho, D. Recent advances in fluorescence lifetime analytical microsystems: Contact optics and CMOS time-resolved electronics. *Sensors* **2017**, *17*, doi:10.3390/s17122800.
 38. Măriuța, D.; Colin, S.; Barrot-Lattes, C.; Le Calvé, S.; Korvink, J.G.; Baldas, L.; Brandner, J.J. Miniaturization of fluorescence sensing in optofluidic devices. *Microfluid. Nanofluidics* **2020**, *24*, 1–28, doi:10.1007/s10404-020-02371-1.
 39. Kuswandi, B.; Nuriman; Huskens, J.; Verboom, W. Optical sensing systems for microfluidic devices: A review. *Anal. Chim. Acta* **2007**, *601*, 141–155. <https://doi.org/10.1016/j.aca.2007.08.046>
 40. Tang, J.; Qiu, G. Recent Development of Optofluidics for Imaging and Sensing Applications. *Chemosensors* **2022**, *10*, doi:<https://doi.org/10.3390/chemosensors10010015>.
 41. Tsao, C.W. Polymer microfluidics: Simple, low-cost fabrication process bridging academic lab research to commercialized production. *Micromachines* **2016**, *7*, doi:10.3390/mi7120225.
 42. Guckenberger, D.J.; De Groot, T.E.; Wan, A.M.D.; Beebe, D.J.; Young, E.W.K. Micromilling: A method for ultra-rapid prototyping of plastic microfluidic devices. *Lab Chip* **2015**, *15*, 2364–2378, doi:10.1039/c5lc00234f.
 43. Yen, C.Y.; Chang, M.C.O.; Shih, Z.F.; Lien, Y.H.; Tsao, C.W. Cyclic block copolymer microchannel fabrication and sealing for microfluidics applications. *Inventions* **2018**, *3*, doi:10.3390/inventions3030049.
 44. Wu, J.; Gu, M. Microfluidic sensing: state of the art fabrication and detection techniques. *J. Biomed. Opt.* **2011**, *16*, 080901, doi:10.1117/1.3607430.
 45. Yeh, P.; Yeh, N.; Lee, C.H.; Ding, T.J. Applications of LEDs in optical sensors and chemical sensing device for detection of biochemicals, heavy metals, and environmental nutrients. *Renew. Sustain. Energy Rev.* **2017**, *75*, 461–468, doi:10.1016/j.rser.2016.11.011.
 46. Yang, H.; Gijs, M.A.M. Micro-optics for microfluidic analytical applications. *Chem. Soc. Rev.* **2018**, *47*, 1391–1458, doi:10.1039/c5cs00649j.
 47. Chen, J.; Loeb, S.; Kim, J. LED revolution: fundamentals and prospects for UV disinfection applications. *Environ. Sci. Water Res. Technol.* **2017**, *3*, 188–202, doi:10.1039/C6EW00241B.
 48. Okamoto, K. *Fundamentals of Optical Waveguides*; 2nd Ed.; Academic Press: San Diego, California, 2006; ISBN 9780125250962.
 49. Kanamori, Y. High-Efficiency Optical Filters Based on Nanophotonics. *IEEJ Trans. Electr. Electron. Eng.* **2021**, 662–672, doi:10.1002/tee.23345.
 50. Sudhakaran, S. What is the difference between CIE LAB, CIE RGB, CIE xyY and CIE XYZ? Available online: <https://wolfcrow.com/what-is-the-difference-between-cie-lab-cie-rgb-cie-xyy-and-cie-xyz/> (accessed on Dec 20, 2019).
 51. Bueno Hernández, D.; Mishra, R.K.; Muñoz, R.; Marty, J.L. Low cost optical device for detection of fluorescence from Ochratoxin A using a CMOS sensor. *Sensors Actuators, B Chem.* **2017**, *246*, 606–614, doi:10.1016/j.snb.2017.02.097.
 52. Armbruster, D.A.; Pry, T. Limit of Blank, Limit of Detection, and Limit of Quantification. *Clin Biochem Rev.* **2008** Aug; 29 Suppl 1(Suppl 1):S49-52. PMID: 18852857; PMCID: PMC2556583.
 53. Geng, Y.; Ling, S. Da; Huang, J.; Xu, J. Multiphase Microfluidics: Fundamentals, Fabrication, and Functions. *Small* **2020**, *16*, 1–20, doi:10.1002/smll.201906357.
 54. Nakahara, Y.; Metten, B.; Tonomura, O.; Nagaki, A.; Hasebe, S.; Yoshida, J.I. Modeling and Design of a Flow-Microreactor-Based Process for Synthesizing Ionic Liquids. *Org. Process Res. Dev.* **2019**, *23*, 641–647, doi:10.1021/acs.oprd.8b00436.
 55. Lauterböck, B.; Moder, K.; Germ, T.; Fuchs, W. Impact of characteristic membrane parameters on the transfer rate of ammonia in membrane contactor application. *Sep. Purif. Technol.* **2013**, *116*, 327–

- 334, doi:10.1016/j.seppur.2013.06.010.
56. de Jong, J.; Geerken, M.J.; Lammertink, R.G.H.; Wessling, M. Porous microfluidic devices - Fabrication and applications. *Chem. Eng. Technol.* **2007**, *30*, 309–315, doi:10.1002/ceat.200600364.
 57. Natrajan, V.K.; Christensen, K.T. The impact of surface roughness on flow through a rectangular microchannel from the laminar to turbulent regimes. *Microfluid. Nanofluidics* **2010**, *9*, 95–121, doi:10.1007/s10404-009-0526-2.
 58. Hardt, S. Modeling and Simulation of Microreactors. In *Modeling of Process Intensification*; Wiley-VCH Verlag GmbH & Co. KGaA, 2007; pp. 25–78 ISBN 9783527311439.
 59. Bretherton, F.P. The motion of long bubbles in tubes. *J. Fluid Mech.* **1961**, *10*, 166, doi:10.1063/1.858832.
 60. Hrnjak, P. Single phase pressure drop in microchannels. *Int. J. Heat Fluid Flow* **2007**, *28*, 2–14, doi:10.1016/j.ijheatfluidflow.2006.05.005.
 61. Asadi, M.; Xie, G.; Sunden, B. A review of heat transfer and pressure drop characteristics of single and two-phase microchannels. *Int. J. Heat Mass Transf.* **2014**, *79*, 34–53, doi:10.1016/j.ijheatmasstransfer.2014.07.090.
 62. Triplett, K.A.; Ghiaasiaan, S.M.; Abdel-Khalik, S.I.; LeMouel, A.; McCord, B.N. Gas-liquid two-phase flow in microchannels Part II: Void fraction and pressure drop. *Int. J. Multiph. Flow* **1999**, *25*, 395–410, doi:10.1016/S0301-9322(98)00055-X.
 63. Serizawa, A.; Feng, Z.; Kawara, Z. Two-phase flow in microchannels. *Exp. Therm. Fluid Sci.* **2002**, *26*, 703–714, doi:10.1201/b19261-22.
 64. Rebrov, E. V. Two-phase flow regimes in microchannels. *Theor Found Chem Eng* **2010**, *44*, 371–383, doi:10.1134/S0040579510040019.
 65. Haase, S. International Journal of Multiphase Flow Characterisation of gas-liquid two-phase flow in minichannels with co-flowing fluid injection inside the channel , part II : gas bubble and liquid slug lengths , film thickness , and void fraction within Taylor flo. *Int. J. Multiph. Flow* **2017**, *88*, 251–269, doi:10.1016/j.ijmultiphaseflow.2016.09.002.
 66. Liu, J.; Li, X.; Yang, Y.; Wang, H.; Kuang, C.; Chen, M.; Hu, J.; Zeng, L.; Zhang, Y. Sensitive Detection of Ambient Formaldehyde by Incoherent Broadband Cavity Enhanced Absorption Spectroscopy Sensitive Detection of Ambient Formaldehyde by Incoherent Broadband Cavity Enhanced Absorption Spectroscopy. *Anal. Chem.* **2020**, *92*, 2697–2705, doi:10.1021/acs.analchem.9b04821.
 67. Foster, F.D.; Stuff, J.R.; Thaxton, K.; Pfannkoch, E.A. Automated Online Desorption and Analysis of DNPH Derivatives of Airborne Aldehydes and Ketones Available online: <https://anatune.co.uk/wp-content/uploads/2018/03/GA9.pdf> (accessed on Mar 18, 2022).
 68. Mann, B.; Grayeski, M.L. New chemiluminescent derivatizing agent for the analysis of aldehydes and ketones by high-performance liquid chromatography with peroxyoxalate chemiluminescence. *J. Chromatogr. A* **1987**, *386*, 149–158, doi:10.1016/S0021-9673(01)94592-3.
 69. Levin, J.O.; Andersson, K.; Lindahl, R.; Nilsson, C.A. Determination of sub-part-per-million levels of formaldehyde in air using active or passive sampling on 2,4-dinitrophenylhydrazine-coated glass fiber filters and high-performance liquid chromatography. *Anal. Chem.* **1985**, *57*, 1032–1035, doi:doi.org/10.1021/ac00283a016.
 70. Dugheri, S.; Bonari, A.; Pompilio, I.; Colpo, M.; Mucci, N.; Montalti, M.; Arcangeli, G.; Brambilla, L.G.A.; Morgagni, V.G.B. Development of an Innovative Gas Chromatography – Mass Spectrometry Method for Assessment of Formaldehyde in the Workplace Atmosphere. *Acta Chromatogr.* **2017**, *29*, 511–514, doi:10.1556/1326.2016.00102.
 71. Lorrain, J.M.; Fortune, C.R.; Dellinger, B. Sampling and Ion Chromatographic Determination of Formaldehyde and Acetaldehyde. *Anal. Chem.* **1981**, *53*, 1302–1305, doi:10.1021/ac00231a038.
 72. Cihelka, J.; Matulková, I.; Civiš, S. Laser diode photoacoustic and FTIR laser spectroscopy of formaldehyde in the 2.3 μm and 3.5 μm spectral range. *J. Mol. Spectrosc.* **2009**, *256*, 68–74,

- doi:10.1016/j.jms.2009.01.017.
73. Hanoune, B.; LeBris, T.; Allou, L.; Marchand, C.; Le Calvé, S. Formaldehyde measurements in libraries: Comparison between infrared diode laser spectroscopy and a DNPH-derivatization method. *Atmos. Environ.* **2006**, *40*, 5768–5775, doi:10.1016/j.atmosenv.2006.05.017.
 74. Blake, R.S.; Monks, P.S.; Ellis, A.M. Proton-Transfer Reaction Mass Spectrometry. *Chem. Rev.* **2009**, *109*, 861–896, doi:10.1002/chin.200923275.
 75. Warneke, C.; Veres, P.; Holloway, J.S.; Stutz, J.; Tsai, C.; Alvarez, S.; Rappenglueck, B.; Fehsenfeld, F.C. Airborne formaldehyde measurements using PTR-MS: calibration, humidity dependence, inter-comparison and initial results. *Atmos. Meas. Tech.* **2011**, *4*, 2345–2358, doi:10.5194/amt-4-2345-2011.
 76. Winkowski, M.; Stacewicz, T. Optical detection of formaldehyde in air in the 3.6 μm range. *Biomed. Opt. Express* **2020**, *11*, 7019–7031, doi:https://doi.org/10.1364/BOE.405384.
 77. Chung, P.R.; Tzeng, C.T.; Ke, M.T.; Lee, C.Y. Formaldehyde gas sensors: A review. *Sensors* **2013**, *13*, 4468–4484, doi:10.3390/s130404468.
 78. Li, H.; Li, Y.; Li, M.; Xu, L.; Li, J. Facile and ultrasensitive electrochemical impedance sensing for formaldehyde based on silver ions doped in controllable and homogeneous silica microspheres. *Sensors Actuators, B Chem.* **2019**, *284*, 657–662, doi:10.1016/j.snb.2019.01.021.
 79. van den Broek, J.; Klein Cerrejon, D.; Pratsinis, S.E.; Güntner, A.T. Selective formaldehyde detection at ppb in indoor air with a portable sensor. *J. Hazard. Mater.* **2020**, *399*, 123052, doi:10.1016/j.jhazmat.2020.123052.
 80. Güntner, A.T.; Abegg, S.; Wegner, K.; Pratsinis, S.E. Zeolite membranes for highly selective formaldehyde sensors. *Sensors Actuators, B Chem.* **2018**, *257*, 916–923, doi:10.1016/j.snb.2017.11.035.
 81. Guo, X.L.; Chen, Y.; Jiang, H.L.; Qiu, X.B.; Yu, D.L. Smartphone-based microfluidic colorimetric sensor for gaseous formaldehyde determination with high sensitivity and selectivity. *Sensors* **2018**, *18*, doi:10.3390/s18093141.
 82. Descamps, M.N.; Bordy, T.; Hue, J.; Mariano, S.; Nonglaton, G.; Schultz, E.; Tran-Thi, T.H.; Vignoud-Despond, S. Real-time detection of formaldehyde by a sensor. *Sensors Actuators, B Chem.* **2012**, *170*, 104–108, doi:10.1016/j.snb.2011.02.032.
 83. Baldelli, A.; Jeronimo, M.; Tinney, M.; Bartlett, K. Real-time measurements of formaldehyde emissions in a gross anatomy laboratory. *SN Appl. Sci.* **2020**, *2*, 1–13, doi:10.1007/s42452-020-2569-7.
 84. Noël, F.; Serra, C.A.; Le Calvé, S. Design of a novel axial gas pulses micromixer and simulations of its mixing abilities via computational fluid dynamics. *Micromachines* **2019**, *10*, 1–16, doi:10.3390/mi10030205.
 85. Tremblay, P.; Savard, M.M.; Vermette, J.; Paquin, R. Gas permeability, diffusivity and solubility of nitrogen, helium, methane, carbon dioxide and formaldehyde in dense polymeric membranes using a new on-line permeation apparatus. *J. Memb. Sci.* **2006**, *282*, 245–256, doi:10.1016/j.memsci.2006.05.030.
 86. Seyfioglu, R.; Odabasi, M. Investigation of air-water exchange of formaldehyde using the water surface sampler: Flux enhancement due to chemical reaction. *Atmos. Environ.* **2006**, *40*, 3503–3512, doi:10.1016/j.atmosenv.2006.01.048.
 87. Becker, A.; Andrikopoulou, C.; Bernhardt, P.; Trocquet, C.; Le Calvé, S. On-line gaseous formaldehyde detection based on a closed-microfluidic-circuit analysis. *Chemosensors* **2020**, *8*, 8–10, doi:10.3390/CHEMOSENSORS8030057.
 88. Allou, L.; El Maimouni, L.; Le Calvé, S. Henry's law constant measurements for formaldehyde and benzaldehyde as a function of temperature and water composition. *Atmos. Environ.* **2011**, *45*, 2991–2998, doi:10.1016/j.atmosenv.2010.05.044.
 89. Allouch, A.; Guglielmino, M.; Bernhardt, P.; Serra, C.A.; Le Calvé, S. Transportable, fast and high sensitive near real-time analyzers: Formaldehyde detection. *Sensors Actuators, B Chem.* **2013**, *181*,

- 551–558, doi:10.1016/j.snb.2013.02.043.
90. Liu, X.; Guo, Z.; Roache, N.F.; Mocka, C.A.; Allen, M.R.; Mason, M.A. Henry's law constant and overall mass transfer coefficient for formaldehyde emission from small water pools under simulated indoor environmental conditions. *Environ. Sci. Technol.* **2015**, *49*, 1603–1610, doi:10.1021/es504540c.
 91. Winkelman, J.G.M. Absorption of formaldehyde in water, PhD Thesis, Rijksuniversiteit Groningen, 2003.
 92. Leriche, M.; Deguillaume, L.; Chaumerliac, N. Modeling study of strong acids formation and partitioning in a polluted cloud during wintertime. *J. Geophys. Res. Atmos.* **2003**, *108*, doi:10.1029/2002jd002950.
 93. Barth, M.C.; Kim, S.W.; Skamarock, W.C.; Stuart, A.L.; Pickering, K.E.; Ott, L.E. Simulations of the redistribution of formaldehyde, formic acid, and peroxides in the 10 July 1996 Stratospheric-Tropospheric Experiment: Radiation, Aerosols, and Ozone deep convection storm. *J. Geophys. Res. Atmos.* **2007**, *112*, doi:10.1029/2006JD008046.
 94. Jayne, J.T.; Worsnop, D.R.; Kolb, C.E.; Swartz, E.; Davidovits, P. Uptake of gas-phase formaldehyde by aqueous acid surfaces. *J. Phys. Chem.* **1996**, *100*, 8015–8022, doi:10.1021/jp953196b.
 95. PubChem Formaldehyde Available online: <https://pubchem.ncbi.nlm.nih.gov/compound/Formaldehyde> (accessed on Mar 18, 2022).
 96. Guglielmino, M. Développement d'une nouvelle méthode analytique du formaldéhyde dans l'air basée sur un dispositif microfluidique, PhD Thesis, Université de Strasbourg, 2014.
 97. Wibisono, Y.; Cornelissen, E.R.; Kemperman, A.J.B.; Meer, W.G.J. Van Der; Nijmeijer, K. Two-phase flow in membrane processes: A technology with a future. *J. Memb. Sci.* **2014**, *453*, 566–602, doi:10.1016/j.memsci.2013.10.072.
 98. Salthammer, T. Photophysical properties of 3,5-diacetyl-1,4-dihydrolutidine in solution: application to the analysis of formaldehyde. *J. Photochem. Photobiol. A Chem.* **1993**, *74*, 195–201, doi:10.1016/1010-6030(93)80117-R.
 99. Mariano, S.; Wang, W.; Brunelle, G.; Bigay, Y.; Tran Thi, T.H. Colorimetric detection of formaldehyde: A sensor for air quality measurements and a pollution-warning kit for homes. *Procedia Eng.* **2010**, *5*, 1184–1187, doi:10.1016/j.proeng.2010.09.323.
 100. Babikian, S.; Li, G.P.; Bachman, M. A Digital Signal Processing-Assisted Microfluidic PCB for On-Chip Fluorescence Detection. *IEEE Trans. Components, Packag. Manuf. Technol.* **2017**, *7*, 846–854, doi:10.1109/TCPMT.2017.2691673.
 101. Ghosh, K.K.; Burns, L.D.; Cocker, E.D.; Nimmerjahn, A.; Ziv, Y.; Gamal, A. El; Schnitzer, M.J. Miniaturized integration of a fluorescence microscope. *Nat. Methods* **2011**, *8*, 871–878, doi:10.1038/nmeth.1694.
 102. Fang, X.X.; Li, H.Y.; Fang, P.; Pan, J.Z.; Fang, Q. A handheld laser-induced fluorescence detector for multiple applications. *Talanta* **2016**, *150*, 135–141, doi:10.1016/j.talanta.2015.12.018.
 103. Pan, J.Z.; Fang, P.; Fang, X.X.; Hu, T.T.; Fang, J.; Fang, Q. A low-cost palmtop high-speed capillary electrophoresis bioanalyzer with laser induced fluorescence detection. *Sci. Rep.* **2018**, *8*, 1–11, doi:10.1038/s41598-018-20058-0.
 104. Harmon, D.M.; Chen, C.F.; Halford, J.H. Portable Fluorescence Detection Platform with Integrating Sphere. In Proceedings of the the Annual International Conference of the IEEE Engineering in Medicine and Biology Society, EMBS; Honolulu, Hawaii, 2018; Vol. 2018-July, pp. 2889–2892.
 105. Brammer, M.; Mappes, T. Modular Platforms for Optofluidic Systems Modular Platforms for Optofluidic Systems. *Optofluidics* **2014**, 1–10, doi:10.2478/optof-2013-0001.
 106. Lee, Y.; Kim, B.; Oh, I.; Choi, S. Optofluidic Modular Blocks for On-Demand and Open-Source Prototyping of Microfluidic Systems. *Small* **2018**, *14*, 1802769, doi:10.1002/smll.201802769.
 107. Hierlemann, A.; Brand, O.; Hagleitner, C.; Baltes, H. Microfabrication techniques for chemical/biosensors. *Proc. IEEE* **2003**, *91*, 839–863.

108. Gründler, P. *Chemical sensors: An introduction for scientists and engineers*; Springer Berlin Heidelberg, 2007; ISBN 9783540457428.
109. Benito-Peña, E.; Valdés, M.G.; Glahn-Martínez, B.; Moreno-Bondi, M.C. Fluorescence based fiber optic and planar waveguide biosensors. A review. *Anal. Chim. Acta* **2016**, *943*, 17–40, doi:10.1016/j.aca.2016.08.049.
110. Yue, W.; Zhang, L.; Guo, Z.; Jiang, S.; Bai, C. Portable and modularized fluorometer based on optical fiber. *Ninth Int. Symp. Precis. Eng. Meas. Instrum.* **2015**, *9446*, 94464I, doi:10.1117/12.2182022.
111. Rodríguez-Ruiz, I.; Masvidal-Codina, E.; Ackermann, T.N.; Llobera, A. Photonic lab-on-chip (PhLOC) for enzyme-catalyzed reactions in continuous flow. *Microfluid. Nanofluidics* **2015**, *18*, 1277–1286, doi:10.1007/s10404-014-1526-4.
112. Matteucci, M.; Triches, M.; Nava, G.; Kristensen, A.; Pollard, M.R.; Berg-Sørensen, K.; Taboryski, R.J. Fiber-based, injection-molded optofluidic systems: Improvements in assembly and applications. *Micromachines* **2015**, *6*, 1971–1983, doi:10.3390/mi6121468.
113. Østergaard, P.F.; Lopacinska-Jørgensen, J.; Pedersen, J.N.; Tommerup, N.; Kristensen, A.; Flyvbjerg, H.; Silahatoglu, A.; Marie, R.; Taboryski, R. Optical mapping of single-molecule human DNA in disposable, mass-produced all-polymer devices. *J. Micromechanics Microengineering* **2015**, *25*, doi:10.1088/0960-1317/25/10/105002.
114. Hatch, A.C.; Ray, T.; Lintecum, K.; Youngbull, C. Continuous flow real-time PCR device using multi-channel fluorescence excitation and detection. *Lab Chip* **2014**, *14*, 562–568, doi:10.1039/c3lc51236c.
115. Bhargava, K.C.; Thompson, B.; Malmstadt, N. Discrete elements for 3D microfluidics. *Proc. Natl. Acad. Sci. U. S. A.* **2014**, *111*, 15013–15018, doi:10.1073/pnas.1414764111.
116. Ackermann, T.N.; Giménez-Gómez, P.; Muñoz-Berbel, X.; Llobera, A. Plug and measure-a chip-to-world interface for photonic lab-on-a-chip applications. *Lab Chip* **2016**, *16*, 3220–3226, doi:10.1039/c6lc00462h.
117. Ngernsutivorakul, T.; Cipolla, C.M.; Dugan, C.E.; Jin, S.; Morris, M.D.; Kennedy, R.T.; Esmonde-White, F.W.L. Design and microfabrication of a miniature fiber optic probe with integrated lenses and mirrors for Raman and fluorescence measurements. *Anal. Bioanal. Chem.* **2017**, *409*, 275–285, doi:10.1007/s00216-016-9999-5.
118. Shao, L. Optofluidics in Microstructured Optical Fibers. *Micromachines* **2018**, *9*, 145, doi:10.3390/mi9040145.
119. Ertman, S.; Lesiak, P.; Woli, T.R.; Paper, I. Optofluidic Photonic Crystal Fiber-Based Sensors. *J. Light. Technol.* **2017**, *35*, 3399–3405, doi:10.1109/JLT.2016.2596540.
120. Li, J.; Nallappan, K. Optimization of hollow-core photonic Bragg fibers towards practical sensing implementations. *Opt. Mater. Express* **2019**, *9*, 1640, doi:10.1364/ome.9.001640.
121. Huang, Y.; Xu, Y.; Yariv, A. Fabrication of functional microstructured optical fibers through a selective-filling technique. *Appl. Phys. Lett.* **2004**, *85*, 5182–5184, doi:10.1063/1.1828593.
122. Chen, D.; Yang, T.-J.; Wu, J.-J.; Shen, L.; Liao, K.-L.; He, S. Band-rejection fiber filter and fiber sensor based on a Bragg fiber of transversal resonant structure. *Opt. Express* **2008**, *16*, 16489, doi:10.1364/oe.16.016489.
123. Shang, L.; Zheng, K. Design of Hollow Core Bragg Fibers for a Compact Fluorescence Sensing Scheme. *IEEE Photonics J.* **2017**, *9*, doi:10.1109/JPHOT.2017.2677582.
124. Yang, X.; Yuan, T.; Yue, G.; Li, E.; Yuan, L. Optofluidic integrated in-fiber fluorescence online optical fiber sensor. *Sensors Actuators, B Chem.* **2015**, *215*, 345–349, doi:10.1016/j.snb.2015.04.003.
125. Dandin, M.; Abshire, P.; Smela, E. Optical filtering technologies for integrated fluorescence sensors. *Lab Chip* **2007**, *7*, 955–977, doi:10.1039/b704008c.
126. Bates, K.E.; Lu, H. Optics-integrated microfluidic platforms for biomolecular analyses. *Biophys. J.* **2016**, *110*, 1684–1697, doi:10.1016/j.bpj.2016.03.018.

127. Sugioka, K.; Xu, J.; Wu, D.; Hanada, Y.; Wang, Z.; Cheng, Y.; Midorikawa, K. Femtosecond laser 3D micromachining: A powerful tool for the fabrication of microfluidic, optofluidic, and electrofluidic devices based on glass. *Lab Chip* **2014**, *14*, 3447–3458, doi:10.1039/c4lc00548a.
128. He, F.; Liao, Y.; Lin, J.; Song, J.; Qiao, L.; Cheng, Y.; Sugioka, K. Femtosecond Laser Fabrication of Monolithically Integrated Microfluidic Sensors in Glass. *Sensors (Switzerland)* **2014**, *14*, 19402–19440, doi:10.3390/s141019402.
129. Sugioka, K.; Cheng, Y. Femtosecond laser processing for optofluidic fabrication. *Lab Chip* **2012**, *12*, 3576–3589, doi:10.1039/c2lc40366h.
130. Gu, Y.; Bragheri, F.; Valentino, G.; Morris, K.; Bellini, N.; Osellame, R. Ferrofluid-based optofluidic switch using femtosecond laser-micromachined waveguides. *Appl. Opt.* **2015**, *54*, 1420, doi:10.1364/ao.54.001420.
131. Joseph, K.A.J.; Haque, M.; Ho, S.; Aitchison, J.S.; Herman, P.R. Femtosecond laser direct-write of optofluidics in polymer-coated optical fiber. In Proceedings of the Frontiers in Ultrafast Optics: Biomedical, Scientific, and Industrial Applications XVII; International Society for Optics and Photonics.: San Francisco, California, 2017; Vol. 10094, p. 1009414.
132. Serhatlioglu, M.; Elbuken, C.; Ortac, B.; Solmaz, M.E. Femtosecond laser fabrication of fiber based optofluidic platform for flow cytometry applications. In Proceedings of the Optical Fibers and Sensors for Medical Diagnostics and Treatment Applications XVII; SPIE, 2017; Vol. 10058, pp. 103–110.
133. Paiè, P.; Bragheri, F.; Claude, T.; Osellame, R. Optofluidic light modulator integrated in lab-on-a-chip. *Opt. Express* **2017**, *25*, 7313, doi:10.1364/oe.25.007313.
134. Guduru, S.S.K.; Scotognella, F.; Chiasera, A.; Sreeramulu, V.; Criante, L.; Vishnubhatla, K.C.; Ferrari, M.; Ramponi, R.; Lanzani, G.; Vázquez, R.M. Highly integrated lab-on-a-chip for fluorescence detection. *Opt. Eng.* **2016**, *55*, 097102, doi:10.1117/1.oe.55.9.097102.
135. Siudzinska, A.; Miszczuk, A.; Marczak, J.; Komorowska, K. Fluorescent sensing with Fresnel microlenses for optofluidic systems. *Opt. Eng.* **2017**, *56*, 057106, doi:10.1117/1.OE.56.5.057106.
136. Ricciardi, S.; Frascella, F.; Angelini, A.; Lamberti, A.; Munzert, P.; Boarino, L.; Rizzo, R.; Tommasi, A.; Descrovi, E. Optofluidic chip for surface wave-based fluorescence sensing. *Sensors Actuators, B Chem.* **2015**, *215*, 225–230, doi:10.1016/j.snb.2015.03.063.
137. Watts, B.R.; Zhang, Z.; Xu, C.-Q.; Cao, X.; Lin, M. Integration of optical components on-chip for scattering and fluorescence detection in an optofluidic device. *Biomed. Opt. Express* **2012**, *3*, 2784, doi:10.1364/boe.3.002784.
138. Obahiagbon, U.; Smith, J.T.; Zhu, M.; Katchman, B.A.; Arafa, H.; Anderson, K.S.; Blain Christen, J.M. A compact, low-cost, quantitative and multiplexed fluorescence detection platform for point-of-care applications. *Biosens. Bioelectron.* **2018**, *117*, 153–160, doi:10.1016/j.bios.2018.04.002.
139. Shin, Y.-H.; Barnett, J.Z.; Gutierrez-Wing, M.T.; Rusch, K.A.; Choi, J.-W. A portable fluorescent sensing system using multiple LEDs. *Microfluid. BioMEMS, Med. Microsystems XV* **2017**, *10061*, 100610M, doi:10.1117/12.2261292.
140. Shin, Y.H.; Barnett, J.Z.; Song, E.; Gutierrez-Wing, M.T.; Rusch, K.A.; Choi, J.W. A portable fluorescent sensor for on-site detection of microalgae. *Microelectron. Eng.* **2015**, *144*, 6–11, doi:10.1016/j.mee.2015.01.005.
141. Novo, P.; Chu, V.; Conde, J.P. Integrated fluorescence detection of labeled biomolecules using a prism-like PDMS microfluidic chip and lateral light excitation. *Lab Chip* **2014**, *14*, 1991–1995, doi:10.1039/c4lc00241e.
142. Balsam, J.; Ossandon, M.; Bruck, H.A.; Rasooly, A. Modeling and design of micromachined optical Söller collimators for lensless CCD-based fluorometry. *Analyst* **2012**, *137*, 5011–5017, doi:10.1039/c2an35729a.
143. Berner, M.; Hilbig, U.; Schubert, M.B.; Gauglitz, G. Laser-induced fluorescence detection platform

- for point-of-care testing. *Meas. Sci. Technol.* **2017**, *28*, doi:10.1088/1361-6501/aa7810.
144. Jang, D.H.; Yoo, J.C. Miniaturized fluorometer based on total internal reflector and condensing mirror. *J. Opt. Soc. Korea* **2013**, *17*, 81–85, doi:10.3807/JOSK.2013.17.1.081.
 145. Persichetti, G.; Grimaldi, I.A.; Testa, G.; Bernini, R. Multifunctional optofluidic lab-on-chip platform for Raman and fluorescence spectroscopic microfluidic analysis. *Lab Chip* **2017**, *17*, 2631–2639, doi:10.1039/c7lc00460e.
 146. Llobera, A.; Juvert, J.; González-Fernández, A.; Ibarlucea, B.; Carregal-Romero, E.; Büttgenbach, S.; Fernández-Sánchez, C. Biofunctionalized all-polymer photonic lab on a chip with integrated solid-state light emitter. *Light Sci. Appl.* **2015**, *4*, doi:10.1038/lssa.2015.44.
 147. Robbins, H.; Sumitomo, K.; Tsujimura, N.; Kamei, T. Integrated thin film Si fluorescence sensor coupled with a GaN microLED for microfluidic point-of-care testing. *J. Micromechanics Microengineering* **2018**, *28*, doi:10.1088/1361-6439/aa9e6d.
 148. Kang, D.; Gai, B.; Thompson, B.; Lee, S.; Malmstadt, N.; Yoon, J. Flexible Opto-Fluidic Fluorescence Sensors Based on Heterogeneously Integrated Micro-VCSELs and Silicon Photodiodes. *ACS Photonics* **2016**, *6*, 912–918, doi:10.1021/acsp Photonics.6b00080.
 149. Parks, J.W.; Olson, M.A.; Kim, J.; Ozcelik, D.; Cai, H.; Carrion, R.; Patterson, J.L.; Mathies, R.A.; Hawkins, A.R.; Schmidt, H. Integration of programmable microfluidics and on-chip fluorescence detection for biosensing applications. *Biomicrofluidics* **2014**, *8*, doi:10.1063/1.4897226.
 150. Measor, P.; Phillips, B.S.; Chen, A.; Hawkins, A.R.; Schmidt, H. Tailorable integrated optofluidic filters for biomolecular detection. *Lab Chip* **2011**, *11*, 899–904, doi:10.1039/c0lc00496k.
 151. Özbakır, Y.; Jonas, A.; Kiraz, A.; Erkey, C. Aerogels for Optofluidic Waveguides. *Micromachines* **2017**, *8*, 98, doi:10.3390/mi8040098.
 152. Nittala, P.V.K.; Sen, P. Scaling a Fluorescent Detection System by Polymer-Assisted 3-D Integration of Heterogeneous Dies. *J. Microelectromechanical Syst.* **2018**, *27*, 896–909, doi:10.1109/JMEMS.2018.2856935.
 153. Rodríguez-Ruiz, I.; Teychené, S.; Van Pham, N.; Radajewski, D.; Lamadie, F.; Llobera, A.; Charton, S. Broadcasting photonic lab on a chip concept through a low cost manufacturing approach. *Talanta* **2017**, *170*, 180–184, doi:10.1016/j.talanta.2017.04.010.
 154. Torres-mapa, M.L.; Singh, M.; Simon, O.; Mapa, J.L.; Machida, M.; Günther, A.; Roth, B.; Heinemann, D.; Terakawa, M.; Heisterkamp, A. Fabrication of a Monolithic Lab-on-a-Chip Platform with Integrated Hydrogel Waveguides for Chemical Sensing. *Sensors (Switzerland)* **2019**, *19*, 4333, doi:10.3390/s19194333.
 155. Krujatz, F.; Hild, F.; Fehse, K.; Jahnel, M. Exploiting the Potential of OLED-Based Photo-Organic Sensors for Biotechnological Applications. *Chem. Sci. J.* **2016**, *7*, doi:10.4172/2150-3494.1000134.
 156. Williams, G.; Backhouse, C.; Aziz, H. Integration of organic light emitting diodes and organic photodetectors for lab-on-a-chip bio-detection systems. *Electron.* **2014**, *3*, 43–75, doi:10.3390/electronics3010043.
 157. Jeong, H.; Shin, H.; Lee, J.; Kim, B.; Park, Y.-I.; Yook, K.S.; An, B.-K.; Park, J. Recent progress in the use of fluorescent and phosphorescent organic compounds for organic light-emitting diode lighting. *J. Photonics Energy* **2015**, *5*, 057608, doi:10.1117/1.jpe.5.057608.
 158. Yersin, H. *Highly efficient OLEDs: Materials based on thermally activated delayed fluorescence*; Wiley-VCH Verlag GmbH & Co. KGaA, 2018; ISBN 9783527691722.
 159. Jansen-van Vuuren, R.D.; Armin, A.; Pandey, A.K.; Burn, P.L.; Meredith, P. Organic Photodiodes: The Future of Full Color Detection and Image Sensing. *Adv. Mater.* **2016**, 4766–4802, doi:10.1002/adma.201505405.
 160. Lefèvre, F.; Juneau, P.; Izquierdo, R. Integration of fluorescence sensors using organic optoelectronic components for microfluidic platform. *Sensors Actuators B. Chem.* **2015**, *221*, 1314–1320, doi:10.1016/j.snb.2015.07.077.

161. Shu, Z.; Kemper, F.; Beckert, E.; Eberhardt, R.; Tünnermann, A. Highly sensitive on-chip fluorescence sensor with integrated fully solution processed organic light sources and detectors. *RSC Adv.* **2017**, *7*, 26384–26391, doi:10.1039/c7ra03841k.
162. Jahns, S.; Iwers, A.F.K.; Balke, J.; Gerken, M. Organic optoelectronics for lab-on-chip fluorescence detection. *tm-Technisches Mess.* **2017**, *84*, 48–51, doi:10.1515/teme-2017-0034.
163. Poorahong, S.; Lefevre, F.; Perron, M.C.; Juneau, P.; Izquierdo, R. Integration of optical and electrochemical sensors on a microfluidic platform using organic optoelectronic components and silver nanowires. *Proc. Annu. Int. Conf. IEEE Eng. Med. Biol. Soc. EMBS* **2016**, *2016-October*, 3002–3005, doi:10.1109/EMBC.2016.7591361.
164. Kielar, M.; Dhez, O.; Pecastaings, G.; Curutchet, A.; Hirsch, L. Long-Term Stable Organic Photodetectors with Ultra Low Dark Currents for High Detectivity Applications. *Sci. Rep.* **2016**, *6*, 1–11, doi:10.1038/srep39201.
165. Smith, J.T.; Katchman, B.A.; Lee, Y.K.; O'Brien, B.P.; Bawolek, E.J.; Shah, S.S.; Christen, J.B. Disposable point-of-use optical biosensor for multiple biomarker detection. *IEEE 2014 Biomed. Circuits Syst. Conf. BioCAS 2014 - Proc.* **2014**, 268–271, doi:10.1109/BioCAS.2014.6981714.
166. Katchman, B.A.; Smith, J.T.; Obahiagbon, U.; Kesiraju, S.; Lee, Y.K.; O'Brien, B.; Kaftanoglu, K.; Christen, J.B.; Anderson, K.S. Application of flat panel OLED display technology for the point-of-care detection of circulating cancer biomarkers. *Sci. Rep.* **2016**, *6*, 1–11, doi:10.1038/srep29057.
167. Shakoor, A.; Cheah, B.C.; Al-rawhani, M.A.; Grande, M.; Grant, J.; Carlos, L.; Gouveia, P.; Cumming, D.R.S. CMOS Nanophotonic Sensor With Integrated Readout System. *IEEE Sens. J.* **2018**, *18*, 9188–9194, doi:10.1109/JSEN.2018.2870255.
168. Tanaka, K.; Choi, Y.J.; Moriwaki, Y.; Hizawa, T.; Iwata, T.; Dasai, F.; Kimura, Y.; Takahashi, K.; Sawada, K. Improvements of low-detection-limit filter-free fluorescence sensor developed by charge accumulation operation. *Jpn. J. Appl. Phys.* **2017**, *56*, 04CM09, doi:10.7567/JJAP.56.04CM09.
169. Choi, Y.J.; Takahashi, K.; Matsuda, M.; Hizawa, T.; Moriwaki, Y.; Dasai, F.; Kimura, Y.; Akita, I.; Iwata, T.; Ishida, M.; et al. Filter-less fluorescence sensor with high separation ability achieved by the suppression of forward-scattered light in silicon. *Jpn. J. Appl. Phys.* **2016**, *55*, doi:10.7567/JJAP.55.04EM10.
170. Nakazawa, H.; Yamasaki, K.; Takahashi, K.; Ishida, M.; Sawada, K. A filter - Less multi - Wavelength fluorescence detector. *2011 16th Int. Solid-State Sensors, Actuators Microsystems Conf. TRANSDUCERS'11* **2011**, 100–103, doi:10.1109/TRANSDUCERS.2011.5969147.
171. Măriuța, D.; Baldas, L.; Colin, S.; Barrot-lattes, C.; Calvé, S. Le; Korvink, J.G.; Brandner, J.J. Microfluidic sensing of airborne formaldehyde : towards on-chip integration (oral presentation & poster & proceedings with peer review) To cite this version : HAL Id : hal-02365974. **2019**.
172. Datta-Chaudhuri, T.; Smela, E.; Abshire, P.A. System-on-Chip Considerations for Heterogeneous Integration of CMOS and Fluidic Bio-Interfaces. *IEEE Trans. Biomed. Circuits Syst.* **2016**, *10*, 1129–1142, doi:10.1109/TBCAS.2016.2522402.
173. Lindsay, M.; Member, S.; Bishop, K.; Sengupta, S.; Member, S.; Co, M.; Cumbie, M.; Chen, C.; Johnston, M.L. Heterogeneous Integration of CMOS Sensors and Fluidic Networks Using Wafer-Level Molding. *IEEE Trans. Biomed. Circuits Syst.* **2018**, *12*, 1046–1055, doi:10.1109/TBCAS.2018.2845867.
174. Pang, S.; Han, C.; Lee, L.M.; Yang, C. Fluorescence microscopy imaging with a Fresnel zone plate array based optofluidic microscope. *Lab Chip* **2011**, *21*, 3698–3702, doi:10.1039/c1lc20654k.
175. Bauch, M.; Toma, K.; Toma, M.; Zhang, Q.; Dostalek, J. Plasmon-Enhanced Fluorescence Biosensors: A Review. *Plasmonics* **2014**, *9*, 781–799, doi:10.1007/s11468-013-9660-5.
176. Geddes, C.D. *Surface Plasmon Enhanced, Coupled and Controlled Fluorescence*; John Wiley & Sons, Inc: New Jersey, 2017; ISBN 9781118027936.
177. Hong, L.; Li, H.; Yang, H.; Sengupta, K. Fully Integrated Fluorescence Biosensors On-Chip

- Employing Multi-Functional Nanoplasmonic Optical Structures in CMOS. *IEEE J. Solid-State Circuits* **2017**, *52*, 2388–2406, doi:10.1109/JSSC.2017.2712612.
178. Lu, X.; Hong, L.; Sengupta, K. CMOS Optical PUFs Using Noise-Immune Process-Sensitive Photonic Crystals Incorporating Passive Variations for Robustness. *IEEE J. Solid-State Circuits* **2018**, *53*, 2709–2721, doi:10.1109/JSSC.2018.2850941.
 179. Varsanik, J.S.; Bernstein, J.J. Integrated optic/nanofluidic fluorescent detection device with plasmonic excitation. *J. Micromechanics Microengineering* **2013**, *23*, doi:10.1088/0960-1317/23/9/095017.
 180. Samouda, F.; Colin, S.; Barrot, C.; Baldas, L.; Brandner, J.J. Micro molecular tagging velocimetry for analysis of gas flows in mini and micro systems. *Microsyst Technol* **2015**, *21*, 527–537, doi:10.1007/s00542-013-1971-0.
 181. Sobieszuk, P.; Napieralska, K. Investigations of mass transfer in annular gas-liquid flow in a microreactor. *Chem. Process Eng. - Inz. Chem. i Proces.* **2016**, *37*, 55–64, doi:10.1515/cpe-2016-0006.
 182. Yao, C.; Zhao, Y.; Ma, H.; Liu, Y.; Zhao, Q.; Chen, G. Two-phase flow and mass transfer in microchannels: A review from local mechanism to global models. *Chem. Eng. Sci.* **2021**, *229*, 116017, doi:10.1016/j.ces.2020.116017.
 183. Zhang, J.; Wang, K.; Teixeira, A.R.; Jensen, K.F.; Luo, G. Design and scaling up of microchemical systems: A review. *Annu. Rev. Chem. Biomol. Eng.* **2017**, *8*, 285–305, doi:10.1146/annurev-chembioeng-060816-101443.
 184. Lam, K.F.; Sorensen, E.; Gavriilidis, A. Review on gas-liquid separations in microchannel devices. *Chem. Eng. Res. Des.* **2013**, *91*, 1941–1953, doi:10.1016/j.cherd.2013.07.031.
 185. Huh, D.; Kuo, C.H.; Grotberg, J.B.; Takayama, S. Gas-liquid two-phase flow patterns in rectangular polymeric microchannels: Effect of surface wetting properties. *New J. Phys.* **2009**, *11*, doi:10.1088/1367-2630/11/7/075034.
 186. Jia, J.; Song, Q.; Liu, Z.; Wang, B. Effect of wall roughness on performance of microchannel applied in microfluidic device. *Microsyst. Technol.* **2019**, *25*, 2385–2397, doi:10.1007/s00542-018-4124-7.
 187. Fries, D.M.; Waelchli, S.; Rudolf von Rohr, P. Gas-liquid two-phase flow in meandering microchannels. *Chem. Eng. J.* **2008**, *135*, 37–45, doi:10.1016/j.cej.2007.07.052.
 188. Takeda, K.; Okamoto, S.; Yoshida, K.; Kataoka, I. Effects of curved section on gas-liquid two-phase flow in milli-channel. In Proceedings of the International Conference on Nanochannels, Microchannels, and Minichannels; American Society of Mechanical Engineers, 2013; Vol. 55591, p. V001T03A014.
 189. Yan, J.H.; Laker, T.S.; Ghiaasiaan, S.M. Linear stability of inverted annular gas - Liquid two-phase flow in capillaries. *Int. J. Heat Fluid Flow* **2003**, *24*, 122–129, doi:10.1016/S0142-727X(02)00196-0.
 190. Humphry, K.J.; Ajdari, A.; Fernández-Nieves, A.; Stone, H.A.; Weitz, D.A. Suppression of instabilities in multiphase flow by geometric confinement. *Phys. Rev. E - Stat. Nonlinear, Soft Matter Phys.* **2009**, *79*, 1–5, doi:10.1103/PhysRevE.79.056310.
 191. Sur, A.; Liu, D. Adiabatic air-water two-phase flow in circular microchannels. *Int. J. Therm. Sci.* **2012**, *53*, 18–34, doi:10.1016/j.ijthermalsci.2011.09.021.
 192. Yang, L. Local investigations of gas-liquid mass transfer around Taylor bubbles flowing in straight and meandering millimetric channels using a colorimetric method, PhD Thesis, INSA Toulouse, 2017.
 193. Jesseela, S.; Sobhan, C.B. Numerical modeling of annular flow with phase change in a microchannel. *Int. J. Therm. Sci.* **2015**, *89*, 87–99, doi:10.1016/j.ijthermalsci.2014.10.017.
 194. Guo, Z.; Fletcher, D.F.; Haynes, B.S. Numerical simulation of annular flow hydrodynamics in microchannels. *Comput. Fluids* **2016**, *133*, 90–102, doi:10.1016/j.compfluid.2016.04.017.
 195. Guo, Z.; Fletcher, D.F.; Haynes, B.S. Implementation of a height function method to alleviate spurious currents in CFD modelling of annular flow in microchannels. *Appl. Math. Model.* **2015**, *39*,

- 4665–4686, doi:10.1016/j.apm.2015.04.022.
196. Roudet, M.; Loubiere, K.; Gourdon, C.; Cabassud, M. Hydrodynamic and mass transfer in inertial gas-liquid flow regimes through straight and meandering millimetric square channels. *Chem. Eng. Sci.* **2011**, *66*, 2974–2990, doi:10.1016/j.ces.2011.03.045.
 197. Yue, J.; Chen, G.; Yuan, Q.; Luo, L.; Gonthier, Y. Hydrodynamics and mass transfer characteristics in gas-liquid flow through a rectangular microchannel. *Chem. Eng. Sci.* **2007**, *62*, 2096–2108, doi:10.1016/j.ces.2006.12.057.
 198. Sotowa, K.I. Fluid behavior and mass transport characteristics of gas-liquid and liquid-liquid flows in microchannels. *J. Chem. Eng. Japan* **2014**, *47*, 213–224, doi:10.1252/jcej.13we141.
 199. Fries, D.M.; von Rohr, P.R. Liquid mixing in gas-liquid two-phase flow by meandering microchannels. *Chem. Eng. Sci.* **2009**, *64*, 1326–1335, doi:10.1016/j.ces.2008.11.019.
 200. Sobieszuk, P.; Pohorecki, R.; Cygański, P.; Grzelka, J. Determination of the interfacial area and mass transfer coefficients in the Taylor gas-liquid flow in a microchannel. *Chem. Eng. Sci.* **2011**, *66*, 6048–6056, doi:10.1016/j.ces.2011.08.029.
 201. CUSLER, E.L. *Diffusion: Mass Transfer in Fluid Systems*; Third.; CAMBRIDGE UNIVERSITY PRESS, 2007; ISBN 9780521871211.
 202. Pohorecki, R.; Sobieszuk, P.; Kula, K.; Moniuk, W.; Zieliński, M.; Cygański, P.; Gawiński, P. Hydrodynamic regimes of gas-liquid flow in a microreactor channel. *Chem. Eng. J.* **2008**, *135*, 185–190, doi:10.1016/j.cej.2007.07.039.
 203. Noël, T.; Hessel, V. Membrane microreactors: Gas-liquid reactions made easy. *ChemSusChem* **2013**, *6*, 405–407, doi:10.1002/cssc.201200913.
 204. Wang, Z.F.; Seah, Y.P.; Wang, Z.P. Seamless joining of porous membrane with thermoplastic microfluidic devices. *Microelectron. Eng.* **2013**, *110*, 386–391, doi:10.1016/j.mee.2013.02.074.
 205. Dyrda, K.M.; Wilke, V.; Haas-Santo, K.; Dittmeyer, R. Experimental investigation of the gas/liquid phase separation using a membrane-based micro contactor. *ChemEngineering* **2018**, *2*, 1–26, doi:10.3390/chemengineering2040055.
 206. Femmer, T.; Eggersdorfer, M.L.; Kuehne, A.J.C.; Wessling, M. Efficient gas-liquid contact using microfluidic membrane devices with staggered herringbone mixers. *Lab Chip* **2015**, *15*, 3132–3137, doi:10.1039/c5lc00428d.
 207. Brinkmann, T.; Notzke, H.; Wolff, T.; Zhao, L.; Luhr, S.; Stolten, D. Characterization of a New Flat Sheet Membrane Module Type for Gas Permeation. *Chemie-Ingenieur-Technik* **2019**, *91*, 30–37, doi:10.1002/cite.201800083.
 208. Malankowska, M.; Julian, I.; Pellejero, I.; Rho, H.S.; Schlautmann, S.; Tiggelaar, R.M.; Pina, M.P.; Gardeniers, H.J.G.E.; Mallada, R. Understanding blood oxygenation in a microfluidic meander double side membrane contactor. *Sensors Actuators, B Chem.* **2019**, *288*, 414–424, doi:10.1016/j.snb.2019.02.110.
 209. Karatay, E.; Lammertink, R.G.H. Oxygenation by a superhydrophobic slip G/L contactor. *Lab Chip* **2012**, *12*, 2922–2929, doi:https://doi.org/10.1039/C2LC21296J.
 210. Gerami, A.; Alzahid, Y.; Mostaghimi, P.; Kashaninejad, N.; Kazemifar, F.; Amirian, T.; Mosavat, N.; Ebrahimi Warkiani, M.; Armstrong, R.T. Microfluidics for Porous Systems: Fabrication, Microscopy and Applications. *Transp. Porous Media* **2019**, *130*, 277–304, doi:10.1007/s11242-018-1202-3.
 211. Chen, X.; Shen, J. Review of membranes in microfluidics. *J. Chem. Technol. Biotechnol.* **2017**, *92*, 271–282, doi:10.1002/jctb.5105.
 212. Tsao, C.W.; Wu, Z.K. Polymer microchannel and micromold surface polishing for rapid, low-quantity polydimethylsiloxane and thermoplastic microfluidic device fabrication. *Polymers (Basel)*. **2020**, *12*, 1–15, doi:10.3390/polym12112574.
 213. Suriano, R.; Kuznetsov, A.; Eaton, S.M.; Kiyan, R.; Cerullo, G.; Osellame, R.; Chichkov, B.N.; Levi, M.; Turri, S. Femtosecond laser ablation of polymeric substrates for the fabrication of microfluidic

- channels. *Appl. Surf. Sci.* **2011**, *257*, 6243–6250, doi:10.1016/j.apsusc.2011.02.053.
214. Liu, K.; Xiang, J.; Ai, Z.; Zhang, S.; Fang, Y.; Chen, T.; Zhou, Q.; Li, S.; Wang, S.; Zhang, N. PMMA microfluidic chip fabrication using laser ablation and low temperature bonding with OCA film and LOCA. *Microsyst. Technol.* **2017**, *23*, 1937–1942, doi:10.1007/s00542-016-2924-1.
 215. Yuen, P.K.; Goral, V.N. Low-cost rapid prototyping of flexible microfluidic devices using a desktop digital craft cutter. *Lab Chip* **2010**, *10*, 384–387, doi:10.1039/b918089c.
 216. Islam, M.; Natu, R.; Martinez-Duarte, R. A study on the limits and advantages of using a desktop cutter plotter to fabricate microfluidic networks. *Microfluid. Nanofluidics* **2015**, *19*, 973–985, doi:10.1007/s10404-015-1626-9.
 217. Peng, L.; Deng, Y.; Yi, P.; Lai, X. Micro hot embossing of thermoplastic polymers: A review. *J. Micromechanics Microengineering* **2014**, *24*, doi:10.1088/0960-1317/24/1/013001.
 218. Yang, S.; Devoe, D.L. Microfluidic Device Fabrication by Thermoplastic Hot-Embossing. *J. Micromech. Microeng* **2013**, *24*, 013001, doi:10.1007/978-1-62703-134-9.
 219. Mair, D.A.; Geiger, E.; Pisano, A.P.; Fréchet, J.M.J.; Svec, F. Injection molded microfluidic chips featuring integrated interconnects. *Lab Chip* **2006**, *6*, 1346–1354, doi:10.1039/b605911b.
 220. Attia, U.M.; Marson, S.; Alcock, J.R. Micro-injection moulding of polymer microfluidic devices. *Microfluid. Nanofluidics* **2009**, *7*, 1–28, doi:10.1007/s10404-009-0421-x.
 221. Scott, S.; Ali, Z. Fabrication Methods for Microfluidic Devices: An Overview. *Micromachines* **2021**, *12*, 319, doi:10.3390/mi12030319.
 222. Reyes, D.R.; Van Heeren, H.; Guha, S.; Herbertson, L.; Tzannis, A.P.; Ducree, J.; Bissig, H.; Becker, H. Accelerating innovation and commercialization through standardization of microfluidic-based medical devices. *Lab Chip* **2021**, *21*, 9–21, doi:10.1039/d0lc00963f.
 223. Gao, K.; Liu, J.; Fan, Y.; Zhang, Y. Ultra-low-cost fabrication of polymer-based microfluidic devices with diode laser ablation. *Biomed. Microdevices* **2019**, *21*, 83, doi:10.1007/s10544-019-0433-6.
 224. Rodrigues, R.O.; Lima, R.; Gomes, H.T.; Silva, A.M.T. Polymer microfluidic devices: An overview of fabrication methods. *U.Porto J. Eng.* **2015**, *1*, 67–79, doi:10.24840/2183-6493_001.001_0007.
 225. Ravi-Kumar, S.; Lies, B.; Zhang, X.; Lyu, H.; Qin, H. Laser ablation of polymers: a review. *Polym. Int.* **2019**, *68*, 1391–1401, doi:10.1002/pi.5834.
 226. Mohammed, M.I.; Zainal Alam, M.N.H.; Kouzani, A.; Gibson, I. Fabrication of microfluidic devices: Improvement of surface quality of CO2 laser machined poly(methylmethacrylate) polymer. *J. Micromechanics Microengineering* **2017**, *27*, 15021, doi:10.1088/0960-1317/27/1/015021.
 227. Hansen, T.S.; Selmeczi, D.; Larsen, N.B. Fast prototyping of injection molded polymer microfluidic chips. *J. Micromechanics Microengineering* **2010**, *20*, doi:10.1088/0960-1317/20/1/015020.
 228. Matthias Worgull *Hot embossing: Theory and Technology of Microreplication*; William Andrew: Burlington, MA, 2009; ISBN 978-0-8155-1579-1.
 229. Hecke, M.; Schomburg, W.K. Review on micro molding of thermoplastic polymers. *J. Micromechanics Microengineering* **2004**, *14*, doi:10.1088/0960-1317/14/3/R01.
 230. Ma, X.; Li, R.; Jin, Z.; Fan, Y.; Zhou, X.; Zhang, Y. Injection molding and characterization of PMMA-based microfluidic devices. *Microsyst. Technol.* **2020**, *26*, 1317–1324, doi:10.1007/s00542-019-04662-2.
 231. Temiz, Y.; Lovchik, R.D.; Kaigala, G. V.; Delamarche, E. Lab-on-a-chip devices: How to close and plug the lab? *Microelectron. Eng.* **2015**, *132*, 156–175, doi:10.1016/j.mee.2014.10.013.
 232. Guzman, J.M.C.C.; Tayo, L.L.; Liu, C.C.; Wang, Y.N.; Fu, L.M. Rapid microfluidic paper-based platform for low concentration formaldehyde detection. *Sensors Actuators, B Chem.* **2018**, *255*, 3623–3629, doi:10.1016/j.snb.2017.09.080.
 233. Liu, C.C.; Wang, Y.N.; Fu, L.M.; Huang, Y.H. Microfluidic paper-based chip platform for formaldehyde concentration detection. *Chem. Eng. J.* **2018**, *332*, 695–701, doi:10.1016/j.cej.2017.09.128.
 234. Weng, X.; Chon, C.H.; Jiang, H.; Li, D. Rapid detection of formaldehyde concentration in food on a polydimethylsiloxane (PDMS) microfluidic chip. *Food Chem.* **2009**, *114*, 1079–1082,

- doi:10.1016/j.foodchem.2008.10.027.
235. Fu, L.; Wang, Y.; Liu, C. An integrated microfluidic chip for formaldehyde analysis in Chinese herbs. *Chem. Eng. J.* **2014**, *244*, 422–428, doi:10.1016/j.cej.2014.01.085.
 236. Pang, X.; Lewis, A.C. A microfluidic lab-on-chip derivatisation technique for the measurement of gas phase formaldehyde. *Anal. Methods* **2012**, *4*, 2013–2020, doi:10.1039/c2ay25028d.
 237. Weber, M.J. *Handbook of optical materials*; CRC Press LLC: Boca Raton, FL, USA, 2003; ISBN 0849335124.
 238. Aspnes, D.E.; Studna, A.A. Dielectric functions and optical parameters of Si, Ge, GaP, GaAs, GaSb, InP, InAs, and InSb from 1.5 to 6.0 eV. *Phys. Rev. B* **1983**, *27*, 985–1009. <https://doi.org/10.1103/PhysRevB.27.985>
 239. ULS24 Product Brief Product overview. Available online: http://www.anitoa.com/docs/uls24_brief.pdf (accessed on Mar 18, 2022).
 240. Ding, Z.; Xu, C.; Wang, Y.; Pellegrini, G. Ultra-low-light CMOS biosensor complements microfluidics to achieve portable diagnostics. *Procedia Technol.* **2017**, *27*, 39–41, doi:10.1016/j.protcy.2017.04.019.
 241. Belman, S. The fluorimetric determination of formaldehyde. *Anal. Chim. Acta* **1963**, *29*, 120–126, doi:[https://doi.org/10.1016/S0003-2670\(00\)88591-8](https://doi.org/10.1016/S0003-2670(00)88591-8).
 242. Gianluca Morini Pressure-Driven Single-Phase Liquid Flows. In *Encyclopedia of Microfluidics and Nanofluidics*; Springer New York, 2015; p. 2846 ISBN 978-1-4614-5490-8.
 243. ePTFE Porosity : How it is created, how it affects the functional performance, and how to combine different porosities in one application Available online: <https://ipeweb.com/fluoroflex-eptfe/eptfe-porosity-creation-functional-performance-how-to-combine-different-porosities-in-one-application/> (accessed on Mar 18, 2022).
 244. Tjaden, B.; Cooper, S.J.; Brett, D.J.L.; Kramer, D.; Shearing, P.R. On the origin and application of the Bruggeman correlation for analysing transport phenomena in electrochemical systems. *Curr. Opin. Chem. Eng.* **2006**, *12*, 44–51, doi:10.1016/j.coche.2016.02.006.
 245. Sunaga, Y.; Haruta, M.; Takehara, H.; Ohta, Y.; Motoyama, M.; Noda, T.; Sasagawa, K.; Tokuda, T.; Ohta, J. Implantable CMOS imaging device with absorption filters for green fluorescence imaging. In *Proceedings of the Optical Techniques in Neurosurgery, Neurophotonics, and Optogenetics*; SPIE: San Francisco, California, 2014; Vol. 8928, pp. 114–119.
 246. Perfilov, V. Mathematical modelling of membrane separation, PhD Thesis, University of Chemistry and Technology Prague, 2018.
 247. Weissberg, H.L. Effective Diffusion Coefficient in Porous Media. *J. Appl. Phys.* **1963**, *2636*, doi:10.1063/1.1729783.
 248. Mackie, J.S.; Meares, P. The Diffusion of Electrolytes in Cation-exchange resin membrane I. Theoretical. *Proc. R. Soc. Lond. A* **1955**, *232*, 498–509, doi:<http://doi.org/10.1098/rspa.1955.0234>.
 249. Liu, Z.; Canada, C.; Huang, C.; Djilali, N. Determination of the effective diffusion coefficient in porous media including Knudsen effects Determination of the effective diffusion coefficient in porous media including Knudsen effects. *Microfluid. Nanofluidics* **2008**, *4*, 257–260, doi:10.1007/s10404-007-0182-3.
 250. Butler, C.; Cid, E.; Billet, A.-M. Modelling of mass transfer in Taylor flow : investigation with the PLIF-I technique. *Chem. Eng. Res. Des.* **2016**, *115* (Part, 292–302, doi:10.1016/j.cherd.2016.09.001.hal-01411112).
 251. Abiev, R.S. Gas-liquid and gas-liquid-solid mass transfer model for Taylor flow in micro (milli) channels: A theoretical approach and experimental proof. *Chem. Eng. J. Adv.* **2020**, *4*, 100065, doi:10.1016/j.cej.2020.100065.
 252. Burkle-Vitzthum, V.; Moulis, F.; Zhang, J.; Commenge, J.M.; Schaer, E.; Marquaire, P.M. Annular flow microreactor: An efficient tool for kinetic studies in gas phase at very short residence times.

- Chem. Eng. Res. Des.* **2015**, *94*, 611–623, doi:10.1016/j.cherd.2014.10.003.
253. Meng, D.; Liu, D.; Wang, G.; Shen, Y.; San, X.; Li, M.; Meng, F. Low-temperature formaldehyde gas sensors based on NiO-SnO₂ heterojunction microflowlers assembled by thin porous nanosheets. *Sensors Actuators, B Chem.* **2018**, *273*, 418–428, doi:10.1016/j.snb.2018.06.030.
254. Wang, Z.; Hou, C.; De, Q.; Gu, F.; Han, D. One-Step Synthesis of Co-Doped In₂O₃ Nanorods for High Response of Formaldehyde Sensor at Low Temperature. *ACS Sensors* **2018**, *3*, 468–475, doi:10.1021/acssensors.7b00896.
255. Alizadeh, T.; Soltani, L.H. Graphene/poly(methyl methacrylate) chemiresistor sensor for formaldehyde odor sensing. *J. Hazard. Mater.* **2013**, *248–249*, 401–406, doi:10.1016/j.jhazmat.2012.12.019.
256. Tao, Z.; Li, Y.; Zhang, B.; Sun, G.; Xiao, M.; Bala, H.; Cao, J.; Zhang, Z.; Wang, Y. Synthesis of urchin-like In₂O₃ hollow spheres for selective and quantitative detection of formaldehyde. *Sensors Actuators, B Chem.* **2019**, *298*, 126889, doi:10.1016/j.snb.2019.126889.
257. Kemmler, J.A.; Pokhrel, S.; Birkenstock, J.; Schowalter, M.; Rosenauer, A.; Bârsan, N.; Weimar, U.; Mädler, L. Quenched, nanocrystalline In₄Sn₃O₁₂ high temperature phase for gas sensing applications. *Sensors Actuators, B Chem.* **2012**, *161*, 740–747, doi:10.1016/j.snb.2011.11.026.
258. Tian, H.; Fan, H.; Li, M.; Ma, L. Zeolitic Imidazolate Framework Coated ZnO Nanorods as Molecular Sieving to Improve Selectivity of Formaldehyde Gas Sensor. *ACS Sensors* **2016**, *1*, 243–250, doi:10.1021/acssensors.5b00236.
259. Menart, E.; Jovanovski, V.; Hočevar, S.B. Novel hydrazinium polyacrylate-based electrochemical gas sensor for formaldehyde. *Sensors Actuators, B Chem.* **2017**, *238*, 71–75, doi:10.1016/j.snb.2016.07.042.
260. Ghaffari, S.A.; Caron, W.O.; Loubier, M.; Normandeau, C.O.; Viens, J.; Lamhamedi, M.S.; Gosselin, B.; Messaddeq, Y. Electrochemical impedance sensors for monitoring trace amounts of NO₃ in selected growing media. *Sensors* **2015**, *15*, 17715–17727, doi:10.3390/s150717715.
261. Chang, X.; Wu, X.; Guo, Y.; Zhao, Y.; Zheng, J.; Li, X. SnSO₄ modified ZnO nanostructure for highly sensitive and selective formaldehyde detection. *Sensors Actuators, B Chem.* **2018**, *255*, 1153–1159, doi:10.1016/j.snb.2017.05.023.
262. Kudo, H.; Suzuki, Y.; Gessei, T.; Takahashi, D.; Arakawa, T.; Mitsubayashi, K. Biochemical gas sensor (bio-sniffer) for ultrahigh-sensitive gaseous formaldehyde monitoring. *Biosens. Bioelectron.* **2010**, *26*, 854–858, doi:10.1016/j.bios.2010.07.099.
263. Zhao, X.; Ji, C.; Ma, L.; Wu, Z.; Cheng, W.; Yin, M. An Aggregation-Induced Emission-Based “turn-On” Fluorescent Probe for Facile Detection of Gaseous Formaldehyde. *ACS Sensors* **2018**, *3*, 2112–2117, doi:10.1021/acssensors.8b00664.
264. AL4021 Formaldehyde Monitor - Instruction Manual Available online: <https://www.aerolaser.de/fileadmin/downloads/AL4021-manual-Rev.2.2.pdf> (accessed on Mar 18, 2022).
265. Venkatraman, V.; Steckl, A.J. Integrated OLED as excitation light source in fluorescent lateral flow immunoassays. *Biosens. Bioelectron.* **2015**, *74*, 150–155, doi:10.1016/j.bios.2015.06.049.
266. Hong, L.; Lu, X.; Sengupta, K. Nano-optical systems in CMOS. In Proceedings of the 2017 IEEE 60th International Midwest Symposium on Circuits and Systems (MWSCAS); IEEE: Medford, MA, United States, 2017; pp. 906–909.

Appendices

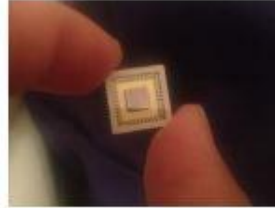
A1. ULS24 ANITOA CMOS-image sensor Data Sheet



ULS24 Product Brief

Product overview

The Anitoa ULS24 is an ultra-low-light CMOS image sensor. Its low cost, small form factor and high level of integration make it optimally suited for use in a portable device in medical, scientific and industrial applications. An example of such application is a field portable nucleic-acid-test (NAT) system that performs molecular sensing based-on fluorescence or chemiluminescence signaling principles.



ULS24 is built on 0.18um CMOS process at a world-leader specialty semiconductor foundry.

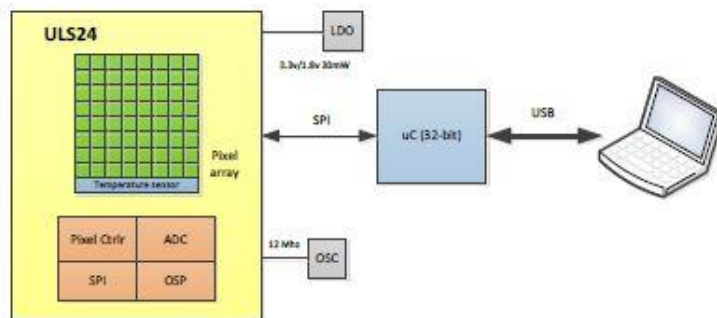


Figure 1. ULS24 Chip Application Block Diagram

Features

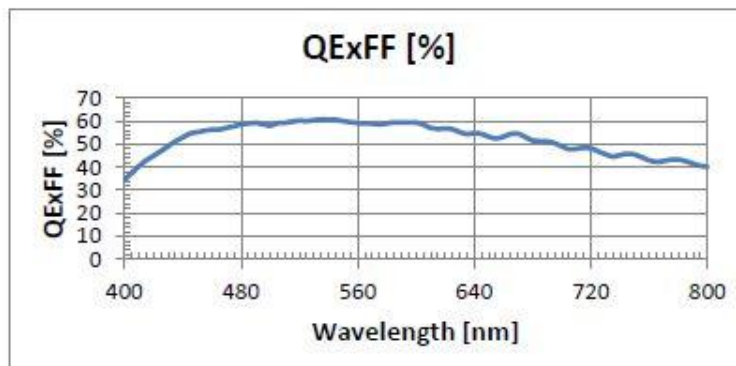
- Ultra low-light sensitivity. Detection threshold $\sim 3.0 \times 10^{-6}$ lux.
- Low dark current, high SnR (> 13 dB at detection threshold).
- 12-bit ADC. Dual gain mode.
- Wide dynamic range (> 85 dB). Excellent linearity ($< 0.6\%$).
- Digital interface through Serial Peripheral Interface (SPI).
- Built-in junction temperature sensor.
- 3.3V and 1.8V power supply, 30mW max power.
- Operating temperature range $-15^\circ\text{C} - 85^\circ\text{C}^1$.

¹ The image sensor can meet noise spec at junction temperature up to 55°C .

Key parameters

Imager size	4.9mm x 4.8mm; Sensing area: 3.6mm x 3.6mm
Active pixels	24x24
Pixel size	150um x 150um (4 can be combined into a 300um x 300um "big pixel")
Integration time	100us - 100 seconds, software controlled
ADC resolution	12-bit
Signal Interface	Serial Peripheral Interface (SPI), 4 wires
Responsivity	135V/lux-sec @550nm in high-gain mode 540V/lux-sec @550nm in high-gain 4-bin mode 4200V/lux-sec with 2850k light in high-gain 4-bin mode
Detection threshold (550nm)	$\sim 3.0 \times 10^{-6}$ lux or $\sim 4.4 \times 10^{-7}$ uW/cm ²
Dynamic range	>85dB, in dual gain mode
SnR	13dB minimum at detection threshold
Non-linearity error	Low gain mode: <0.5%; high gain mode: <0.6%
Supply	3.3V (analog); 1.8V (digital)
Power consumption	< 30mW
Operating temperature	-15 – 85 °C (up to 55 °C to meet optical performance spec).
Temperature sensor spec	± 0.3 °C accuracy. -15 to 85 °C range. Need calibration.
Packaging	48-pin CLCC

Quantum efficiency (QE) x Fill factor (FF) vs. Wavelength:



ULS 24 Solution Kit

The ULS24 Solution Kit is available as an "out of box" solution to allow the user to conveniently evaluate ULS24. The ULS 24 Solution Kit includes the ULS24 Sensor IC, an interface board, and software (ULVision). This solution kit can readily interface with a PC via USB.



Figure 2. ULS24 Solution Kit

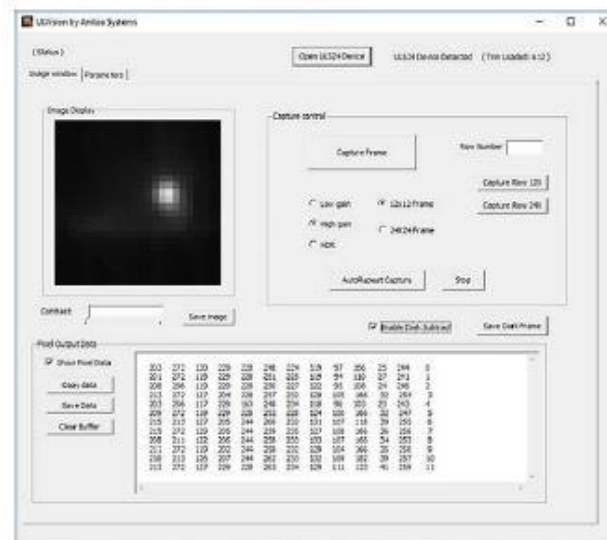


Figure 3. ULVision software

Applications

Biomedical and life science

Molecular sensing/imaging based fluorescence and chemiluminescence signaling principles.

- DNA and RNA quantification, fluorescent-based
- Miniaturized qPCR system or digital qPCR
- Fluorescence or chemiluminescence-based Immunoassay/ELISA
- DNA or Protein microarray
- Pyro-sequencing
- Capillary electrophoresis
- Cell sorting/Imaging flow cytometry
- Fluorescence Images Guided Surgery (FIGS)

Industrial and scientific

- Quantum dot spectrometer
- Hazard and chemical-threat detection instruments



Figure 4. ULS24-based fluorescence and chemiluminescence cameras. Left top: 1-channel system fluorescent imager with ULS24, with filter installed; and ULS24 with C-mount lens interface for chemiluminescence imaging. Left bottom: 2 channel imager with integrated 2 channel UV excitation LED for tissue imaging. Right: ULS24 used in a lensless configuration for chemiluminescence read out in a microfluidic application.

Application data showcase

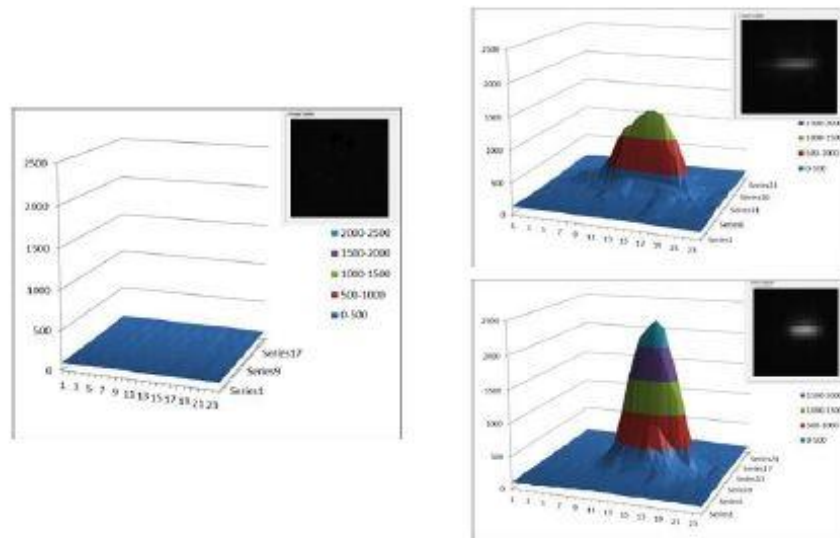


Figure 5. ULS24 measuring fluorescent emission from immunoassay test, at 3 different signal levels. Left: dark input; right top: medium signal level; right bottom: strong signal level

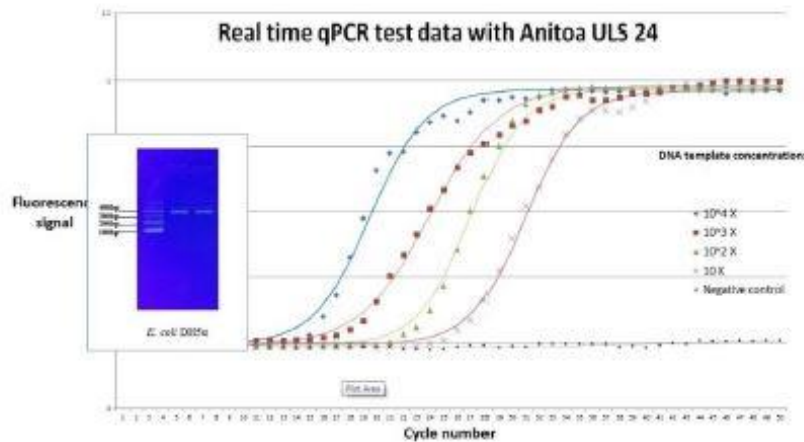


Figure 6. ULS24 successfully applied in qPCR to detect E Coli. (DH5a) bacteria, with as low as 10 copies/reaction detection limit.

A2. Excitation Light Emitting Diode Data Sheet



ROITHNER LASERTECHNIK GmbH

WIEDNER HAUPTSTRASSE 76 1040 VIENNA AUSTRIA
TEL. +43 1 586 52 43 -0. FAX. -44 OFFICE@ROITHNER-LASER.COM



Rev. 1.1 19.12.2018

SMB1N-420H-02

- Violet High Power LED
- 420 nm, 420 mW
- SMD package, PA9T
- Dimension: 5.0 x 5.2 x 5.5 mm
- Viewing Angle: 22°



Description

SMB1N-420H-02 is a surface mount InGaN High Power LED with a typical peak wavelength of **420 nm** and radiation of **420 mW**. It comes in SMD package (PA9T) with silver plated soldering pads (lead free solderable), copper heat sink, and molded with silicone resin.

Maximum Ratings ($T_{CASE}=25^{\circ}C$)

Parameter	Symbol	Values		Unit
		Min.	Max.	
Power Dissipation	P_D		1900	mW
Forward Current	I_F		500	mA
Pulse Forward Current *1	I_{FP}		1000	mA
Reverse Voltage	V_F		5	V
Thermal Resistance	R_{THJA}		10	K/W
Junction Temperature	T_J		120	$^{\circ}C$
Operating Temperature	T_{CASE}	- 40	+ 100	$^{\circ}C$
Storage Temperature	T_{STO}	- 40	+ 100	$^{\circ}C$
Lead Solder Temperature *2	T_{SLD}		+ 250	$^{\circ}C$

*1 duty=1%, pulse width = 10 μ s

*2 must be completed within 5 seconds

Electro-Optical Characteristics ($T_{CASE}=25^{\circ}C$)

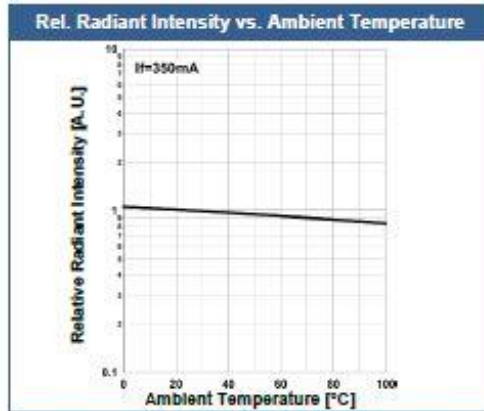
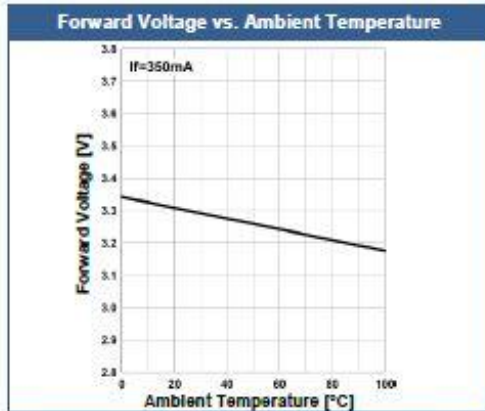
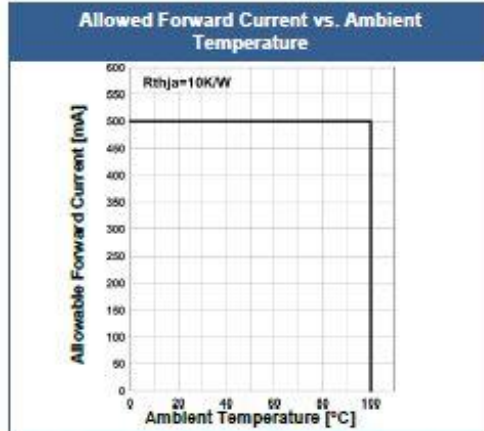
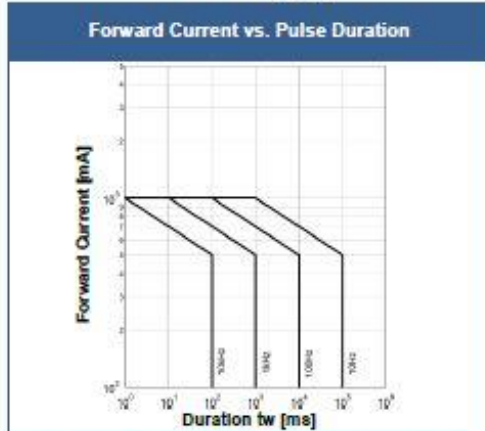
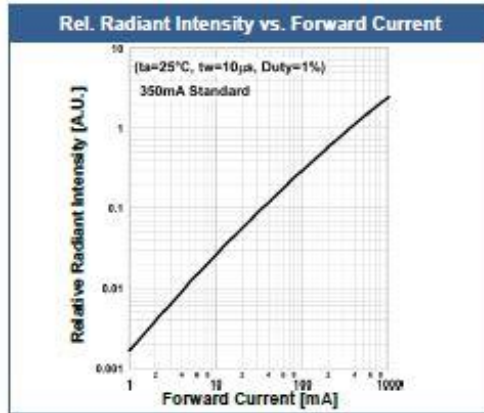
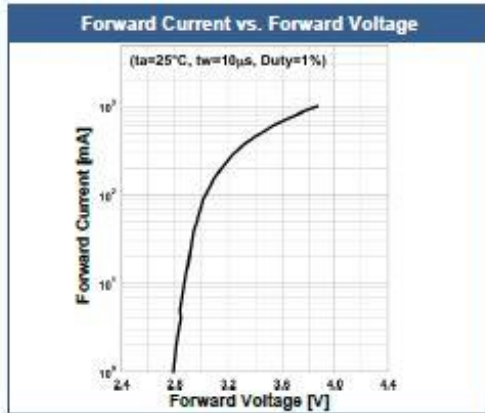
Parameter	Symbol	Conditions	Values			Unit
			Min.	Typ.	Max.	
Peak Wavelength	λ_P	$I_F=350mA$	410		430	nm
Dominant Wavelength	λ_D	$I_F=350mA$		431		nm
Half Width	$\Delta\lambda$	$I_F=350mA$		13		nm
Forward Voltage	V_F	$I_F=350mA$		3.3	3.8	V
	V_{FP}	$I_{FP}=700mA$		3.8		
Radiated Power *	P_O	$I_F=350mA$		420		mW
		$I_{FP}=700mA$		770		
Radiant Intensity *2	I_E	$I_F=350mA$		1100		mW/sr
		$I_{FP}=700mA$		200		
Luminous Flux	Φ_V	$I_F=350mA$		3.0		lm
Viewing Angle	φ	$I_F=100mA$		22		deg.
Rise Time	t_r	$I_F=350mA$		30		ns
Fall Time	t_f	$I_F=350mA$		80		ns

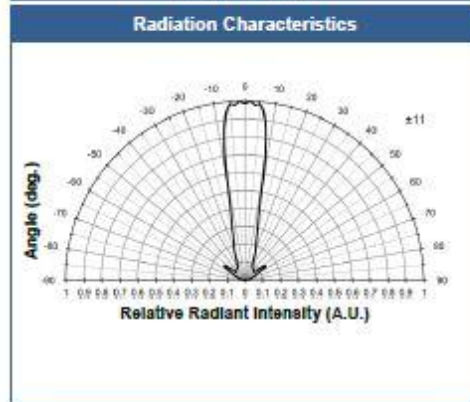
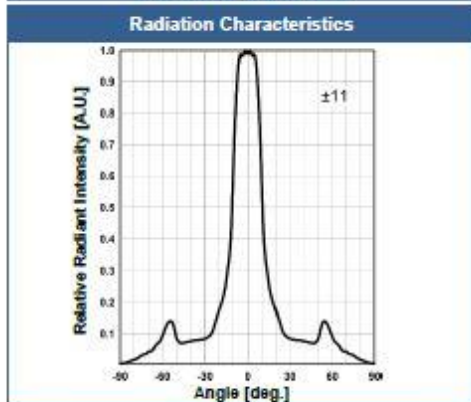
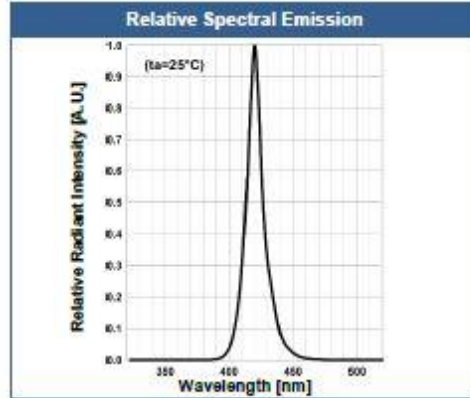
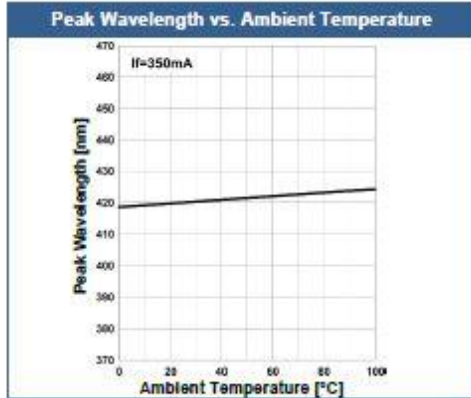
*1 measured by S3584-08

*2 measured by CIE127-2007 Condition B

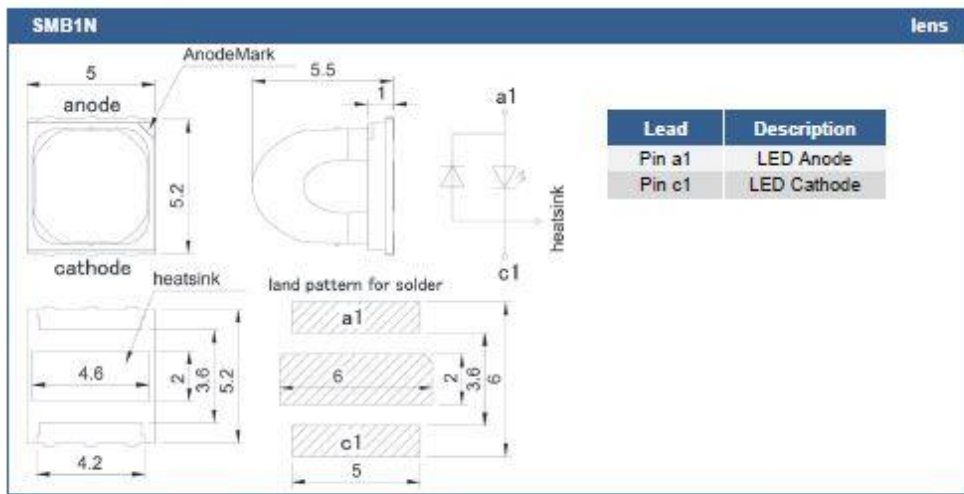


Typical Performance Curves





Outline Dimensions



All Dimensions in mm



Precautions

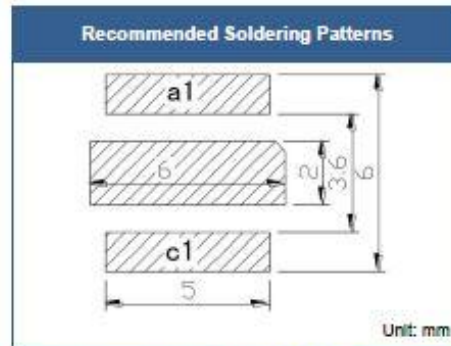
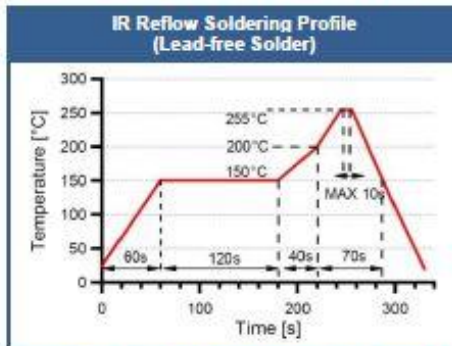
Soldering:

- Do avoid overheating of the LED
- Do avoid electrostatic discharge (ESD)
- Do avoid mechanical stress, shock, and vibration
- Do only use non-corrosive flux
- Do not apply current to the LED until it has cooled down to room temperature after soldering

Recommended soldering conditions:

This LED is designed to be reflow soldered on to a PCB. If dip soldered or hand soldered, its reliability cannot be guaranteed.

Nitrogen reflow soldering is recommended. Air flow soldering conditions can cause optical degradation, caused by heat and/or atmosphere.



Above table specifies the maximum allowed duration and temperature during soldering. It is strongly advised to perform soldering at the shortest time and lowest temperature possible.

Cleaning:

Cleaning with isopropyl alcohol, propanol, or ethyl alcohol is recommended
DO NOT USE acetone, chloroform, trichloroethylene, or MKS
DO NOT USE ultrasonic cleaners

Static Electricity:

LEDs are sensitive to electrostatic discharge (ESD). Precautions against ESD must be taken when handling or operating these LEDs. Surge voltage or electrostatic discharge can result in complete failure of the device.

Radiation:

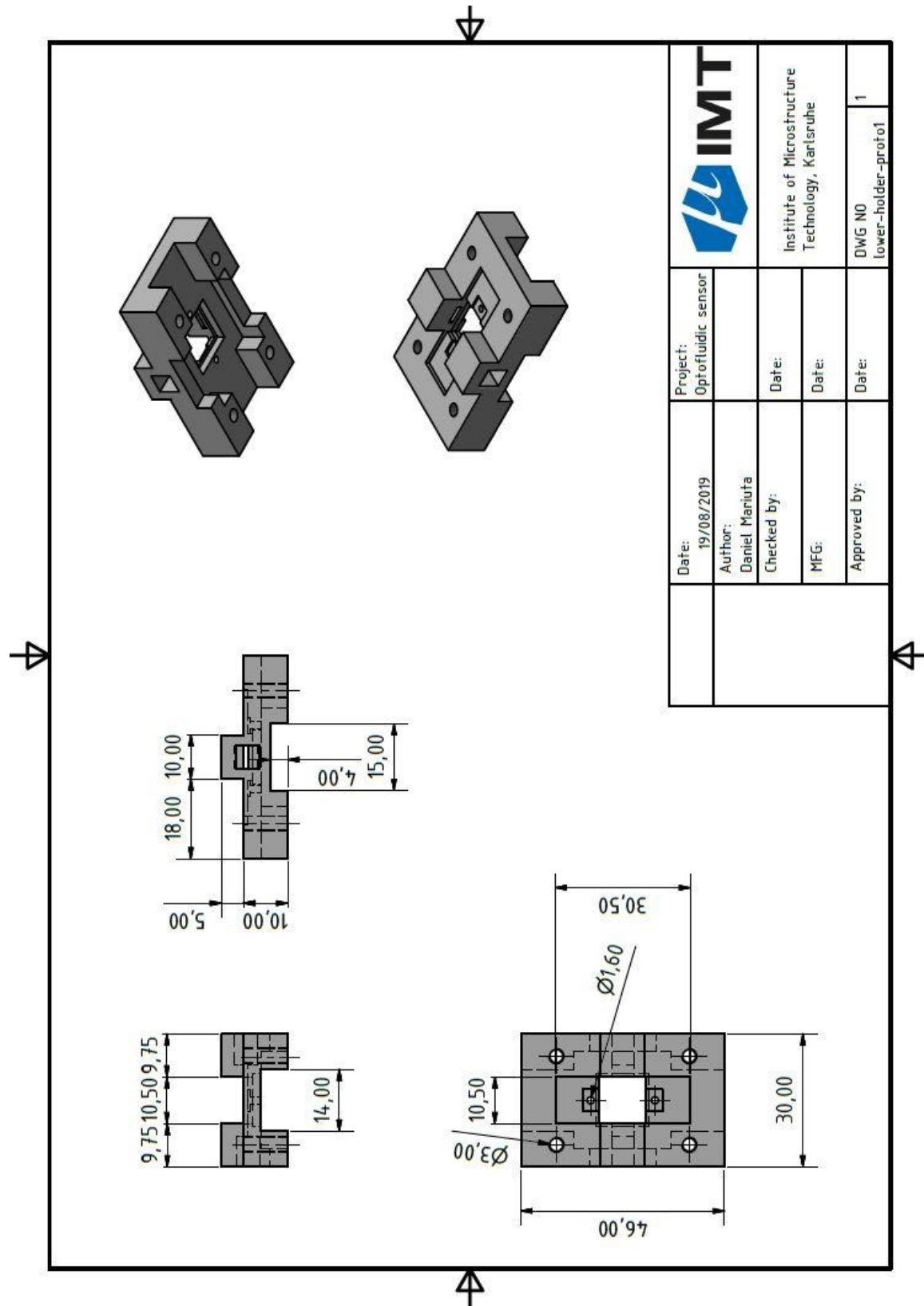
During operation these LEDs do emit high intensity light, which is hazardous to skin and eyes, and may cause cancer. Do avoid exposure to the emitted light. Protective glasses are recommended. It is further advised to attach a warning label on products/systems.

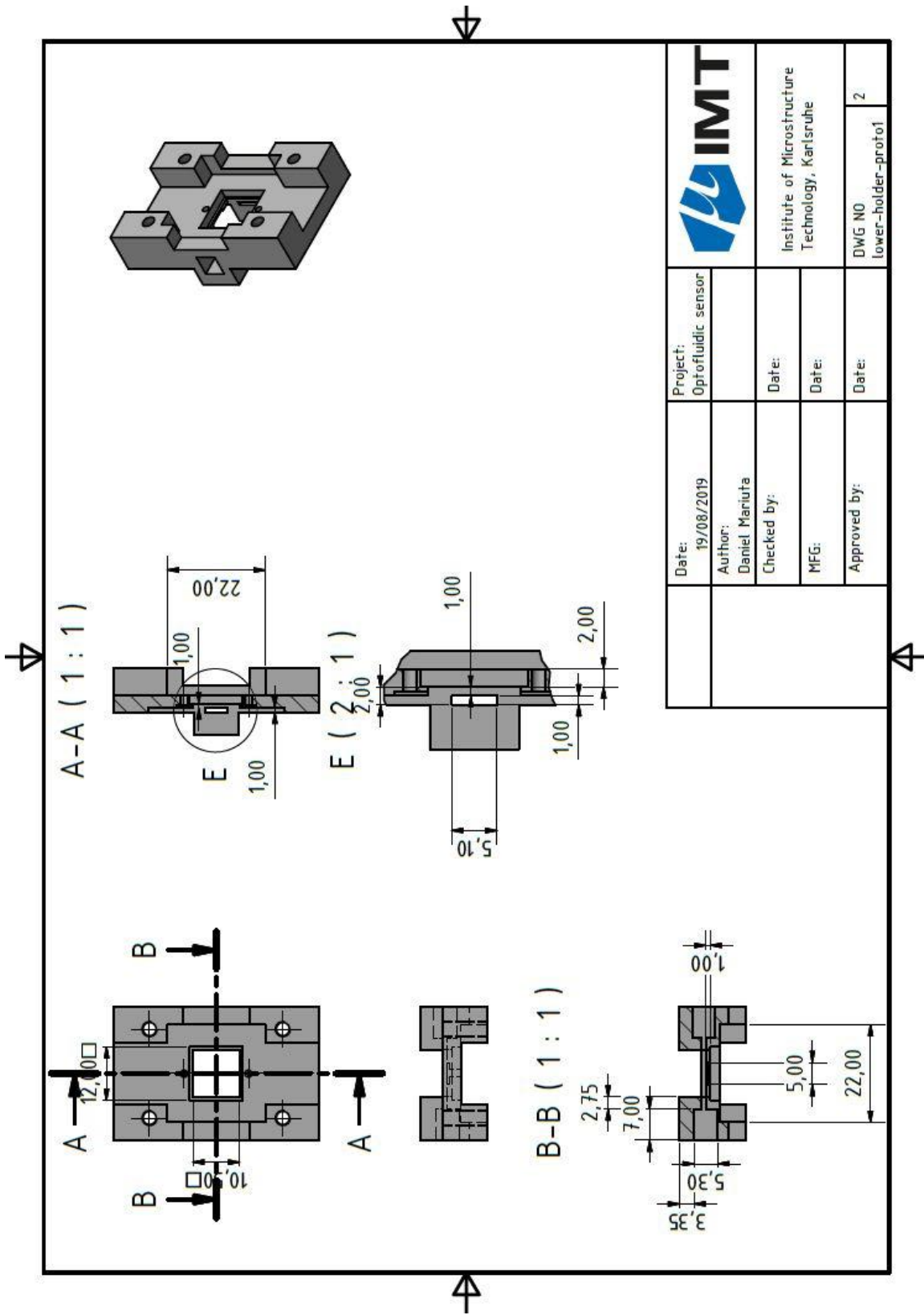
Operation:


Do only operate LEDs with a current source.

Running these LEDs from a voltage source will result in complete failure of the device. Current of a LED is an exponential function of the voltage across it. Usage of current regulated drive circuits is mandatory.

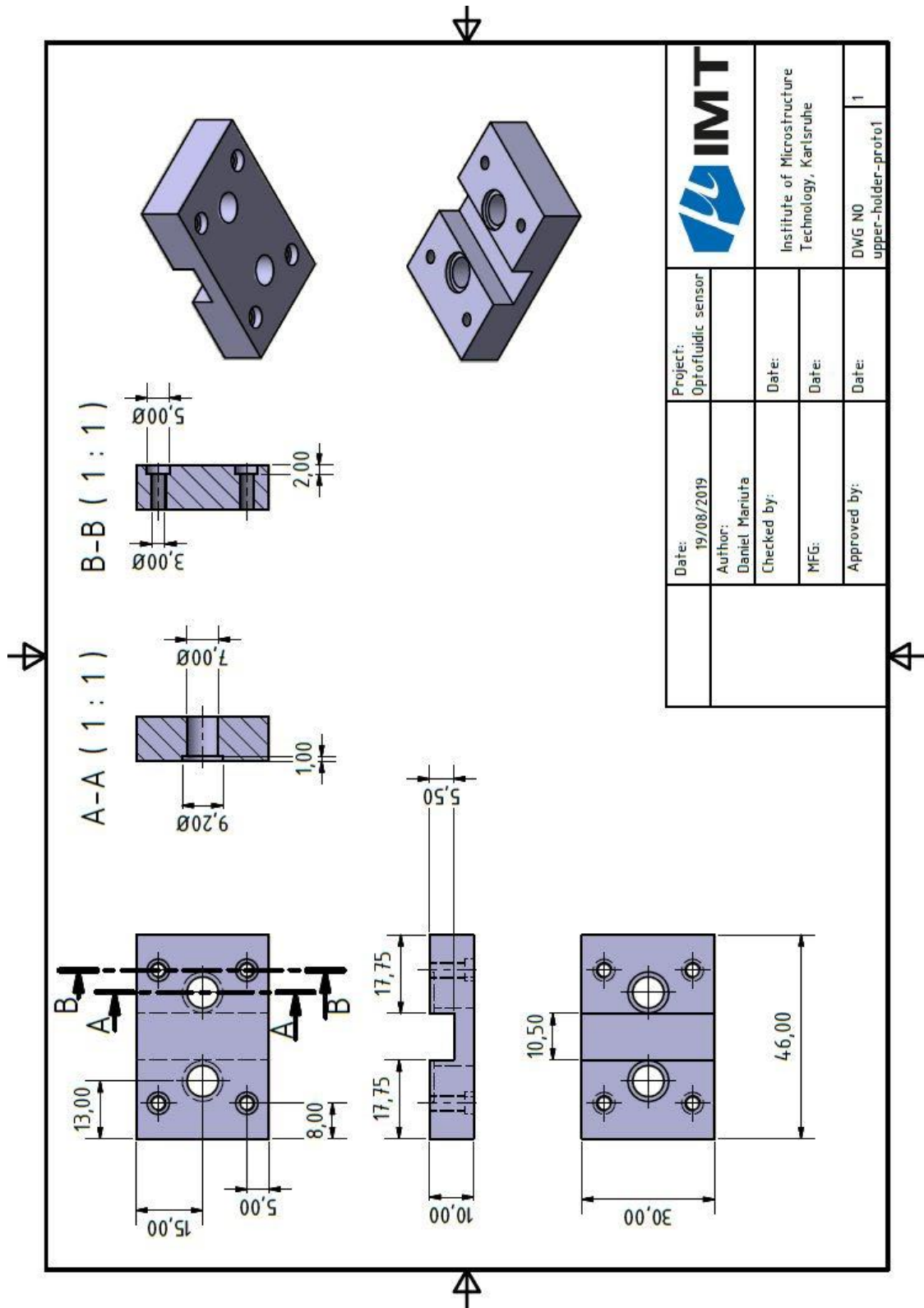
A3. Technical drawing of the fluorescence detector lower holder






		Institute of Microstructure Technology, Karlsruhe		DWG NO lower-holder-protol 2	
Date:	19/08/2019	Project:	Opröfluidic sensor	Date:	
Author:	Daniel Mariuta	Checked by:		Date:	
MFG:		Approved by:		Date:	

A4. Technical drawing of the fluorescence detector upper holder



		Project: Optofluidic sensor	
		Date: 19/08/2019	Date:
Author: Daniel Mariuta		Date:	Date:
Checked by:		MFG:	Date:
Approved by:		Date:	
DWG NO		1	
upper-holder-protot			

A5. Hydrophobic membrane Data Sheet

DATA SHEET



aspire® ePTFE Membrane Laminate

Product Type: QL217
Description: Hydrophobic ePTFE Membrane Laminate
 Functional Layer: PTFE
 Backer Material: Polypropylene

Reference Pore Size	Nominal 0.2 µm
Air Permeability	0.07 – 0.25 ft ³ /ft ² /min @ 125 Pa (2.1 – 7.6 mL/min/cm ² @ 125Pa), ASTM D737
Thickness	0.006 – 0.010 inches (0.15 – 0.25mm), ASTM D1777
Wet Mullen's Burst	>35 PSI (2.4 bar), ASTM D751
Water Entry Pressure	>60 PSI (4 bar), MEM-QA-W-071
IPA Bubble Point	≥17 PSI (1.2 bar), ASTM F316
Available Dimensions	OEM membranes as custom slit roll goods. Membrane vents in customized shapes.

All above data is nominal and provided for information only and is subject to change. All metric conversions are approximate.

The CLARCOR Industrial Air Difference

We have a history of continuous innovation behind our premium grade products and treatments. The broadest portfolio of membrane products in the industry as well as custom solutions. It's not only unique, it's only available from CLARCOR Industrial Air.

For more information, contact your **aspire** representative at CLARCOR Industrial Air:

11501 Outlook Street, Suite 100 | Overland Park, KS 66211

T: +1.800.821.2222 | T: +1.816.358.8400 | F: +1.816.353.1873 | Email: aspire@clarcor.com

www.CLARCORIndustrialAir.com

©2014 BHA A&E, LLC. All rights reserved. **aspire** is a registered trademark of BHA A&E, LLC. (BHD-00-P-034 (03/2017))

A6. Convective-diffusive transfer mechanism in gas-liquid membrane-based interaction

Two-phase flows separated by membranes are advantageous because their hydrodynamics are easier controllable and reproducible, although membranes can work only for limited periods of time due to the fouling and ageing phenomena occurring.

The mass-transfer process in convective-diffusive flows separated by hydrophobic membranes is represented in Fig. A.6.1. The additional resistance imposed by the membrane, $R_m = \frac{1}{k_m}$, is influenced by its mode of operation. The pores of the membrane can be completely gas-filled in hydrophobic membranes, partially-liquid-filled, or liquid-filled. R_m increases proportionally with the length of the pore filled with liquid.

The ideal case is represented by the fully-gas filled pores when R_m is minimized, and the least desired scenario is the case of fully-liquid filled pores (wetted pores) when R_m is maximized.

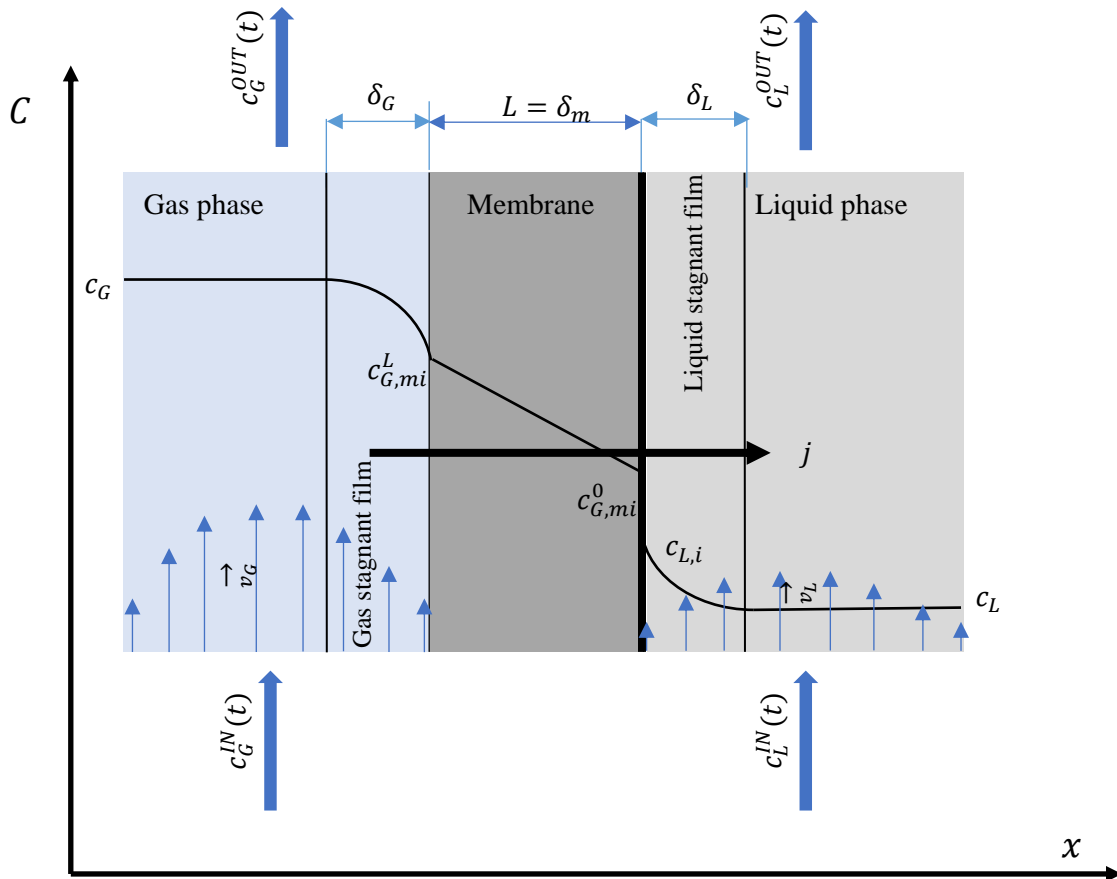


Figure A.6.1. Two-film transport model for a membrane-based gas-liquid mass transfer from the gas phase towards the liquid phase, where x is the length, C is the concentration, \vec{v}_G is the gas velocity vector, \vec{v}_L is the liquid velocity vector, j is the total mass flux, δ_G is the gas stagnant film thickness, δ_L is the liquid stagnant film thickness, δ_m is the thickness of the membrane, c_G is the gas bulk concentration, c_L is the liquid bulk concentration.

In this situation, the membrane is named “fouled”. To avoid this situation, liquid entry pressure, p_{LEP} , has been introduced:

$$p_{LEP} = \frac{\beta \gamma_L \cos \theta}{d_p} \quad (\text{A.6.1.})$$

In Eq. A.6.1., β is a dimensionless parameter depending on the geometry of the pore. If the pore is cylindrical, $\beta = 1$. If not, $0 < \beta < 1$. γ_L is the liquid surface tension. The condition to be respected for fully-gas filled pores is:

$$p > p_{LEP} \quad (\text{A.6.2.})$$

The flux across the membrane can be assumed constant. Usually, the transfer process considered in a membrane is only diffusion.

The mean free path, λ , of the molecular diffusion process into the pore of a membrane relative to the reference pore diameter dictates the diffusion mechanism occurring. Though, diffusion in porous media is classified depending on the Knudsen number, Kn . Kn is the ratio between the mean free path, λ , and the diameter of the pore, d_p . In flows where $Kn < 0.01$, the diffusion is molecular. If $Kn > 10$, then Knudsen diffusion, D_{Kn} , governs. In $10 < Kn < 0.01$ range, a transition diffusion regime takes place in which both molecular and Knudsen diffusion occurs simultaneously. Knudsen diffusion can be calculated using the equation:

$$D_{Kn} = \frac{1}{3} d_p \sqrt{\frac{8k_B T}{\pi M}} \quad (\text{A.6.3.})$$

In transition diffusion regime, the effective membrane diffusion coefficient is given by Eq. A.6.4. where D_G is the gas molecular diffusion in the binary mixture.

$$D_{eff} = \left(\frac{1}{D_{Kn}} + \frac{1}{D_G} \right)^{-1} \quad (\text{A.6.4.})$$

Therefore, diffusion through membranes occurs with a smaller diffusion coefficient, known as the effective diffusion coefficient, D_{eff} . Moreover, in gas-diffusion through gas-filled pores, D_{eff} influences the permeability and the permeance of the membrane. Additionally, the permeability is influenced by the membrane thickness, L , its porosity, ε_m , and its tortuosity, τ_m .

Permeability is a membrane characteristic inversely proportional to the tortuosity of the pore.

Tortuosity and porosity are linked together by a couple of correlations. When the pores are cylindrical, the Bruggeman model can be applied (see Tjaden *et al.*, [244] and Anne [246]):

$$\tau_m = \varepsilon_m^{-1/2} \quad (\text{A.6.5.})$$

A couple of correlations were introduced to estimate the effective diffusivity, D_{eff} , across the membrane, such as that proposed by Weissberg [247] as function of the void fractions and physical diffusion coefficient of the gas, another proposed by Mackie and Meares [248], or presented by Liu *et al.*, [249] who determined a correlation for the effective diffusion coefficient considering Knudsen diffusion.

The flux, j , in thin membranes can be found by combining Fick’s law with the concentration profiles:

$$j_m = \frac{D_{eff} \varepsilon_m}{\delta_m \tau_m} (c_{G,mi}^L - c_{G,mi}^0) = \frac{D_{eff} \varepsilon_m}{\delta_m \tau_m} \left(c_{G,mi}^L - \frac{c_L}{H^{cc}} \right) \quad (\text{A.6.6.})$$

In Eq. A.6.6., the $\frac{D_{eff}\varepsilon_m}{\delta_m\tau_m}$ ratio is actually the membrane-mass-transfer coefficient, k_m . Resistance-in-Series of the two-film theory for gas-liquid membrane interactions results after coupling the Eq. A.6.6. to the flux equations on each side of the interface (see Eqs. A.6.9. – A.6.10.).

$$j_G = k_G(c_G - c_{G,i}) \quad (\text{A.6.7.})$$

$$j_L = k_L(c_L - c_{L,i}) \quad (\text{A.6.8.})$$

$$\frac{1}{K_L} = \frac{1}{k_L} + \frac{H^{cc}}{k_m} + \frac{H^{cc}}{k_G} \quad (\text{A.6.9.})$$

$$\frac{1}{K_G} = \frac{1}{H^{cc}k_L} + \frac{1}{k_m} + \frac{1}{k_G} \quad (\text{A.6.10.})$$

Simplified kinetic model to describe the convective-diffusive transport

Further, a simplified kinetic model describing the convective-diffusive transport in a membrane assumed to have cylindrical pores has been described as an alternative to the model presented above (see Fig. A.6.2.).

HCHO trapping from a microfluidic gas stream into a reagent stream is mathematically described using a convection-diffusion equation that is assumed to govern the flow of the molecules in the channels, separated by the porous membrane. In equilibrium at temperature T ,

$$n_L = H(T) n_G \quad (\text{A.6.11.})$$

n_L and n_G are equilibrium number densities of molecules in the liquid and gas phase, respectively, if the solution is in the ideal regime. If not, Eq. A.6.11. has to be replaced by a more complicated relationship. However, any change in Eq. A.6.11. does not affect the model described below.

If n_L and n_G denote arbitrary values of densities in the liquid and the gas with the system not being in equilibrium. Then, the liquid phase injects J^+ molecules per time unit and area unit into the gas. According to Henry's law,

$$J^+ = \alpha \frac{n_L}{H(T)} \sqrt{\frac{RT}{2\pi}} \quad (\text{A.6.12.})$$

α stands for the accommodation coefficient. On the other hand, the flux of the gas phase molecules condensing (trapped) onto the liquid phase is

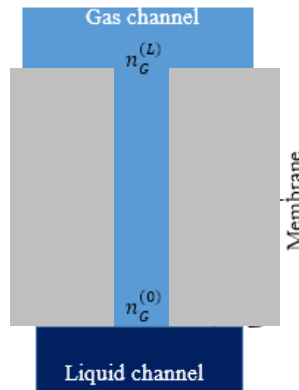


Figure A.6.2. Cylindrical pore assumed in the alternative kinetic model with $\tau_m = 1$.

$$J^- = \alpha n_g \sqrt{\frac{RT}{2\pi}} \quad (\text{A.6.13.})$$

Hence, the total net solute molecules flux across the interface is:

$$J = \alpha \sqrt{\frac{RT}{2\pi}} \left(\frac{n_L}{H(T)} - n_G \right) \quad (\text{A.6.14.})$$

$J = 0$, when n_L and n_G follow Henry's law.

It is assumed that convection is negligible within nanopores and diffusion is the main mechanism. In addition, diffusion will be considered quasi-steady inside a pore:

$$n_G(x) = n_G^{(0)} + \frac{n_G^{(L)} - n_G^{(0)}}{L} x \quad (\text{A.6.15.})$$

Fick's law of number densities is similar with the one written in terms of concentrations:

$$J = -D_{eff} \frac{\partial n_G}{\partial x} \quad (\text{A.6.16.})$$

Combining Eqs. A.6.13. and A.6.15. results to:

$$\frac{n_G^{(L)} - n_G^{(0)}}{L} = -\frac{1}{D} \alpha \sqrt{\frac{RT}{2\pi}} \left(\frac{n_L}{H(T)} - n_G^{(0)} \right) \quad (\text{A.6.17.})$$

$$n_G^{(0)} = \frac{n_G^{(L)} + \alpha \sqrt{\frac{RT}{2\pi}} \frac{L}{D_{G,eff}} \frac{n_L}{H(T)}}{1 + \alpha \sqrt{\frac{RT}{2\pi}} \frac{L}{D_{G,eff}}} \quad (\text{A.6.18.})$$

It should be noted that Eq. 6.176 allows to compute J knowing the molecular densities, $n_G(L)$ and $n_G(0)$ in the gas channel and the liquid channel. It will be assumed that the convection-diffusion eq. governs the flow of the molecules in the channels, separated by the porous membrane. Now the liquid channel is considered with assumption that $\alpha_r n_L$ is a sink term due to chemical reaction.

$$\frac{\partial n_L}{\partial t} + V_x(y, z) \frac{\partial n_L}{\partial x} = D_L \nabla^2 n_L - \alpha_r n_L \quad (\text{A.6.19.})$$

The average of n_L over a channel section is considered.

$$\Phi_L(x, t) = \frac{1}{S} \int dy dz n_L, S = L_y \cdot L_z \quad (\text{A.6.20.})$$

Substituting in Eq. 2.1.65. and integrating leads to:

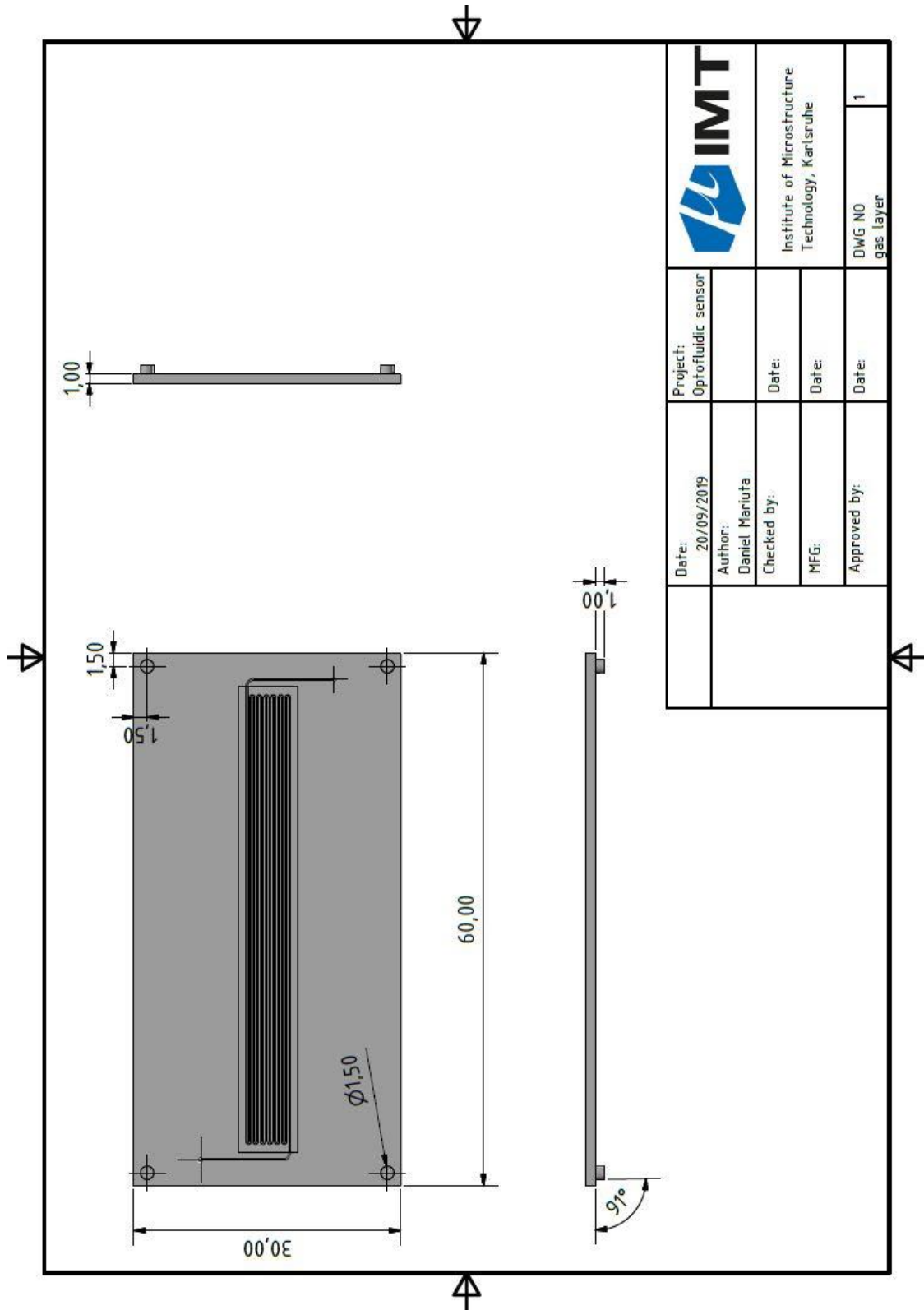
$$\frac{\partial \Phi_L}{\partial t} + \bar{V}_L \frac{\partial \Phi_L}{\partial x} = D_L \frac{\partial^2 \Phi_L}{\partial x^2} - \alpha_r \Phi_L + \frac{1}{L_y} J A_f \quad (\text{A.6.21.})$$

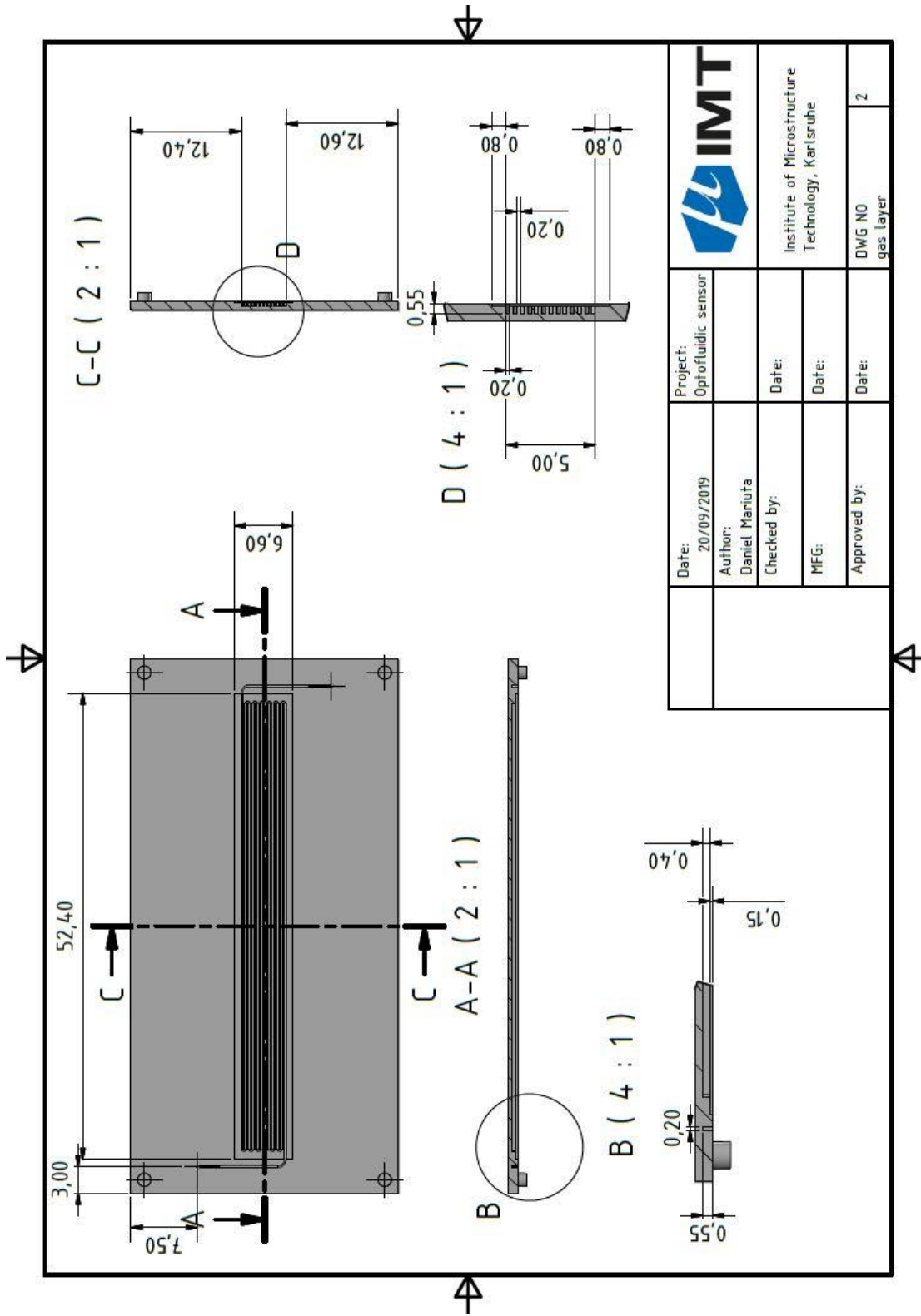
\bar{V} is the average flow velocity across the channel section and A_f is the fraction of permeable membrane area. A_f is given by the porosity, ε_m . Applying the same assumptions for the gas layer, a similar equation result.


$$\frac{\partial \Phi_G}{\partial t} + \bar{V}_G \frac{\partial \Phi_G}{\partial x} = D_G \frac{\partial^2 \Phi_G}{\partial x^2} - \frac{1}{L_y} J A_f \quad (\text{A.6.22.})$$

Replacing the number densities with concentrations and α_r with k' , the Eqs. A.6.19. – A.6.22. can be used to estimate the time-dependent concentration profiles from inlet towards outlet in both the gas and the liquid phases in a 3D model.

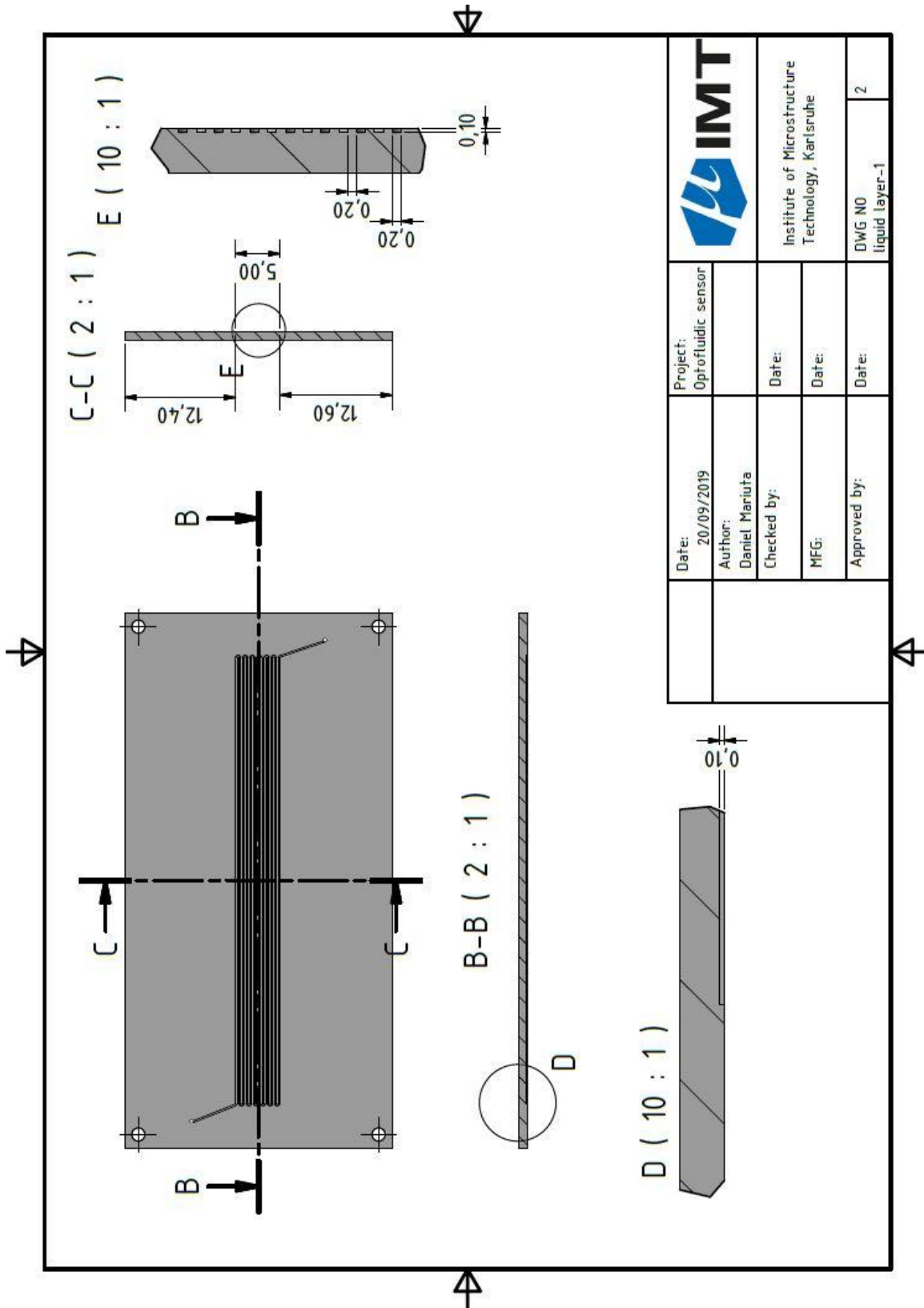
A7. Technical drawing of the gas carrying layer




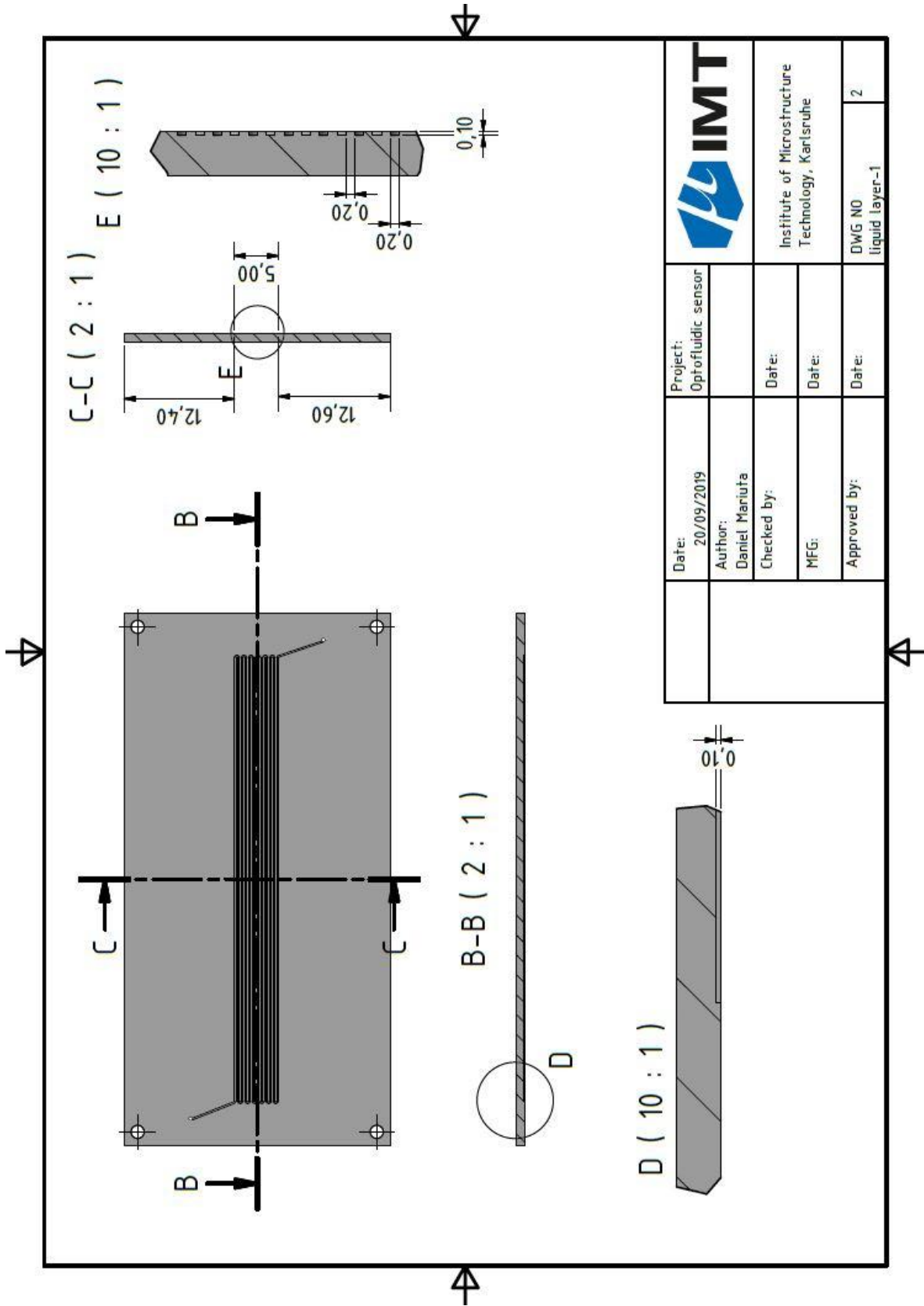



		Institute of Microstructure Technology, Karlsruhe		DWG NO	2
		gas layer			
Date:	20/09/2019	Project:	Optofluidic sensor	Date:	
Author:	Daniel Mariuta	Checked by:		Date:	
MFG:		Approved by:		Date:	

A8. Technical drawing of the liquid carrying layer



	Institute of Microstructure Technology, Karlsruhe		DWG NO	liquid layer-1	2
	Project: Oprofluidic sensor	Date:	Date:	Date:	Date:
Date: 20/09/2019	Author: Daniel Mariuta	Checked by:	MFG:	Approved by:	



	Project:	Optofluidic sensor
	Date:	20/09/2019
Author:	Daniel Mariuta	Date:
Checked by:		Date:
MFG:		Date:
Approved by:		Date:
DWG NO	liquid layer-1	2

A9. Convection-diffusion mass-transfer in slug flows

Slug and annular flows are the flow patterns usually used as direct gas-liquid contacting. Since slug flow is a more stable and easier to reproduce pattern [181]. Generally, the mass-transfer in slug flows is described using the Eq. A.9.1, where u_{TP} is the total superficial velocity of the two phases and a is the surface-to-volume ratio.

$$u_{TP} \frac{dc}{dx} = k_L a (c_G - c_G^*) \quad (\text{A.9.1})$$

A recent summary of the correlations found in literature to determine the overall-mass transfer coefficients, $k_L a$, is presented in Butler *et al.*, [250] and Abiev *et al.*, [251]. Mass transfer has two components in slug flows; one is represented by the transfer in the caps and one by the transfer in the liquid film (see Fig. A10.1., a). The total gas-liquid interface area is given by the lateral interface (liquid film-bubble) and the perpendicular one (slug-bubble). Generally, the lateral interface contributes with approximately 90% of the total interface at the mass transfer final efficiency [63]. Therefore, if the liquid film does not exist, as it usually occurs in hydrophobic channels, the mass transfer efficiency is drastically reduced. Thus, hydrophilicity of the channel is crucial in order to maintain the liquid film near walls.

The mass transfer in slug flows is enhanced by the intense recirculation taking place in the slugs [198] (see Fig. A9.1., b, c). Though, while the transfer in the slugs is convection dominated, the film transfer is dominated by diffusion. Fries *et al.*, [187,199] and Sotowa *et al.*, [198] showed that mass transfer is slightly enhanced by the curved sections of meandering channels [196]. Larger Dean numbers are observed in meandering channels, leading to a more efficient mixing. In this work, it was also concluded that Higbie's model overpredicted the mass

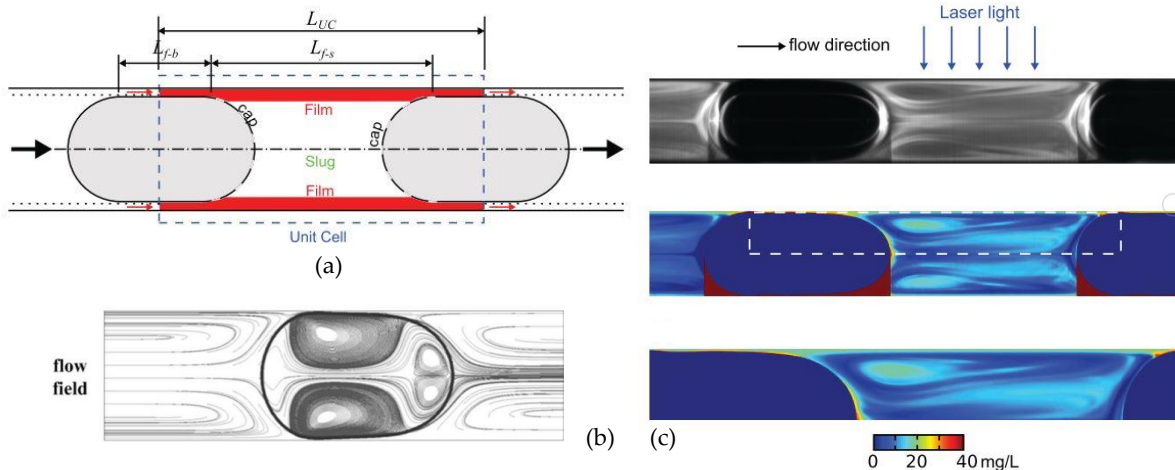


Figure A.9.1. (a) Slug flow configurations with two gas bubbles located at distance L_{UC} one from the other, the liquid film, and the slug located in between the bubbles. (b) Streamline configuration in the gas bubble and the slug neighbouring it. (c) Experimental visualization of the concentration fields of oxygen in the slug and near the gas-liquid interface. Reproduced with permission from Butler *et al.*, [250].

transfer coefficients in annular flows and slug flows [196,200]. The overprediction occurs mainly in the cases where saturation of liquid films interrupts the transfer flux.

A10. Convection-diffusion mass-transfer in annular flows

In the freshly published review of Yao *et al.* [182] the authors suggested the mass transfer in annular flows as a possibility that needs much more attention in the near future since the field is not yet fully characterized. Large interface area characterizing this flow regime maximize the surface-to-volume ratio, a , and by consequence the volumetric-mass-transfer coefficient, $k_L a$.

However, gas-liquid contactors/microreactors based on annular flow are scarcely studied [181] despite their potential superiority for particular applications, apparently as a consequence of the short contact time between the phases [128].

The difficulty in characterization and prediction of annular flows originates from the Kelvin–Helmholtz instabilities of the gas-liquid interface [252]. The interface instabilities are influenced by the wettability of the microchannel wall [185], roughness [186], curved sections of the microchannel [187,188], and pulsations of the systems used to stream the fluids in.

One rare analysis of annular flow mass-transfer is given by Sobieszuk *et al.* [200]. They analyzed the volumetric-mass-transfer coefficients for the absorption of CO₂ in water and compared them to those obtained in slug flows. The absorption rate in annular flow is defined as:

$$N = k_L a c_{Ai}^{AV} V \quad (\text{A.10.1.})$$

$$c_{Ai}^{AV} = \frac{c_{i1} - c_{i2}}{\ln \frac{c_{i1}}{c_{i2}}} \quad (\text{A.10.2.})$$

$$r = \frac{\sqrt{2}}{2} d_H - \delta \quad (\text{A.10.3.})$$

$$a = \frac{2\pi r L}{V} \quad (\text{A.10.4.})$$

In these equations, c_{Ai}^{AV} is the average gas concentration at the interface, r is the radius of the gas cylinder, δ is the liquid film thickness, c_{i1} is the species concentration at inlet, and c_{i2} is the species concentration at outlet [200].

Comparing the $k_L a$ values obtained for various total superficial velocities in annular flow with the $k_L a$ values obtained for CO₂ absorption in slug flow by the same authors, it was concluded that $k_L a$ of annular flows are around two orders of magnitude lower [181,200]. One experimental observation in this study highlights the enhancement of $k_L a$ once the total superficial velocity increases.

Annular flow still lacks complete experimental observation [189]. For a straight channel, Humphry *et al.*, [190] showed that by making the channel width comparable with the channel height, the interface instabilities can be suppressed. Sur *et al.*, [191] observed that usually the thickness of the liquid film decreases with the diameter of the microchannel.

Takeda *et al.*, [188] presented the hydrodynamic effects of two-phase flows in meandering millichannels. An interesting observation from this study states that in a hydrophobic channel

the pressure drop tends to reach its local maximum at the transition from the slug flow towards the slug-annular flow. In the hydrophilic channel, this effect is not observed since walls are always wetted. Up to the author's knowledge, there is no experimental method for visualization of the annular mass-transfer from a phase to another, as it was developed and validated for slug flows [192].

List of publications

Journal articles

1. Daniel Măriuța, Stéphane Colin, Christine Barrot-Lattes, Stéphane Le Calvé, Jan G. Korvink, Lucien Baldas & Jürgen J. Brandner, **Miniaturization of fluorescence sensing in optofluidic devices**. *Microfluid Nanofluid* 24, 65 (2020).
<https://doi.org/10.1007/s10404-020-02371-1>.
(7469 accesses , 17 citations)
2. Mariuta, D.; Govindaraji, A.; Colin, S.; Barrot, C.; Le Calvé, S.; Korvink, J.G.; Baldas, L.; Brandner, J.J. **Optofluidic Formaldehyde Sensing: Towards On-Chip Integration**. *Micromachines* 2020, 11, 673.
<https://doi.org/10.3390/mi11070673>
(2523 accesses, 2 citations)

Conferences with proceedings

1. 10th International Conference on Chemistry and Chemical Engineering (ICCCE 2019), July 22-24, University of Oxford, Oxford, the United Kingdom.

Daniel Mariuta, Lucien Baldas, Stéphane Colin, Stéphane Le Calvé, Jan Gerrit Korvink, et al.. **Prototyping a miniaturized microfluidic sensor for real-time detection of airborne formaldehyde**. *International Journal of Chemical Engineering and Applications*, 2020, 11 (1), pp.23-28. ff10.18178/ijcea.2020.11.1.774ff.

2. International Symposium on Thermal Effects in Gas flows In Microscale (ISTEGIM), October 24-25, 2019, Ettlingen, Germany.

Conferences

1. 29th Mediterranean Conference on Control and Automation (MED2021), June 22-25, 2021, Bari, Italy.
2. Third MIGRATE International Workshop, June 2018, Bastia, France.
3. MicroFluidics and Non-Equilibrium Gas Flows Conference 2018, 28th of February - 2nd of March, Strasbourg, France
4. Second MIGRATE Summer School & Workshop, 26 – 30 June, 2017, Sofia, Bulgaria.